Deploying Structures:
Concepts and Analysis

Dissertation submitted to the University of Cambridge
for the Degree of Doctor of Philosophy

by

Simon David Guest

Corpus Christi College

May, 1994

To my parents

Acknowledgments

The work described in this dissertation was carried out in the Department of Engineering at the University of Cambridge between October 1990 and March 1994.

First and foremost my thanks go to my supervisor, Dr. S. Pellegrino for his help, guidance and friendship; his unflagging enthusiasm was inspiring. Also I would like to thank Dr. J.F. Clemmet and R. Dace of BAe Space Systems for many helpful suggestions and discussions.

I would like to thank all those who have helped me with practical aspects of the work. In particular my thanks go to Keith Seffen and Tom Wedgwood, who carried out much of the practical work on foldable cylinders as part of their final year undergraduate projects, and to Roger Denston, for all his help and advice. Also I am grateful to Irathane UK for supplying Irathane coated plates.

I would like to thank all of the Structures Research Group, and in particular Antony Darby, Alan Kwan, Praveen Kumar, Tim Ibell, Earl Lancaster, Cam Middleton, Gopal Srinivasan and Zhong You, for their friendship, and their contribution to many memorable and enjoyable occasions.

Finally I would like to thank my wife, Karen, for her support and encouragement throughout this work, and most particularly while I wrote this dissertation.

Financial support was received from the Science and Engineering Research Council and BAe Space Systems in the form of a CASE studentship, and travel grants were received from Corpus Christi College and the Engineering Department.

Declaration

The author declares that, except for commonly understood and accepted ideas, or where specific reference is made to the work of other authors, the contents of this dissertation are his own work, and includes nothing that is the outcome of work done in collaboration. This dissertation has not been previously submitted, in part or in whole, to any University or institution for any degree, diploma, or other qualification. This dissertation is presented in 163 pages.

Abstract

Deployable structures are structures which can fold, either for transportation or for storage. The main application of deployable structures is for use in space. Launch vehicles are limited in size, while large structures are required for many current and proposed uses of space. Because of the high cost of failures, however, the space industry is conservative in its use of deployable structures. This dissertation is an attempt to inject new ideas into the field of deployable structures.

Three concepts for deployable structures are presented. Two of the concepts are new, a generic class of foldable cylinders, and a new solid surface deployable reflector. The third concept is an old idea for folding a membrane, which has been re-analysed and extended. Some analysis is done for each of these concepts to prove their viability.

Foldable cylinders are triangulated cylinders which fold axially into a compact stack of plates. The concept of foldable cylinders is introduced, and a geometric approach to their folding is pursued. This provides valuable insights into the folding process. Folding is also modelled computationally, which explains the behaviour observed during experiments. A number of these cylinders have been manufactured and tested.

Folding a membrane by wrapping it around a central hub was first proposed in the 1960's. Most recently it has been suggested as a method of folding a space-sail. Previous work on this concept is reviewed, and a new analysis of the fold pattern is presented. This corrects a number of errors in previous work, and suggests ways in which the concept can be extended.

A solid surface deployable antenna is presented. This is a new method of folding an antenna, suggested by the wrapping fold pattern. It improves on previous concepts, as it both shows a large reduction in size when folded, and requires no complex mechanical components. The folding of the antenna is modelled with a new technique, using dual quaternions to represent rigid body displacements. This analysis is used to optimise the design of the antenna to minimise deformation during folding. A simple proof of concept model of the antenna has been manufactured and tested.

Keywords

Deployable structure, Deployable antenna, Folding, Membrane folding, Finite Displacements, Finite rotations, Quaternions

CONTENTS

1. INTRODUCTION

Deployable structures are structures that can be easily reduced in size for transportation or storage. A number of everyday structures could be classed as deployable; tents and umbrellas are two simple examples.

Current interest in deployable structures arises mainly from their potential in space. Many space applications, both current and proposed, require large structures in space. Typical examples include satellites for communications, earth observation, astronomy, and space exploration. However, launch vehicles, such as NASA's space shuttle, are, and for the foreseeable future will continue to be, limited in size.

The space industry, because of the high cost of failures in space, tend to be conservative in their use of deployable structures. This dissertation is an attempt to inject new ideas and concepts into the field of deployable structures. These concepts may suggest new, and better, ways of doing old tasks, or make possible new applications for spacecraft.

The dissertation is split into three parts. Each part introduces a concept, and gives some general analysis concerning the shape and unfolding characteristics of that concept. The three concepts are: a method for folding a cylinder; a method for folding a membrane; a method for folding an antenna with a rigid surface. Of these concepts, the first and the third are completely new. The second concept, the method of folding a membrane, has been suggested a number of times before, but this dissertation gives the first correct analysis of the fold pattern, which also suggests a number of ways that the folding concept can be extended.

The dissertation proceeds as follows. Chapter 2 gives a brief overview of previous work in deployable structures, and goes into more depth on other work relevant to each of the three concepts developed.

Chapters 3, 4, and 5 make up Part I of the dissertation, the work on foldable cylinders. Chapter 3 introduces foldable cylinders, and pursues a geometric approach to understanding the range of their potential configurations, and their folding properties. Chapter 4 presents a more detailed computer analysis of the cylinders, which explains a number of features observed during their folding. Chapter 5 describes the construction and test of a number of practical foldable cylinders, and also makes some additions to the computer model to further explain some of the observed experimental behaviour.

Chapter 6 makes up Part II of the dissertation. It explains an established concept of wrapping a membrane about a central hub. It presents a new analysis of this fold pattern, and suggests a number of new ways of extending the concept.

Chapters 7, 8, and 9 make up Part III of the dissertation, the development of a new solid surface deployable antenna. This antenna was inspired by the wrapping fold pattern of Part II. Chapter 7 develops a theory, based on the use of dual quaternions, which can analyse systems of rigid bodies undergoing finite rotations and displacements; this is an essential precursor to the work on designing the antenna. Chapter 8 describes the design process for the antenna, and Chapter 9 describes a model that was made and tested to prove this concept.

Chapter 10 concludes the dissertation, and describes a number of ways in which each of the concepts could be advanced further.

2. REVIEW OF PREVIOUS WORK

This chapter reviews previous work that is relevant to this dissertation. The first section gives a brief overview of the field of deployable structures, showing examples of why deployable structures are required, and some typical deployable structure concepts. The aim of this section is to establish the reasons for doing the work in this dissertation, and to set that work in context. It is not meant as a complete review of work on deployable structures; there are many alternative sources where such reviews may be found (NASA, 1984; Roederer & Rahmat-Samii, 1989; Hedgepeth, 1989; Kwan, 1991; Pellegrino, 1994).

The remaining three sections of the chapter go into more depth on work specifically relevant to each of the three concepts developed later in the dissertation.

2.1. Deployable Structures

The main reason for recent interest in deployable structures has been their potential application in space. Launch vehicles which put satellites into space are limited in size. The largest presently in use is NASA's space shuttle; it has a cargo bay 4.6 m in diameter, and 18.3 m long. Many present and proposed space missions require structures larger than this.

One way of making a structure fit into the limited space available for launch is to fold it, and then to automatically deploy it once in space. Another option is to use erectable structures that are taken to space in pieces, and put together in orbit, either by man, or by robots. However, it has been realised that using men in space is not only dangerous, but also expensive, because extra safety precautions are required. Robots are not sufficiently advanced to be able to autonomously erect a complex structure in space. This leaves deployable structures as the only viable option for almost all large space structures.

Another reason for using deployable (or erectable) structures in space is the high loads due to vibration experienced by a structure during launch. By using a deployable structure, a lightweight structure can be safely packaged and protected during this critical time.

There are a large number of possible applications which require large structures in space. These structures may be required for astronomy, earth observation, communications, or to provide solar power.

A common use of deployable structures is as deployable solar panels to provide the power requirements of modern satellites. The solar panels of the Hubble Space Telescope are a well-known example (Cawsey, 1982).

An example of a proposal to use large structures in space for astronomy has been the QUASAT project (Jordan *et al.*, 1984). This satellite is proposed to form part of a Very Long Baseline Interferometer, which would be used to study high-energy astronomical events such as quasars. The project requires an antenna on the spacecraft with a diameter of 15–20m.

Large antennae are also proposed for many communication satellites (Knouse & Weber, 1984). The advantage of a large antenna in space is that it enables the earth-based receivers and transmitters to be smaller in size, and to require less power. This is an obvious advantage for, e.g., a satellite-based mobile communication systems.

A large number of concepts have been proposed, and some used, as deployable structures. These concepts can generally be split into one-, and two-dimensional deployable structures.

One-dimensional deployable structures are typically used to move payloads away from the main body of the spacecraft, or as actuators in larger systems. Concepts for one-dimensional deployable structures include coilable masts (which will be mentioned in more detail in Section 2.2), thin shell masts such as STEM (Rimrott, 1967), and pantographic structures (Kwan *et al.*, 1993).

Two dimensional deployable structures include solar arrays and antennae. Antennae will be considered in more detail in Section 2.4. Concepts for solar arrays include those based on solid panels, e.g. de Kam (1984), and others where the arrays are made of furlable blankets, e.g. Cawsey (1982).

Although this overview has concentrated on space applications, there is scope for using deployable structures on earth. Generally, most rapidly assembled structures on earth may be considered as erectable (e.g. Bailey Bridges). However, deployable structures are used for a number of applications. Examples include retractable covers for space-stadia (O'Conner, 1992), or pneumatic structures (Dent, 1980).

2.2. Previous Work Relevant to Foldable Cylinders

Part I of this dissertation introduces a class of foldable cylinders. This is a new concept, and there is little previous work which is directly relevant to it. There are, however, two areas which have certain similarities, and so are worth mentioning.

The first of these areas is coilable masts, a common type of deployable structure. The best known example of this type of structure is the Astromast (Eiden *et al.*, 1984), but coilable masts have also been developed in Japan, the Simplex, and the Hingeless masts (Okazaki *et al.*, 1986). An example of an Astromast during deployment is shown in Figure 2.1. The way these coilable masts fold is similar to the way foldable cylinders fold. In particular, in coilable masts a transition zone is formed between the stowed and the extended parts of the mast. This behaviour is very similar to the formation of a transition zone in foldable cylinders, which is studied in more detail in Chapter 4.

The second area of work relevant to foldable cylinders is the buckling of thin-walled cylinders under axial compression. A common post-buckled shape for these cylinders is a diamond mode, where the surface is broken into well-defined triangles connected by inward folds around the circumference of the cylinder, and outward folds running helically around the cylinder. This is often known as the Yoshimura pattern (Yoshimura, 1955), and can be seen in many text books on buckling, e.g.

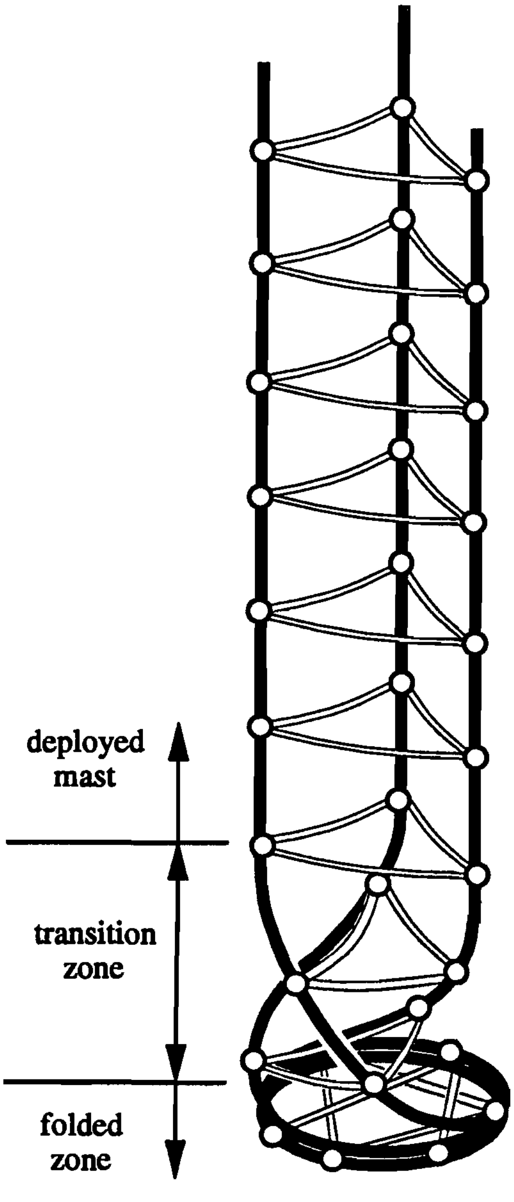

Figure 2.1. An Astromast during deployment. Diagonal bracing cables have been omitted for clarity.

Timoshenko and Gere (1980, page 469).

At first sight, the Yoshimura pattern appears similar to foldable cylinders. Both are developable surfaces where the surface is split into triangles, connected by fold lines. However, the important new feature of foldable cylinders is that the fold pattern possesses a second inextensional configuration where all the triangles fold on top of one another. In contrast, any Yoshimura pattern gives a unique configuration, so changing the configuration requires a change of fold pattern.

2.3. Previous Work on Folding Membranes

Part II of this thesis is concerned with folding a membrane by wrapping it around a central hub. Unlike the other concepts in this dissertation, this is not a new idea. A number of people since the 1960's have considered folding thin sheets in this way. The idea can first be found, very much in an embryonic form, in a patent by Huso (1960). Huso invented a sheet reel for compactly folding the tarpaulin cover of a car. His device consists of a fixed part, connected to the car roof, and a rotatable hub connected to the tarpaulin: when the hub is rotated the tarpaulin is gradually wound onto it. Huso (1960) shows a sketch of the expected folding pattern: each fold appears to start tangential to the hub.

A similar, but more refined folding pattern was introduced in two patents by Lanford (1961; 1963). He patented the folding apparatus shown in Figure 2.2, where the regular spacing of hill and valley folds is achieved by means of guiding wires tensioned by weights. This produces a fully-folded sheet with a regular saw tooth edge. The fold lines, sketched in Figure 2.2(a), are not straight; they were described as of helical shape by Lanford.

A third contribution was made in a patent by Scheel (1974). Scheel's fold pattern is shown in Figure 2.3. Three different types of folds are identified in the patent: a set of major folds approximately tangent to the hub, a set of intermediate folds bisecting the major folds, and a set of minor folds parallel to the major folds. Scheel's fold pattern is very similar to Lanford's; its major differences are that the hub in the folded configuration is at one end of the packaged membrane, and that the minor folds limit the height of the folded package. It will be shown in Section 6.2.3 that Scheel's major and intermediate folds can be obtained as a degenerate case of a general fold pattern based on Lanford's fold pattern.

A similar method of folding a membrane was used for the folding of a mesh antenna (Wade & McKean, 1981), where the mesh and a number of ribs are wrapped around a central hub.

The most recent advance on the idea of wrapping a membrane around a hub was made by Temple and Oswald (1989). They realised that the fold lines on the deployed membrane could not be straight. Instead of relying on folding devices to fold their membrane, and thus to form the fold lines, they derived an approximate equation for the fold lines and, having made a template, pre-formed the folds in a membrane before folding it. A number of simple paper models which could be easily folded and unfolded were made in this way.

An alternative method of folding a membrane was put forward by Miura (1980), (Miura *et al.*, 1980). Miura's fold pattern is a variation on the fold pattern often

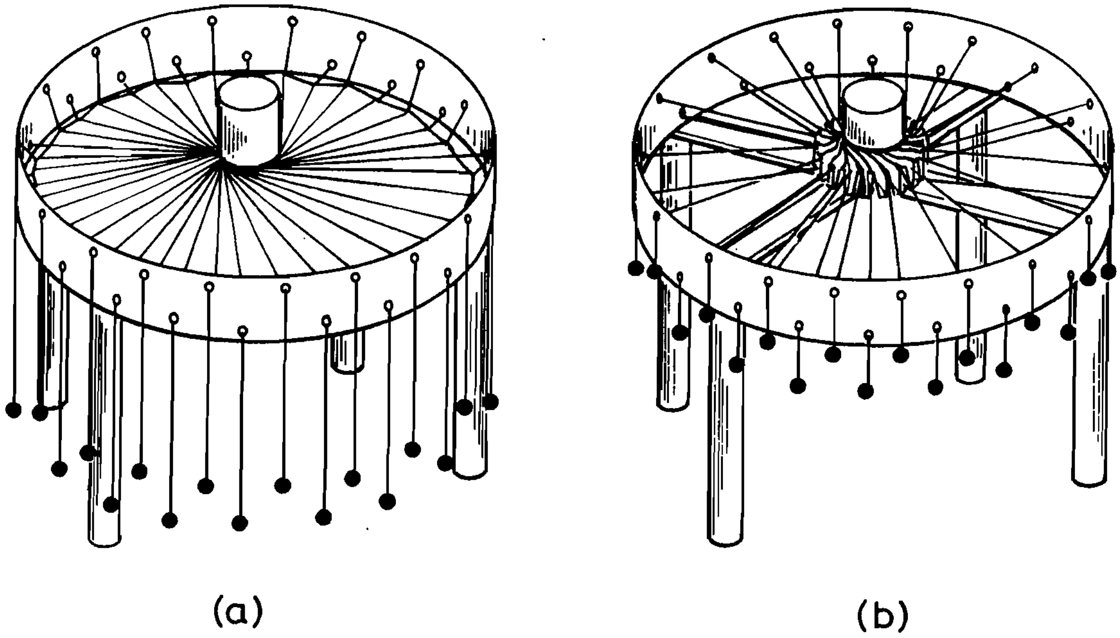

Figure 2.2. Lanford's folding apparatus: (a) Before folding. (b) After folding (by rotation of the central hub).

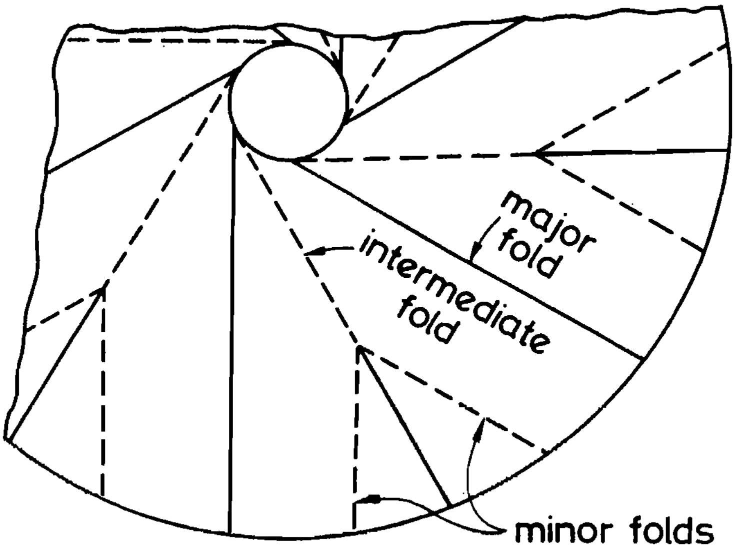

Figure 2.3. Scheel's fold pattern. Valley folds are shown by dashed lines.

used to fold a map, where all the folds in one direction are formed initially, and this package is then folded in the perpendicular direction. The fold pattern formed in this way is shown in Figure 2.4(a). The fold lines intersect at 28 inner vertices: at each vertex there are two pairs of collinear folds. Figure 2.4(b) shows Miura's variation on this pattern. The standard pattern has been changed so that the fold lines meeting at an inner vertex are no longer perpendicular to each other. What is apparently a small change to the fold pattern drastically changes the way the membrane folds. Instead of the sheet being sequentially folded, first in one direction and then in the perpendicular direction, the folding is now coupled so that one motion will open or close the membrane. Miura's pattern also has the advantage that none of the folds has to form around several layers of previously formed folds, which tends to stress the membrane. This advantage is shared by the wrapping fold pattern.

2.4. Previous Work on Deployable Antennae

Deployable antennae are probably the most important element in deployable structures research. The maximum diameter of launch vehicles limits solid reflectors to no more than approximately 4 m in diameter, but antennae larger than this are required for earth observation, astronomy and communications.

Deployable antennae can broadly be split into two categories, those with a furlable reflector surface, and those with a solid reflector surface. Furlable antennae are antennae where the surface itself can be folded; when deployed, their shape is maintained by some external structure or force. This category can be further subdivided into mesh antennae, and inflatable antennae.

The main functional difference between the unfurlable and solid-surface antennae is the accuracy of the reflecting surface they can form. Typically, a reflector surface has to have an r.m.s. accuracy of $\lambda/100$–$\lambda/25$, depending on the application, where λ is the wavelength of the signal. For frequencies of 20–30 GHz, this implies a surface accuracy of 0.1–0.6 mm r.m.s., which can only be achieved by a solid-surface antenna. Even at frequencies somewhat below this, achieving sufficient accuracy with a furlable antenna requires a complex structure, and a great deal of care and fine adjustment, and a solid surface antenna may prove to be more suitable. At much lower frequencies however, e.g. 1 GHz, furlable antennae are certainly appropriate. Part III of this dissertation is concerned with solid surface antennae, but a brief overview of furlable antennae will be given first.

A furlable antenna does not always require a continuous reflective surface. For frequencies up to 30 GHz a fine metallised mesh can be used instead. Most deployable antenna concepts have been mesh antennae. The reasons for this are two-fold. Firstly, the need for large antennae is greatest at low frequencies. High frequencies can transmit the same power using a smaller reflector. Secondly, mesh antennae are much easier to fold than solid surface antennae.

Most mesh antennae consist of two elements. The mesh itself is usually supported on a cable network; this cable network is then supported and tensioned by a deployable backbone. Examples of this type include Miura's Tension Truss Antenna (Miura & Miyazak, 1989), You and Pellegrino's Deployable Mesh Reflector

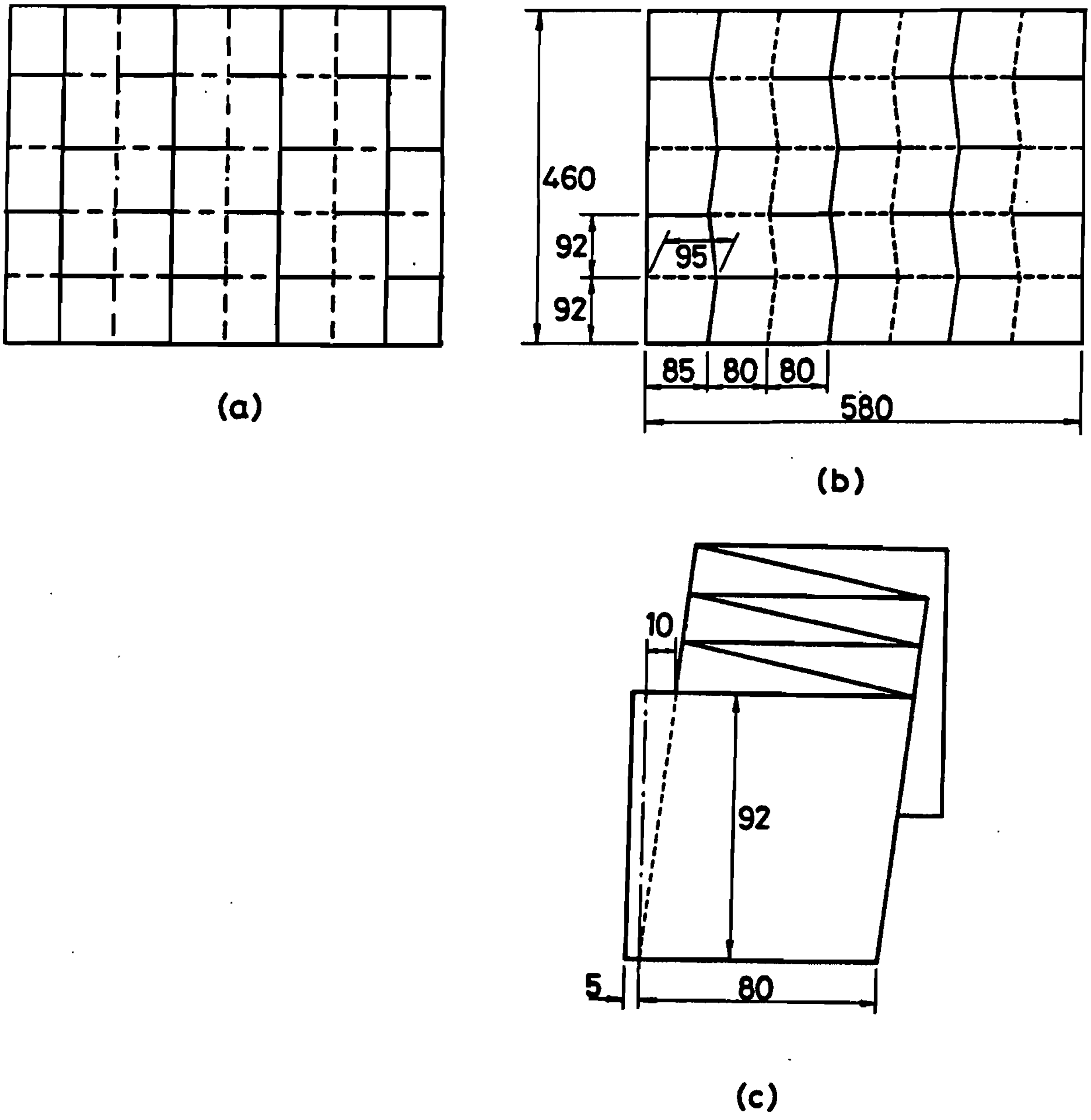

(a)

(b)

(c)

Figure 2.4. (a) Standard fold pattern. (b) Fold pattern from Miura *et al.*, (1980), fully extended. (c) Same pattern, fully folded. Valley folds are shown by dashed lines.

(You & Pellegrino, 1994), and the Harris Corporation's Hoop Column Antenna (Campbell *et al.*, 1988)

Mesh antennae generally fold well. For example, a 15 m diameter Hoop Column has been built which packages into a cylinder 0.9 m in diameter, and 2.7 m long. A typical reported accuracy for mesh antennae is the 1.55 mm r.m.s. error for this antenna (Campbell *et al.*, 1988). This was achieved after fine adjustments to the surface.

The other type of furlable deployable antennae are inflatable antennae. Inflatable antennae manufactured by L'Garde have successfully flown (Roederer & Rahmat-Samii, 1989). ESA and Contraves have developed an inflatable antenna that can be cured by sunlight, i.e. it hardens after inflation (Bernasconi, 1984). A 10 m version of the antenna is designed to achieve an r.m.s. accuracy of 2 mm (Rusch, 1992). However, there have been difficulties in maintaining an accurate shape during curing.

Although most interest in deployable structures has been in furlable antennae, there is also a need for large antennae which can operate at higher frequencies. A range of projects that would require such precision reflectors has been given by Hedgepeth (1989).

Solid surface deployable antenna can be split into two categories: antennae with a supporting structure, and antennae without a supporting structure. There are good reasons for building antennae where the surface is supported by a truss structure. Missions have been proposed, such as for NASA's Large Deployable Reflector (LDR), which require extremely accurate reflectors, in this case for an infrared telescope. LDR would require a 20 m antenna with an r.m.s. surface accuracy of 2 μm. This is well beyond the sort of accuracy that would be possible without a supporting structure (compare the accuracies given below), and would probably require an active structure. A number of concepts have been put forward for such an antenna, e.g. the Sequentially Deployed Precision Reflector (Hedgepeth, 1989), or the Precision Segmented Reflector (Bush *et al.*, 1991). However, all of these either require some extremely complex deployment mechanism, or some erectable components. In order to have a simple, autonomous, deployment mechanism, structures without a supporting truss have to be considered. These structures fill the gap between what mesh antennae can reasonably be expected to achieve, and the sort of accuracies required for some large and expensive science missions.

Two concepts for thin panel, solid surface antennae, without a supporting structure, have previously been proposed. These will be examined in more depth, as it is this type of antenna which is developed in Part III. A comparison of the packing efficiencies of the various concepts considered below is given in Table 9.1, comparing them with the concept developed in this dissertation.

The first, and simplest, concept is the TRW Sunflower (Archer & Palmer, 1984), shown in Figure 2.5. It has a particularly simple way of folding, but does not achieve a great reduction in size. It is reported to be capable of achieving an r.m.s. surface accuracy of 0.13 mm for a 10 m antenna.

An extension of the Sunflower is shown in Figure 2.6 (Hedgepeth, 1989). However, it is not clear from the literature how this concept works. It appears to lose the elegant simplicity of the original Sunflower, but achieves a much improved

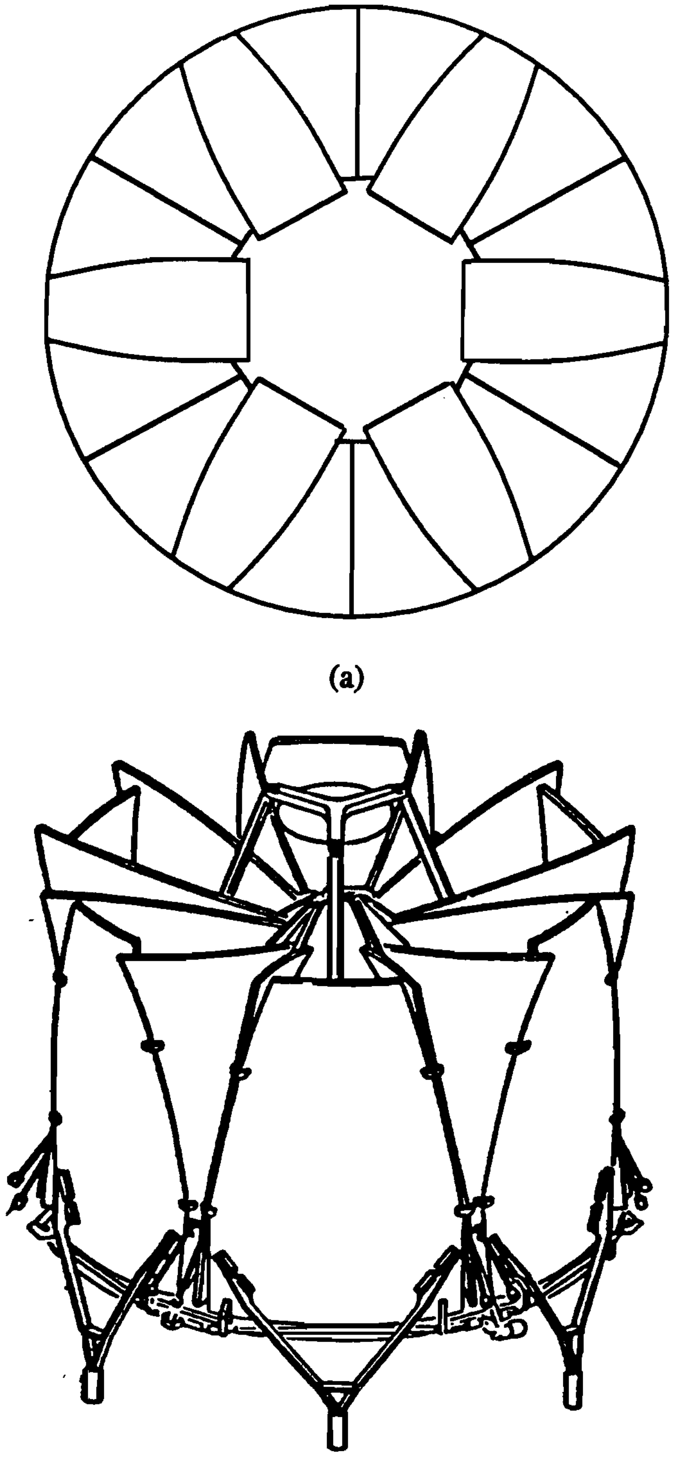

(a)

(b)

Figure 2.5. TRW Sunflower: (a) Fully deployed, plan view. (b) Fully folded.

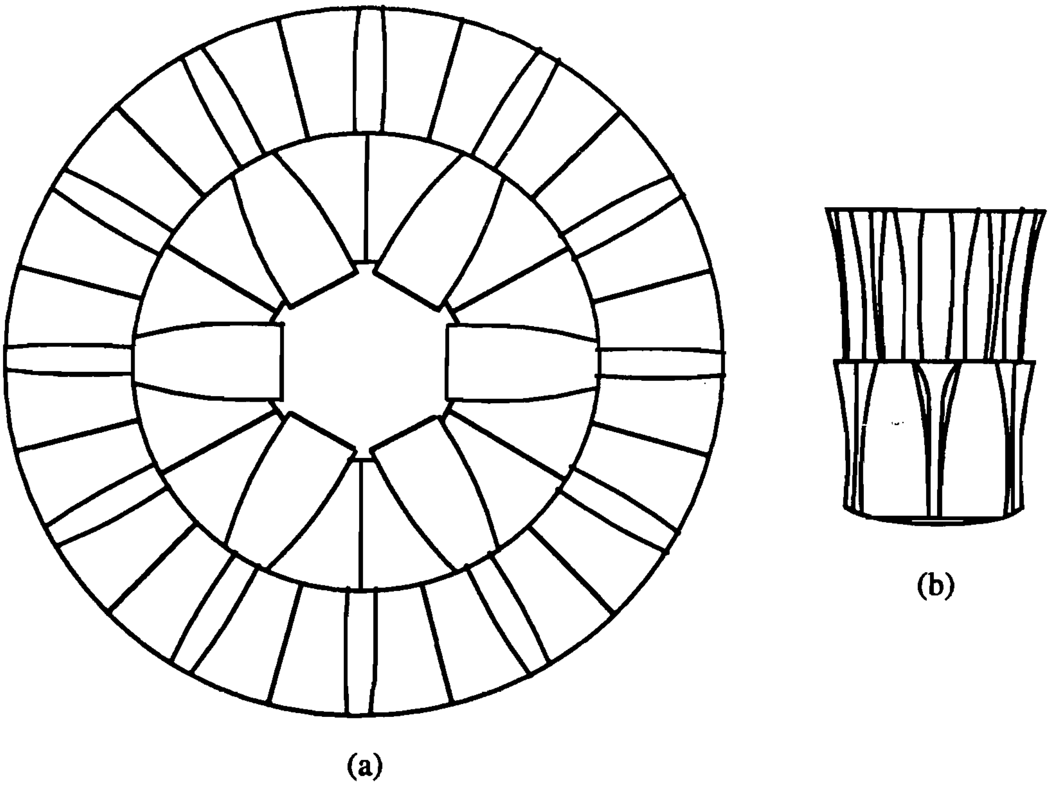

Figure 2.6. TRW Extended Sunflower: (a) Fully deployed, plan view. (b) Fully folded.

packing efficiency

A recent concept is ESA/Dornier's DAISY antenna. This concept has been used for two different antenna designs. The first design, for infrared astronomy, is the FIRST antenna, shown folded in Figure 2.7. It unfolds in a similar way to the MEA reflector considered next. Note that each panel has its own supporting truss structure. It has been designed to achieve an extremely high surface accuracy of 8 μm for an 8 m antenna (Kwan, 1991).

The other design based on the DAISY concept is the ESA/Dornier MEA reflector (Specht, 1990). This antenna is considered in some detail, as it is the most recent thin panel, solid surface antenna developed. The antenna is split into a central hub, surrounded by 24 folding panels. In order to fold, each panel rotates inward, and also twists, about its connection with the central hub. A computer simulation of the MEA reflector deploying is shown in Figure 2.8.

The deployment mechanism is shown in more detail in Figure 2.9. Each of the folding panels is attached to the central hub by two revolute joints, one of which allows rotation about a radial axis (the turning hinge), and the other about a tangential axis (the folding hinge). These two hinges are connected by a folding/turning bracket. Deployment is driven by a central disk which rotates, and is connected by 24 driving struts to the folding/turning brackets, causing simultaneous rotation about the folding hinge of all 24 panels. Neighbouring panels are connected by coupling struts at the outer rim of the antenna, and this couples

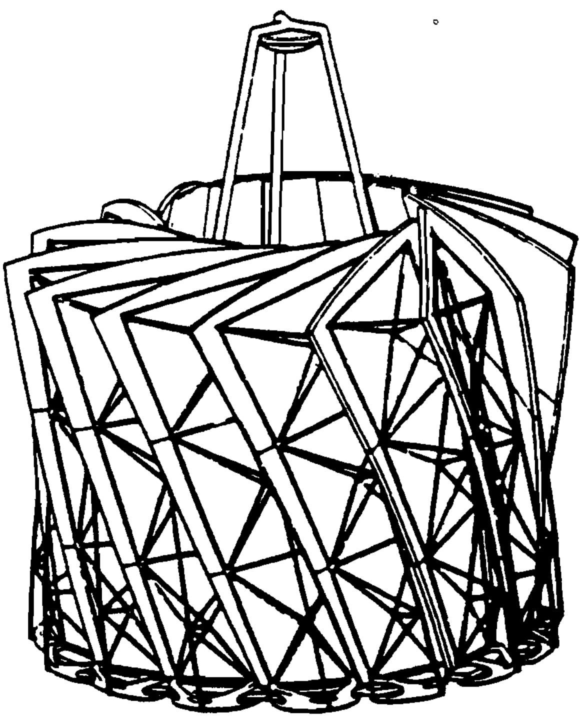

Figure 2.7. FIRST Antenna, fully folded.

the folding and twisting motions. Full deployment is achieved by a single motor rotating the driving disk through a range of 54°.

The MEA reflector is designed for communications at 20–30 GHz. It has a 4.7 m diameter, and is designed to achieve a 0.2 mm r.m.s. surface accuracy. A full-size model of the antenna has been manufactured and tested.

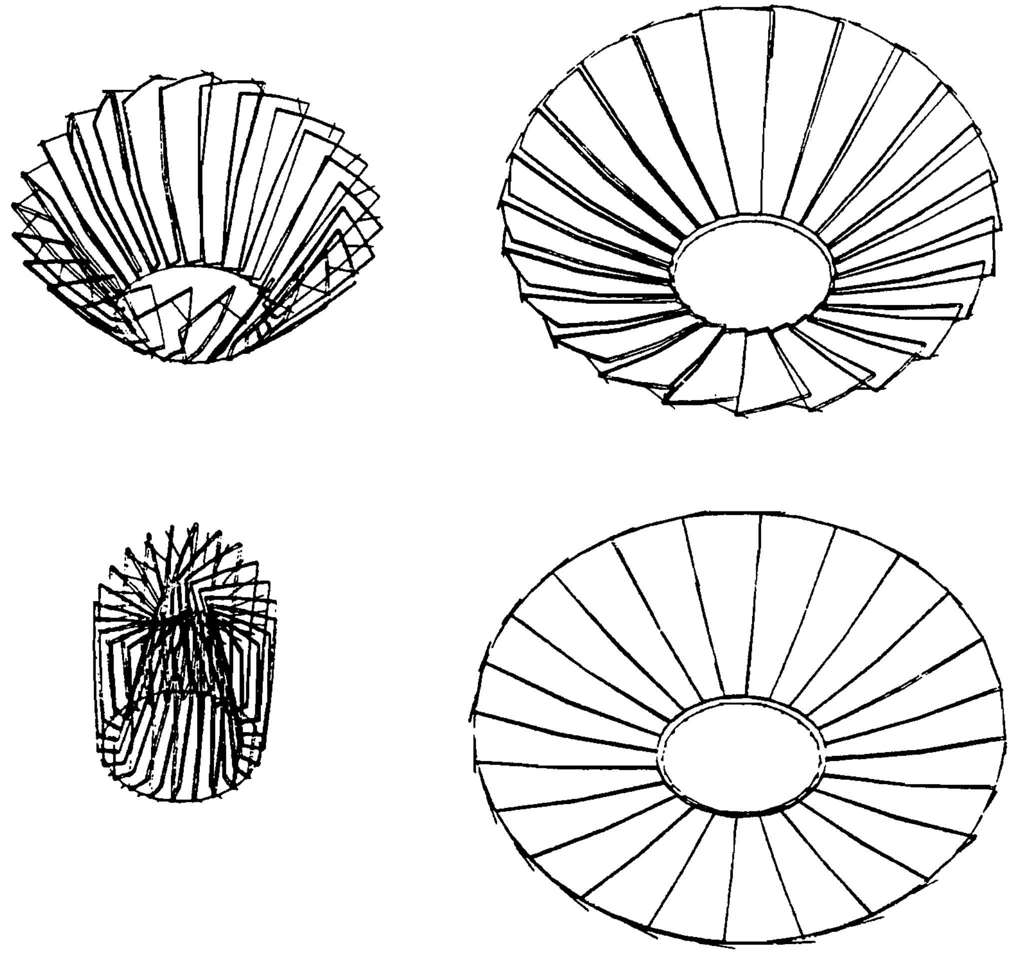

Figure 2.8. MEA Antenna, computer simulation of deployment.

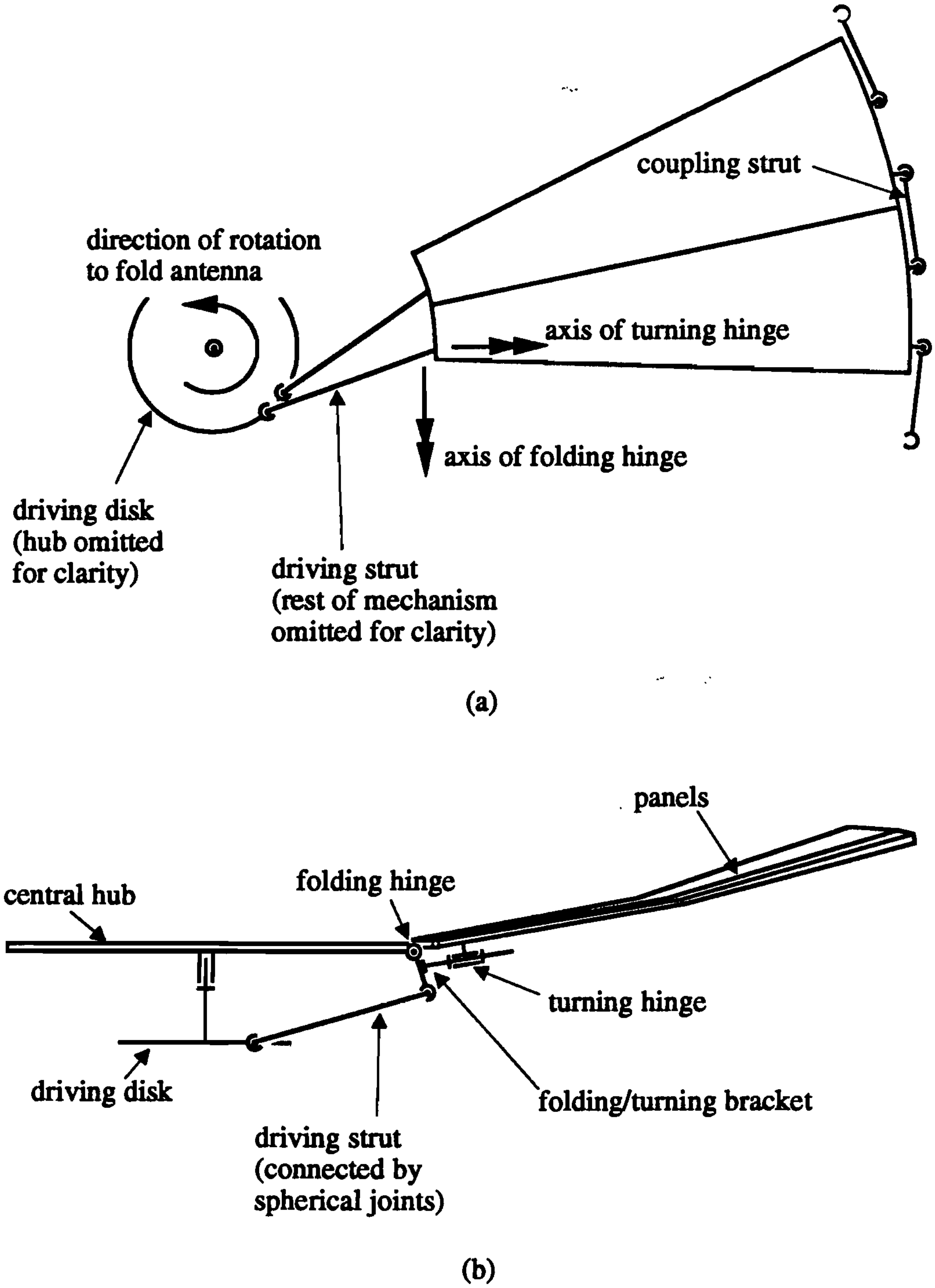

Figure 2.9. MEA Antenna, schematic of deployment mechanism: (a) Plan view, with hub removed for clarity. (b) Side view.

Part I

Foldable Cylinders

3. GEOMETRIC CONSIDERATIONS

The work on foldable cylinders described here was inspired by a cardboard model of a triangulated cylindrical shell made by C.R. Calladine during an investigation of the mechanics of biological structures. This model consisted of identical triangular panels on a helical strip, and had a small-displacement internal inextensional mechanism. It was decided to explore the possibility of transforming this small-displacement mechanism into a large-displacement motion by which a triangulated cylindrical shell could be folded down to a compact stack of plates. A number of arrangements have been found that allow this; only small strains, whose magnitude can be made as small as required by choosing suitable design parameters, are imposed during folding. A general way of approaching the problem has been discovered which considers all possible triangulated cylinders of this generic type. In all the cylinders considered it has been assumed that the plates have negligible thickness.

This chapter describes the general configuration of a triangulated cylinder based on one or more helical strips, and identifies those particular configurations which are suitable for folding. Estimates of strain levels in the plates during folding are found, based on the simplifying assumptions that the folding process is uniform and that only one side of each triangle can change its length. In Chapter 4 these assumptions are removed and the folding of some particular cylinders is simulated.

The chapter is organised as follows. Section 3.1 introduces foldable tubes by describing some examples which have a particularly simple geometry, and showing how simple models can be made. Section 3.2 introduces a general configuration in terms of three sets of helices lying on a cylindrical surface. The intersection of these helices define the corners of the triangles forming the faceted cylinder. General expressions for the side lengths of the triangles are derived in terms of the parameters defining these helices. With these tools, Section 3.3 examines the folding properties of a range of cylinders. Section 3.4 draws some conclusions from the chapter, and Section 3.5 explores an interesting and paradoxical configuration of foldable cylinder.

3.1. Some Simple Examples

Figure 3.1 shows photographs of the folding of a particular triangulated cylinder when a flat plate on the top is gradually pushed down. In Figure 3.1(a) the model is nearly fully extended; only a few triangular plates have been packaged. Then, as a small axial force is applied to the top plate, more and more triangles become part of the prismatic stack at the top of the cylinder and, in Figure 3.1(c), only a few triangles are still extended. The packaged configuration of this particular cylinder is a heptagonal prism. All foldable cylinders made from isosceles triangles,

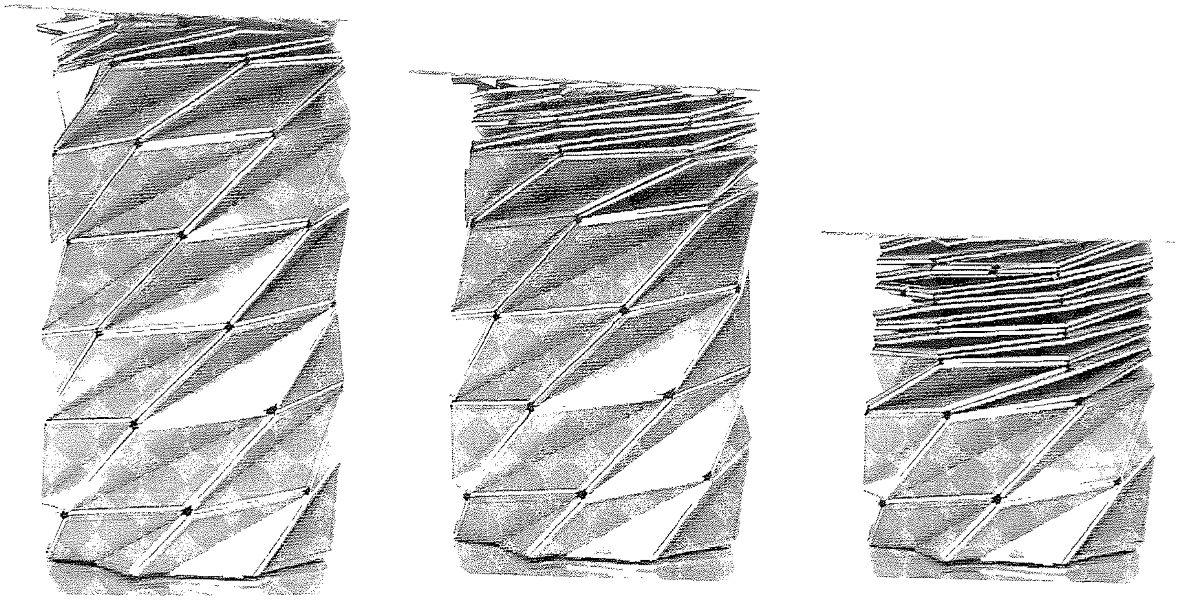

Figure 3.1. Folding sequence of a triangulated cylinder with $m = 1$, $n = 8$, $l_b/l_a = 1$, $l_c/l_a = 1.802$ (parameters defined in Section 3.2). This model is made of Al-alloy plates connected by flexible plastic hinges; its fully-extended height is approximately 250 mm.

like this one, fold down to prisms. They are a special case for which the general parameter n, defined in Section 3.2, becomes equal to one plus the number of sides in the packaged configuration. Hence, the triangulated cylinder of Figure 3.1 has $n = 8$.

Figure 3.2 shows line drawings of triangulated cylinders with $n = 6$, 7 and 8. As for all cylinders considered in this chapter, they are strain free both in their fully extended and fully folded configurations. In each cylinder all triangles are identical, and their sides are denoted by a, b and c. These particular cylinders are made from isosceles triangles and hence their geometry is quite easy to analyse. For example, for $n = 7$ all corners of the triangles in the packaged configuration coincide with the corners of a hexagon, as shown in Figure 3.2(b.ii). Thus, the lengths of sides a and b, $l_a = l_b$, are related to the length of side c, l_c, by the relationship

$$l_c = 2\sin\left(\frac{\pi}{2} - \frac{\pi}{n-1}\right) l_a = 2\sin\left(\frac{\pi}{3}\right) l_a = \sqrt{3}\, l_a \tag{3.1}$$

A simple model of this cylinder can be made from a single sheet of thin cardboard, prepared as shown in Figure 3.3. Three sets of parallel lines are scored on this sheet: the a- and b-lines are equidistant and intersect at an angle of $\pi/3$; the c-lines (scored on the reverse of the sheet) pass through these intersections. The sheet is then folded along these lines, the a- and b-lines forming hill folds, and the c-lines forming valley folds. Finally, the opposite edges of the sheet are

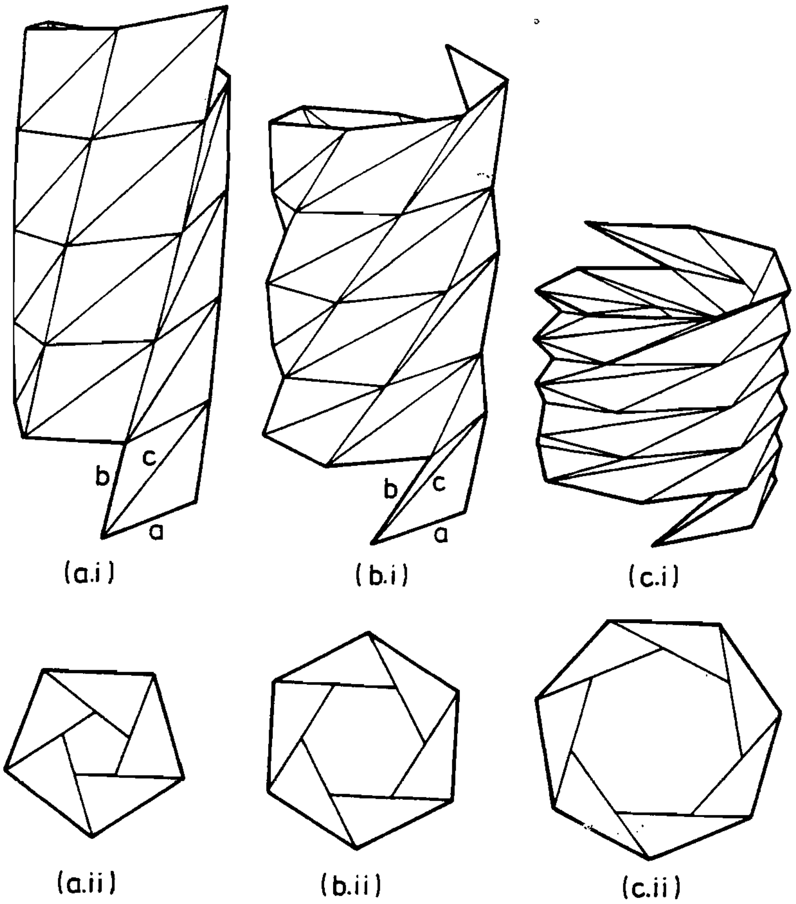

Figure 3.2. Triangulated cylinders with $m = 1$ and (a) $n = 6$, (b) $n = 7$, and (c) $n = 8$. (i) Fully extended, side view. (ii) Fully folded, plan view. All cylinders have $l_b/l_a = 1$.

glued together (in Figure 3.3 sides A-A, B-B etc.) to form the cylinder shown in Figure 3.2(b.i). A number of cardboard models have been made in this way, not only for $n = 7$, but also for $n = 6$ and $n = 8$. The axial force required to fold these models is quite small, and the strains induced are sufficiently small that the models can survive substantially undamaged a small number of folding/unfolding cycles. However, it quickly becomes clear that the strains imposed by folding become lower as the the value of n is increased. This observation has been confirmed by detailed computations in Chapter 4.

Having used these specific examples for illustration, the next section goes on to formulate a general framework for considering all cylinders of this generic type.

3.2. A Geometric Framework

A general description of triangulated cylinders made from identical triangular plates arranged on helical strips, like those of Figures 3.1 and 3.2, can be based on the observation that the sides of the triangles form discretised versions of three sets of helices. The nodes of the triangulated cylinders lie on the intersection of these helices, as shown in Figure 3.4. The sets of helices are described by the sides

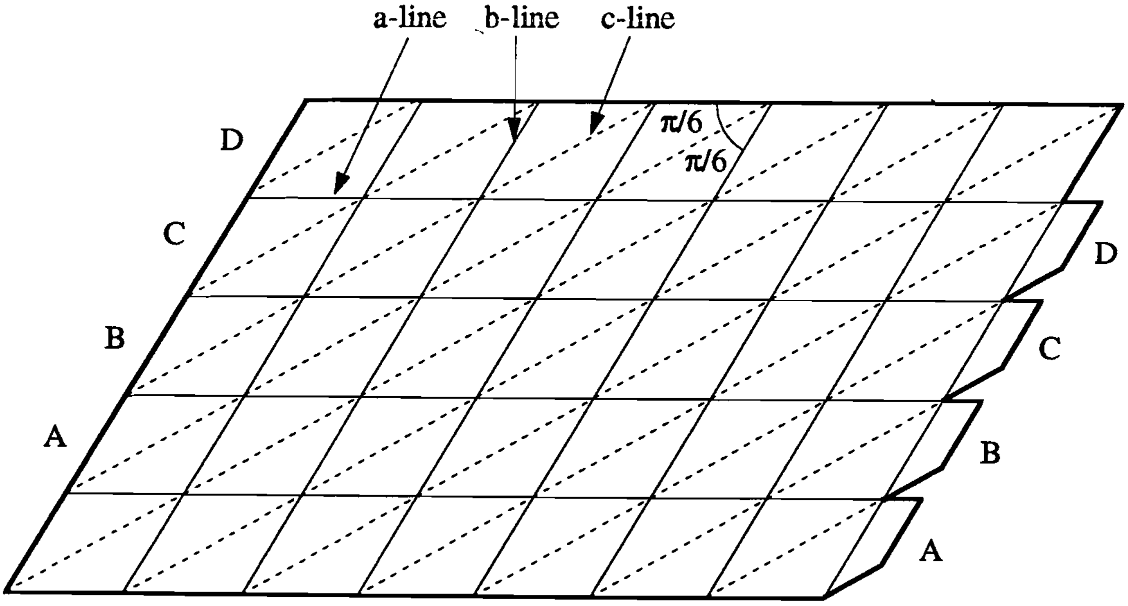

———— Hill folds (score on this side)

- - - - - - - - Valley Folds (score on reverse)

A-A, B-B etc. Sides to be joined.

Figure 3.3. How to make a foldable cylinder with $m = 1$, $n = 7$, $l_b/l_a = 1$.

of the triangles which form the discretised helices, i.e. they are called the a-, b-, and c-helices.

All helices in one set are identical, apart from a rotation about the axis of the helix. A full set can be defined as a single helix with multiple starts, and hence can be described by the following three parameters (Coxeter, 1980):

1. The number of helices in the set, i.e. the number of starts of the helix (for example, in Figure 3.1 the a-helix has one start, the b-helix seven starts, and the c-helix eight starts).
2. The radius, which has the same value for all helices of Figure 3.4 since they all lie on the same circular cylindrical surface.
3. The angle that the helix makes with a plane perpendicular to the axis of the helix. This angle can be greater than $\pi/2$ for a left-handed helix.

The positions of the nodes, and hence the configuration of a triangulated cylinder, are fully defined by any two of the three helices described above, as the third has to pass through the intersections of the other two. The a- and b-helix will be used to describe a triangulated cylinder, therefore it is necessary to give the parameters defining these helices. They are:

r the radius;

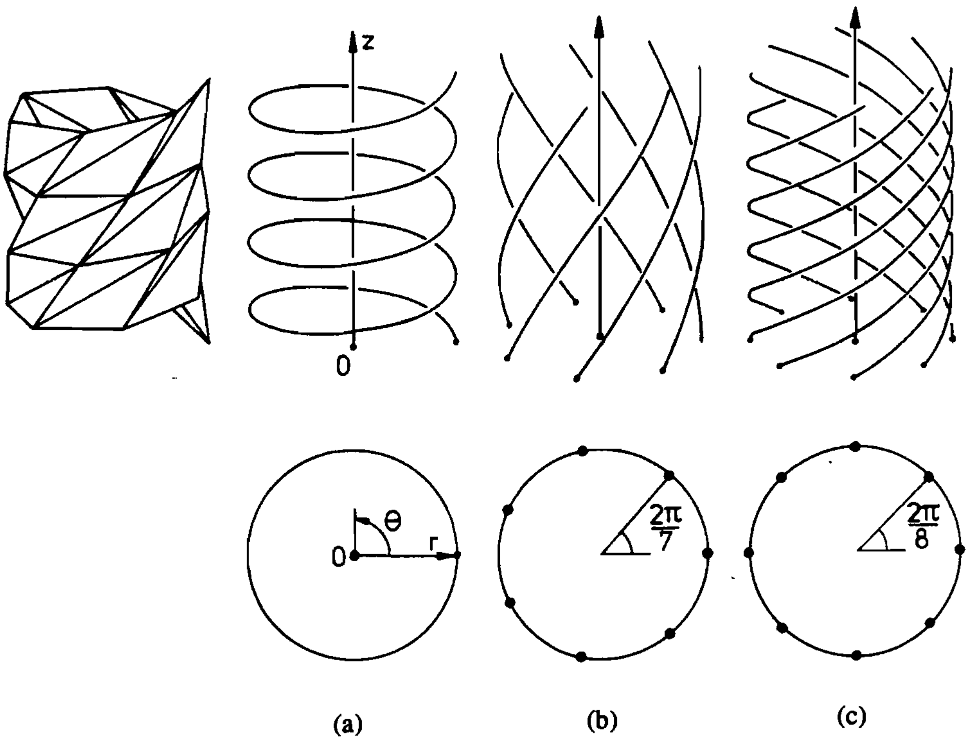

Figure 3.4. Description of a triangulated cylinder in terms of three sets of helices shown in side and plan views: (a) Single-start a-helix, $m = 1$. (b) Seven-start b-helix, $n = 7$. (c) Eight-start c-helix, $m + n = 8$. The first start of all helices is at $(r, 0, 0)$ in the coordinate system shown in (a).

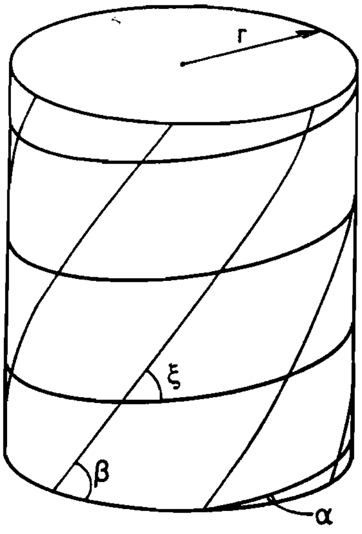

Figure 3.5. Coordinate cylinder and parameters defining a- and b-helices.

α, β the angles that the a- and b-helices, respectively, make with a plane perpendicular to their axis;

m, n the number of starts of the a- and b-helices, respectively.

The parameters r, α, β are shown in Figure 3.5. The a-helix has the equation

$$z = r\theta \tan(\alpha) \tag{3.2}$$

Similarly, the first start of the b-helix is defined by

$$z = r\theta \tan(\beta) \tag{3.3}$$

and the second start by

$$z = r\left(\theta - \frac{2\pi}{n}\right) \tan(\beta) \tag{3.4}$$

which gives $z = 0$ when $\theta = 2\pi/n$. Note that in equations 3.2–3.4, $0 < \theta < \infty$: a complete turn of a helix corresponds to an increase in the value of θ by 2π.

A node numbering system is defined where nodes are numbered along the a-helices: node (i, j) is the j-th node on the i-th start of the a-helix.

The next task is to obtain the coordinates of enough neighbours of node (1, 1) to be able to calculate the three side lengths of the triangles. The cylindrical coordinate system to be used, O, r, θ, z, is defined in Figure 3.4(b): node (i, j) has coordinates $(r, \theta_{i,j}, z_{i,j})$. $\theta_{i,j}$ is defined such that $0 \leq \theta_{i,j} < 2\pi$ and hence suitable multiples of 2π will be added to it when it is substituted into equations 3.2–3.4. Node (1, 1) has coordinates $(r, 0, 0)$.

For simplicity, the case $m = 1$ is considered first. Figure 3.6(a) shows that the coordinates required to calculate the three side-lengths are those of nodes (1, 2), $(1, n + 1)$, and $(1, n + 2)$. The θ-coordinates of these nodes are calculated: the r-coordinate is constant, and the z-coordinates can be found from equation 3.2.

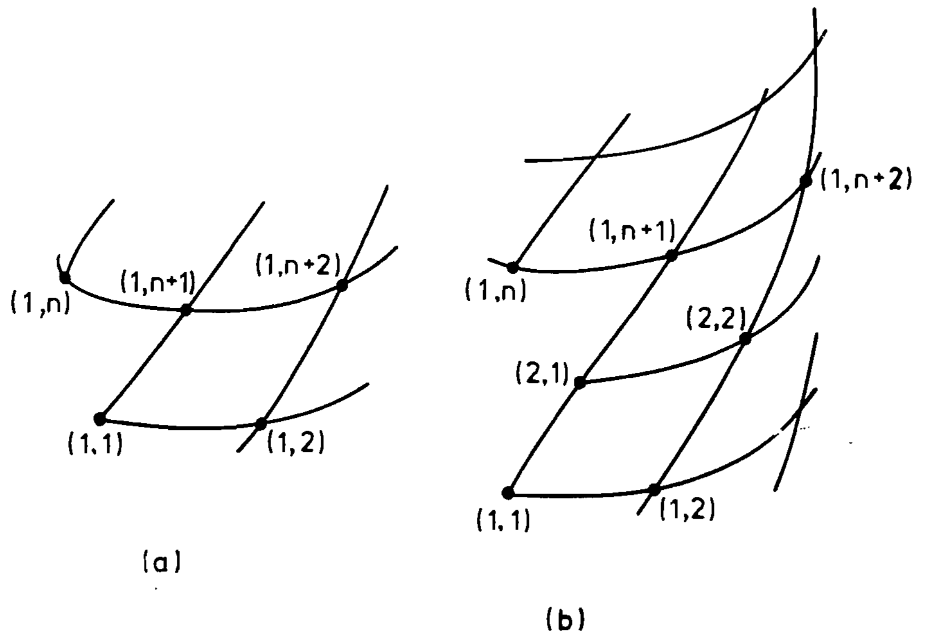

Figure 3.6. Neighbours of node (1,1) for a triangulated cylinder with (a) $m = 1$ and (b) $m = 2$. The c-helices are not shown.

At node (1, 2) the a-helix and the second start of the b-helix intersect and so, from equations 3.2 and 3.4

$$r\theta_{1,2}\tan(\alpha) = r\left(\theta_{1,2} - \frac{2\pi}{n}\right)\tan(\beta)$$

which gives

$$\theta_{1,2} = \frac{2\pi}{n(1-q)} \tag{3.5}$$

where

$$q = \frac{\tan(\alpha)}{\tan(\beta)} \tag{3.6}$$

At node $(1, n+1)$ the second turn of the a-helix and the first start of the b-helix intersect and so, from equations 3.2–3.3

$$r(\theta_{1,n+1} + 2\pi)\tan(\alpha) = r\theta_{1,n+1}\tan(\beta)$$

(Note that 2π has been added to $\theta_{1,n+1}$ on the l.h.s. as the intersection is on the second turn of the a-helix.) This gives

$$\theta_{1,n+1} = \frac{2q\pi}{1-q} \tag{3.7}$$

From Figure 3.6(a), $\theta_{1,n+2} = \theta_{1,2} + \theta_{1,n+1}$ and therefore

$$\theta_{1,n+2} = \frac{2(1+qn)\pi}{n(1-q)} \tag{3.8}$$

For cases where $m > 1$ the nodes connected to node (1,1) are those shown in Figure 3.6(b), i.e. nodes (1, 2), (2, 1) and (2, 2). This is true for any $m > 1$. The expression for $\theta_{1,2}$ remains that of equation 3.5. The expression for $\theta_{1,n+1}$ does not change either, but it is now $\theta_{2,1}$ which is required, and so from Figure 3.6(b)

$$\theta_{2,1} = \frac{\theta_{1,n+1}}{m} = \frac{2q\pi}{m(1-q)} \tag{3.9}$$

Similarly to before, $\theta_{2,2} = \theta_{1,2} + \theta_{2,1}$, giving

$$\theta_{2,2} = \frac{2(m+nq)\pi}{mn(1-q)} \tag{3.10}$$

All relevant θ-coordinates are now defined. The final step is to calculate the side lengths l_a, l_b, and l_c in terms of the parameters defining the helices. In general, the distance l between node (1, 1) and a node with coordinates $(r,\ \theta,\ z)$ is

$$l = \sqrt{\left(2r\sin\left(\frac{\theta}{2}\right)\right)^2 + z^2}$$

For node (1, 2), $l = l_a$, $\theta = \theta_{1,2}$, and from equation 3.2, $z = r\theta_{1,2}\tan(\alpha)$. Hence

$$l_a = \sqrt{\left(2r\sin\left(\frac{\pi}{n(1-q)}\right)\right)^2 + \left(\frac{2\pi r}{n(1-q)}\tan(\alpha)\right)^2} \tag{3.11}$$

The equations for l_b and l_c are the same if $m = 1$ or $m > 1$, but are arrived at by a different route. To calculate l_b, if $m = 1$, node $(1,\ n+1)$ with $\theta = \theta_{1,n+1}$ is used, or if $m > 1$, node (2, 1) with $\theta = \theta_{2,1}$ is used. The z-coordinate in both cases is

$$z = \frac{n}{m}z_{1,2} = \frac{n}{m}r\theta_{1,2}\tan(\alpha)$$

and l_b, again for both cases, is

$$l_b = \sqrt{\left(2r\sin\left(\frac{q\pi}{m(1-q)}\right)\right)^2 + \left(\frac{2\pi r}{m(1-q)}\tan(\alpha)\right)^2} \tag{3.12}$$

Similarly, to calculate l_c, if $m = 1$, node $(1,\ n+2)$ with $\theta = \theta_{1,n+2}$ is used, or if $m > 1$, node (2, 2) with $\theta = \theta_{2,2}$ is used. For both cases

$$z = \left(1 + \frac{n}{m}\right) z_{1,2} = \frac{m+n}{m} r\theta_{1,2}\tan(\alpha)$$

and

$$l_c = \sqrt{\left(2r\sin\left(\frac{(m+nq)\pi}{mn(1-q)}\right)\right)^2 + \left(\frac{2(m+n)\pi r}{mn(1-q)}\tan(\alpha)\right)^2} \tag{3.13}$$

Given the parameters which define the helices of a triangulated cylinder, it is possible to work out the sizes of the triangular panels from equations 3.11–3.13. Equally, it is possible to work backwards and, given a set of side lengths l_a, l_b and l_c, and the topological parameters m, n, work out the parameters of a corresponding set of helices.

3.3. Folding Properties

The results of Section 3.2 can be used to select particular layouts of triangulated cylinders which are suitable for folding, i.e. where both the extended and folded configurations are strain free. They can also be used to investigate the folding process, with the assumption that the folding process is uniform. The triangular plates are allowed to deform, but each must deform by the same amount so they remain identical to one another. This assumption may appear rather restrictive, particularly because Figure 3.1 shows clearly that the deformation pattern in any partially packaged configuration is not uniform: it consists of a fully-folded region at the top of the cylinder, a fully-extended region at the bottom, and an intermediate transition region. This transition region would then be expected to accommodate any strain induced. This localisation cannot be captured if it is assumed that all triangles remain identical. However many useful insights into the folding process can be obtained. This restriction has been removed in the more detailed calculations contained in Chapter 4.

The simplest way of approaching the problem is to investigate the geometric configurations of cylinders with l_b/l_a = constant. This is equivalent to assuming that all deformation can be modelled in terms of changes of l_c only. With these hypotheses, the folding properties of any particular type of triangulated cylinder, defined by l_b/l_a, m, and n can be effectively investigated on a plot of the variation of l_c/l_a with ξ, where

$$\xi = \beta - \alpha \tag{3.14}$$

as shown in Figure 3.5. Note that l_a is being used as an overall scaling factor. Obviously $0 \leq \xi < \pi$: configurations with $\xi = 0$ have zero height and will be referred to as fully folded. All plots presented in this section have been obtained by solving numerically the non-linear system of four equations, 3.11, 3.12, 3.13 and 3.14 for the four unknowns r/l_a, α, β, and l_c/l_a. The values of l_b/l_a, m, n, and ξ are fixed for each solution. The function fsolve, in the Optimisation Toolbox of the programming language MATLAB (MathWorks, 1992), has been used. A closed-form solution has not been searched for.

There is an upper limit on the value of l_b/l_a for practical foldable tubes. This comes about because the inner edges (the c-sides) of the triangles cannot cross the z-axis without penetrating one other. This condition is most severe when $\xi = 0$. Geometry in this folded shape then shows that the limit is

$$\frac{l_b}{l_a} \leq \frac{\sin\left(\frac{(n-2)\pi}{2(m+n)}\right)}{\sin\left(\frac{(m+2)\pi}{2(m+n)}\right)} \tag{3.15}$$

An equality sign would correspond to the c-sides lying along diameters of the coordinate cylinder.

Figure 3.7(a) shows a plot of l_c/l_a vs. ξ for triangulated cylinders with $m = 1$, $n = 7$ and for three different values of l_b/l_a. Consider initially the case $l_b/l_a = 0.5$. The figure shows that l_c decreases monotonically as ξ increases. Indeed, this is the type of behaviour that would be expected if all triangles were in a plane, rather than being wrapped in a tube. Within obvious limits, any value of l_c/l_a is associated with a unique configuration of the cylinder. The case $l_b/l_a = 1$

(isosceles triangles) is more interesting, since now l_c/l_a initially increases with ξ and then, having reached a maximum, starts decreasing. This is the because the curvature of the cylindrical surface, on which all corner nodes lie, is becoming significant. In this case any triangulated cylinder with $l_c/l_a \geq \sqrt{3}$ admits two different, totally unstrained configurations. In particular, $l_c/l_a = \sqrt{3}$ gives one configuration where $\xi = 0$ and one where $\xi = 0.867$. This is the same cylinder which has been analysed, by much simpler means, in Section 3.1. The third curve in Figure 3.7(a), for the case $l_b/l_a = 1.5$, shows similar behaviour, but now with a more marked maximum. This curve shows that triangulated cylinders with $l_b/l_a = 1.5$ and $l_c/l_a = 1.800$ are strain free both when $\xi = 0$ and when $\xi = 1.587$, but going from one configuration to the other requires large deformations.

Similar considerations apply to other triangulated cylinders. For example, Figure 3.7(b) shows similar curves for the case $m = 2$, $n = 7$. Note that the three curves in this figure refer to lower values of l_b/l_a than in the case $m = 1$ because the upper limit on l_b/l_a, equation 3.15, is lower.

A more general way of plotting data for the case $m = 1$, $n = 7$ is a contour plot of l_c/l_a for the full range of ξ and l_b/l_a, Figure 3.8(a). A broken line marks those configurations of the cylinder which also admit a strain-free folded configuration with $\xi = 0$, and hence can be folded flat. The value $l_b/l_a = 0.788$ is the lowest possible for fully foldable cylinders. Note that the contour $l_c/l_a = 1.75$, for example, indicates that cylinders with $l_b/l_a = 1.039$ require fairly small strains to go from $\xi = 0$ to $\xi = 0.940$. The contour $l_c/l_a = 1.64$ (not shown) is even flatter, thus allowing ξ to vary in the range 0–0.4 with less than 0.1% variation in l_b/l_a. Finally, note that the upper limit on l_b/l_a is 1.497, from equation 3.15. Figure 3.8(b) plots the corresponding values of r/l_a: folding, i.e. decreasing ξ, always implies a reduction of r.

3.4. Conclusions

The general geometric formulation of Section 3.2, together with the sample plots of the type presented in Section 3.3 are very powerful tools for the design of foldable cylinders. With this approach it is possible to go well beyond the fairly intuitive foldable cylinders presented in Section 3.1, all of which had $m = 1$ and $l_b/l_a = 1$. Having the freedom to alter these two parameters can be very useful in the design of foldable cylinders that have to meet some specified requirements. With the hypothesis that l_a and l_b remain constant during folding, while l_c varies, preliminary estimates of strains during folding are easy to obtain.

3.5. A Cylinder with an Infinitesimal Mechanism?

An interesting feature of the plots in Figure 3.7 is that they identify some special triangulated cylinders whose l_c/l_a is an analytical maximum. For example, the special configuration of a cylinder with $m = 1$, $n = 7$ and $l_b/l_a = 1.5$ occurs for $\xi = 0.839$ and hence $l_c/l_a = 2.162$, see Figure 3.7(a). Any cylinder made to be strain-free in such a configuration can change its ξ by an infinitesimal amount without any first-order changes of length in the triangular panels. Indeed, Calladine's

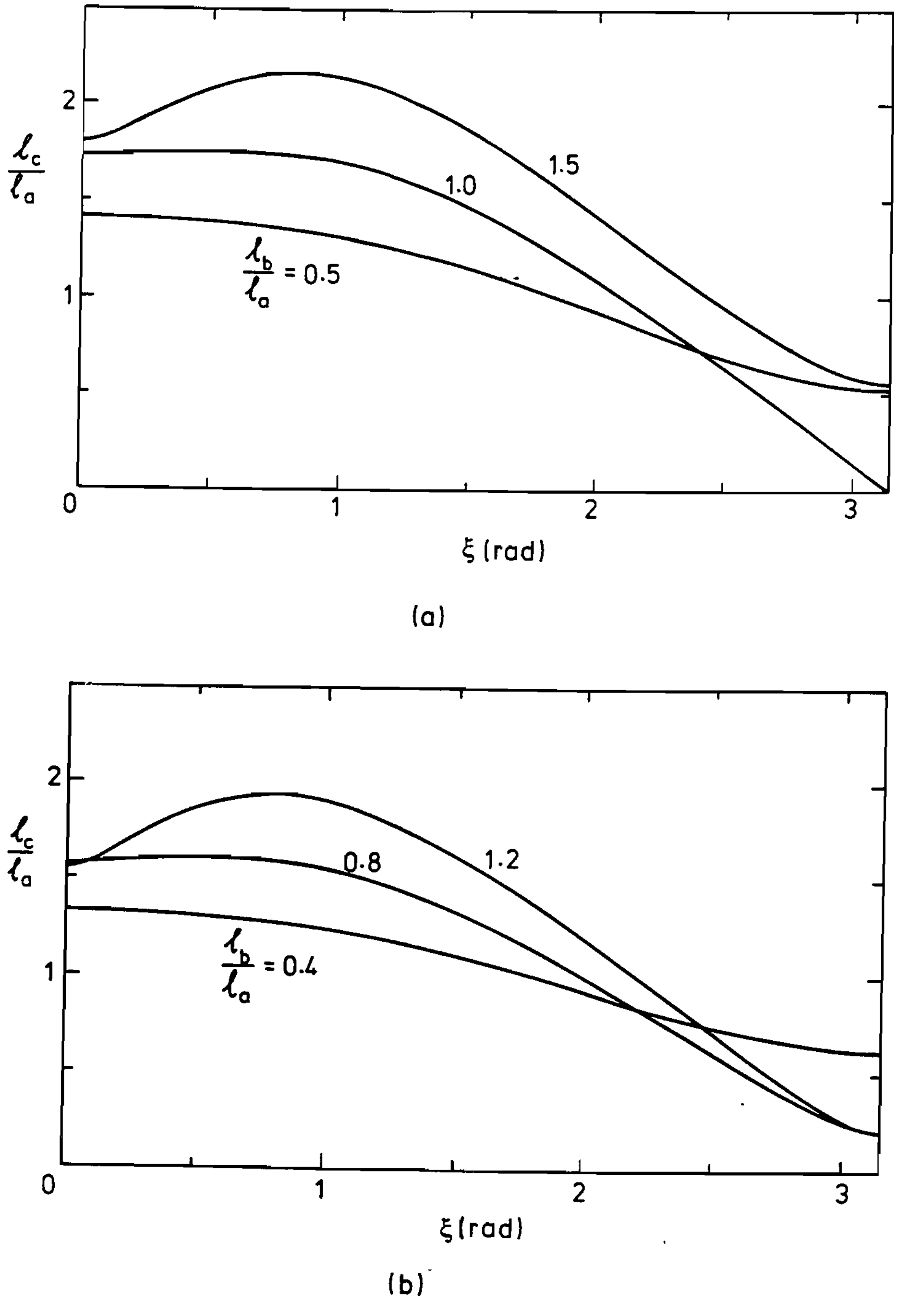

(a)

(b)

Figure 3.7. Plots of l_c/l_a vs. ξ for triangulated cylinders with (a) $m = 1$ and (b) $m = 2$. $n = 7$ in both cases.

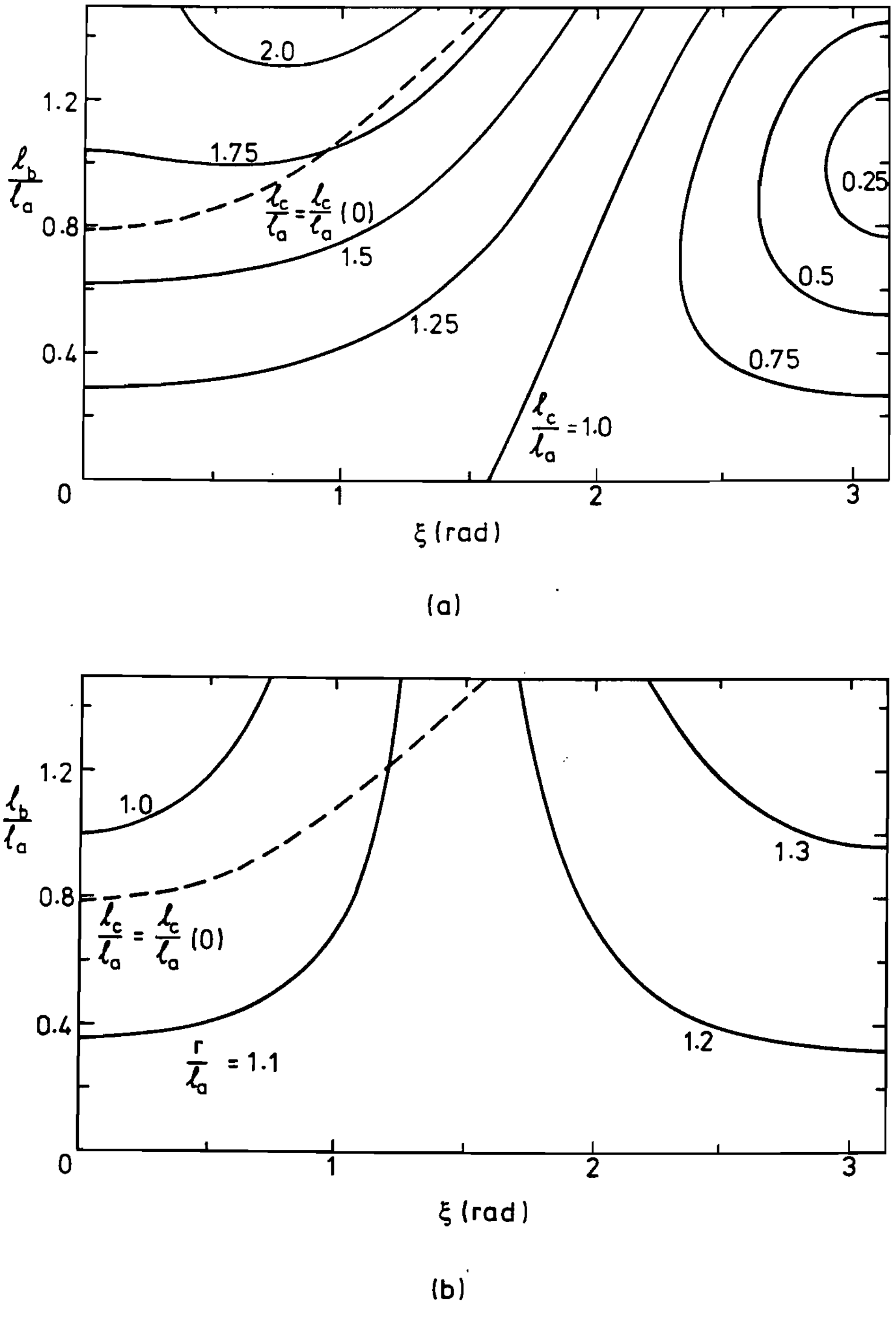

Figure 3.8. Contour plots of (a) l_c/l_a and (b) r/l_a for triangulated cylinders with $m = 1$ and $n = 7$.

model, referred to in the introduction to the chapter, had this property and the analysis in this chapter has produced a whole group of cylinders with the same property as a by-product.

It is well known, see Calladine (1978) for example, that special, singular configurations of an assembly of pin-jointed bars are obtained when the length of one bar, or a group of bars, is a maximum. It might be expected that the configurations corresponding to the maxima of Figure 3.7 should have such a property. However, careful calculations using the truss model described in Chapter 4 show that they do not. There is no reduction in the rank of the equilibrium matrix for these particular configurations.

The reason why the special configurations are not singular configurations is because only uniform configurations were considered in the analysis leading to the plots in Figure 3.7. The maxima of l_c/l_a are, indeed, the largest when this constraint is enforced. However, if this constraint is removed, non-uniform configurations with larger l_c/l_a can be obtained.

A paradox, however, remains. Cylinders in these special configurations obviously have a mechanism corresponding to ξ varying by a small amount, but do not show the normal characteristics of an infinitesimal mechanism. The paradox can be solved by looking closely at the finite mechanisms within the cylinder. All foldable cylinders have two finite mechanisms; they are not important in the folding process, and normally remain localised to the end of the cylinder. For a cylinder at the special configuration, however, these mechanisms involve movement of all the nodes within the cylinder. A particular combination of the two mechanisms produces a uniform change within the cylinder which corresponds to a change in ξ. Thus, what appears to be an infinitesimal mechanism is a finite mechanism which, for a small part of its path only, produces a uniform change in the cylinder's configuration.

4. COMPUTATIONAL MODELLING OF THE FOLDING PROCESS

Chapter 3 introduced foldable cylinders, and gave some preliminary estimates of the strains imposed in the cylinder during folding. These estimates were based on the simplifying assumption that folding was uniform throughout the cylinder. In this chapter a computational approach is outlined which looks in more detail at the folding process of some particular cylinders. Attention is restricted to cylinders that, in terms of the geometric parameters introduced in Chapter 3, have $m = 1$ and $l_b/l_a = 1$, and hence can be packaged into prismatic stacks of plates. Three cylinders of this type are considered, with n = 6, 7, and 8. The way they fold when pressed down by a flat plate is analysed. Of prime interest is the level of straining induced by this process and the force required to fold the cylinder. Also of interest is the shape of the transition region immediately ahead of the fully packaged region, and the decay pattern of the strain field. Such information is needed for the design, manufacture and testing of foldable cylinders. Indeed, only after obtaining results from this investigation was it possible to manufacture the cylinders described in Chapter 5.

In Section 4.1 a simple computational approach is set out which can handle the inherent non-linearities of the cylinder. The results from this approach for the three different cylinders are presented in Section 4.2, and these results and the assumptions of the method are discussed in Section 4.3.

4.1. Computational Model

A simple analytical model of a triangulated cylinder is a truss structure having linear-elastic bars of equal cross-section along the edges of the triangles. The bars are connected by frictionless pin-joints at the nodes of the cylinder. There are three types of bars, a, b, c, lying on the edges labelled thus in Figure 3.4. The bottom n nodes of the structure are fully fixed. The structure is compressed by a frictionless, rigid plate which is connected to a rigid foundation at a single point. To simulate the folding process, this point is gradually drawn towards the bottom end of the structure. For simplicity, the thickness of the triangular plates making up the cylinder is neglected. The computational model is shown in figure 4.1.

The model is greatly simplified. However, it will be shown later that it can capture key aspects of the folding process that have been observed experimentally. It also proves useful to make comparisons between triangulated cylinders with different parameters.

The algorithm to simulate the folding process that is presented here is based on a Force Method approach. This requires that the overall equilibrium, com-

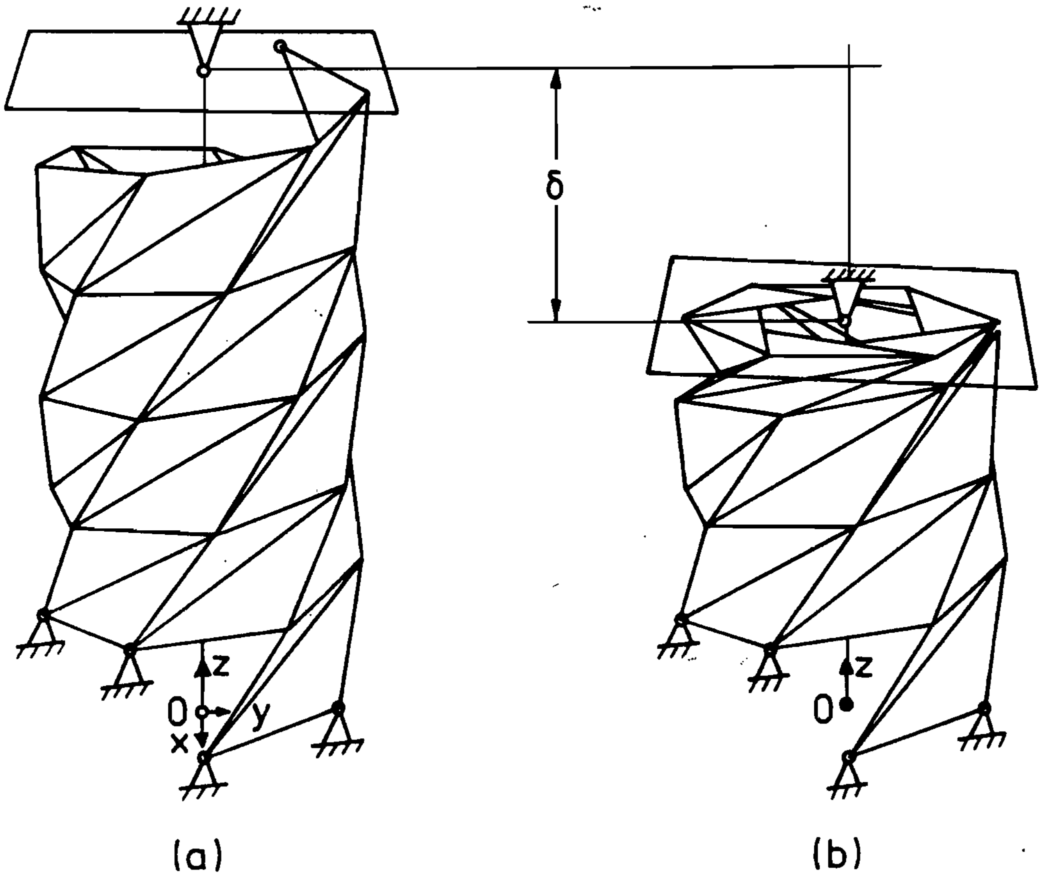

Figure 4.1. Triangulated cylinder with $m = 1$, $n = 7$, $l_b/l_a = 1$, and $l_c/l_a = \sqrt{3}$, folded by moving down a rigid plate: (a) Fully extended configuration. (b) Partially folded configuration. The bottom n nodes of the cylinder are fully restrained. The co-ordinate system O, x, y, z has the z-axis aligned with the axis of the cylinder; the bottom node lies in the $x - y$ plane.

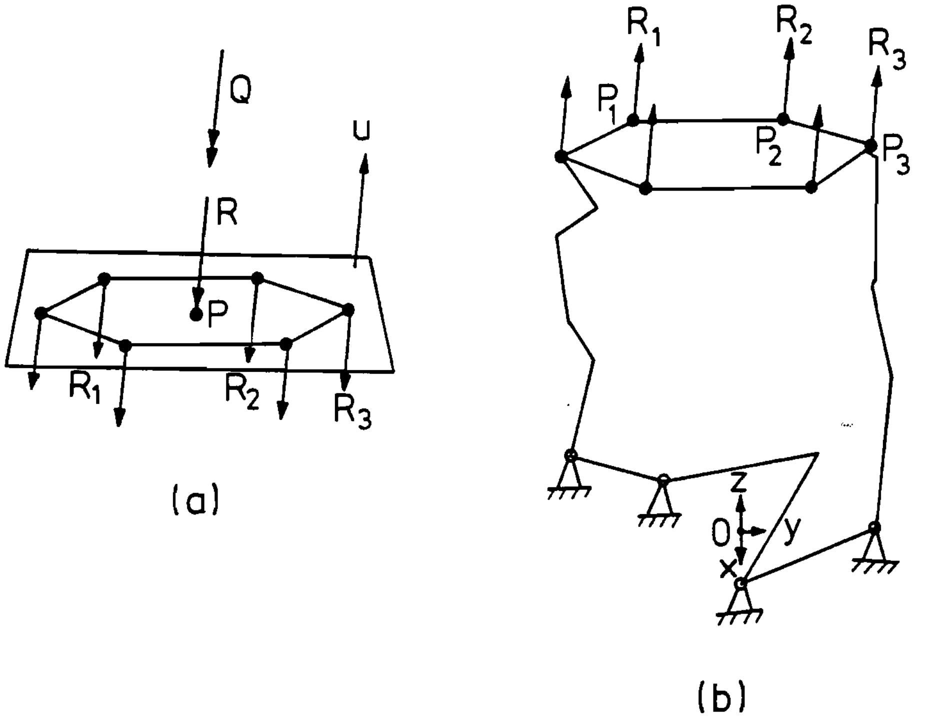

Figure 4.2. (a) Forces acting on the loading plate. (b) The corresponding forces on the top k nodes of the cylinder.

patibility and flexibility matrices are available for any given configuration of the cylinder. These matrices are obtained by assembling the basic matrices of two types of elements, the pin-jointed bars and the rigid loading plate. There is no difficulty in setting up the matrices for a pin-jointed bar (Livesley, 1975). The loading plate, however, is not a standard element, and so a brief explanation is given on how to set up the three matrices required, based on the hypothesis that all forces acting on the loading plate are orthogonal to it.

Consider the loading plate shown in Figure 4.2(a), whose current configuration is defined by the position of point **P** and by the unit normal vector **u**. The plate is acted upon by k interaction forces between the plate and the k joints of the cylinder in contact with it. Equal and opposite forces act upon the top k joints of the cylinder, as shown in Figure 4.2(b). The plate is also acted upon by a force of magnitude R and a couple of magnitude Q, applied to it by the foundation through the connecting hinge at **P**. All of these forces, as well as the vector representing Q, are orthogonal to the plate, i.e. parallel to **u**. In addition to point **P**, the k points on the plate which are in contact with nodes of the cylinder are defined as $\mathbf{P}_1 \ldots \mathbf{P}_k$; an interaction force of magnitude R_i passes through point $\mathbf{P}_i$. Initially, only compressive values of R_i, i.e. opposite to those shown in Figure 4.2, are physically meaningful. Later in the folding process, when plates have stacked on top of one another, some tensile R_i's may be possible. No restrictions on the signs of R_i will be imposed in this study in the spirit of simplicity. The small effect this is likely to have on the results is discussed later.

In general, there are six independent equations of equilibrium for a rigid body.

However, the plate is under the action of a system of parallel forces and so two equations of force equilibrium are identically satisfied. Hence, only the equilibrium of forces in the **u**-direction, and the equilibrium of moments about any point has to be considered. Equilibrium of forces gives the simple matrix equation

$$\begin{pmatrix} 1 & \cdots & 1 & 1 \end{pmatrix}\begin{pmatrix} R_1 \\ \vdots \\ R_k \\ R \end{pmatrix} = 0 \tag{4.1}$$

Moment equilibrium is taken about a set of axes parallel to x, y, and z (defined in Figure 4.2(b)) and passing through $\mathbf{P}$. This particular choice is made because of its kinematic implications, which will be seen later. The three moment components of the interaction force at $\mathbf{P}_i$ are $((\mathbf{P}_i - \mathbf{P}) \times \mathbf{u})R_i$, hence the three equations of moment equilibrium for the plate can be written in the form

$$\begin{pmatrix} (\mathbf{P}_1 - \mathbf{P}) \times \mathbf{u} & \cdots & (\mathbf{P}_k - \mathbf{P}) \times \mathbf{u} & \mathbf{u} \end{pmatrix}\begin{pmatrix} R_1 \\ \vdots \\ R_k \\ Q \end{pmatrix} = \begin{pmatrix} 0 \\ 0 \\ 0 \end{pmatrix} \tag{4.2}$$

The right hand sides of equations 4.1 and 4.2 have been set directly equal to zero because there are no external forces acting on the plate. Note that the reactions R and Q have been put among the internal forces as values to be calculated.

By assembling together equations 4.1 and 4.2 a system of four equations in $k+2$ generalised stresses is obtained; the 4 by $k+2$ coefficient matrix is the equilibrium matrix $\mathbf{A}_p$ for the plate:

$$\begin{pmatrix} 1 & \cdots & 1 & 1 & 0 \\ & & & 0 & \\ (\mathbf{P}_1 - \mathbf{P}) \times \mathbf{u} & \cdots & (\mathbf{P}_k - \mathbf{P}) \times \mathbf{u} & 0 & \mathbf{u} \\ & & & 0 & \end{pmatrix}\begin{pmatrix} R_1 \\ \vdots \\ R_k \\ R \\ Q \end{pmatrix} = \begin{pmatrix} 0 \\ 0 \\ 0 \\ 0 \end{pmatrix} \tag{4.3}$$

The transpose of $\mathbf{A}_p$ relates the kinematic variables corresponding to the static variables in equation 4.3 (Livesley, 1975). The $k+2$ generalised strains, corresponding to the vector on the left hand side of equation 4.3, are the extensions e_i of the connectors between the plate and the top k joints of the cylinder, together with the displacement of point $\mathbf{P}$ in the **u**-direction, δ_{P_u}, and the plate rotation ϕ about the **u**-axis. The four generalised displacements, corresponding to the vector on the right hand side of equation 4.3 are δ_{P_u}, α, β, γ. The variable δ_{P_u} appears both as an internal and external variable, and so it should be no surprise that the corresponding kinematic equation is a simple identity. The variables α, β, γ are the small rotations of the plate about the x-, y-, and z-axis, respectively. The system of kinematic equations is

$$\begin{pmatrix} 1 & ((\mathbf{P}_1 - \mathbf{P}) \times \mathbf{u})^{\mathrm{T}} \\ \vdots & \vdots \\ 1 & ((\mathbf{P}_k - \mathbf{P}) \times \mathbf{u})^{\mathrm{T}} \\ 1 & 0 \quad 0 \quad 0 \\ 0 & \mathbf{u}^{\mathrm{T}} \end{pmatrix} \begin{pmatrix} \delta_{P_u} \\ \alpha \\ \beta \\ \gamma \end{pmatrix} = \begin{pmatrix} e_1 \\ \vdots \\ e_k \\ \delta_{P_u} \\ \phi \end{pmatrix} \tag{4.4}$$

The third matrix required by the Force Method is straightforward: because the plate and its foundation are rigid, all entries in the $k+2$ by $k+2$ flexibility matrix F_P must be zero.

The above formulation, with four external variables, is not the most compact possible. Two equilibrium equations, force equilibrium perpendicular to the plate, and moments in the plane of the plate, are obviously identically satisfied. Therefore only two external variables are needed. Also the internal variables R and Q could be removed and calculated separately. Thus the size of all three matrices for the plate could be reduced by two rows and two columns, but this would involve more complex computations for updating the plate position, and separately calculating R.

The matrices derived above are assembled together with the matrices for the pin-jointed bars to form the overall matrices for the cylinder. Let N be the total number of nodes in the cylinder and B the total number of bars. Because the bottom n nodes are fully fixed to a rigid foundation, the corresponding $3n$ equilibrium equations need not be considered. At the top of the cylinder the k nodes in contact with the rigid plate do not need any special treatment, apart from noting that each of these joints is subject to an interaction force of magnitude R_i, as shown in Figure 4.2(b), as well as to the axial forces in the bars connected to it. Hence, there are $3(N-n)+4$ equilibrium equations in $B+k+2$ generalised stresses $\boldsymbol{\sigma}$, and the overall equilibrium matrix $\mathbf{A}$ has size $3(N-n)+4$ by $B+k+2$. Similarly, the generalised strain vector $\boldsymbol{\epsilon}$ has size $B+k+2$, while the generalised displacement vector $\mathbf{d}$ has size $3(N-n)+4$. The flexibility matrix $\mathbf{F}$ has size $B+k+2$ by $B+k+2$.

With these matrices, the folding of a triangulated cylinder can be analysed. Initially the cylinder is set up in its fully-extended configuration, as in Section 3.2, but using the Cartesian coordinate system defined in Figure 4.1(a). The loading plate is set initially parallel to the $x-y$ plane and the connection point $\mathbf{P}$ has co-ordinates $\mathbf{P} = (0, 0, z_P)$, where z_P is also the z-coordinate of the top node of the cylinder. Initially, this is the only node which is in contact with the loading plate, hence $k=1$.

To compute the folding sequence, the value of z_P is decreased in small steps; δ, the overall shortening of the cylinder, shown in Figure 4.1(b), is equal to the difference between the initial z_P and its current value. In each step the starting configuration is based on the shape of the cylinder computed at the end of the previous step, only z_P is changed. This imposes strains in the k connectors between the plate and the cylinder and, because these connectors are rigid, these strains must be relieved through suitable displacements. If the imposed strains are compatible they can be relieved simply by a displacement from the current configuration. This is always the case at the beginning of the folding process and, indeed, at this point the configuration of the loading plate is not uniquely defined. In this formulation a unique configuration is selected by minimising the generalised displacement. In general, however, the imposed strains have an incompatible component which sets up a state of self-stress in the system. Note that, with this approach, the folding of the cylinder is achieved simply by moving one of its boundaries, i.e. without applying any external forces. Because the force on the loading plate is treated as an internal force, this analysis simulates a displacement controlled test.

The cylinder is a highly non-linear system. The equilibrium matrix $\mathbf{A}$ is very sensitive to small geometry changes in the bars close to the plate. A further source of non-linearity is the variability in k, the number of nodes in contact with the plate. Because of this non-linearity, the algorithm performs a series of Newton-Raphson iterations to find the new shape of the cylinder, and the corresponding value of R, for each imposed value of z_P.

In each iteration the equilibrium matrix is calculated as outlined above, and the strain vector $\boldsymbol{\varepsilon}_0$ is assembled from the strains in the bars and the extensions of the k connectors between the plate and the top nodes of the cylinder. The strains in the bars are given by the difference between the current length and the initial, unstrained length. The extensions of the k plate-cylinder connectors are equal to the distance from the plate to the nodes in the $\mathbf{u}$-direction. The negative of the strain vector, $-\boldsymbol{\varepsilon}_0$, is imposed on the cylinder in an attempt to return it to its strain-free configuration. In general, however, $-\boldsymbol{\varepsilon}_0$ will have an incompatible component, and so will set up a state of self stress within the structure. The singular value decomposition of the equilibrium matrix is used to calculate the stresses $\boldsymbol{\sigma}$ and the displacements $\mathbf{d}$ induced by $-\boldsymbol{\varepsilon}_0$, following the method in section 4 of Pellegrino (1993).

The final part of the iteration is to update the configuration of the cylinder. This means updating not only the nodal coordinates, but also the orientation of the plate, $\mathbf{u}$. A check must be made to see if the $(k+1)$st node has passed through (i.e. come into contact with) the plate. If so, k is increased by one. This completes one Newton-Raphson iteration.

The iterations continue until both the displacement $\mathbf{d}$ imposed during the final iteration is sufficiently small, and no new nodes were added to the plate during the final iteration. This configuration is then correct, within the allowed tolerance, for the particular value of z_P imposed. The strain in the cylinder and the force R are then found by performing another iteration, as explained above, but without imposing the displacement vector $\mathbf{d}$ calculated (which should anyway be very small).

4.2. Results

Results are first presented for the triangulated cylinder shown in Figure 4.1(a). It has $m = 1$, $n = 7$, $l_b/l_a = 1$, and $l_c/l_a = \sqrt{3}$. According to Chapter 3, an unrestrained cylinder with these parameters has two strain-free configurations, one fully folded, the other fully extended. Figure 4.1(a) shows the fully extended configuration.

The cylinder is modelled as a pin-jointed truss, as discussed in Section 4.1: the total numbers of joints and bars are $N = 36$ and $B = 86$; bars joining two fully restrained nodes have been removed. All bars have equal axial stiffness AE. In the extended configuration node 1 (at the bottom of the cylinder) has $z = 0$, while node 36 (at the top of the cylinder) has $z = 4.175l_a$. The bottom $n = 7$ nodes are fully restrained: the z-coordinate of the last restrained node is $0.716l_a$. Clearly the folding of the cylinder cannot go past this point. The rigid plate at the top of the cylinder is set initially in contact with node 36, hence $z_P = 4.175l_a$ and $k = 1$. At this stage $\delta = 0$. Starting from this configuration the plate is lowered by decreasing z_P in steps of $l_a/100$.

Results from a simulation involving approximately 300 steps are shown in Figures 4.3–4.8. Figure 4.3 shows dimensionless plots of the force R, supplied by the foundation to the top plate, and the strain energy U in the cylinder. The cylinder begins to fold under zero force, hence remaining strain free, until $k = 4$. Then R starts increasing until, when $k = 8$, it reaches a peak, and then reduces. Subsequently, R oscillates periodically around zero. The strain energy increases considerably when k goes from 3 to 9, but then remains approximately constant. The strain energy plots actually show a slow increase, due to end effects in the top part of the cylinder, since the fully-folded region does not yet contain enough bars to allow the natural decay of strain to take place.

Figure 4.4 shows some more details of the steady state regime; the periodic variation of R is directly related to changes in k. R is negative, i.e. tensile, just before a new node comes into contact with the plate. At this point there is a sudden stiffness increase caused by the activation of an extra constraint, corresponding to an increment in the value of k. As δ is further increased, R increases until a limit point; it then decreases until the beginning of a new cycle. Note that in this simulation R is negative at the beginning and end of a cycle, which is incorrect, as the plate is only imposing a unilateral constraint. In practice a small spring-back of the folded region is likely to occur.

The folding cylinder is a continuously softening system, with

$$\frac{d^2R}{d\delta^2} < 0$$

wherever this quantity is defined, but the system is periodically stiffened as new nodes come into contact with the top plate. Although unusual, this behaviour has some similarities with the axial crushing of cellular materials (Gibson & Ashby, 1986).

Strain variation during steady state folding is considered next. For a clear picture of strain distribution it is best to consider the axial strain ε_c in the 28 c-bars, plotted in Figure 4.5. Similar plots could be obtained for the a- or b-bars. As the plate is pushed down, the most significant part of the strain field, say $\varepsilon_c > 10^{-3}$, simply translates from right to left, i.e. from the top towards the bottom of the cylinder. However, a region involving less significant compressive strains gradually builds up in the wake of the shape-transition region and the strain energy associated with it is responsible for the slow strain energy increase during steady state folding discussed earlier.

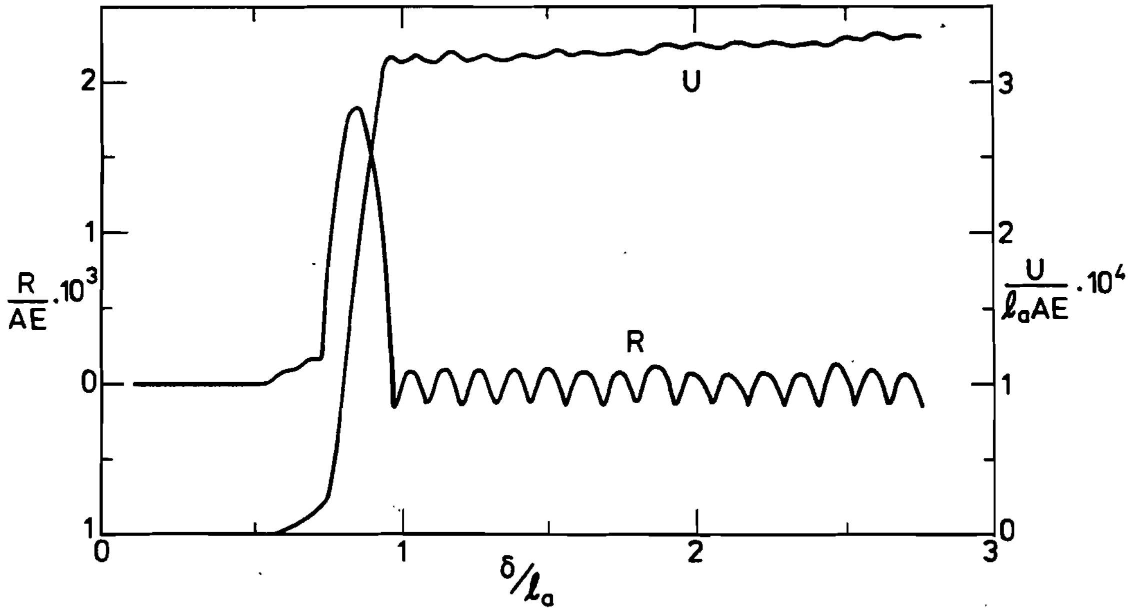

Figure 4.3. Folding of cylinders with $m = 1$, $n = 7$, $l_b/l_a = 1$, and $l_c/l_a = \sqrt{3}$. Plots of R and U in the cylinder.

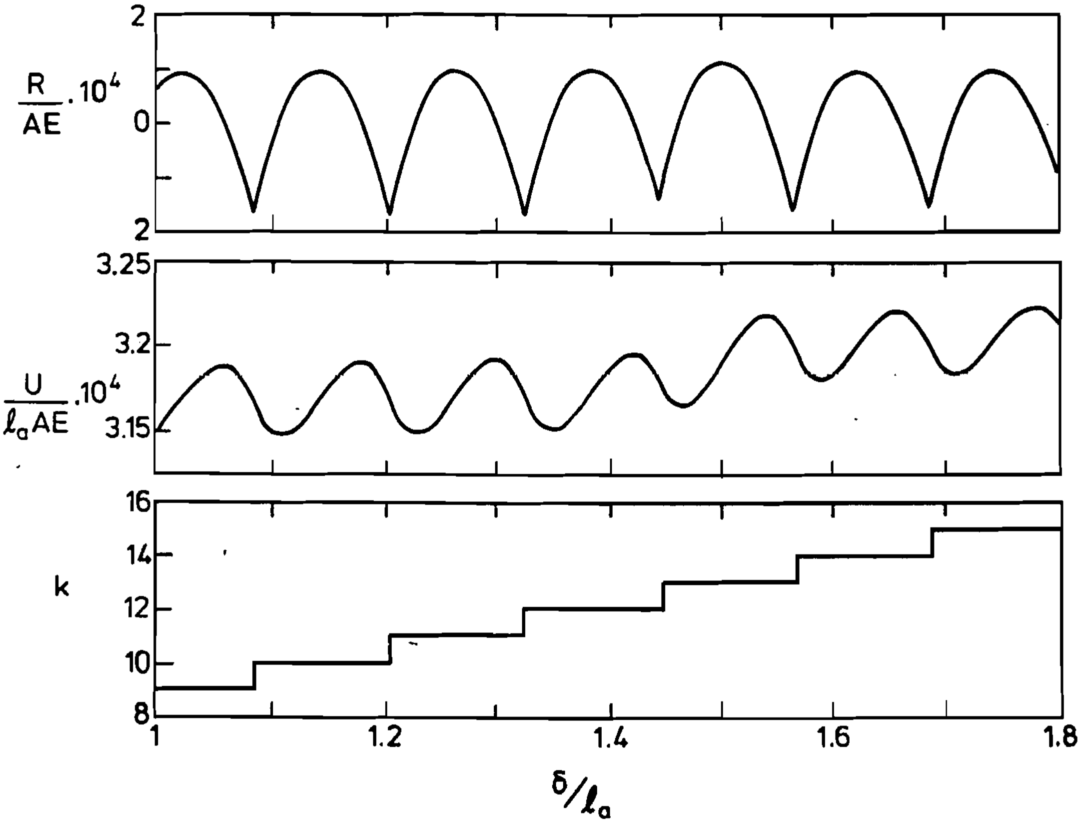

Figure 4.4. Folding of cylinders with $m = 1$, $n = 7$, $l_b/l_a = 1$, and $l_c/l_a = \sqrt{3}$. Detailed data for steady state phase.

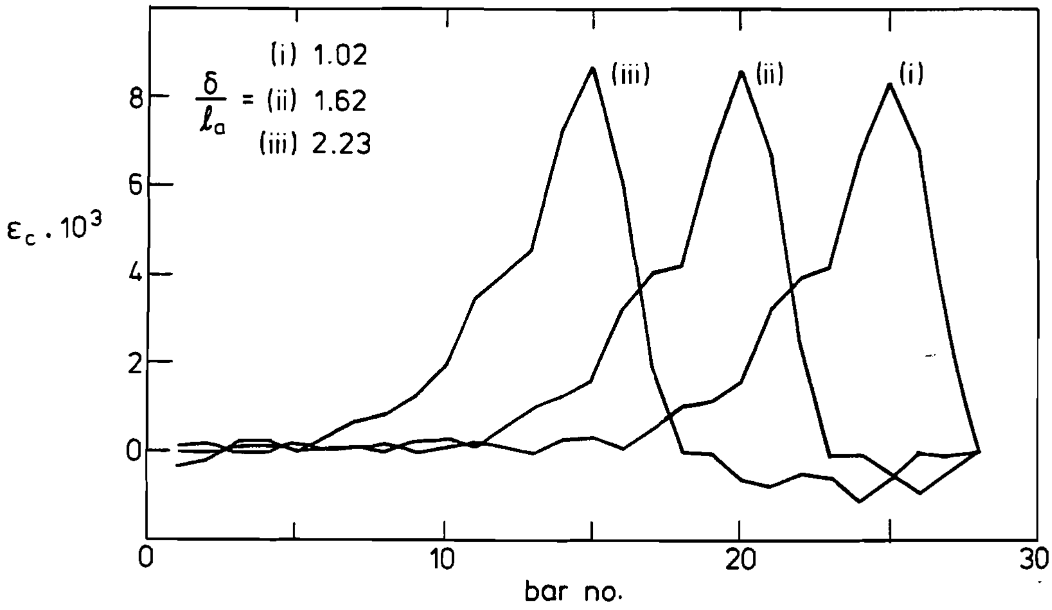

Figure 4.5. Folding of cylinders with $m = 1$, $n = 7$, $l_b/l_a = 1$, and $l_c/l_a = \sqrt{3}$. ε_c, the strains in the c-bars, during steady state folding. Bars take the number of their bottom node, and nodes are numbered going up on the a-helix. Discrete values have been joined, for legibility.

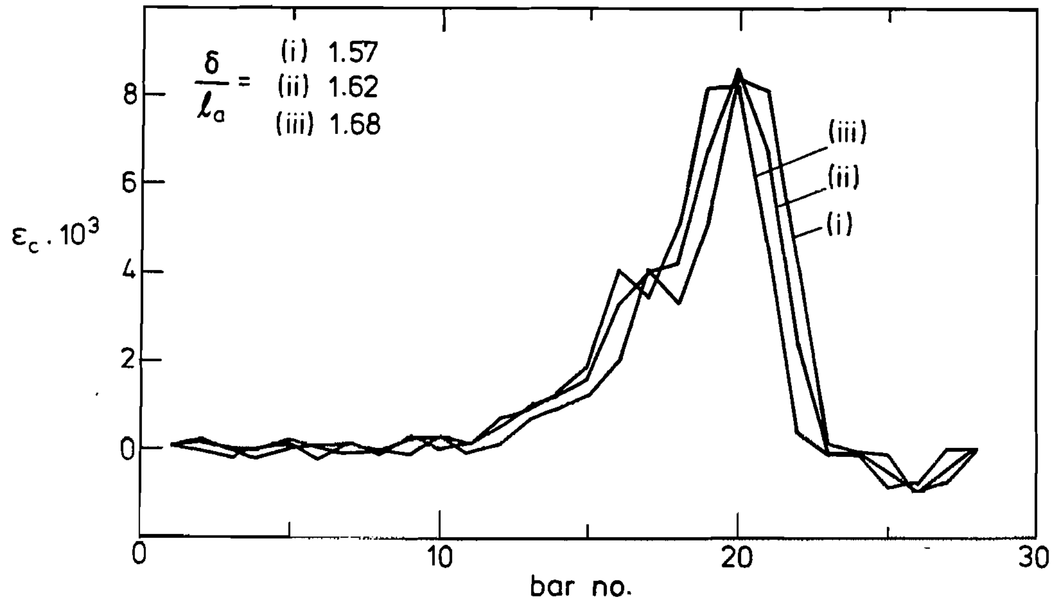

Figure 4.6. Folding of cylinders with $m = 1$, $n = 7$, $l_b/l_a = 1$, and $l_c/l_a = \sqrt{3}$. Detail of changes in ε_c during one folding cycle.

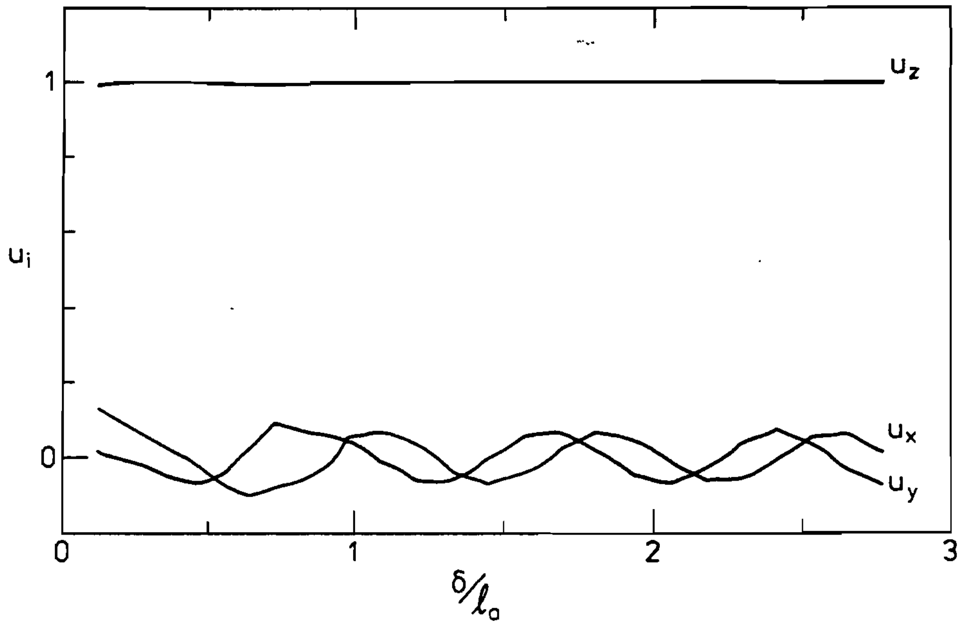

Figure 4.7. Folding of cylinders with $m = 1$, $n = 7$, $l_b/l_a = 1$, and $l_c/l_a = \sqrt{3}$. Three components of u.

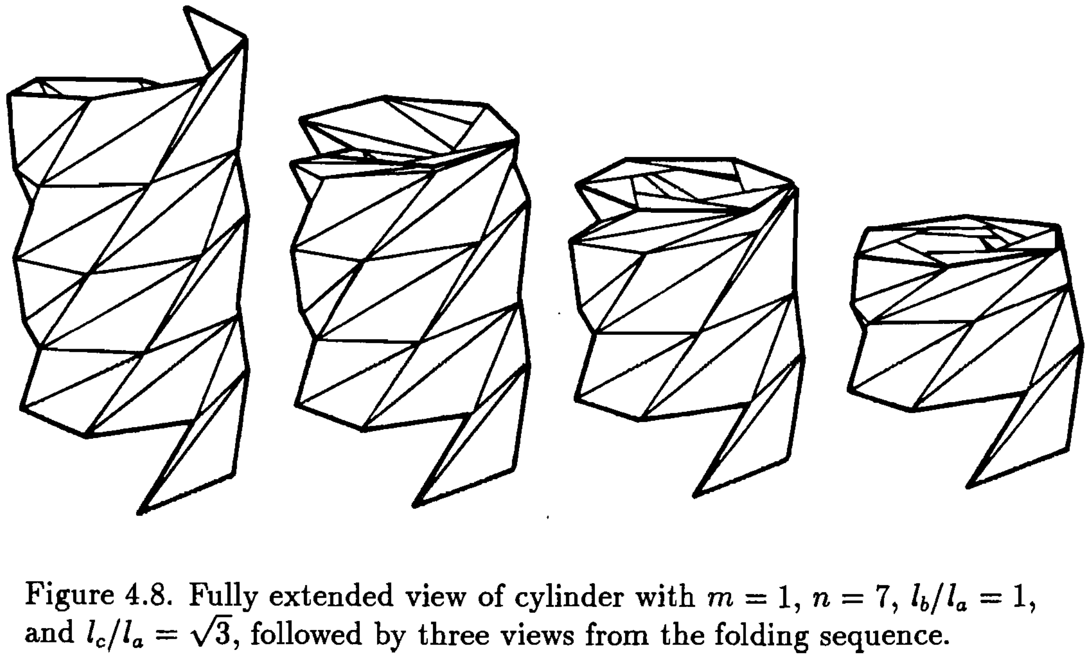

Figure 4.8. Fully extended view of cylinder with $m = 1$, $n = 7$, $l_b/l_a = 1$, and $l_c/l_a = \sqrt{3}$, followed by three views from the folding sequence.

The most significant feature of Figure 4.5 is the peak strain attained: here $\varepsilon_{c\,\mathrm{max}} = 8.7 \times 10^{-3}$. For the a- and b-bars, the (compressive) peak strains are 5.0×10^{-3} and 6.9×10^{-3} respectively.

Figure 4.6 shows strain plots, again for the c-bars only, (i) just after a node has come into contact with the plate, (ii) when R reaches its peak, and (iii) just before a new node comes into contact with the plate. Here, $k = 14$ throughout. Note that the peak strain remains essentially unchanged during this cycle.

Figure 4.7 shows the orientation of the loading plate by means of plots of the x-, y-, and z-components of $\mathbf{u}$. The plate normal essentially describes a small conical motion about the z-axis. Figure 4.8 shows four views from the simulation process, including the initial configuration.

Next, the behaviour of the three cylinders shown in Figure 3.2 are compared, to gain further insight into the folding process. One of them is the triangulated cylinder examined above, with $m = 1$, $n = 7$, $l_b/l_a = 1$, and $l_c/l_a = \sqrt{3}$. The two other cylinders also have $m = 1$ and $l_b/l_a = 1$: the first has $n = 6$ and $l_c/l_a = 1.618$; the second has $n = 8$ and $l_c/l_a = 1.802$. Both of these cylinders have been analysed by the technique described above.

For the cylinder where $n = 6$ a pin-jointed truss with $N = 31$ and $B = 74$ has been considered. In the fully extended configuration $z_P = 4.912 l_a$. To initiate the correct folding pattern, the simulation has to start with three nodes in contact with the plate. If a smaller number is chosen, the top plates start folding outwards and quickly the process comes to halt. Figure 4.9 shows plots of the force R and of the strain energy U during folding. As for $n = 7$, there is a large force peak and a corresponding increase in strain energy soon after the beginning of the process; afterwards, R oscillates around zero and U remains approximately constant. Figure 4.10 shows the strain field in the c-bars; as in Figure 4.5 the most significant part of the strain field simply translates from right to left. Qualitatively these results are the same as for the earlier cylinder, but the key difference between the cases $n = 6$ and $n = 7$ is in the magnitudes of forces and strains: R_{max} and $\varepsilon_{c\,\mathrm{max}}$ are respectively 14 and 4 times higher for $n = 6$ than for $n = 7$.

For the cylinder where $n = 8$ a pin-jointed truss with $N = 49$ and $B = 122$ has been considered. When fully extended it has $z_P = 2.818 l_a$. Starting from this position the plate has been lowered gradually: the folding behaviour of this cylinder, see Figures 4.11 and 4.12, is essentially identical to the earlier cases. Note that the trend towards lower forces and strains continues: R_{max} and $\varepsilon_{c\,\mathrm{max}}$ are respectively 150 and 17 times higher for $n = 7$ than for $n = 8$. The complete set of values is available for comparison in Table 4.1.

Table 4.1. $\varepsilon_{\mathrm{max}}$ and R_{max} in cylinders with $m = 1$ and $l_b/l_a = 1$.

n	$\lvert\varepsilon_a\rvert_{\mathrm{max}}$	$\lvert\varepsilon_b\rvert_{\mathrm{max}}$	$\lvert\varepsilon_c\rvert_{\mathrm{max}}$	R_{max}/AE
6	2.0×10^{-2}	2.7×10^{-2}	3.6×10^{-2}	2.6×10^{-2}
7	5.0×10^{-3}	6.9×10^{-3}	8.7×10^{-3}	1.8×10^{-3}
8	3.5×10^{-4}	4.1×10^{-4}	$5.2 \times 10^{-\cancel{3}4}$	1.2×10^{-5}

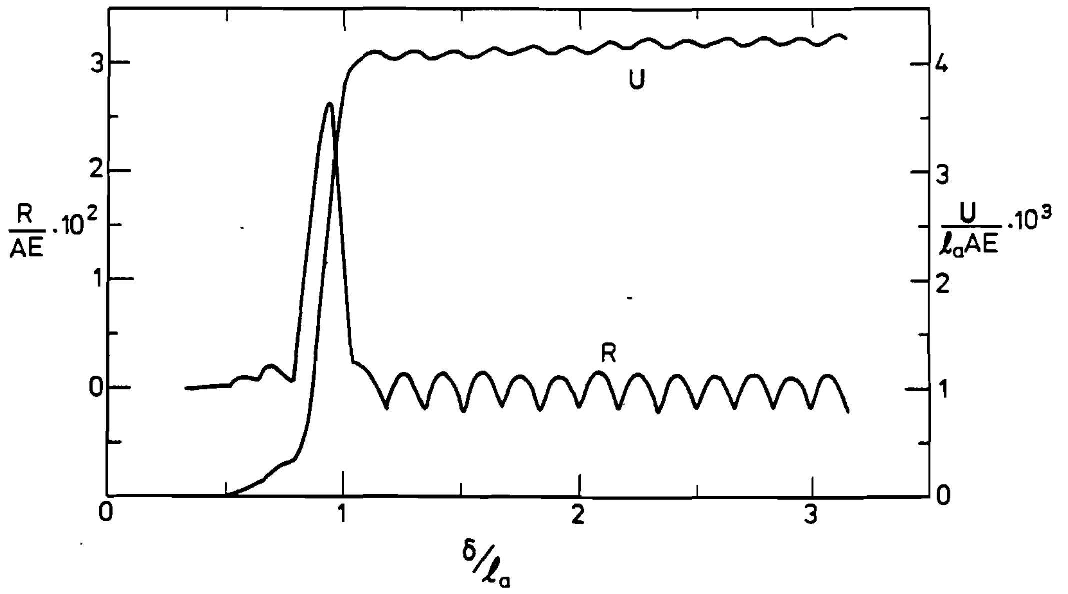

Figure 4.9. Folding of cylinders with $m = 1$, $n = 6$, $l_b/l_a = 1$, and $l_c/l_a = 1.618$. Plots of R and U in the cylinder.

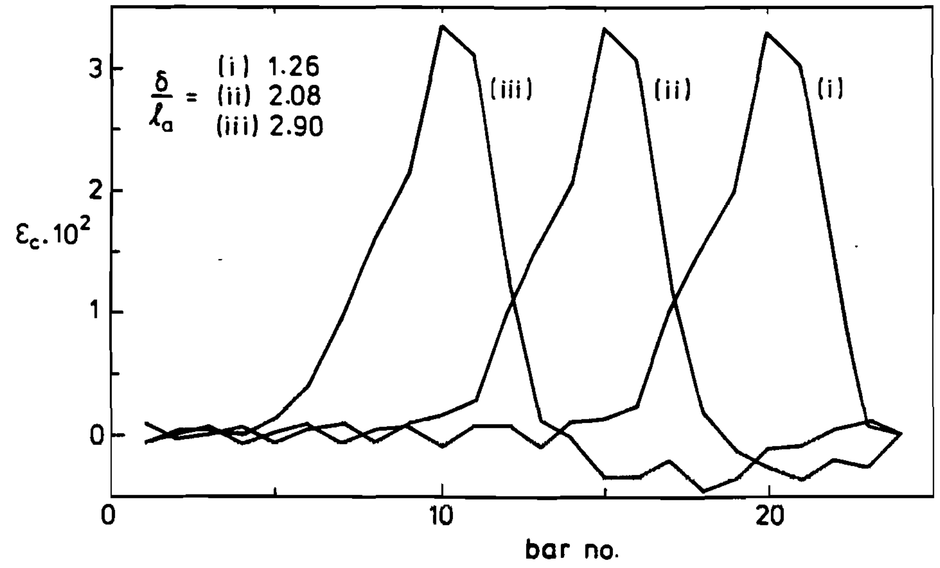

Figure 4.10. Folding of cylinders with $m = 1$, $n - 6$, $l_b/l_a = 1$, and $l_c/l_a = 1.618$. ε_c, during steady state folding.

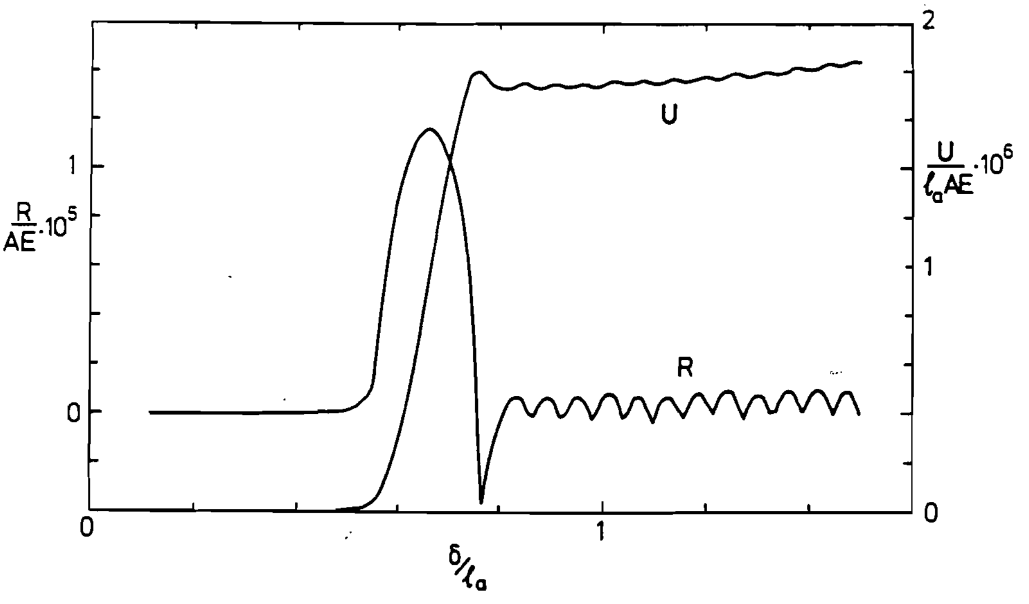

Figure 4.11. Folding of cylinders with $m = 1$, $n = 8$, $l_b/l_a = 1$, and $l_c/l_a = 1.802$. Plots of R and U in the cylinder.

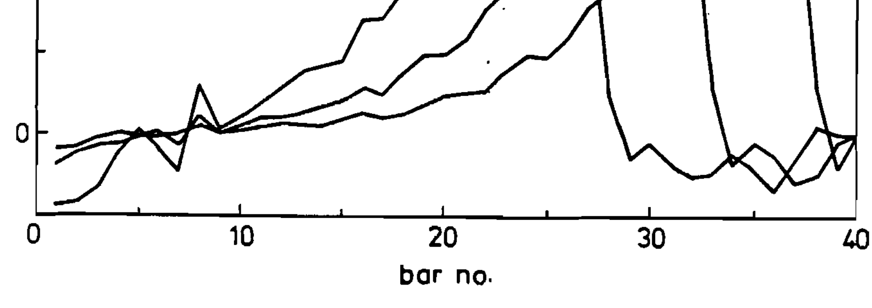

Figure 4.12. Folding of cylinders with $m = 1$, $n = 8$, $l_b/l_a = 1$, and $l_c/l_a = 1.802$. ε_c, during steady state folding.

4.3. Discussion

Before discussing the results obtained in this chapter it is necessary to comment on the validity of the assumptions behind the approach used, namely that a triangulated cylinder can be modelled as a simple pin-jointed truss and that plate thickness can be neglected. Although more complex models could be considered, it would be pointless to do this in a purely conceptual study. More detailed models would need to be firmly based on the mechanical features of a particular triangulated cylinder. For example, in the model shown in Figure 3.1 the plates are connected by thin plastic links which are very flexible in comparison with the plates, and the deformation of such a system is concentrated in these connections. If, on the other hand, more traditional mechanical hinges are used, the effects of joint tolerance would have to be considered. One important inherent assumption of the pin-jointed truss model is that the hinges have zero stiffness. Hinge stiffness is considered in Section 5.3.1 as an explanation of observed experimental behaviour. It does not cause significant increases in the peak strains seen in Table 4.1, but does change the force required to fold the cylinder. Regarding the second assumption, plate thickness is unlikely to play a significant role because its effects are not cumulative, unlike, for instance, the wrapping of a membrane around a central hub which is considered in Chapter 6.

The simulations presented in Section 4.2 have revealed that the folding of a triangulated cylinder consists of two phases. The first, unsteady, phase involves a gradual build-up of strain energy under a large applied force, which might provide an effective self-locking feature. During this phase a shape transition region from the fully extended to the fully folded part of the cylinder is formed and, once the energy barrier that prevents folding has been overcome, a second, steady state phase of the process begins. During this phase the shape transition region moves towards the bottom of the cylinder under almost zero force. These results qualitatively explain many of the experimental results obtained in Chapter 5.

In the three cylinders which have been analysed in this chapter, both the peak force, and the peak strain, decrease rapidly as n increases, as noted in Section 3.4, but the role played by this particular parameter should not be over-valued. The aim of this study was a characterisation of the general folding behaviour of triangulated cylinders, for which three cylinders which fold down to simple prisms were selected. Although a detailed investigation of the relative effects of varying design parameters has not been attempted, it can be noted that the key factor determining peak force and peak strain is the size of the geometric incompatibility shown in, for example, Figure 3.7. The particular combination of the parameters m, n, l_b/l_a, and l_c/l_a which leads to it is not very significant. Thus, for example, a similar range of $\varepsilon_{\max}$ and $R_{\max}$ to that obtained here, for $n = 6, 7, 8$ and $m = 1$ and $l_b/l_a = 1$, could be obtained with constant n, by varying l_b/l_a.

Finally, it is interesting to compare the present simulations of the folding process with the approach pursued in Chapter 3. A comparison has been made in Table 4.2 for the case $m = 1$, $n = 7$, $l_b/l_a = 1$, and $l_c/l_a = \sqrt{3}$. The table also gives modified peak strains, estimated in the spirit of Chapter 3 but allowing all bar lengths to vary simultaneously with constant ratios l_c/l_a and l_b/l_a. Note that these simplified estimates are higher than the predictions obtained with the

Table 4.2. Predictions in for cylinders with $\mathring{m} = 1$, $n = 7$, $l_b/l_a = 1$, and $l_c/l_a = \sqrt{3}$.

	$\lvert\varepsilon_a\rvert_{\max}$	$\lvert\varepsilon_b\rvert_{\max}$	$\lvert\varepsilon_c\rvert_{\max}$
Chapter 3	0	0	2.5×10^{-2}
Chapter 3 (modified)	1.2×10^{-2}	1.2×10^{-2}	1.3×10^{-2}
Chapter 4	5.0×10^{-3}	6.9×10^{-3}	8.7×10^{-3}

present method, and are hence safe for the preliminary design of foldable cylinders.

5. EXPERIMENTS

This chapter describes a number of foldable cylinders that have been designed, manufactured and tested. These cylinders were either aimed at possible applications, or were designed simply to validate the theoretical work in chapters 3 and 4. A summary of the geometry of the cylinders that were manufactured is given in Table 5.1.

Two possible applications have been considered for foldable cylinders. One is a collapsible fuel tank for hydrazine, a highly corrosive fuel used for satellite thrusters. The tank would collapse as hydrazine was burnt. This would prevent sloshing of the remaining fuel in the tank, and would make attitude control of the spacecraft easier.

The other application considered is to use a foldable cylinder as a shroud to protect thin walled booms, cabling or pipework from the space environment. This would have been particularly apt for the Hubble Space Telescope, where thermal shock on a thin walled deployable boom has been causing the spacecraft to vibrate.

Section 5.1 describes the manufacture of the models. The results of compression tests on the models are described in Section 5.2. These test show some characteristics not predicted by the simulations in Chapter 4. The computer model is therefore modified slightly, in Section 5.3, to explore several possible explanations for the observed behaviour. Section 5.4 concludes this chapter, and also the work on foldable cylinders.

Table 5.1. Experimental Foldable Cylinders

	m	n	l_a(mm)	l_b(mm)	l_c(mm)
Cu-Be and steel	1	7	124.8	104.7	205.3
Nylon-66	1	7	80.0	67.1	131.6
Irathane and Al-alloy. Cylinder no. 1	1	8	50.0	50.0	90.1
Irathane and Al-alloy. Cylinder no. 2	1	7	50.0	50.0	86.6

5.1. Manufacture

5.1.1. Cu-Be and Steel Cylinder

A cylinder was manufactured using a copper beryllium alloy (Cu-Be) as a hinge material. Cu-Be was used because it has a large elastic strain range when it has been correctly heat-treated. This means that a thin strip of Cu-Be can be elastically bent around a small radius. This feature is desirable so that the cylinder remains elastic during folding, and also has a compact folded shape. A Cu-Be cylinder such as this would be suitable for an application such as the collapsible hydrazine fuel tank.

The cylinder was made from a flat sheet, as described in Section 3.1, and shown schematically in Figure 3.3. It was made from a 0.1 mm thick sheet of Cu-Be, which was stiffened everywhere apart from the hinge-lines by sandwiching the Cu-Be between triangles of 0.5 mm thick steel plate. These plates were then spot-welded in place. The join between the two edges of the sheet to finally form the cylinder was also made in this way, with the two edges of the Cu-Be sheet running through the centre of the triangular plates. (Note that steel could not be used for a hydrazine tank, as the steel and the hydrazine would react. Other stiffening materials would be used instead).

A section of the Cu-Be sheet, stiffened by steel plates, but before forming into a cylinder, is shown in Figure 5.1(a). The steel triangles were placed 6 mm apart on the Cu-Be sheet to allow an elastic hinge to form. Also, the corners of the steel plates were rounded, to increase the width of the unrestrained Cu-Be sheet near the intersection of hinge lines. The hinges around a node are shown in the extended and folded configuration of the cylinder in Figure 5.1(b,c). One problem with this method of construction is the detail of folds around a node. Inevitably there is an incompatibility where concave and convex folds meet. At this point a crease forms in the Cu-Be sheet, causing plastic deformation. Thus the aim of purely elastic folding was not entirely fulfilled.

The base of the cylinder was fully restrained by casting it into an epoxy base. The cylinder is shown after manufacture, but before folding, in Figure 5.2.

5.1.2. Nylon-66 Cylinder

A cylinder was made from a 1 mm thick sheet of Nylon-66. Fold lines were formed by removing material from the outside of folds, leaving a 0.35 mm layer of Nylon to bend and form the hinge. The material was removed using a router, a portable milling machine.

The fold pattern was formed on the sheet, as in Figure 3.3, except that again the edge of the sheet occurred in the middle of a set of triangles rather than along a hinge. The cylinder was formed by joining these two edges. The edges were joined by removing material from both sides, overlapping these sections, and gluing them using Evo-Stick. The base of the cylinder was fully restrained by casting it into an epoxy base. The final forming of the cylinder was a difficult process, and after manufacture it was noted that a number of the hinges had cracked.

The completed cylinder is shown in Figure 5.3.

5.1.3. Irathane and Aluminium-Alloy Cylinder

Two of the cylinders described in Section 3.1 as simple examples have been made from Irathane and Al-alloy. These cylinders were not made with any particular application in mind, but rather to demonstrate the feasibility of such cylinders.

A sheet of 0.9 mm thick aluminium alloy plate was coated with a 0.7 mm thick layer of Irathane on both sides. Irathane is a flexible polyurethane. The Al-alloy

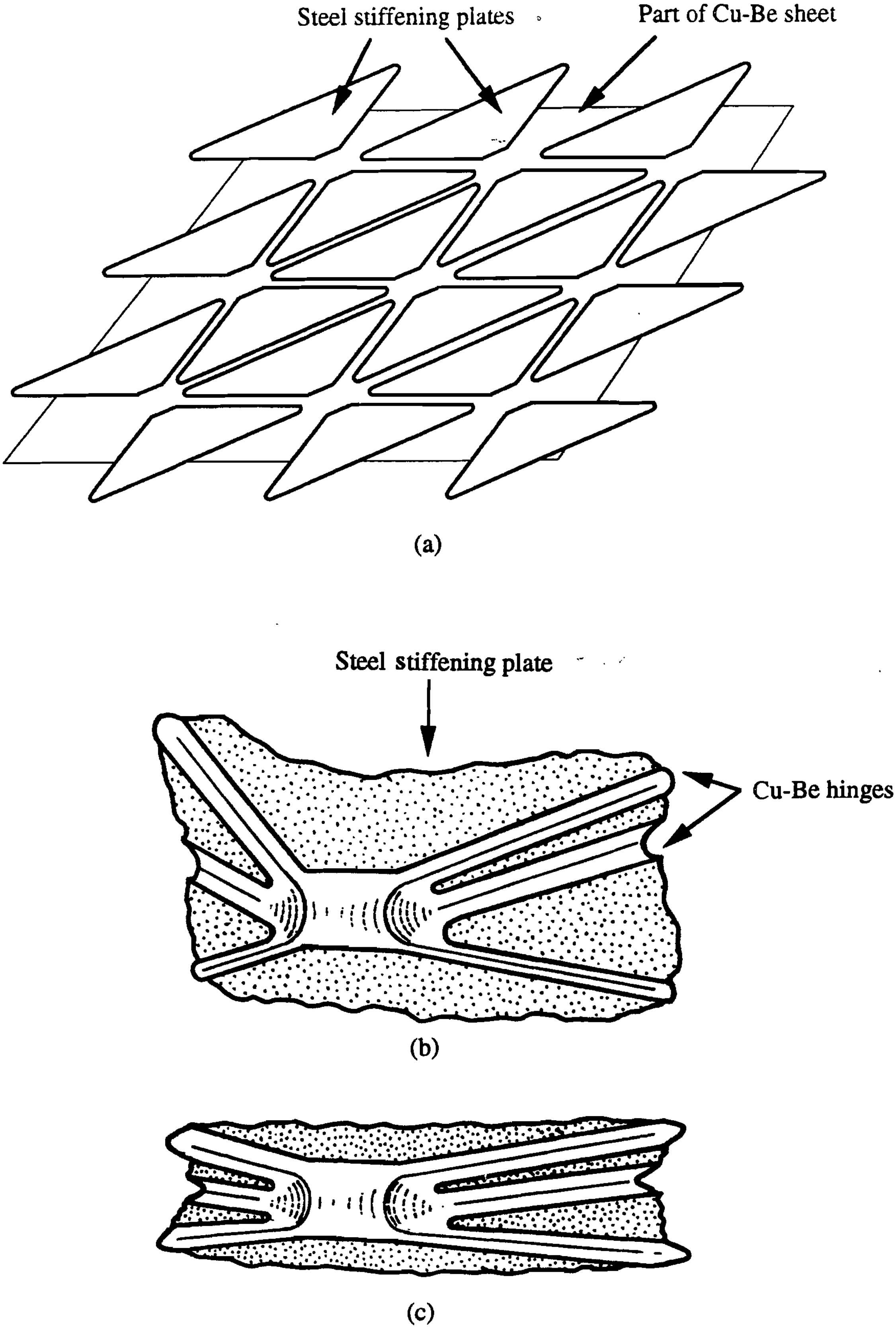

Figure 5.1. (a) Cu-Be sheet stiffened by steel plate during the manufacture of the cylinder. (b, c) Detail of the folds around a node, (b) when the cylinder is extended, and (c) when the cylinder is folded.

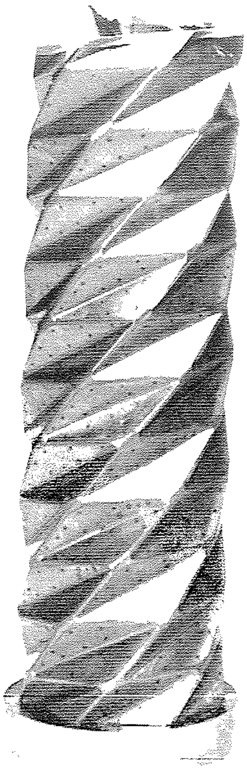

Figure 5.2. The Cu-Be and steel cylinder.

provides stiffness for the triangles, and the Irathane was used to form the hinges.

Hinges were formed by removing material from the outside of the hinge-line, using a milling machine. Both one layer of the Irathane, and the Al-alloy were removed, leaving the other layer of Irathane to form the hinge.

Two sheets of Al-alloy coated with Irathane were milled to the correct fold pattern. The left and right hand edges of the sheet were again formed halfway between two fold-lines. The final cylinder was formed by joining together sets of half-plates on opposite edges of the sheet. The bases of both cylinders were fully restrained before testing

The two cylinders manufactured by this method are shown in Figure 5.4.

5.2. Test Results

All of the cylinders described in the previous section were tested to find the force required during the folding process. They were compressed using a Howden testing machine in a displacement controlled mode. The base of all of the cylinders were fully fixed, as described in the Section 5.1. The top of the cylinders were loaded using a plate which was attached to the testing machine through a ball joint, thus allowing the plate to change its orientation.

The load was measured by a load cell at the top of the testing machine. The results presented show the compressive load on the cylinder, and have therefore been corrected to include the weight of the loading plate.

Figure 5.3. The Nylon-66 cylinder.

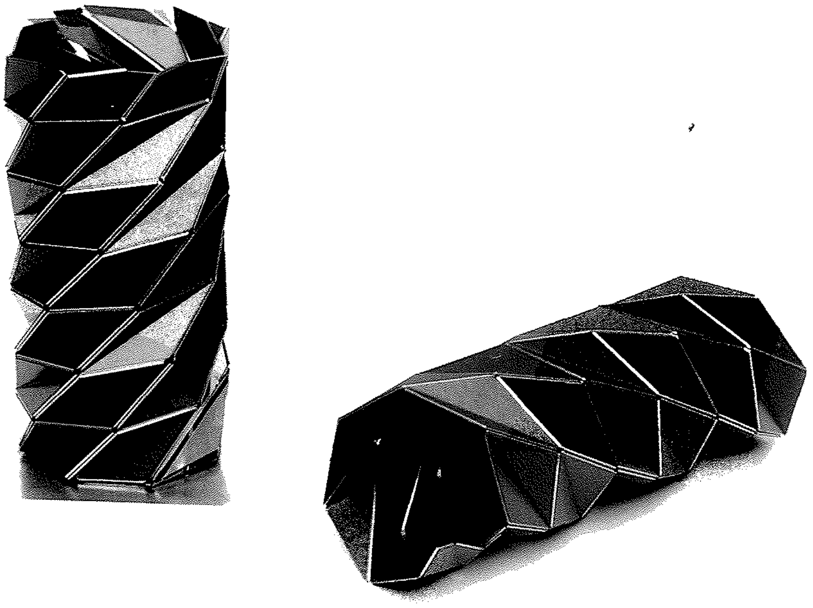

Figure 5.4. Two Irathane and Al-alloy cylinders: Cylinder no. 1, vertical; Cylinder No. 2, horizontal.

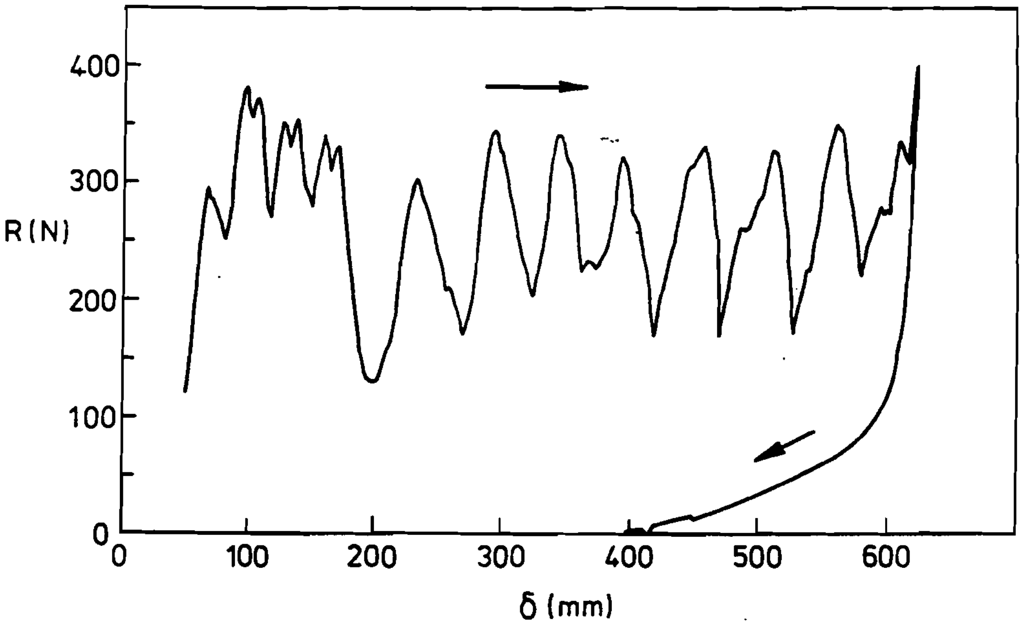

Figure 5.5. Compressive force during the first compression test on the Cu-Be and steel cylinder.

5.2.1. Cu-Be and Steel Cylinder

Four compression tests were performed on the Cu-Be and steel model described in Section 5.1.1. A plot of the force required to fold the cylinder during the first compression test is shown in Figure 5.5. Figure 5.6 shows four photographs taken during this test. As can be seen from Figure 5.6(a) the cylinder had to be initially slightly folded to fit in the testing machine.

The plot of force during folding can be more readily understood by knowing the change in the relative height coordinates of two successive nodes between the open and closed configuration. The difference in height between two nodes on the a-helix is 9 mm, and on the b-helix 64 mm. It can be seen that the basic periodicity of the plot has a wavelength corresponding to successive nodes on the b-helix folding.

One important effect shown in the photographs is the formation of a second transition zone close to the base of the cylinder. This occurred when the cylinder had been compressed by 125 mm. For the rest of the test it was this transition zone which moved up through the cylinder. A possible reason for the formation of this second transition zone is the weight of the cylinder, which led to a compressive force approximately 55N greater in the second transition zone than in the top transition zone.

During the test, whenever the force was rising no new nodes would fold. A number of nodes would then fold in quick succession as the force dropped.

When fully folded, the cylinder had a height of 242 mm, compared with an original height of 872 mm. 150 mm of the compressed height was accounted for by the part of the cylinder fixed open at the base.

When the test was reversed, and the top plate moved up, the cylinder showed

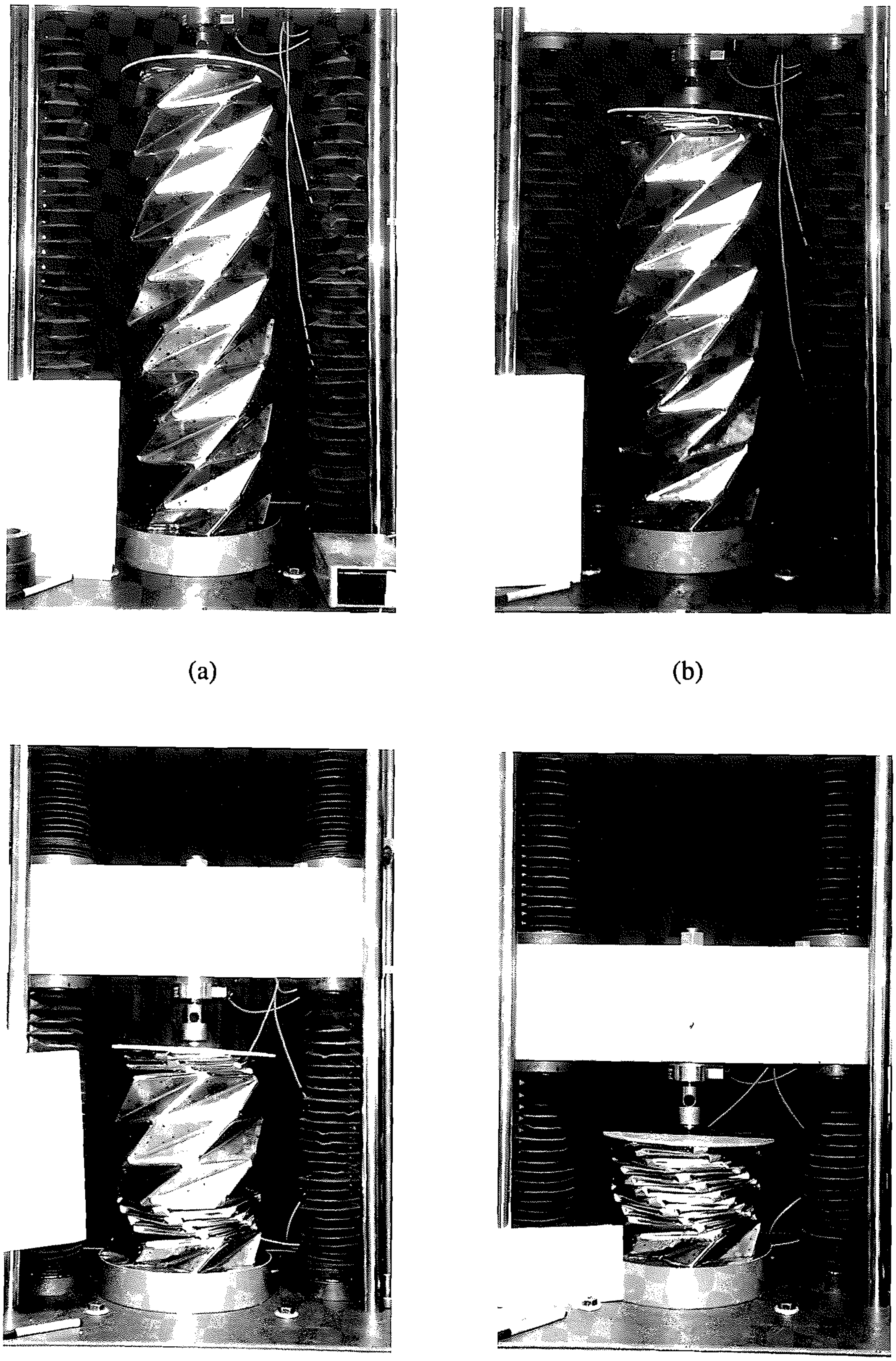

(a) (b)

(c) (d)

Figure 5.6. Photographs taken during the folding of the Cu-Be and steel cylinder: (a) Initial state, (b) $\delta = 100\,\mathrm{mm}$, (c) $\delta = 400\,\mathrm{mm}$, (d) $\delta = 630\,\mathrm{mm}$, fully folded.

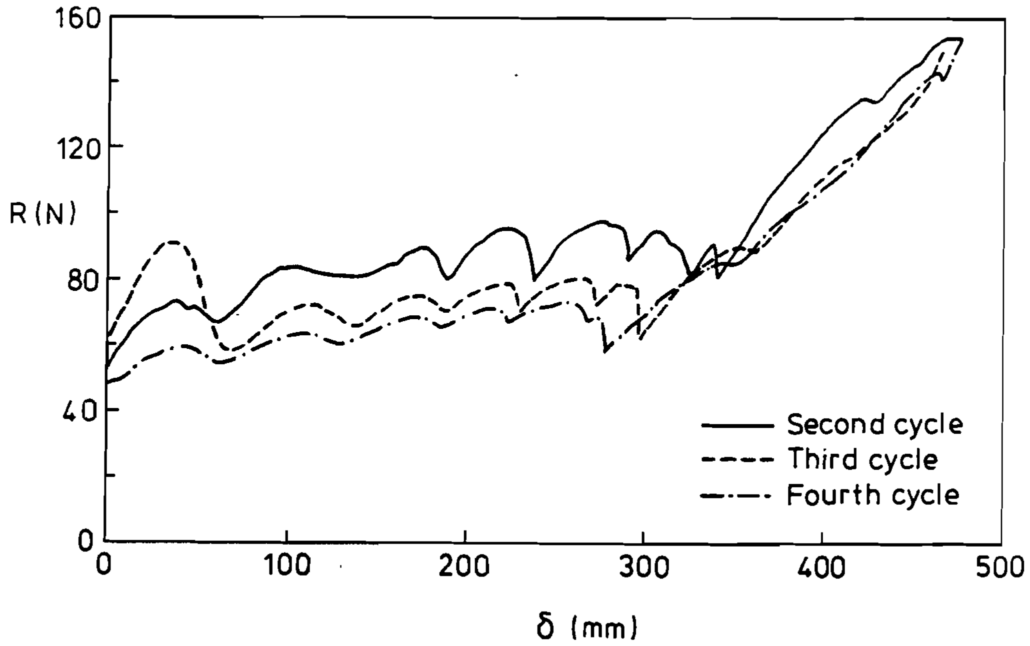

Figure 5.7. Compressive force during the second, third and fourth compression test on the Cu-Be and steel cylinder.

some spring-back, and regained a height of 540 mm. Closer inspection of the Cu-Be around the nodes showed that the creases seen in Figure 5.1 had moved by 1-2 mm closer together. Stretching the cylinder caused these creases to move back towards their original position, and the cylinder to regain an extended configuration. The creases did not, however, return completely to their original position, and the cylinder only regained a height of 763 mm, compared with an original height of 872 mm.

Three further tests were performed on the cylinder. After each test the cylinder was pulled back towards its original configuration. The force required to fold the cylinder in each case is plotted in Figure 5.7. In each test the cylinder folded by forming a transition zone close to the base of the cylinder, which then moved up through the cylinder as the test proceeded. The force plotted is that in the transition zone, and so the original data has been modified to account for the steadily decreasing weight of the portion of the cylinder above the transition zone. Again during the test a number of nodes would fold each time the force decreased.

For each of the further three test performed the change in the relative height coordinates of two successive nodes between the open and closed configuration is 7 mm along the a-helix, and 45 mm on the b-helix. Note that these values are smaller than for the original test, as the plastic deformation around the nodes reduced the height of the cylinder. Again the basic periodicity of the force has a wavelength corresponding to successive nodes on the b-helix folding.

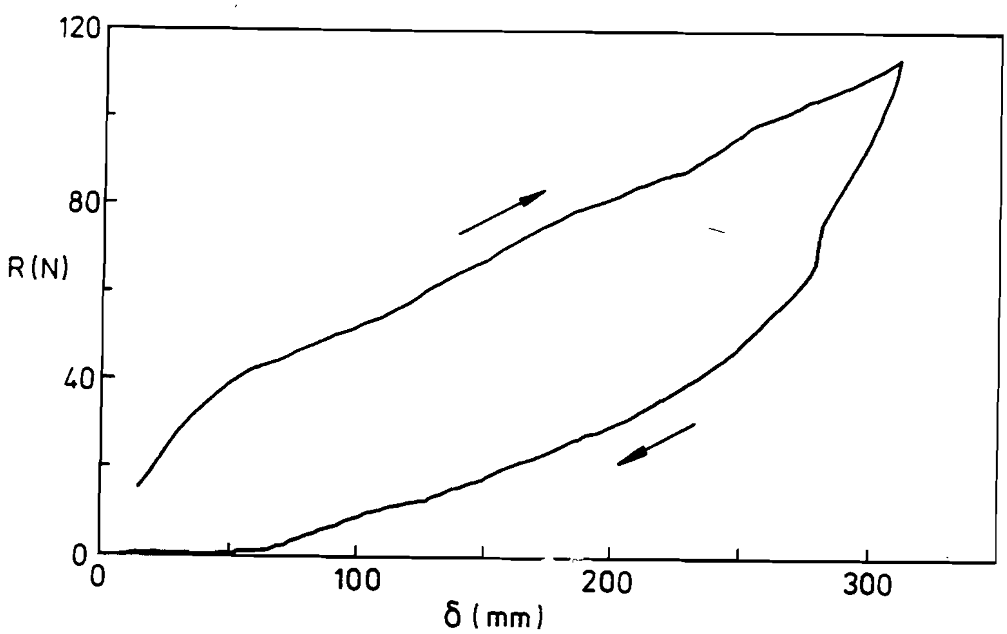

Figure 5.8. Compressive force during a 5 mm/minute compression test on the Nylon-66 cylinder.

5.2.2. Nylon-66 Cylinder

A number of compression tests were performed on the Nylon-66 cylinder described in Section 5.1.2. These tests were performed at different compression rates, as Nylon-66 has strain rate dependent stress-strain properties. However, the results of only one test are presented. Each of the others qualitatively showed the same results, but with slightly larger forces for the quicker tests.

The force plot for a compression performed at 5 mm/minute is shown in Figure 5.8. Photographs taken during this test are shown in Figure 5.9. The results of this test are rather unexpected. The force plot shows none of the periodicity seen in all of the other cylinders tested.

The cylinder initially forms a transition zone at its top, as can be seen in Figure 5.9(b). However, as the test proceeds, the cylinder starts to fold in a number of different places, as can be seen in Figure 5.9(c). Generally these other areas of folding initiated at folds were the Nylon had cracked.

When the test was reversed the cylinder unfolded in the reverse order of folding, but under a reduced load.

5.2.3. Irathane and Aluminium-Alloy Cylinders

The results of the compression test on the Irathane and Al-alloy cylinder no. 1 are shown in Figure 5.10. As for the Cu-Be and steel cylinder, these results can be more readily understood by knowing the change in the relative height coordinates of two successive nodes between the open and closed configuration. The difference between two nodes on the a-helix is 2.7 mm, and on the b-helix 22 mm. It can be seen that the basic periodicity of the plot has a wavelength corresponding to

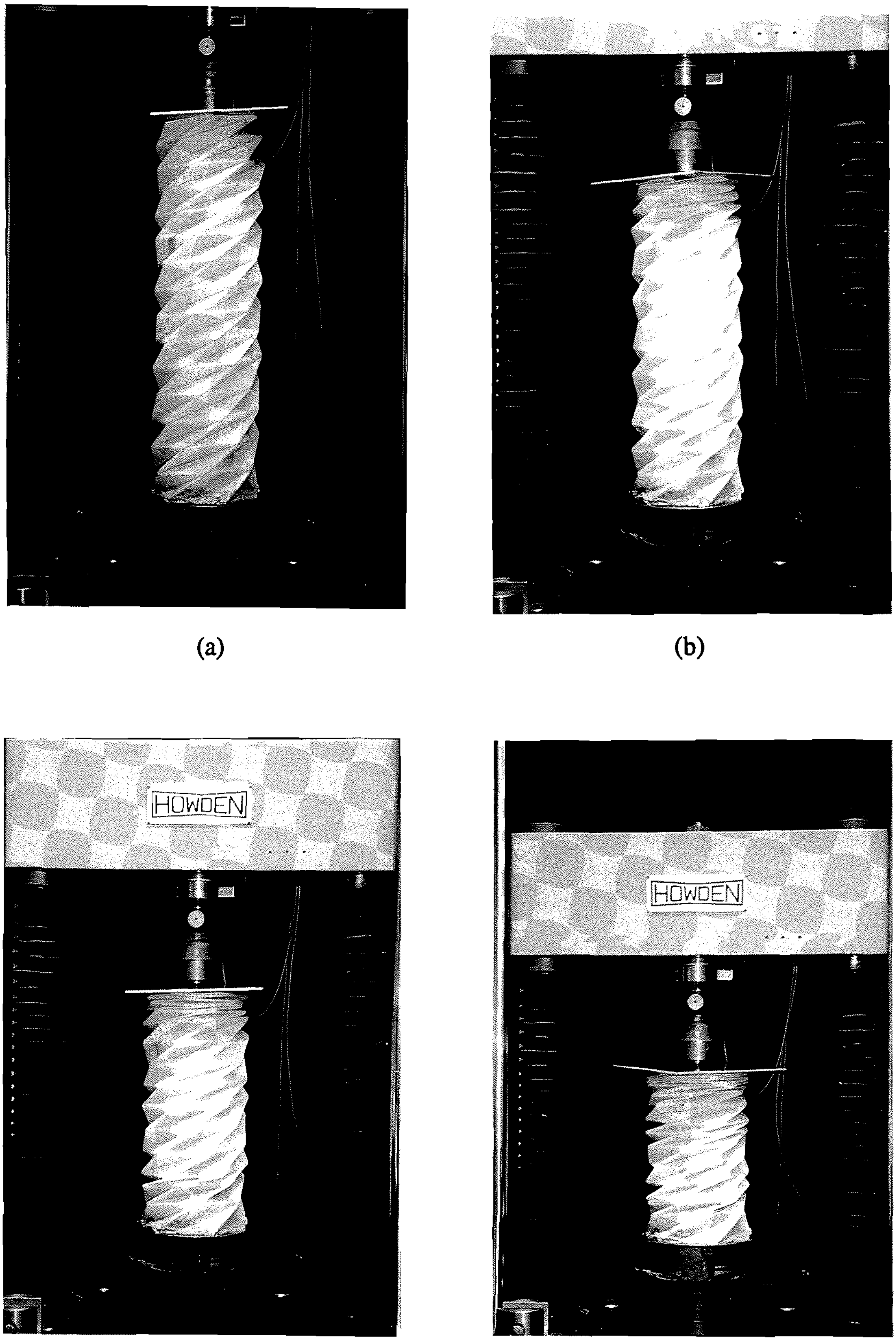

(a) (b)

(c) (d)

Figure 5.9. Photographs of folding the Nylon-66 cylinder: (a) Initial state, (b) $\delta = 100\,\mathrm{mm}$, (c) $\delta = 200\,\mathrm{mm}$, (d) $\delta = 300\,\mathrm{mm}$, fully folded.

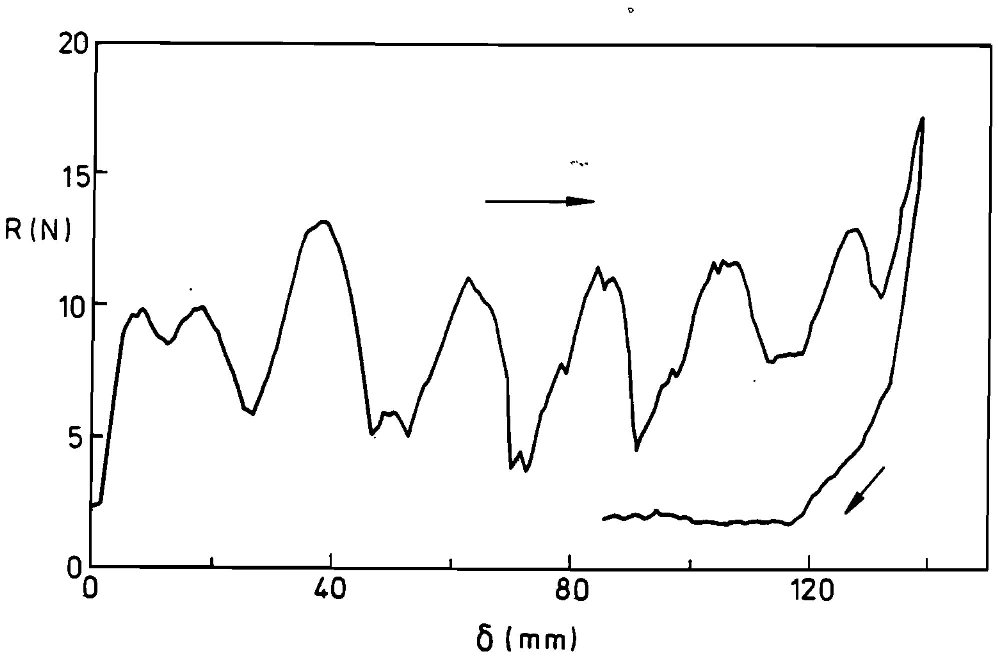

Figure 5.10. Compressive force during folding for the Irathane and Al-alloy cylinder no. 1.

successive nodes on the b-helix folding.

The cylinder formed one transition zone at the top of the cylinder, which moved down the cylinder as the the test proceeded. As for the Cu-Be and steel cylinder, no nodes would fold while the force was rising, but a number would fold in quick succession when the force was reducing.

The results of the compression test on the Irathane and Al-alloy cylinder no. 2 are shown in Figure 5.11. For this case the change in the relative height coordinates of two successive nodes between the open and closed configuration is ~~2.7~~ 4.0 mm along the a-helix, and ~~2.2~~ 28 mm on the b-helix. In contrast with the previous case, however, there is no consistent periodicity in the results.

The cylinder again formed one transition zone at the top of the cylinder, which moved down the cylinder as the the test proceeded. Again, no nodes would fold while the force was rising, but a number would fold in quick succession when the force was reducing.

5.2.4. Discussion

Apart from the Nylon-66 cylinder, all the cylinders tested had a number of features in common. They all initially formed a transition zone, as predicted in Chapter 4. This transition zone then moved through the cylinder. Generally the zone moved from the top down, as predicted, but for the Cu-Be and steel cylinder it moved from the bottom up, due to the self-weight of the cylinder.

The shapes of the force plots measured during the folding of the cylinders also have a number of similarities. They all show a periodic variation of the force. In two of the cylinders, the Cu-Be and steel cylinder, and the Irathane and Al-alloy

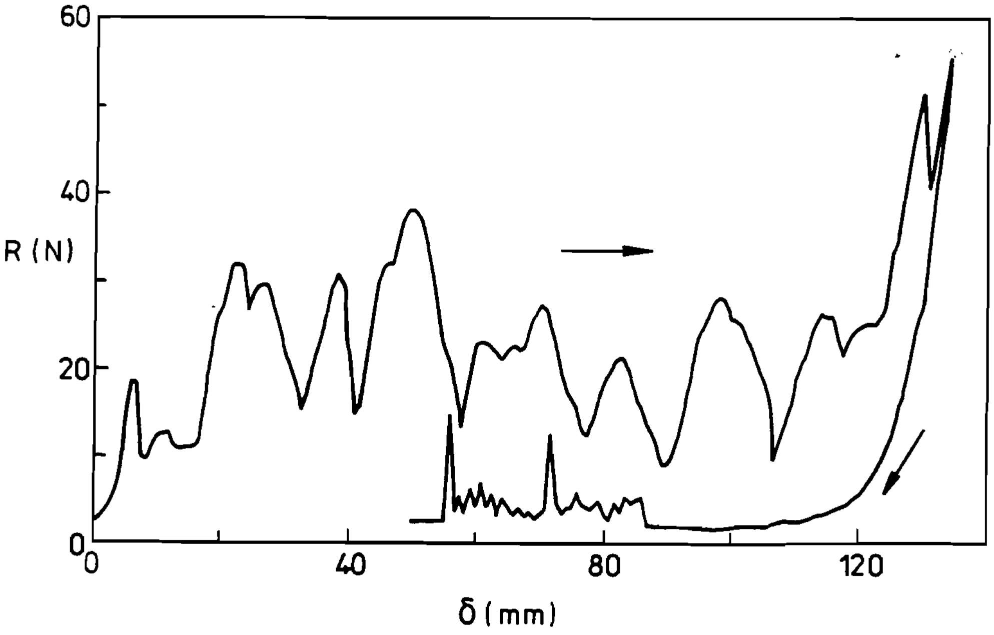

Figure 5.11. Compressive force during folding for the Irathane and Al-alloy cylinder no. 2.

cylinder no. 1, the wavelength of this variation corresponds to the folding of one node along the b-helix, i.e. of n nodes on the a-helix. In the Irathane and Al-alloy cylinder no. 2 the period of variation showed no obvious pattern.

Comparing the results for all cylinders except the Nylon-66 cylinder with those produced from the computer simulation in Chapter 4, a number of similarities can be seen. In both the simulation and the tests, the mode of deformation of the cylinder are similar. A transition zone forms, which then moves through the cylinder. Comparing the plots of force from the computations with the experimental results, both cases show the force varying around a constant value as the transition zone moves through the cylinder.

There are, however, a number of discrepancies between the computational results and the test results. One is that the force in the experimental results does not vary about zero, but about an average compressive force. This implies that some strain energy is being stored in the cylinder during the folding process. Another discrepancy is that the variation of the force does not correspond to successive nodes on the a-helix folding. Indeed, for two of the cylinders tested it corresponded to successive nodes on the b-helix folding. A third discrepancy is the absence in the experimental results of any sign of the initial force peak as the transition zone forms.

There are two obvious explanations for the discrepancies between the computational and the experimental results. The first is the effect of hinge elasticity. The original computer model assumed momentless hinges, and so the folded state had zero strain energy. In reality, some energy must be put into the hinges to cause them to fold. Thus, as the transition zone moves down the cylinder, energy must be put into the cylinder to fold more hinges, and so the average compressive force must be greater than zero.

The second explanation for the discrepancies is the effect of errors during manufacture. The most obvious source of these is the final joining process to transform a sheet into a cylinder. This is difficult in practice. A misfit here would lead to the force plot showing a periodicity, not as successive nodes on the a-helix fold, but as complete turns of the a-helix fold. The more random periodicity shown by one of the Irathane and Al-alloy cylinders could be due to more distributed errors, as this was an early attempt at making a cylinder, and it had already been damaged by a number of demonstrations prior to the test.

The reasons for the exceptional nature of the Nylon-66 cylinder are not clear. One possible explanation is that the rate-dependent nature of the material prevents strains being quickly released, halting the expected reduction in the force folding the cylinder. However, even tests performed very slowly (1 mm/minute) showed qualitatively the same behaviour, but with a lower force level.

A more likely explanation is the effect of errors during manufacture. The final joining process to transform the sheet of Nylon into a cylinder was particularly difficult. The final seam was not always aligned well, and errors became worse towards the base of the cylinder. This caused a number of joints near the base of the cylinder to crack. In contrast with the constant error assumed above, the effect of an increasing error in the cylinder would be to make it progressively more difficult to fold. Also the cracked hinges would tend to initiate the folding that occurs away from the transition zone, as seen in Figure 5.9.

5.3. Modifications to Computer Model

In order to validate the reasons suggested in the previous section for the discrepancies between experimental results, and those predicted by the computer model in Chapter 4, a number of changes were made to the computer simulation. The first change was to modify the model so that it no longer assumed momentless hinges. The second change was to modify the model to simulate the effect of a final misalignment during the manufacture of the cylinders.

5.3.1. Elastic Hinges

The aim of this section is to incorporate elastic hinges into the computational model described in Chapter 4. These hinges will apply a couple to the triangular plate on each side of the hinge; equilibrium is maintained by additional forces at the nodes, applied perpendicular to the plate. The elastic couple is treated as an internal stress. Externally the nodes are, as previously, only loaded by forces and not moments. A more complex model which included external moments would be pointless, as these would anyway be set to zero in the analysis.

The elastic hinge element is a non-standard element in the Force Method, and so its implementation is described in detail. Consider a typical elastic hinge, connecting the two triangular plates shown in Figure 5.12(a). The hinge and the plates are defined by the four nodes s, t, u and v, which have position vectors $\mathbf{p_s}$, $\mathbf{p_t}$, $\mathbf{p_u}$ and $\mathbf{p_v}$. The equilibrium and compatibility relationships for the plates themselves have been defined in the previous chapter, using bar elements.

Presented here is the equilibrium relationship between the hinge element and additional forces perpendicular to the plate which keep the element in equilibrium. The compatibility and flexibility relationships are also defined.

An exploded view of the two plates, showing the forces and moments applied to each plate, is shown in Figure 5.12(b). The hinge exerts a moment M (positive in the direction shown) on each plate. Forces $\mathbf{r}_s$, $\mathbf{r}_t$, $\mathbf{r}_u$ and $\mathbf{r}_v$ are applied at the node s, t, u and v. All the forces applied to one plate are perpendicular to that plate. Forces $\mathbf{r}_s$ and $\mathbf{r}_t$ are each made up of two components, $\mathbf{r}_{s1}$ and $\mathbf{r}_{t1}$ are perpendicular to plate stu, and $\mathbf{r}_{s2}$ and $\mathbf{r}_{t2}$ are perpendicular to plate stv. An equilibrium relationship can be set up for each plate in turn.

Consider plate stu. For simplicity, the vectors $\mathbf{a} = \mathbf{p}_t - \mathbf{p}_s$, and $\mathbf{b} = \mathbf{p}_u - \mathbf{p}_s$ are introduced. The vector $\mathbf{a} \times \mathbf{b}$ (where $\times$ is the standard vector cross product) is perpendicular to the plate (s, t and v will not be collinear if they define a plate), and so the forces can be written

$$\mathbf{r}_{s1} = \left(\frac{\|\mathbf{r}_{s1}\|}{\|\mathbf{a} \times \mathbf{b}\|}\right) \mathbf{a} \times \mathbf{b}$$

$$\mathbf{r}_{t1} = \left(\frac{\|\mathbf{r}_{t1}\|}{\|\mathbf{a} \times \mathbf{b}\|}\right) \mathbf{a} \times \mathbf{b}$$

$$\mathbf{r}_{u} = \left(\frac{\|\mathbf{r}_{u}\|}{\|\mathbf{a} \times \mathbf{b}\|}\right) \mathbf{a} \times \mathbf{b}$$

Consider moment equilibrium about s. The force $\mathbf{r}_u$ exerts a moment $\mathbf{b} \times \mathbf{r}_u$, the force $\mathbf{r}_{t1}$ exerts a moment $\mathbf{a} \times \mathbf{r}_{t1}$, and the hinge exerts a moment $(M/\|a\|)\mathbf{a}$. Therefore moment equilibrium gives the three-dimensional vector equation

$$\mathbf{b} \times \mathbf{r}_u + \mathbf{a} \times \mathbf{r}_{t1} + \left(\frac{M}{\|\mathbf{a}\|}\right) \mathbf{a} = \mathbf{0}$$

Rewriting the forces as above then gives

$$\left(\frac{\|\mathbf{r}_u\|}{\|\mathbf{a} \times \mathbf{b}\|}\right) \mathbf{b} \times \mathbf{a} \times \mathbf{b} + \left(\frac{\|\mathbf{r}_{t1}\|}{\|\mathbf{a} \times \mathbf{b}\|}\right) \mathbf{a} \times \mathbf{a} \times \mathbf{b} + \left(\frac{M}{\|\mathbf{a}\|}\right) \mathbf{a} = \mathbf{0}$$

The vector triple products can then be expanded

$$\mathbf{b} \times \mathbf{a} \times \mathbf{b} = (\mathbf{b} \cdot \mathbf{b})\mathbf{a} - (\mathbf{b} \cdot \mathbf{a})\mathbf{b} = \|\mathbf{b}\|^2\mathbf{a} - (\mathbf{a} \cdot \mathbf{b})\mathbf{b}$$

$$\mathbf{a} \times \mathbf{a} \times \mathbf{b} = (\mathbf{a} \cdot \mathbf{b})\mathbf{a} - (\mathbf{a} \cdot \mathbf{a})\mathbf{b} = (\mathbf{a} \cdot \mathbf{b})\mathbf{a} - \|\mathbf{a}\|^2\mathbf{b}$$

where $\cdot$ is the standard vector dot product, and the equation becomes

$$\left(\|\mathbf{r}_u\|\|\mathbf{b}\|^2 + \|\mathbf{r}_{t1}\|(\mathbf{a} \cdot \mathbf{b}) + M\left(\frac{\|\mathbf{a} \times \mathbf{b}\|}{\|\mathbf{a}\|}\right)\right)\mathbf{a} - (\|\mathbf{r}_u\|(\mathbf{a} \cdot \mathbf{b}) + \|\mathbf{r}_{t1}\|\|\mathbf{a}\|^2)\mathbf{b} = \mathbf{0}$$

If this equation is derived for a plate, then $\mathbf{a} \neq \mathbf{0}$, $\mathbf{b} \neq \mathbf{0}$, and $\mathbf{a}$ and $\mathbf{b}$ will not be parallel. This vector equation can therefore be split into two scalar equations

$$\|\mathbf{r}_u\|(\mathbf{a} \cdot \mathbf{b}) + \|\mathbf{r}_{t1}\|\|\mathbf{a}\|^2 = 0 \qquad (5.1)$$

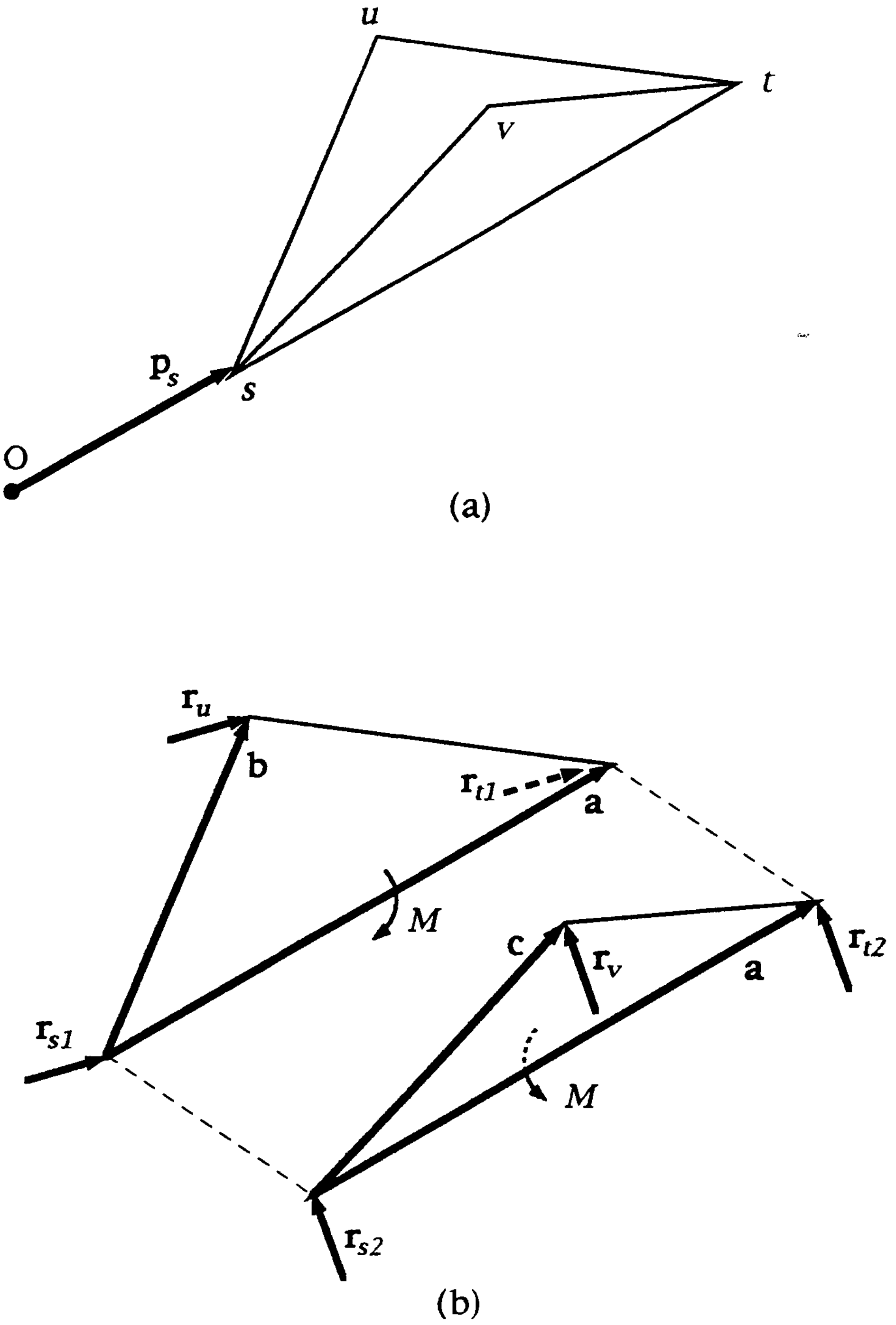

Figure 5.12. Elastic hinge element: (a) Nodes and positions. (b) Exploded view showing forces and moments.

and

$$\|\mathbf{r}_u\|\|\mathbf{b}\|^2 + \|\mathbf{r}_{t1}\|(\mathbf{a}\cdot\mathbf{b}) + M\left(\frac{\|\mathbf{a}\times\mathbf{b}\|}{\|\mathbf{a}\|}\right) = 0 \tag{5.2}$$

A third equation, relating moments acting perpendicular to the plate, is identically zero.

Equations 5.1 and 5.2 can be solved for $\|\mathbf{r}_u\|$, giving

$$\|\mathbf{r}_u\| = -M\left(\frac{\|\mathbf{a}\times\mathbf{b}\|\|\mathbf{a}\|}{\|\mathbf{a}\|^2\|\mathbf{b}\|^2 - (\mathbf{a}\cdot\mathbf{b})^2}\right)$$

This equation can be simplified using the identity

$$\|\mathbf{a}\|^2\|\mathbf{b}\|^2 - (\mathbf{a}\cdot\mathbf{b})^2 = \|\mathbf{a}\times\mathbf{b}\|^2$$

To give

$$\|\mathbf{r}_u\| = -M\left(\frac{\|\mathbf{a}\|}{\|\mathbf{a}\times\mathbf{b}\|}\right)$$

And hence an equilibrium relationship between M and $\mathbf{r}_u$

$$\mathbf{r}_u = -M\left(\frac{\|\mathbf{a}\|}{\|\mathbf{a}\times\mathbf{b}\|^2}\right)\mathbf{a}\times\mathbf{b} \tag{5.3}$$

Also, substituting back into equation 5.1 gives an equilibrium relationship between M and $\mathbf{r}_{t1}$

$$\mathbf{r}_{t1} = M\left(\frac{(\mathbf{a}\cdot\mathbf{b})}{\|\mathbf{a}\times\mathbf{b}\|^2\|\mathbf{a}\|}\right)\mathbf{a}\times\mathbf{b} \tag{5.4}$$

An equilibrium relationship between M and $\mathbf{r}_{s1}$ can now be found by considering force equilibrium on the plate *stu*

$$\mathbf{r}_{s1} + \mathbf{r}_{t1} + \mathbf{r}_u = \mathbf{0}$$

giving

$$\mathbf{r}_{s1} = -M\left(\frac{(\mathbf{a}\cdot\mathbf{b}) - \|\mathbf{a}\|^2}{\|\mathbf{a}\times\mathbf{b}\|^2\|\mathbf{a}\|}\right)\mathbf{a}\times\mathbf{b} \tag{5.5}$$

Very similar relationships can be set up for the triangular plate *stv*. The only differences are that the moment applied by the hinge, M, acts in the opposite sense on this plate, and a vector $\mathbf{c} = \mathbf{p}_v - \mathbf{p}_s$ is used instead of $\mathbf{b}$. The relationships obtained are

$$\mathbf{r}_v = M\left(\frac{\|\mathbf{a}\|}{\|\mathbf{a}\times\mathbf{c}\|^2}\right)\mathbf{a}\times\mathbf{c} \tag{5.6}$$

$$\mathbf{r}_{t2} = -M\left(\frac{(\mathbf{a}\cdot\mathbf{c})}{\|\mathbf{a}\times\mathbf{c}\|^2\|\mathbf{a}\|}\right)\mathbf{a}\times\mathbf{c} \tag{5.7}$$

$$\mathbf{r}_{s2} = M\left(\frac{(\mathbf{a}\cdot\mathbf{c}) - \|\mathbf{a}\|^2}{\|\mathbf{a}\times\mathbf{c}\|^2\|\mathbf{a}\|}\right)\mathbf{a}\times\mathbf{c} \tag{5.8}$$

Equations 5.3–5.8 can be used to form the 12×1 equilibrium matrix for this element, $\mathbf{A}_h$ relating the internal stress M to the external forces in equilibrium with it, $\mathbf{r}_s$, $\mathbf{r}_t$, $\mathbf{r}_u$ and $\mathbf{r}_v$

$$\begin{pmatrix} -\left(\frac{(\mathbf{a}\cdot\mathbf{b})-\|\mathbf{a}\|^2}{\|\mathbf{a}\times\mathbf{b}\|^2\|\mathbf{a}\|}\right)\mathbf{a}\times\mathbf{b}+\left(\frac{(\mathbf{a}\cdot\mathbf{c})-\|\mathbf{a}\|^2}{\|\mathbf{a}\times\mathbf{c}\|^2\|\mathbf{a}\|}\right)\mathbf{a}\times\mathbf{c} \\ \left(\frac{(\mathbf{a}\cdot\mathbf{b})}{\|\mathbf{a}\times\mathbf{b}\|^2\|\mathbf{a}\|}\right)\mathbf{a}\times\mathbf{b}-\left(\frac{(\mathbf{a}\cdot\mathbf{c})}{\|\mathbf{a}\times\mathbf{c}\|^2\|\mathbf{a}\|}\right)\mathbf{a}\times\mathbf{c} \\ -\left(\frac{\|\mathbf{a}\|}{\|\mathbf{a}\times\mathbf{b}\|^2}\right)\mathbf{a}\times\mathbf{b} \\ \left(\frac{\|\mathbf{a}\|}{\|\mathbf{a}\times\mathbf{c}\|^2}\right)\mathbf{a}\times\mathbf{c} \end{pmatrix} M = \begin{pmatrix} \mathbf{r}_s \\ \mathbf{r}_t \\ \mathbf{r}_u \\ \mathbf{r}_v \end{pmatrix}$$

The transpose of $\mathbf{A}_h$ is the compatibility matrix of the hinge element, relating the rotation of the hinge to the displacement of the four nodes, s, t, u, and v. The unstrained state of the hinge element is when it is flat, i.e. when s, t, u and v are coplanar.

Finally the flexibility matrix is described, which relates the moment developed in the hinge, M, to its rotation. Obviously this is a 1×1 matrix. The flexibility of a continuous hinge is inversely proportional to its length, and so the flexibility matrix, $\mathbf{F}_h$ is given by

$$\mathbf{F}_h = \left(\frac{f}{\|\mathbf{p}_t - \mathbf{p}_s\|}\right) \cdot \frac{1}{AE}$$

The factor f is a parameter which can be varied to simulate the effect of different hinge flexibilities, and AE is the axial stiffness of the bars in the model.

In the rest of the computer model, described in Chapter 4, the triangular plates are simulated as bars lying along the edges of the plates, which are set to have a flexibility proportional to their length. Therefore the ratio (flexibility of a bar element) : (flexibility of corresponding hinge element) $= l : (f/l) = 1 : (f/l^2)$, where l is length of the bar/hinge.

The hinge elements for the cylinder are incorporated with the elements described in Chapter 4 to give enlarged equilibrium, compatibility and flexibility matrices for the entire structure. The simulation of the folding process then proceeds as before, except that the strain vector ε_0, the opposite of which is imposed on the structure to return it to a strain-free configuration, now incorporates the rotations of the hinge elements away from their unstrained, flat, configuration.

Simulations were performed for cylinders which incorporated the new hinge element, and have parameters $m = 1$, $n = 7$, $l_b/l_a = 1$ and $l_c/l_a = \sqrt{3}$. They are made up of $N = 36$ nodes and $B = 86$ bars. In addition to this there are also now $H = 76$ hinge elements. The same cylinder, without hinge elements, was the first to be analysed in Section 4.2.

Each simulation consists of approximately 300 compression steps of size $0.01 l_a$, using the algorithm described in Section 4.1. Simulations were performed using different values of the flexibility factor, f. The results for $f = 1 \times 10^6$, $f = 1 \times 10^5$ and $f = 1 \times 10^4$ are presented in Figures 5.13 and 5.14. Note that decreasing f corresponds to making the hinge stiffer.

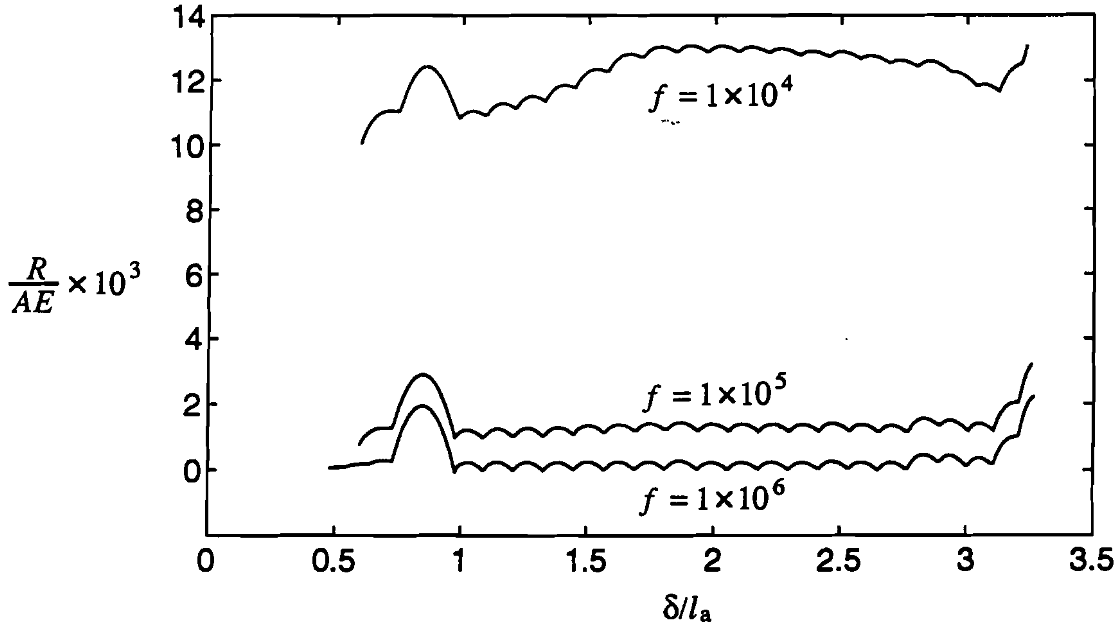

Figure 5.13. Compressive force R in the cylinder during the folding of cylinders with $m = 1$, $n = 7$, $l_b/l_a = 1$, $l_c/l_a = \sqrt{3}$, for different values of hinge flexibility, f.

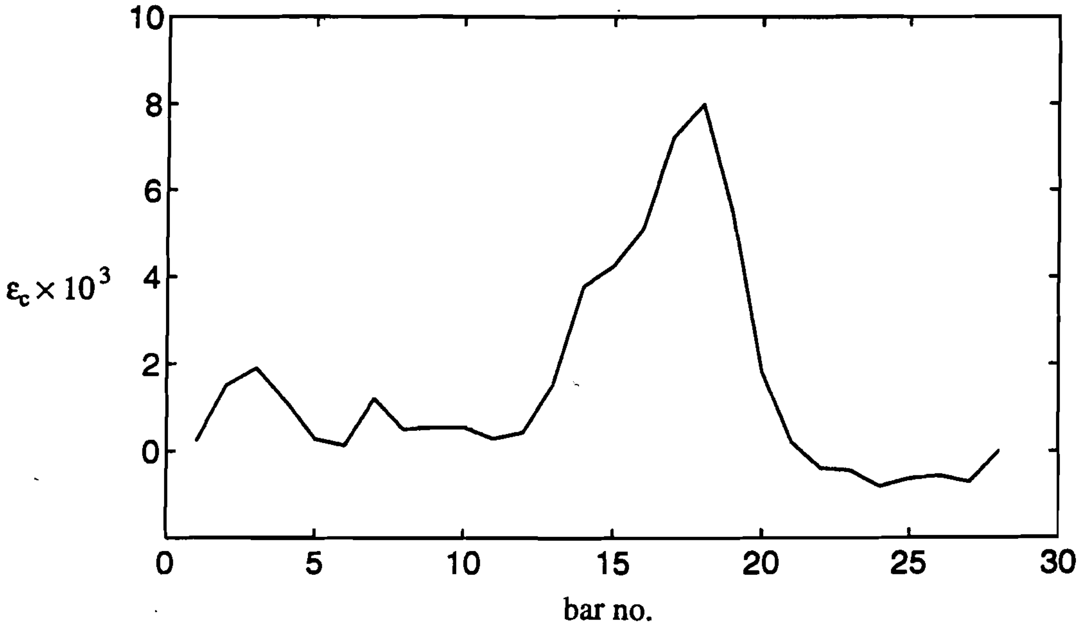

Figure 5.14. Distribution of ε_c, when $\delta = 1.91 l_a$ during the folding of cylinders with $m = 1$, $n = 7$, $l_b/l_a = 1$, $l_c/l_a = \sqrt{3}$ and $f = 1 \times 10^4$. Bars take the number of their bottom node, and nodes are numbered going up on the a-helix. Discrete values have been joined, for legibility.

Figure 5.13 shows the compressive force R developed in the cylinder for the three different stiffnesses of hinge. Each of the plots shows the force rising at the end, this is the interaction of the transition zone with the base.

When $f = 1 \times 10^6$ the force plot appears very similar to the results presented previously for a momentless hinge in Figure 4.3. The stiffness of the hinge has very little effect.

When $f = 1 \times 10^5$ some changes are evident. After a larger initial force peak, corresponding to the transition zone forming *in the bars*, there is a gentle rise in the average force as the transition zone continues to incorporate the bending of more hinges. The initial transition zone includes bars which are at the edge of the cylinder, and hence are not hinges between plates. As the transition zone moves down the cylinder, these edges become fully folded, while new bars are taken into the transition zone which *are* also hinges, and therefore a steady state has not been reached. The transition zone is fully formed further down the cylinder, when *all* the bars incorporated in it are also hinges. After this time, there is a steady state part of the plot as it moves down the cylinder. Note that there is an average compressive force in the cylinder during the steady state phase, as energy must now be put into the cylinder to fold the hinges.

When $f = 1 \times 10^4$ the force plot is significantly changed. The formation of the transition zone is now more obviously a two stage process, and the forces involved are much higher. The force required to form the initial transition zone is now seven times higher than for the case with momentless hinges. More importantly, the steady state part of this plot involves compressive forces larger than those in the initial force peak. The steady state part of this curve is rather short, as the cylinder that is being simulated is small, and the effect of the base quickly becomes important. Results are presented later for a longer cylinder, which better shows the steady state part of the plot.

Figure 5.14 shows the strain in the c-bars when the cylinder has been compressed by $\delta = 1.91 l_a$ for $f = 1 \times 10^4$, which corresponds to a peak in the force plot. The plots for $f = 1 \times 10^5$ and $f = 1 \times 10^6$ are similar, but with slightly lower strains. The plot is presented for $\delta = 1.91 l_a$ rather than $\delta = 1.62 l_a$, as used in ~~section~~ Section 4.2, so that the transition zone has had time to fully form. The peak strain in the c-bars is only 3% higher when $f = 1 \times 10^4$ than for the case with momentless hinges.

Thus, although having elastic hinges significantly affects the force developed during the folding of the cylinder, it makes very little difference to the deformations induced in the cylinder during folding. Comparing the case $f = 1 \times 10^4$ with the case for momentless hinges, the peak force increases by seven times, combined with significant changes in the profile of the force plot, while the deformation (measured by the strain in the c-bars) increases by only 3%.

The results for the force developed in a longer cylinder are shown in Figure 5.15. For this simulation a longer version of the cylinder presented above, with $f = 1 \times 10^4$ was used, in order to better show steady state folding. A cylinder with $N = 50$, $B = 128$ and $H = 118$ was simulated using 400 compression steps of size $0.01 l_a$. The initial part of the plot is indistinguishable from the shorter case, but the longer cylinder allows the steady state folding to continue further.

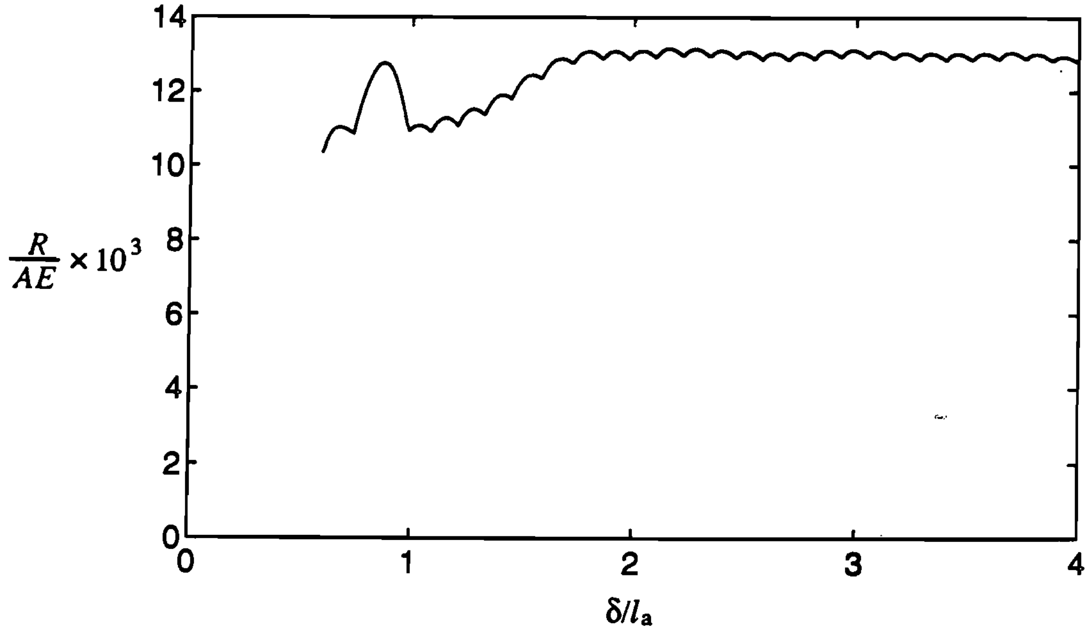

Figure 5.15. Compressive force R in the cylinder during folding of cylinders with $m = 1$, $n = 7$, $l_b/l_a = 1$, $l_c/l_a = \sqrt{3}$, and $f = 5 \times 10^3$.

5.3.2. Manufacturing Errors

Manufacturing errors were simulated by making the bars which cross the final join-line of the cylinder too long by a factor e, where e is a parameter to be varied. Simulations were performed for cylinders, with parameters $m = 1$, $n = 1$, $l_b/l_a = 1$ and $l_c/l_a = \sqrt{3}$, and made up of $N = 36$ nodes and $B = 86$ bars. Again, this cylinder, without manufacturing errors, was the first to be analysed in Section 4.2. The cylinders were compressed in approximately 300 steps of size $0.01 l_a$ using the algorithm described in Section 4.1. Simulations were performed using values of e of 0.1%, 1% and 2.5%. The results are shown in Figures 5.16–5.19.

Figures 5.16–5.18 show the variation in R, the compressive force in the cylinder, for three different values of manufacturing error. When $e = 0.1\%$ (Figure 5.16) the force plot is very similar to the case when the error is zero, presented in Figure 4.3. When $e = 1\%$ (Figure 5.17), however, the steady state part of the plot becomes periodic with a wavelength corresponding to the folding of $n = 7$ nodes of the cylinder. The manufacturing error prevents the folding from proceeding smoothly.

Similar results are seen when $e = 2.5\%$ (Figure 5.18). Again the results are periodic with a wavelength corresponding to the folding of $n = 7$ nodes. The variation in force is greater than for $e = 1\%$ as larger errors make it more difficult to fold parts of the cylinder.

A plot of strain in the c-bars for $e = 1\%$ is shown in Figure 5.19. The strains are shown when the displacement $\delta = 1.71 l_a$, as this corresponds to the largest peak force during a cycle. Note that, comparing the results in Figure 4.6 for a cylinder without manufacturing errors, the peak strain has not significantly

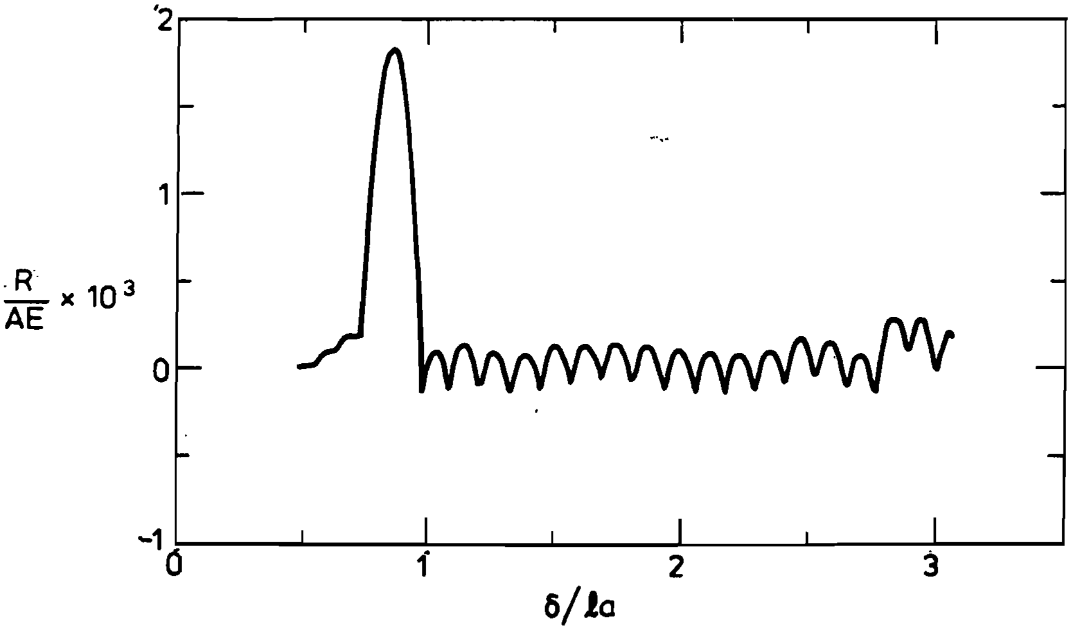

Figure 5.16. Compressive force R in the cylinder during the folding of cylinders with $m = 1$, $n = 7$, $l_b/l_a = 1$, $l_c/l_a = \sqrt{3}$, and manufacturing error, $e = 0.1\%$.

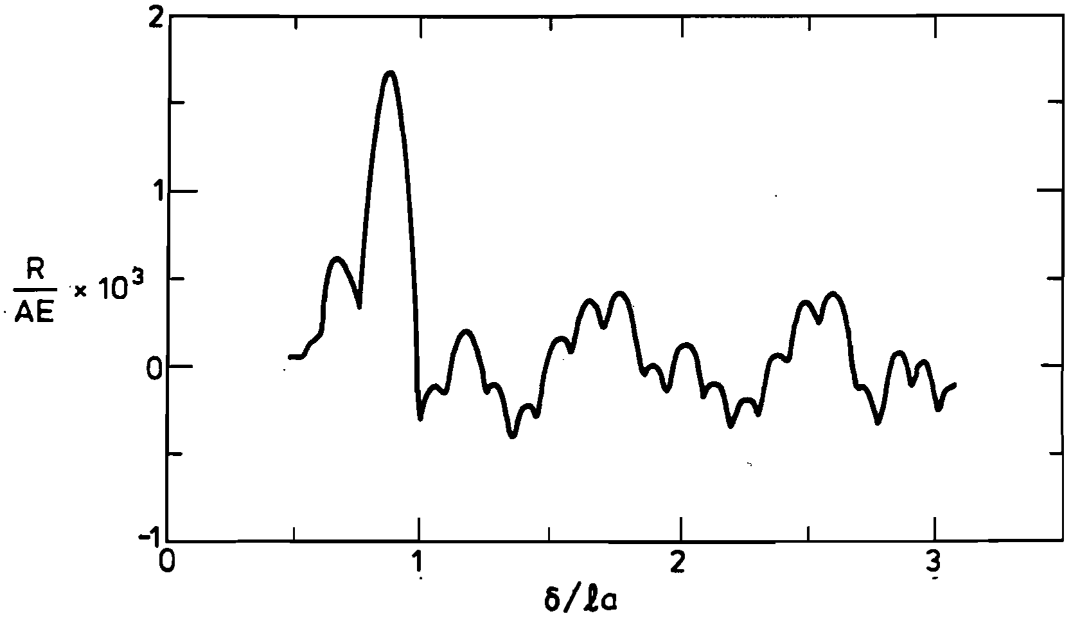

Figure 5.17. Compressive force R in the cylinder during the folding of cylinders with $m = 1$, $n = 7$, $l_b/l_a = 1$, $l_c/l_a = \sqrt{3}$, and manufacturing error, $e = 1\%$.

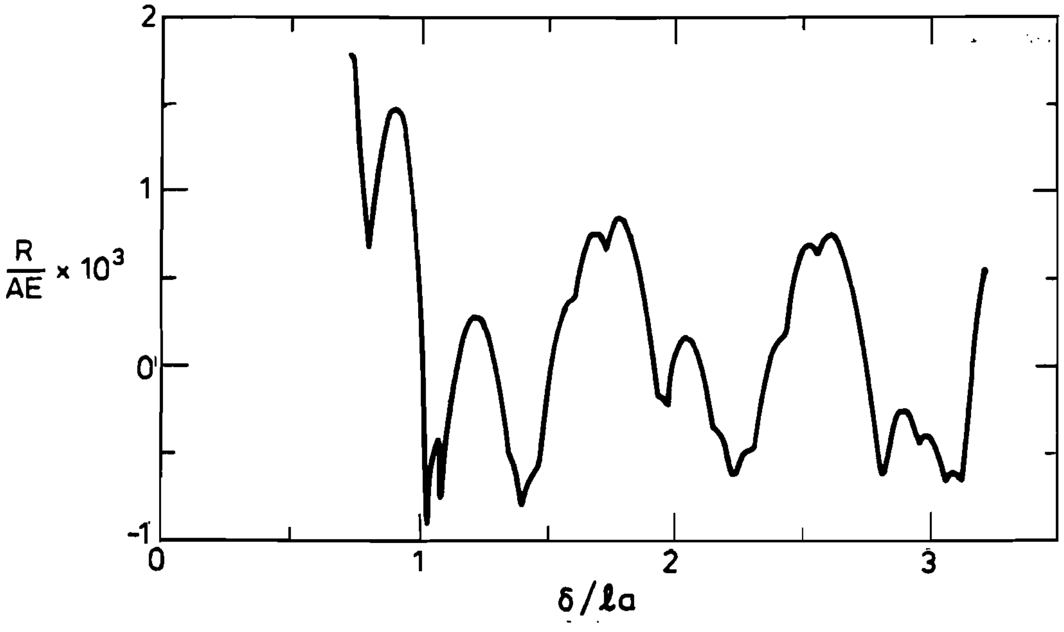

Figure 5.18. Compressive force R in the cylinder during the folding of cylinders with $m = 1$, $n = 7$, $l_b/l_a = 1$, $l_c/l_a = \sqrt{3}$, and manufacturing error, $e = 2.5\%$.

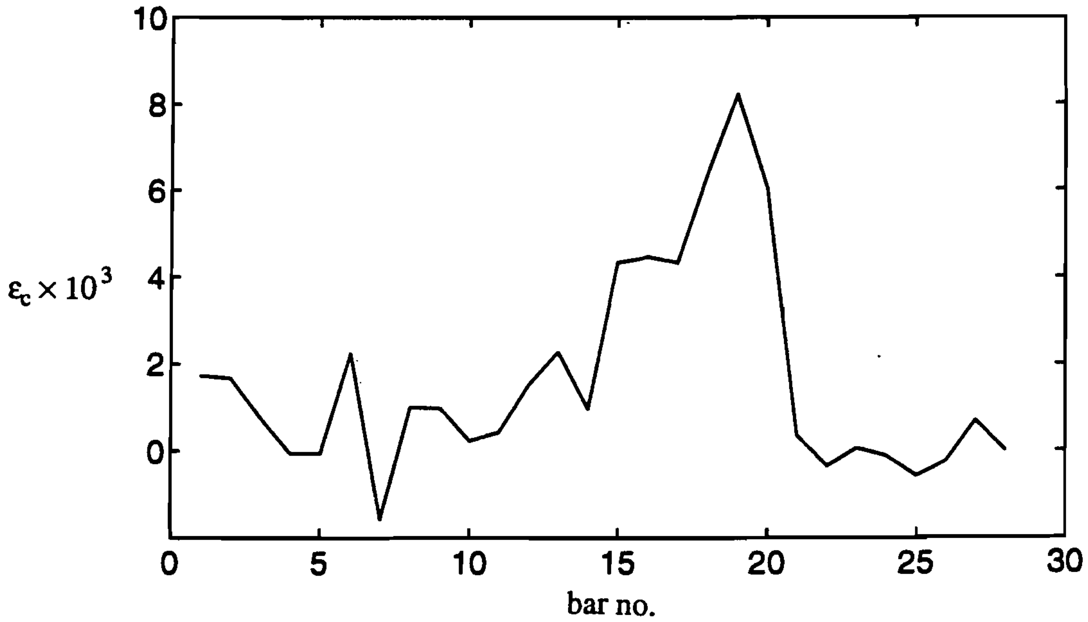

Figure 5.19. Distribution of ε_c when $\delta = 1.76 l_a$ during the folding of cylinders with $m = 1$, $n = 7$, $l_b/l_a = 1$, $l_c/l_a = \sqrt{3}$ and manufacturing error, $e = 1.0\%$.

changed. However, because of the incompatibility introduced by making some bars longer, higher levels of strain are introduced elsewhere in the cylinder. The corresponding plot for $e = 2.5\%$ is not shown, as these distributed strains make the plot difficult to read. A careful examination of the strains for the $e = 2.5\%$ case shows the peak strain in the c-bars to be 12% higher than for the case with zero error.

The large strains seen near the base in Figure 5.19 are partly due to the way the simulation is performed. The base nodes are clamped before the manufacturing errors are introduced. A more careful simulation would reduce the strains in the bars close to the base, but this would little affect the strain elsewhere.

5.3.3. Discussion

This section has explored two possible explanations for why observed experimental behaviour differs from that predicted in Chapter 4.

Adding non-momentless hinges to the simple model has the effect of raising the average compressive force to fold the models above zero, an effect seen in all of the cylinders tested. Indeed a hinge stiffness $l^2/(1 \times 10^4)$ times the axial stiffness of the corresponding bar led to this compressive force being similar in size to the force required to form the initial transition zone. This may therefore also be a reason for there being no obvious initial force peak during the forming of the transition zone in the experimental results, as this force is no greater than the forces later in the folding process.

It may be considered that a hinge stiffness of $l^2/(1 \times 10^4)$ times the axial stiffness of the rods is unrealistic. Indeed, a test on an Irathane and Al-alloy hinge showed the Irathane hinge stiffness to be of the order of $l^2/(2 \times 10^6)$ times the stiffness of the Al-alloy plate measured along the hinge. This comparison, however, misses the point of the simulation. The deformation of the bars in the model is not meant to directly simulate the deformation of the triangular plates. The deformation of the bars represents whatever is the primary mode of deformation of the cylinder during folding. The representation has been deliberately left vague, as this mode of deformation varies for different types of cylinder. For the Irathane and Al-alloy cylinder, this primary mode of deformation is shear deformation in the hinges. Adding elastic hinge elements to the model is meant as a way of qualitatively exploring this as an explanation of experimental observation.

Introducing manufacturing errors into the simple model changes the behaviour during steady state folding. The force developed, while still oscillating about zero, no longer has a period whose wavelength corresponds to the folding of one node, but corresponds to the folding of n nodes. Superimposed on this can be seen the effect of individual nodes folding. This behaviour is very similar to that seen in the experimental tests.

The maximum error introduced in the length of a bar was 2.5%. This corresponds to a misalignment during final fabrication of 3 mm for the Cu-Be and steel cylinder, and of 1 mm for the Irathane and Al-alloy cylinder. Errors of this magnitude could certainly have been introduced.

Finally, it should be noted that, although the changes to the model described here have radically changed some aspects of the compressive behaviour of the cylinder, the internal deformation of the cylinder during folding has not changed greatly. The maximum internal deformation, as measured by the strain in the c-bars of the model, has risen by no more than 12% in any simulation performed. Thus the original model remains a valid tool for predicting and comparing many aspects of the behaviour of foldable cylinders.

5.4. Conclusions

This chapter has shown the practical realisation of the more theoretical work described in the previous two chapters. It has shown foldable cylinders to be a viable concept, and has gone some way in addressing the practical issues involved.

The geometric modelling techniques described in Chapter 3 have been of use during the experimental work. Neither the Cu-Be and steel, nor the Nylon-66 cylinder were of the simple type which fold down to polygons. Both were designed using the helical geometric model to limit the amount of deformation that was allowed during folding.

The computational modelling techniques of Chapter 4 have been shown to predict many of the characteristics seen in the folding of foldable cylinders. Also, the usefulness of having a simple computational model has also been shown, as it can easily be modified to test the validity of different explanations for observed experimental behaviour.

Part II

Wrapping Fold Pattern

6. INEXTENSIONAL WRAPPING OF FLAT MEMBRANES

The folding of thin, flat sheets is a matter of daily routine. A letter is often folded twice to fit in its envelope; maps are often folded into a narrow concertina pattern.

This chapter is concerned with the folding of a flat, thin membrane so that it wraps around a central hub as shown in Figure 6.1. It can be seen that the folding pattern consists of a symmetric set of hill and valley folds. This folding pattern was proposed by Temple and Oswald (Cambridge Consultants Ltd., 1989) for the design of a solar sail. For launch the sail would be wrapped around the circular body of the spacecraft, forming a package about 4 m in diameter; once in orbit it would deploy into a 276 m diameter disk which would use solar pressure to sail to Mars. Wright (1991) gives a general introduction to solar sailing.

The aim of this chapter is to obtain a simple understanding of the fold pattern, and to be able to calculate the fold pattern for real membranes. A review of previous work on wrapping and other ways of folding a membrane was given in Section 2.3. Section 6.1 introduces some theoretical work on the folding of membranes that is useful in the analysis of the fold pattern. In Section 6.2 the fold pattern is analysed. Initially the simplifying assumption that the membrane has zero thickness is made, which leads to some key properties of the folding pattern being found. The patterns for a zero-thickness membrane do not, however, work well in practice, and so the same approach is extended to membranes with non-zero thickness. The folding process is discussed in Section 6.3.

6.1. Theory on Inextensional Folding of Membranes

Miura (1989) formulated a simple set of rules for a set of fold lines meeting at a single point in a flat inextensional sheet. He assumed that the Gaussian curvature where the folds meet must remain zero. (See Calladine (1983, chapter 5) for an introduction to the Gaussian curvature at a vertex.) Miura showed that, if two fold lines meet then they must be collinear, and that it is impossible for three fold lines to meet. He also showed that, when four fold lines meet, one of the folds must be of opposite sign to the other three, i.e. one valley and three hill folds, or one hill and three valley folds. This is the rule most of interest in this chapter. All the intersections between folds in the fold patterns considered will be of this type, except for a degenerate case considered in Section 6.2.2 which has five folds meeting at a point.

Duncan and Duncan (1982) and Johnson and Wu (1980) have also considered the folding of an inextensional sheet. They considered curved fold lines by means of intrinsic geometry. Among other things, it can be seen from their work that

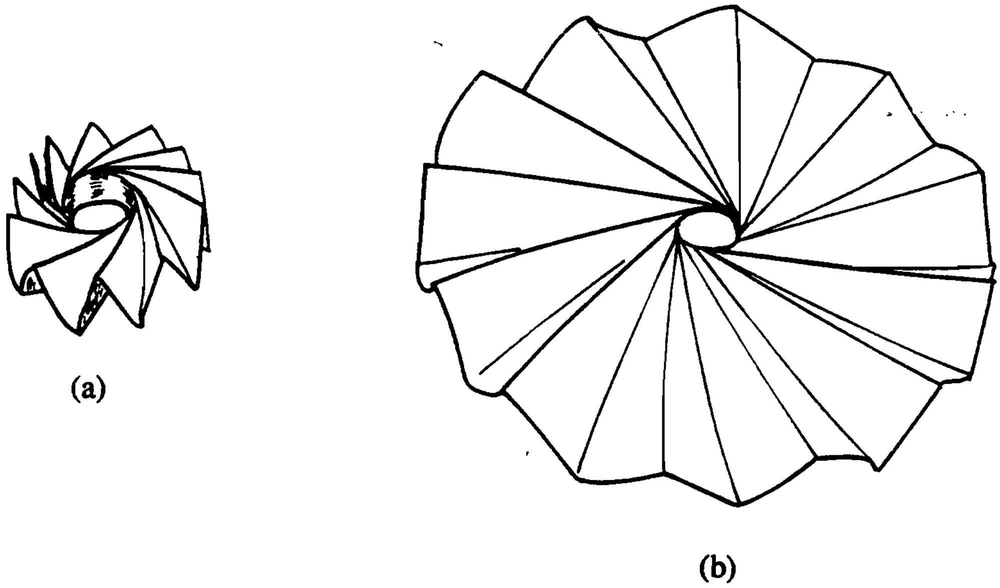

Figure 6.1. The basic fold pattern for $n = 24$: (a) Almost fully folded. (b) Almost fully deployed.

curved fold lines will only be possible if the membrane on *both* sides of the fold bends. This can also be seen as a limit case of Miura's rule for four folds meeting at a point.

6.2. Calculating the Fold Pattern

An initial consideration for the wrapping fold pattern must be the shape of the hub. In previous work this has always been assumed to be circular. However, considering the work on curved fold lines outlined in the previous section, it becomes clear that this is impossible for a truly inextensional fold pattern. Folding one of the curved folds adjacent to the hub would require the hub to bend to a specific shape, while another fold would require a different shape, and this clearly cannot happen. The solution to the problems of using a circular hub is to instead use a polygonal hub.

The fold pattern will be considered initially for a regular n-sided hub, where only four folds meet at every vertex; in Figure 6.1 $n = 24$. Irregular hubs will be considered in Section 6.2.2, and a case where more than four folds meet at a vertex in Section 6.2.3. Using the terminology of Scheel (1974) the folds which originate from a hub vertex and extend to the edge of the sheet will be called *major folds*. Apart from the degenerate case considered in Section 6.2.3 only one major fold originates from each hub vertex, and so there are n major folds.

There are two restrictions on the shape of the polygonal hub. An obvious restriction is that n must be even for fold patterns which have only one major fold per vertex, as each hill major fold will require a corresponding valley major fold. The other restriction is that only convex polygons are allowed, as the fold pattern will not work at any re-entrant corners. The reason for this will be shown in Section 6.2.2.

6.2.1. Membranes of Zero Thickness with a Regular Hub

Figure 6.2(a) shows the fold pattern for a membrane of zero thickness with a hexagonal hub. This section shows how this pattern was obtained.

Initially the angles between fold lines intersecting at a hub vertex are considered. Consider vertex B shown in Figure 6.2(b) (although any vertex would do as the pattern has n-fold rotational symmetry). Given the hub angle α, the angles β, γ and δ must be calculated. Obviously, because the sum of the inner angles in an n-sided, regular polygon is $(n-2)\pi$

$$\alpha = \left(1 - \frac{2}{n}\right)\pi \tag{6.1}$$

Also, as the angular defect at every point of the membrane, point B in particular, is zero (Calladine, 1983, chapter5)

$$\alpha + \beta + \gamma + \delta = 2\pi \tag{6.2}$$

Two further equations can be obtained by considering the fully wrapped configuration. The membrane around vertex B is shown when wrapped in Figure 6.2(c). As the membrane has zero thickness, in plan view it coincides with the edge of the hub. Therefore lines BC, DE, FG are vertical in the wrapped configuration, which implies

$$\angle \mathrm{ABC} = \delta = \frac{\pi}{2} \tag{6.3}$$

and also that

$$\gamma - \beta = \frac{\pi}{2} \tag{6.4}$$

Given equation 6.1, the solution of the system of equations 6.2–6.4 is

$$\beta = \frac{\pi}{n}, \gamma = \frac{\pi}{2} + \frac{\pi}{n}, \delta = \frac{\pi}{2} \tag{6.5}$$

which completely defines the fold pattern in the region next to the hub. Note that the major fold BD bisects the external angle of the polygon.

The remainder of the fold pattern can now be defined. In Figure 6.2(c) the folds BC, DE, FG end up vertical, and hence have to be parallel. They are also equidistant because in Figure 6.2(c) they pass through adjacent vertices of the regular hub. With reference to Figure 6.2(a), this shows that type b folds are parallel and equidistant. By symmetry, the same is true for type d folds. Finally, it can be seen that B, D and F and also A, C, E and G, are collinear because type c folds pass through the intersections of folds b and d in Figure 6.2(a).

The complete folding pattern can now be drawn. First an n-sided regular polygon representing the hub is drawn: its sides are alternately hill and valley folds. Then, n major fold lines are drawn, each forming an angle $\beta = \pi/n$ with a side of the polygon. Finally, the n sets of equally spaced, parallel folds b and d are drawn, orthogonal to the sides of the hub.

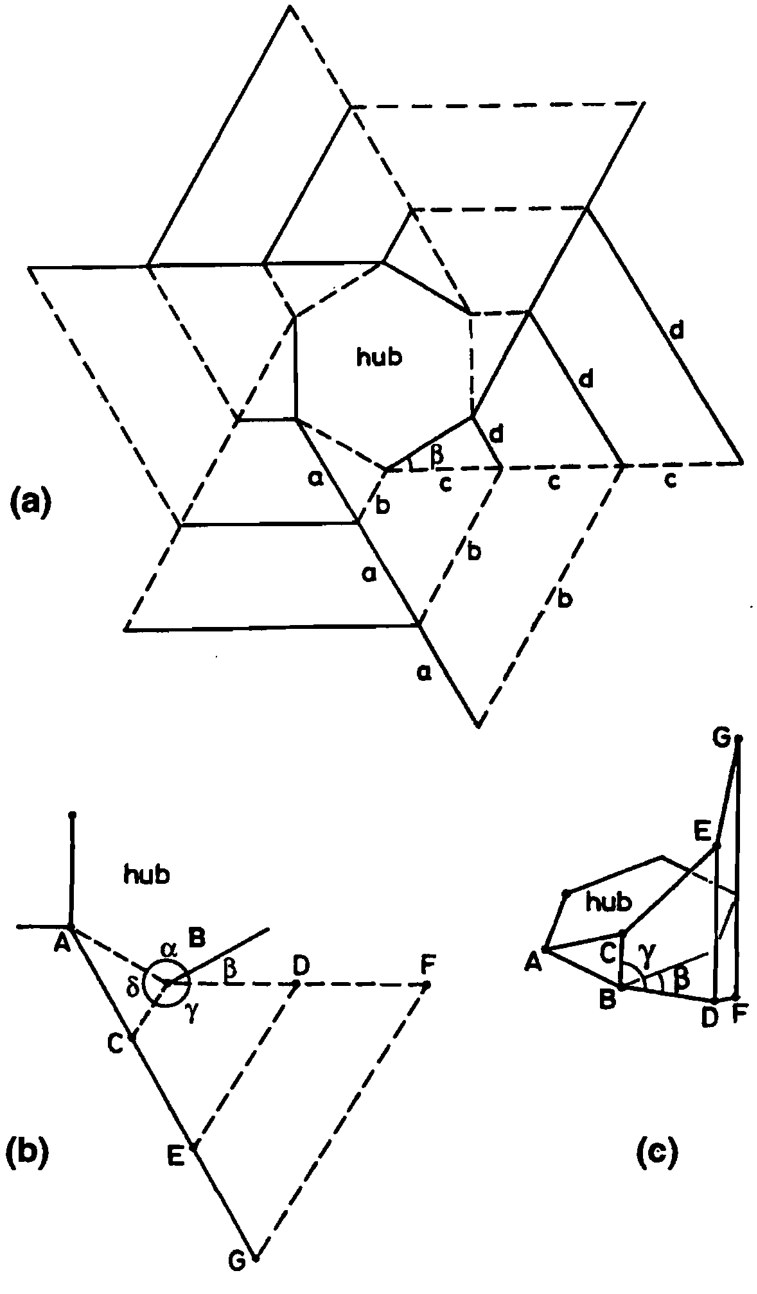

Figure 6.2. (a) Fold pattern for $n = 6$ and $t = 0$. (b) Detail of (a). (c) Wrapped configuration of membrane panels in (b). Valley folds are shown by dashed lines.

6.2.2. Membranes of Zero Thickness with an Irregular Hub

There is no requirement for the hub to be a regular polygon. The same reasoning used in Section 6.2.1 can be applied using an irregular polygon as a hub, although now different equations have to be solved at each vertex. Considering an inner hub angle α_i at vertex i, where $i = 1 \dots n$, this gives

$$\beta_i = \frac{\pi}{2} - \frac{\alpha_i}{2}, \gamma_i = \frac{\pi}{2} + \frac{\alpha_i}{2}, \delta_i = \frac{\pi}{2} \tag{6.6}$$

from which the folds next to the hub can be drawn, as before. The n major folds remain straight, and there is no difficulty in then completing the fold pattern.

The reason for not allowing non-convex hubs can now be seen. For a re-entrant vertex, $\alpha_i > \pi$, giving, from equation 6.6, $\beta_i < 0$, which is obviously impossible.

It is interesting to consider the case of an irregular polygon with equal sides but angles equal only at alternate vertices, e.g. for $n = 4$ a rhomboidal, instead of a square hub. In this case, any configuration has $(n/2)$-fold rotational symmetry. When this configuration is folded it looks very similar to the wrapped configuration for a regular hub, except that now the hub has moved up or down within the folded shape.

6.2.3. A Regular, Degenerate Case

The idea of having alternate angles of different sizes can be taken to its limit. For example, starting from the pattern of Figure 6.2(a) and, while keeping the side lengths equal, change the inner angles: $\alpha_1 = \alpha_3 = \alpha_5 \rightarrow \pi/3$ while $\alpha_2 = \alpha_4 = \alpha_6 \rightarrow \pi$. From equation 6.6 $\beta_1 = \beta_3 = \beta_5 \rightarrow \pi/3$ and $\beta_2 = \beta_4 = \beta_6 \rightarrow 0$. Thus, in the limit, the fold pattern shown in Figure 6.3 is obtained, with three major hill folds and three major valley folds, as in the pattern from which it originated.

The fold pattern of Figure 6.3 has three interesting features. Firstly, in the wrapped configuration the hub is at the bottom of the membrane. Secondly, the vertices on the triangular hub are points of intersection of five folds, not just the four seen in the standard case. This is the only case considered in this chapter where this is true. Thirdly, this fold pattern has important similarities with the fold pattern described by Scheel, and shown in Figure 2.3. The only differences are that Scheel's pattern is drawn with six hub vertices rather than three, that the folds marked b and d in Figure 6.3 are omitted from Scheel's pattern, and that Scheel's pattern is drawn with a circular hub, which has been shown to be impossible for a truly inextensional folding pattern.

Although obtained as a special, degenerate case of the fold pattern of Figure 6.2(a), the pattern of Figure 6.3 and many others with the same key feature of having five folds meeting at each hub vertex could be obtained directly from an approach similar to that in Section 6.2.1. There is one key difference: because at each vertex there are five angles but only four geometrical conditions on them, there is now some freedom in the solution, and hence several different wrapped configurations can be obtained. The pattern of Figure 6.3 satisfies the additional condition that two angles external to the hub are equal to $\pi/2$, hence the wrapped membrane has a flat lower edge, level with the hub. Many other choices are pos-

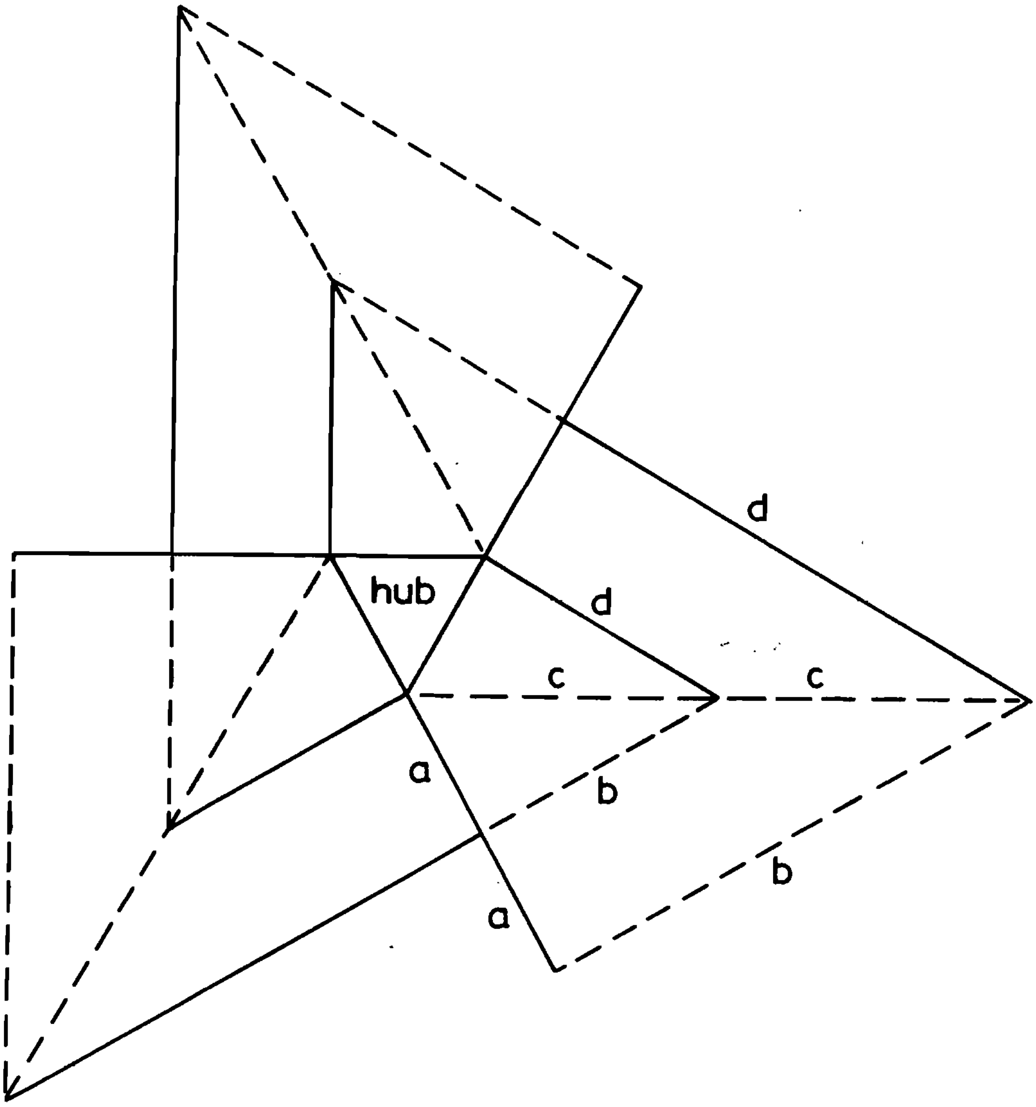

Figure 6.3. Degenerate version of the fold pattern in Figure 6.2(a). Valley folds are shown by dashed lines.

sible; for example, the lower edge of the membrane could be made to lie on a conical surface, entirely above the hub.

6.2.4. Membranes With Non-Zero Thickness

The fold patterns derived in the previous section can be modified to account for a small membrane thickness $t > 0$. For the sake of simplicity, only the basic fold pattern will be considered, based on regular polygonal hubs, as in Figure 6.2(a). Thus all of the symmetry considerations in Section 6.2.1 are still valid. The approach could be readily extended to irregular hubs and to degenerate cases.

Obviously, the wrapped membrane will no longer coincide with the edge of the hub, a consideration which greatly simplified the analysis in Section 6.2.1. To make progress it is crucial that, having removed the unrealistic assumption that $t = 0$, a simple description of the fold pattern is identified that avoids complications in the analysis. An obvious line of attack is to think of the membrane as a series of thick, rigid panels hinged at their edges, but this leads to unnecessarily complex problems of detail where fold lines join.

The approach pursued here is to assume that the wrapping of a membrane with $t > 0$ around an n-sided polygon is essentially equivalent to the wrapping of a membrane with $t = 0$ such that, after folding, its vertices lie on helical curves whose radius increases at a constant rate which is based on t. With this approach the (small) out-of plane bending of each membrane panel is neglected, as is any detailed consideration of the localised bending near each vertex. Although of negligible importance in an overall sense, the deformation and stress state in the membrane near a vertex may need to be analysed separately.

Figure 6.4(a) shows, again for $n = 6$, a plan view of the first major fold after wrapping. In this view it follows a discretised version of an Archimedean spiral. If $t = 0$ it would coincide, of course, with the edge of the hub. The profiles of the other five major fold lines have identical shape in plan view, and so can be obtained by rotation of the first fold line about the centre of the hub. Note that membrane panels such as BCED in Figure 6.2(c) are no longer plane after wrapping, because BC and DE are no longer vertical. BC and DE do, however, still lie in vertical, radial planes.

Let the j-th vertex on the i-th major fold have a position vector $\mathbf{P}_{ij}$. For convenience the cylindrical coordinate system (O, r, q, z), defined in Figure 6.4(c), will be used. In the wrapped configuration, the vertices on the first major fold, assumed to be a hill fold, are

$$\mathbf{P}_{11} = (R, 0, 0)$$

$$\mathbf{P}_{12} = (R + u, 2\pi/n, z_2)$$

$$\mathbf{P}_{13} = (R + 2u, 2\pi/n, z_3)$$

where z_2, z_3, etc. are positive quantities to be determined, and u is the plan distance between successive vertices in one radial plane (see Figure 6.4(c)). Obviously

$$u = \frac{t}{\cos(\pi/n)} \tag{6.7}$$

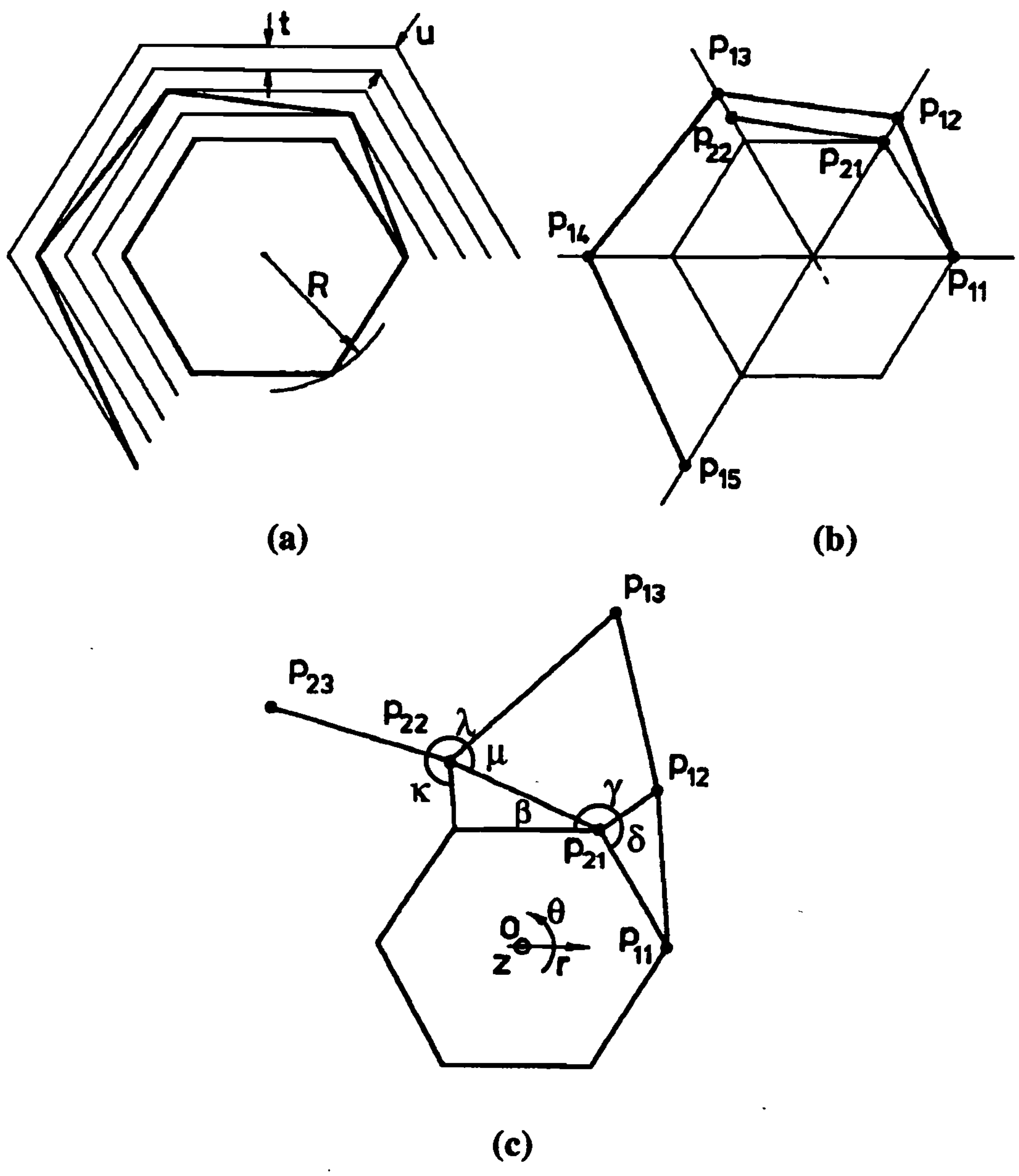

Figure 6.4. (a) Plan view of a major fold line in the wrapped configuration, for $t > 0$. Vertex points $\mathbf{P}_{ij}$ on major folds in (b) wrapped and (c) flat configurations.

For the second major fold, which is a valley fold

$$\mathbf{P}_{11} = (R, 2\pi/n, 0)$$

$$\mathbf{P}_{12} = (R + u, 4\pi/n, -z_2)$$

$$\mathbf{P}_{13} = (R + 2u, 6\pi/n, -z_3)$$

Note that, for simplicity, the thickness t of the hub has been neglected and hence the z-coordinates of all vertices $\mathbf{P}_{i1}$ vanish. Also, by symmetry, the z-coordinates of equal numbered vertices on different folds are equal in absolute value; this would not be true for irregular hubs.

The r, θ coordinates of all vertices, as well as the z-coordinates of hub vertices, are therefore known in the wrapped configuration, but the z-coordinates of non-hub vertices are unknown. However, as in Section 6.2.1 there is a condition on the angular defect at each vertex by which these unknown coordinates can be found. The condition involves the four angles at any vertex. These angles can be found by taking the dot-products of unit vectors between suitably chosen vertices in the wrapped configuration. (Taking dot-products will be accomplished most easily by converting the vectors into cartesian coordinates.) Using the notation shown in Figure 6.4(c), the angles at a hub vertex are

$$\beta = \arccos\left(\frac{(\mathbf{P}_{12} - \mathbf{P}_{11})}{\|\mathbf{P}_{12} - \mathbf{P}_{11}\|} \cdot \frac{(\mathbf{P}_{21} - \mathbf{P}_{11})}{\|\mathbf{P}_{21} - \mathbf{P}_{11}\|}\right) \tag{6.8}$$

$$\gamma = \arccos\left(\frac{(\mathbf{P}_{22} - \mathbf{P}_{21})}{\|\mathbf{P}_{22} - \mathbf{P}_{21}\|} \cdot \frac{(\mathbf{P}_{12} - \mathbf{P}_{21})}{\|\mathbf{P}_{12} - \mathbf{P}_{21}\|}\right) \tag{6.9}$$

$$\delta = \arccos\left(\frac{(\mathbf{P}_{21} - \mathbf{P}_{11})}{\|\mathbf{P}_{21} - \mathbf{P}_{11}\|} \cdot \frac{(\mathbf{P}_{12} - \mathbf{P}_{21})}{\|\mathbf{P}_{12} - \mathbf{P}_{21}\|}\right) \tag{6.10}$$

while the angle α is still given by equation 6.1. Substituting these expressions into equation 6.2, it is possible to solve for the unknown z_2. β and γ can then be calculated from equations 6.8 and 6.9. The fold pattern can now be drawn as far as vertex 2 for each major fold.

To calculate z_3 and hence κ, λ and μ, see Figure 6.4(c), it is possible to express κ, λ, μ in terms of vertex coordinates by equations analogous to 6.8–6.10 and then substitute them into the angular defect condition for vertex $\mathbf{P}_{22}$

$$(\pi - \beta - \delta) + \kappa + \lambda + \mu = 2\pi \tag{6.11}$$

The resulting equation can then be solved for the unknown z_3, and the fold pattern can be drawn as far as the third vertex. Similar equations can be generated for all other vertices, to complete the fold pattern.

Section 6.4 gives two fold patterns, computed as described above and then plotted by computer.

Folding patterns for irregular hubs can be computed by an approach similar to that described above but, because the z-coordinates of corresponding vertices are no longer equal in magnitude, a system of up to n equations in the z-coordinates of these vertices has to be set up and solved, instead of a single equation as above.

6.3. Comments on the Folding Process

It should be noted that all the fold patterns described in this paper have been derived by considering only the flat and wrapped configurations. Hence, bearing in mind the approximations of the approach, everything will fit together in these two configurations. On this basis alone there is no evidence that a continuous inextensional transition from one state to the other is possible (indeed, compare the foldable cylinders described in Part I where such a transition is not possible). However, there is some evidence from physical models that such an inextensional transition is possible. Paper models have survived years of demonstrations without obvious damage.

Recently, Kumar (1993) has shown that such a transition, with certain qualifications, is possible. He used a pin-jointed bar model of a zero thickness membrane, similar to the computational models in Chapter 4. He has followed a mechanism of this model which takes it from the flat to the fully wrapped configuration.

There are a number of points to note about Kumar's results. First, his transition relies on small amounts of bending in both the hub and non-triangular panels. However, this still fits with the aim of an inextensional folding. More importantly, the model does not take into account clashes between panels. In later stages of the folding process the mechanism requires panels to pass through one another by a small amount. Obviously this is impossible, and would lead to some straining in practice. The effect is likely to be small, however, and rapidly decreases with increasing n. Finally the model was only for a zero thickness membrane. Fold patterns for a non-zero thickness membrane are slightly different to those with zero thickness, and so there may possibly be some small amount of straining in these cases. However, a computer model of a non-zero thickness membrane would be difficult to execute, not least because the exact details of what happens at fold lines in the wrapped configuration have been left deliberately vague.

6.4. Actual Wrapping Fold Patterns

Two wrapping fold patterns have been reproduced here. They are suitable for photocopying and making simple paper models. It is suggested that fold lines are lightly scored on the outside of each fold prior to folding. It should be noted that photocopying tends to distort the folding patterns, and so the models may not work perfectly. Also if the patterns are magnified, it should be noted that the corresponding values of t will also be magnified.

The patterns produced here are for the following cases:

1. A hexagonal hub and 2 mm thick membrane with five vertices on each major fold. This pattern is not meant for use with a 2 mm thick sheet (with $R/t = 7.5$ it would be far from thin), but with ordinary photocopying paper, to produce a fairly open wrapped configuration, suitable for simple demonstrations.

2. A 12-sided hub and 0.2 mm thick membrane.

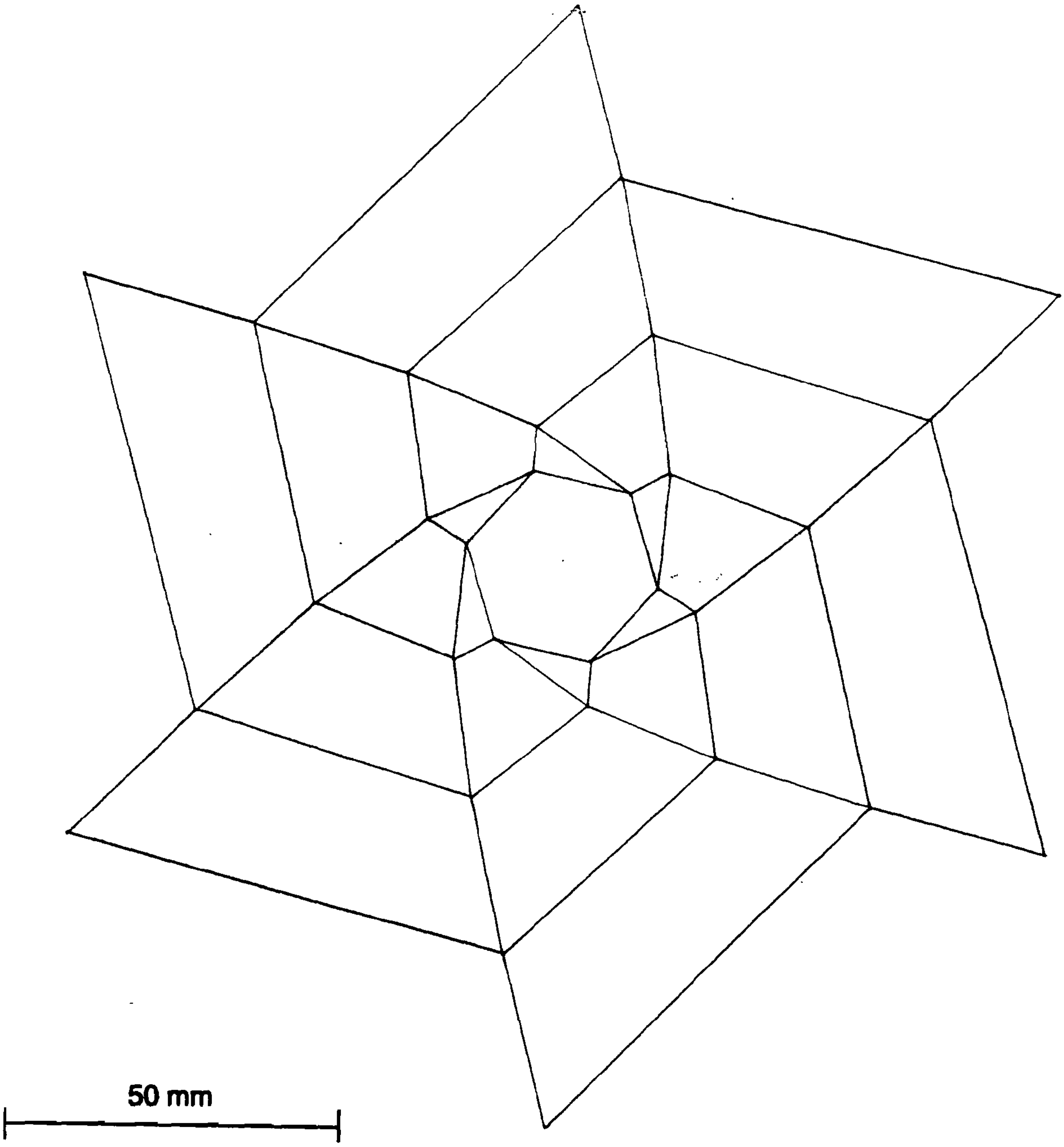

Figure 6.5. Wrapping fold pattern with $n = 6$, $t = 2\,\mathrm{mm}$.

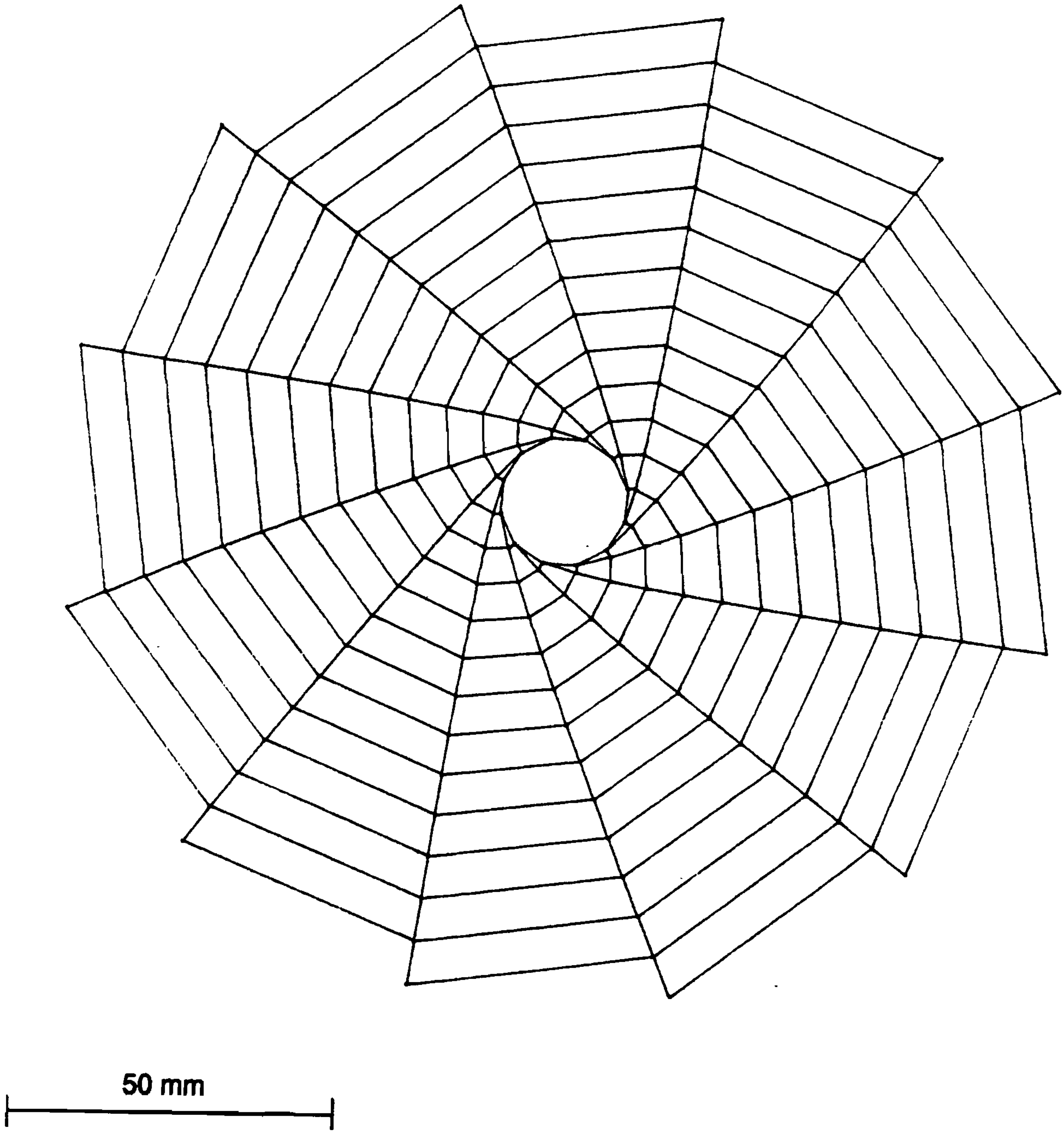

Figure 6.6. Wrapping fold pattern with $n = 12$, $t = 0.2\,\mathrm{mm}$.

Part III

Solid Surface Deployable Antenna (SSDA)

7. ANALYSIS OF MECHANISMS USING DUAL QUATERNIONS

Part III of this dissertation is concerned with the development of a new solid surface deployable antenna. The basic concept is to split a parabolic dish antenna into a number of rigid panels which are hinged together in such a way that they form a simple mechanism, allowing them to compactly fold together. The designs considered draw their inspiration from the wrapping fold pattern considered in Part II. However, while some of the analysis of that fold pattern could be left deliberately vague, as it is used for a flexible membrane, the folding of a number of rigid panels about fixed hinges requires a more rigorous analysis. This chapter explains that analysis.

The theory developed in this chapter gives the ability to calculate the position of points on an open chain of bodies connected by revolute joints after those joints have undergone arbitrary finite rotations. Time, and the derivatives of motion with respect to time, are not considered. Neither are the forces that are associated with motion. This may appear unduly restrictive, but proved useful in the development of the solid surface deployable antenna. It showed the feasibility of concepts, and highlighted problems, e.g. collisions within the structure, or impossible configurations.

The theory is based on the use of *quaternions* as a natural way of handling compound finite rotations, and the extension of this to *dual quaternions* as a way of handling compound finite spatial displacements. The theory is based primarily on a book by McCarthy (1990), but the concept of a screw displacement from Hunt (1978) proved useful, and many further insights into quaternions and rotations were obtained from Altmann (1986; 1989)

Section 7.1 explains some basic theory on rigid body rotations and how the effect of successive finite rotations can be calculated. Section 7.2 introduces quaternions and their algebraic properties, and goes on to show how they can naturally be used to represent rigid body rotations. Some aspects of general rigid body spatial displacements are considered in Section 7.3, then Section 7.4 explains dual numbers and dual quaternions, and how they can be used to represent these general displacements and coordinate transformations. Some proofs of this material are contained separately in Section 7.7, at the end of the chapter.

Section 7.5 develops a new approach in the analysis of mechanisms, based on extracting any required information about a mechanism from the dual quaternions used during its analysis. This approach is developed for one particular type of mechanism, an open chain of bodies connected by revolute hinges, as this will prove useful in Chapter 8. Section 7.6 shows how this new theory can be used for the example of a simple robot arm.

7.1. Rigid Body Rotation

In order to calculate what happens to points on chains of bodies when rotation about various hinges occurs, it is first necessary to understand a simpler problem. What is the net result of two finite rotations of a rigid body? Euler (1775) made the first steps towards understanding this problem.

Euler's theorem states that the general displacement of a rigid body with one point fixed is a rotation about some axis. Euler considered the rotation of a sphere of unit radius. He showed that the net result of two successive rotations applied to the sphere is a rotation of the sphere by a unique angle around a unique axis. Euler proved his theorem algebraically, but did not give a solution by which the axis and angle of the net rotation could be found.

The problem of finding the net result of two rotations was first solved by Rodrigues (1840), using a geometrical construction. The construction which he described is now perversely known as the Euler construction. The Euler construction is described by Altmann (1986, page 156).

Consider two rotations, first by an angle α about an axis $\mathbf{l}$, then by an angle β about an axis $\mathbf{m}$, where $\mathbf{l}$ and $\mathbf{m}$ are both unit vectors. Consider the net result of these rotations as being a rotation by an angle γ about an axis $\mathbf{n}$, where $\mathbf{n}$ is also a unit vector. If a rotation by an angle γ about a unit vector $\mathbf{n}$ is represented symbolically by $R(\gamma\mathbf{n})$, then we can represent the rotations above as

$$R(\gamma\mathbf{n}) = R(\beta\mathbf{m})R(\alpha\mathbf{l}) \tag{7.1}$$

(Note that this equation represents a rotation about the $\mathbf{l}$ axis first).

Rodrigues showed from his construction that

$$\cos\frac{\gamma}{2} = \cos\frac{\beta}{2}\cos\frac{\alpha}{2} - \sin\frac{\beta}{2}\sin\frac{\alpha}{2}\mathbf{m}\cdot\mathbf{l} \tag{7.2}$$

$$\sin\frac{\gamma}{2}\mathbf{n} = \sin\frac{\beta}{2}\cos\frac{\alpha}{2}\overset{m}{\cancel{\mathbf{l}}} + \cos\frac{\overset{\beta}{\cancel{\alpha}}}{2}\sin\frac{\overset{\alpha}{\cancel{\beta}}}{2}\overset{l}{\cancel{\mathbf{m}}} + \sin\frac{\beta}{2}\sin\frac{\alpha}{2}\mathbf{m}\times\mathbf{l} \tag{7.3}$$

where $\cdot$ and $\times$ are the standard vector dot and cross products. These equations give an explicit formula for both γ and $\mathbf{n}$.

7.2. Quaternions, and Their Use in Representing Rotations

Quaternions are a very natural way of representing rotations, but before that connection can be seen it is necessary to explain their algebraic properties. A lucid introduction to quaternions and their connection with rotations is given in Altmann (1989).

Quaternions are an extension of the concept of complex numbers, with three imaginary units, $\mathbf{i}, \mathbf{j}, \mathbf{k}$, rather than just $\mathbf{i}$. These imaginary units have the following properties

$$\mathbf{i}^2 = \mathbf{j}^2 = \mathbf{k}^2 = -1 \tag{7.4}$$

$$\mathbf{ij} = \mathbf{k}, \mathbf{ji} = -\mathbf{k}, \text{ and cyclic permutations, see Table 7.1} \tag{7.5}$$

Table 7.1. Multiplication table for quaternion units.

		second quaternion			
		1	i	j	k
first quaternion	1	1	i	j	k
	i	i	−1	k	−j
	j	j	−k	−1	i
	k	k	j	−i	−1

Then, just as a complex number can be written $a + A\mathbf{i}$, where a and A are real quantities, so a quaternion $\mathcal{A}$ can be written $\mathcal{A} = a + A_x\mathbf{i} + A_y\mathbf{j} + A_z\mathbf{k}$, where a, A_x, A_y and A_z are all real quantities. In this dissertation, quaternions are always denoted by calligraphic letters. The multiplication and addition of quaternions follows normal algebraic rules, but note that quaternions are non-commutative, as can be seen in Table 7.1, and so the order of multiplication does matter. A simple example of quaternion multiplication is the quaternion $(2 + \mathbf{i})$ postmultiplied by the quaternion $(\mathbf{j} + 3\mathbf{k})$

$$\begin{aligned} (2+\mathbf{i})(\mathbf{j}+3\mathbf{k}) &= (2\mathbf{j}+6\mathbf{k}+(\mathbf{ij})+3(\mathbf{ik})) \\ &= (2\mathbf{j}+6\mathbf{k}+\mathbf{k}-3\mathbf{i}) \\ &= (-\mathbf{j}+7\mathbf{k}) \end{aligned}$$

Another notation for quaternions is to consider them as an *ordered pair* of a scalar and a vector quantity (Altmann, 1986). A quaternion $\mathcal{A}$ is thus written

$$\mathcal{A} = a + A_x\mathbf{i} + A_y\mathbf{j} + A_z\mathbf{k} = [\![a, \mathbf{A}]\!] \tag{7.6}$$

where

$$\mathbf{A} = \begin{pmatrix} A_x \\ A_y \\ A_z \end{pmatrix}$$

Consider a second quaternion $\mathcal{B} = [\![b, \mathbf{B}]\!]$. If $\mathcal{A}$ and $\mathcal{B}$ are multiplied according to the rules in Table 7.1 then the result, again written as a couple of a real number and a vector, is

$$\mathcal{AB} = [\![a, \mathbf{A}]\!][\![b, \mathbf{B}]\!] = [\![ab - \mathbf{A}\cdot\mathbf{B}, a\mathbf{B} + b\mathbf{A} + \mathbf{A}\times\mathbf{B}]\!] \tag{7.7}$$

The usefulness of quaternions in handling rotations becomes apparent if the rotations considered earlier are also represented as a couple of a scalar and a vector

$$\mathcal{R}(\alpha\mathbf{l}) = [\![\cos\frac{\alpha}{2}, \sin\frac{\alpha}{2}\mathbf{l}]\!] \tag{7.8}$$

Equation 7.1, $\mathcal{R}(\gamma\mathbf{n}) = \mathcal{R}(\beta\mathbf{m})\mathcal{R}(\alpha\mathbf{l})$ can also be written in this form

$$[\![\cos\frac{\gamma}{2}, \sin\frac{\gamma}{2}\mathbf{n}]\!] = [\![\cos\frac{\beta}{2}, \sin\frac{\beta}{2}\mathbf{m}]\!][\![\cos\frac{\alpha}{2}, \sin\frac{\alpha}{2}\mathbf{l}]\!]$$

However, because of Rodrigues' solution, equations 7.2 and 7.3, $R(\gamma\mathbf{n})$ can also be written as

$$\begin{aligned}&[\![\cos\frac{\gamma}{2}, \sin\frac{\gamma}{2}\mathbf{n}]\!] = \\ &\quad[\![\cos\frac{\beta}{2}\cos\frac{\alpha}{2} - \sin\frac{\beta}{2}\sin\frac{\alpha}{2}\mathbf{m}.\mathbf{l}, \\ &\quad\sin\frac{\beta}{2}\cos\frac{\alpha}{2}\overset{m}{\cancel{\mathbf{l}}} + \cos\frac{\overset{\beta}{\cancel{\alpha}}}{2}\sin\frac{\overset{\alpha}{\cancel{\beta}}}{2}\overset{l}{\cancel{\mathbf{m}}} + \sin\frac{\beta}{2}\sin\frac{\alpha}{2}\mathbf{m}\times\mathbf{l}]\!]\end{aligned} \qquad (7.9)$$

A comparison of equations 7.9 and 7.7 shows that the multiplication rules for these Rodrigues' couples are identical to those for quaternions, and so the Rodrigues' couple in equation 7.8 is a quaternion. The identification of quaternions with rotations follows naturally from the product of two large angle rotations.

The four parameters given in equation 7.8 (a scalar and three vector components) are known as the Euler-Rodrigues parameters, although their close connection with quaternions is rarely made explicit.

There is a superabundance of coordinates in the Euler-Rodrigues parameters. Only three independent parameters are required to define the spherical rotation of a body. However, any set of three parameters chosen to characterise a rotation will have singularities in certain configurations (Wittenburg, 1977, page 25). Also, with only three parameters, calculating the effect of compound rotations becomes difficult. The four Euler-Rodrigues parameters are reduced to the required three by the additional constraint that the vector $\mathbf{l}$ in equation 7.8 is a unit vector, as already mentioned.

7.2.1. Additional Properties of Quaternions

This section defines some particular types of quaternions which will prove useful later in the chapter.

The *identity quaternion*, $\mathcal{I}$ is defined so that

$$\mathcal{A}\mathcal{I} = \mathcal{I}\mathcal{A} = \mathcal{A}$$

It is given by

$$\mathcal{I} = [\![1, \mathbf{0}]\!]$$

which can be easily be checked by substitution into equation 7.7.

The *inverse quaternion* $\mathcal{A}^{-1}$ is defined so that

$$\mathcal{A}\mathcal{A}^{-1} = \mathcal{A}^{-1}\mathcal{A} = \mathcal{I}$$

It is given by

$$\mathcal{A}^{-1} = [\![a, \mathbf{A}]\!]^{-1} = [\![a\cancel{/(a^2 + \mathbf{A}\cdot\mathbf{A})}, -\mathbf{A}]\!] \;/\; (a^2 + A.A) \qquad (7.10)$$

This can also be easily checked by substitution into equation 7.7.

A *unit quaternion* is one where the factor $1/(a^2 + \mathbf{A}\cdot\mathbf{A})$, which appears in equation 7.10, is equal to one. Note that the representation of a rotation in equation 7.8 is a unit quaternion.

A *pure quaternion* is one where the real part, a, is equal to zero.

7.3. Rigid Body Displacements

Having considered rotations, and how they can be represented by quaternions, the next step is to extend these results to the general displacement of a rigid body. Initially some basic aspects of spatial displacements must be considered.

During a general spatial displacement, there are no fixed points in space (cf. a rotational displacement, where there is always a line of points which do not move). However the spatial equivalent of Euler's theorem for rotations is Chasles' theorem (Goldstein, 1980, page 163). Chasles' theorem states that there is a fixed axis within the body (or the body extended) which has the same position in space before and after the displacement. This axis is called the *screw* axis, and the displacement is called a screw, where the body displaces along, and rotates around, the screw axis. The terminology 'screw' implies that the two motions occur simultaneously, but this is not necessarily true. The motion is a superimposition of two motions, a displacement along, and a rotation around, the screw axis.

A screw axis can be represented by its six *Plücker coordinates* (Hunt, 1978, page 304). Consider a line **S** in space, whose direction is given by **w**, a unit vector, and which has a point **p** lying on it, see Figure 7.1. The six Plücker coordinates of this line are then given by $(\mathbf{w}, \mathbf{p} \times \mathbf{w})$. Note that this representation has a superabundance of coordinates, as a line in space can be specified by four parameters. The six parameters are reduced by the two constraints that **w** is a unit vector, and that $\mathbf{p} \times \mathbf{w}$ is obviously orthogonal to **w**. (At first it may seem that the representation of a line requires five parameters, the position of a point on the line, and two parameters to represent direction. However, this leads to infinitely many representations for the *same* line, as the line can then be specified by any of the points on it.)

The concepts of a screw displacement and of a screw axis represented by its Plücker coordinates will prove useful in the next section.

7.4. Dual Quaternions, and Their Use in Representing Rigid Body Displacements

Dual numbers are a useful way of transferring results obtained for spherical displacements, where one point is fixed, to general spatial displacements (Duffy, 1980). In this dissertation, dual quantities are denoted by a caret, ^. Dual numbers are similar to complex numbers, but make use of the operator ϵ instead of the operator **i**. They have the form

$$\hat{a} = a + \epsilon b$$

where a and b are real numbers, and the operator ϵ is manipulated according to the rule

$$\epsilon^2 = \epsilon^3, \cdots = 0 \tag{7.11}$$

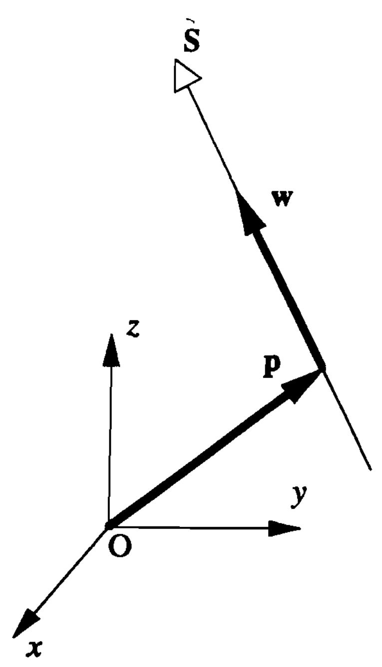

Figure 7.1. A Line in Space.

The multiplication and addition of dual numbers follows normal algebraic rules, apart from the properties of ϵ given in equation 7.11. Thus, having two dual numbers, $\hat{a} = a + \epsilon b$, and $\hat{c} = c + \epsilon d$, their sum is

$$\hat{a} + \hat{c} = (a + c) + \epsilon(b + d)$$

and their product is

$$\hat{a}\hat{c} = ac + \epsilon(ad + bc)$$

Dual numbers prove useful in defining spatial geometry. To do this the *dual angle*, $\hat{\theta}$ between two lines is defined as being

$$\hat{\theta} = \theta + \epsilon d$$

where θ is the ordinary angle between the two lines, and d is the perpendicular distance between them, as shown in Figure 7.2. Note that in this formulation the operator ϵ can be seen as having dimension [length]$^{-1}$.

The sine and cosine of a dual angle are given by

$$\sin\hat{\theta} = \sin\theta + \epsilon d\cos\theta \tag{7.12}$$

$$\cos\hat{\theta} = \cos\theta - \epsilon d\sin\theta \tag{7.13}$$

These relationships can be shown by considering the Taylor series expansion of a function, which, because of the rule for manipulating ϵ given in equation 7.11, gives

$$\begin{aligned} f(\hat{\theta}) &= f(\theta + \epsilon d) = f(\theta) + \epsilon d f'(\theta) + (\epsilon d)^2 f''(\theta)/2 + \cdots \\ &= f(\theta) + \epsilon d f'(\theta) \end{aligned}$$

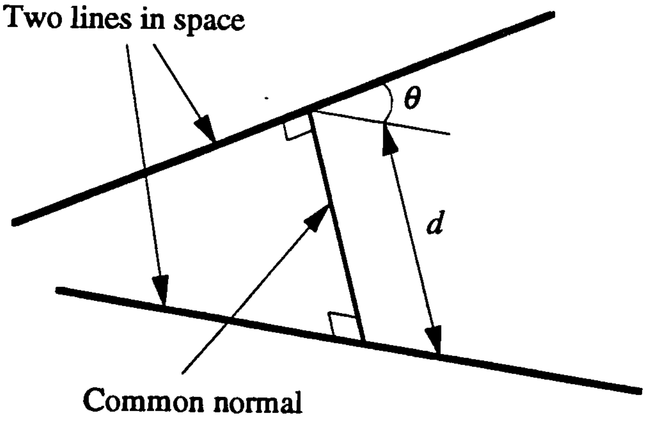

Figure 7.2. The dual angle between two lines, $\hat{\theta} = \theta + \epsilon d$

In defining dual quaternions it will be useful to write the Plücker coordinates of a line as a *dual vector*. Retaining the notation of Figure 7.1 the line $\mathbf{S}$ is written as the dual vector $\hat{\mathbf{w}}$, where

$$\hat{\mathbf{w}} = \mathbf{w} + \epsilon(\mathbf{p} \times \mathbf{w}) \tag{7.14}$$

The quantities defined here, dual angles and dual vectors, can be used to extend the theory of spherical displacements to spatial displacements, see e.g. Duffy (1980). They are used here to define dual quaternions.

Dual quaternions can be used to represent general screw displacements. Consider a finite rigid body displacement, such as that shown in Figure 7.3. The body displaces about a screw axis $\hat{\mathbf{w}}$ (a dual vector defined by the Plücker coordinates of the screw axis), by a dual angle $\hat{\theta}$ (representing a rotation by an angle θ about the screw axis, and a displacement d along it). This displacement can be represented by a dual quaternion, $\hat{\mathcal{A}}$. $\hat{\mathcal{A}}$ can be written in a way analogous to a quaternion representing a rotation

$$\hat{\mathcal{A}} = \cos\frac{\hat{\theta}}{2} + \hat{w}_x \sin\frac{\hat{\theta}}{2}i + \hat{w}_y \sin\frac{\hat{\theta}}{2}j + \hat{w}_z \sin\frac{\hat{\theta}}{2}k$$

or alternatively

$$\hat{\mathcal{A}} = [\![\cos\frac{\hat{\theta}}{2}, \hat{\mathbf{w}}\sin\frac{\hat{\theta}}{2}]\!] \tag{7.15}$$

where the trigonometric functions of dual angles are defined in equations 7.12 and 7.13.

The reason the dual quaternions representing a screw displacement are defined in this way becomes obvious when the net result of two spatial displacements of a body is calculated. Consider a spatial displacement represented by the dual quaternion $\hat{\mathcal{A}}$, followed by a spatial displacement $\hat{\mathcal{B}}$. If $\hat{\mathcal{C}}$ represents the net resultant displacement, then $\hat{\mathcal{C}}$ can be found by dual quaternion multiplication

$$\hat{\mathcal{C}} = \hat{\mathcal{B}}\hat{\mathcal{A}} \tag{7.16}$$

This result is proved in Section 7.7. It is analogous to the result for finite rotations represented by quaternions.

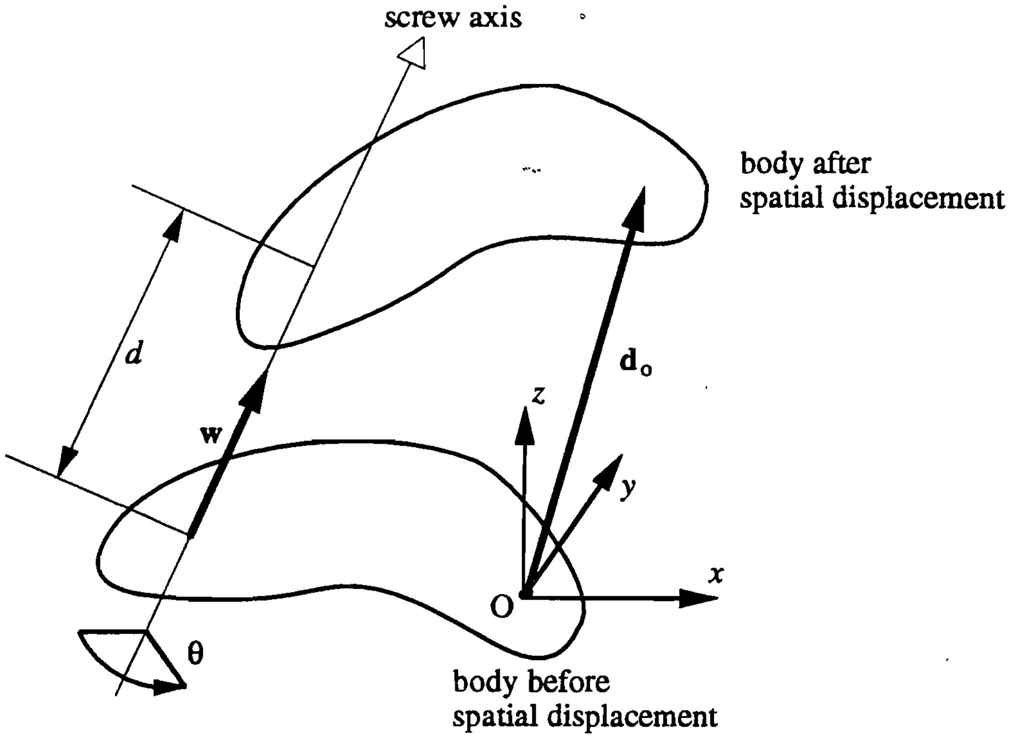

Figure 7.3. A spatial displacement.

An alternative way of considering a dual quaternion $\hat{\mathcal{A}}$ is as a combination of its real and dual parts

$$\hat{\mathcal{A}} = \mathcal{A} + \epsilon\mathcal{A}^0 \tag{7.17}$$

where both $\mathcal{A}$ and $\mathcal{A}^0$ are real quaternions.

The quaternion $\mathcal{A}$ represents the rotation of the body around the screw axis. It is of the same form as the rotation defined in equation 7.8. The dual part of the quaternion, $\mathcal{A}^0$ represents the translation of the body. $\mathcal{A}^0$ can be calculated from the displacement of the point on the body originally coincident with the origin of coordinates, the vector $\mathbf{d}_o$. If a pure quaternion (one with no scalar part) is defined as

$$\mathcal{D} = [0, \mathbf{d}_o]$$

then $\mathcal{A}^0$ is given by

$$\mathcal{A}^0 = \frac{1}{2}\mathcal{D}\mathcal{A} \tag{7.18}$$

It is shown in Section 7.7 that the two alternate ways of defining a dual quaternion representing a displacement, given by equation 7.15, and by equations 7.17 and 7.18, are equivalent.

The dual quaternions representation of displacements again show a superabundance of coordinates. Only six parameters are required to define a rigid body displacement, whereas a dual quaternion has eight parameters. However, there are two constraints implicit in the representation. This can be seen by considering that the dual quaternion in equation 7.15 is derived from the six Plücker coordinates of the screw axis, which themselves have two implicit constraints, as explained earlier.

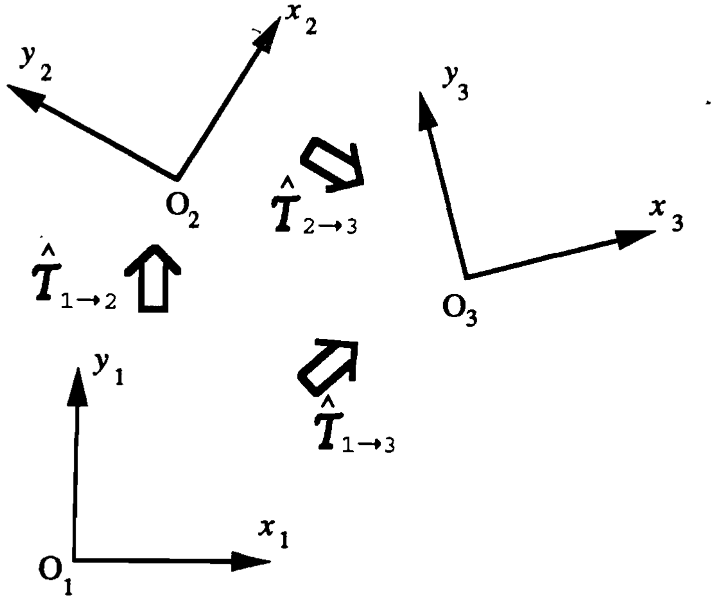

Figure 7.4. Transformations between coordinate systems.

7.4.1. Using Dual Quaternions to Represent Coordinate Transformations

All of the discussion so far has considered the net results of displacements of rigid bodies in a single fixed global coordinate system. However, Section 7.5 will make use of a number of different coordinate systems, with dual coordinates representing the transformation between these coordinate systems. This is done by defining a coordinate transformation as the spatial displacement necessary to move a body originally aligned with one coordinate system to become aligned with another. The dual quaternion, defined in the original coordinate system, which represents this displacement is used to define the coordinate transformation.

Consider two coordinate systems, $[O_1]$ and $[O_2]$. The dual quaternion which represents the rigid body motion from $[O_1]$ to $[O_2]$, $\hat{T}_{1\to2}$ can be used to define $[O_2]$ in coordinate system $[O_1]$. Note that $\hat{T}_{1\to2}$ is defined in terms of coordinate system $[O_1]$. Now consider a third coordinate system $[O_3]$. This is defined, in coordinate system $[O_2]$ by the dual quaternion $\hat{T}_{2\to3}$. *Note that $\hat{T}_{2\to3}$ is defined in a* different *coordinate system to $\hat{T}_{1\to2}$.* The three coordinate systems, and the transformations between them, are shown in Figure 7.4.

Consider the transformation from coordinate system $[O_1]$ to coordinate system $[O_3]$, defined in coordinate system $[O_1]$, and represented by the dual quaternion $\hat{T}_{1\to3}$. $\hat{T}_{1\to3}$ can be found in terms of $\hat{T}_{1\to2}$ and $\hat{T}_{2\to3}$, but not by simple dual quaternion multiplication

$$\hat{T}_{1\to3} \neq \hat{T}_{2\to3}\hat{T}_{1\to2} \tag{7.19}$$

Equation 7.19 would be correct if both $\hat{T}_{1\to2}$ and $\hat{T}_{2\to3}$ were defined in the *same* coordinate system. The correct answer is obtained by reversing the order of multiplication, giving

$$\hat{T}_{1\to3} = \hat{T}_{1\to2}\hat{T}_{2\to3} \tag{7.20}$$

The reason for this reversal in the order of multiplication can be seen by considering all three coordinate systems originally coincident. The dual quaternion $\hat{\mathcal{T}}_{2\to3}$ then defines the transformation of $[O_3]$ from its original position coincident with $[O_2]$ to its correct position in the coordinate system $[O_2]$, as shown in Figure 7.5. The dual quaternion $\hat{\mathcal{T}}_{1\to2}$ then defines the transformation of *both* $[O_2]$ and $[O_3]$ to their correct final positions within coordinate system $[O_1]$, as also shown in Figure 7.5. Obviously $\hat{\mathcal{T}}_{1\to3}$ is the net result of $\hat{\mathcal{T}}_{2\to3}$ *followed by* $\hat{\mathcal{T}}_{1\to2}$, and so, following the rules for dual quaternion multiplication

$$\hat{\mathcal{T}}_{1\to3} = \hat{\mathcal{T}}_{1\to2}\hat{\mathcal{T}}_{2\to3}$$

thus explaining the apparent change in the order of multiplication given in equation 7.20.

7.5. Analysing Mechanisms

The previous sections of this chapter developed the basic theory behind the use of dual quaternions in the analysis of spatial displacements and coordinate transformations. This section will develop this theory to analyse one particular type of mechanism, an open chain of rigid bodies, where each intermediate body in the chain is connected by revolute joints to two other bodies. (A revolute joint is a joint which allows rotation around, but not translation along, the hinge axis. A door hinge is a revolute hinge.) This rather specialised application is developed for use in Chapter 8, however the same approach could be developed for other types of mechanism.

The technique for changing coordinate systems is based on work by McCarthy (1990). In the following analysis, however, a new feature is that the dual quaternion which represents a coordinate transformation is used to provide information on the configuration of bodies in the mechanism, rather than simply using these dual quaternions as operators on other quantities such as vectors. In particular a method will be developed by which the coordinates of any point on the chain can be found for any arbitrary rotation of each of the hinges.

In order to simplify the pictures used in explaining the analysis, each rigid body is considered as two perpendicular bars. Consider a body i, a part of an open chain, which is connected to bodies $(i-1)$ and $(i+1)$ by revolute joints. Body i is represented by two bars; the first bar lies along the axis of the revolute hinge connecting body i to body $i+1$, and the second lies along the common normal to the axes of the two revolute joints on the body. An example is shown in Figure 7.6. Kinematically, this two-bar representation is equivalent to the original body.

Consider one section of an open chain of rigid bodies connected by revolute hinges, as shown in Figure 7.7. (Note that each body has been replaced by its two-bar representation.) Define a line $\mathbf{z}_i$ along the axis of the revolute joint connecting body i to body $i-1$. Define the common normal between $\mathbf{z}_i$ and $\mathbf{z}_{i+1}$ as the line $\mathbf{x}_i$. Define the intersection of $\mathbf{x}_i$ and $\mathbf{z}_i$ as the point $\mathbf{o}_i$, and the intersection of $\mathbf{x}_i$ and $\mathbf{z}_{i+1}$ as the point $\mathbf{a}_i$. These points and lines are all shown in Figure 7.7.

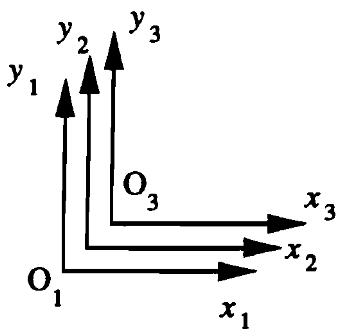

1. Coincident coordinate systems

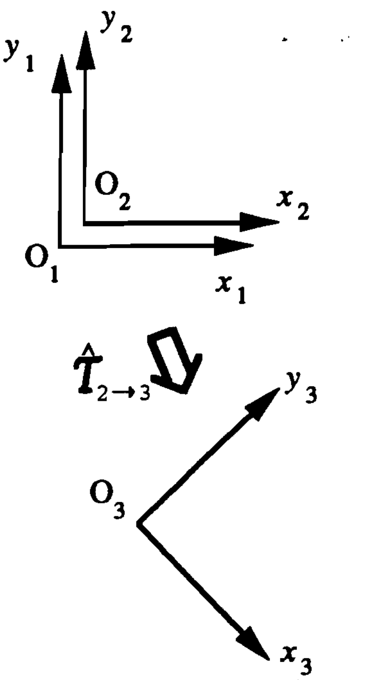

2. After transformation $\hat{T}_{2\to3}$

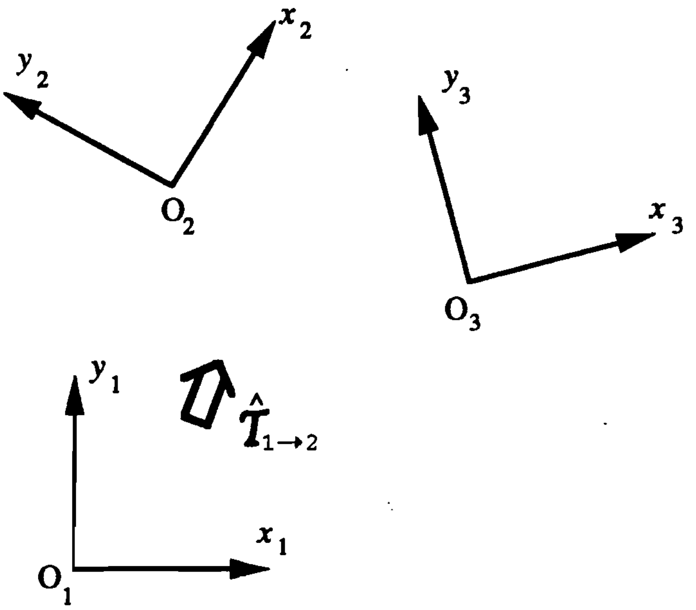

3. After transformation $\hat{T}_{2\to3}$ followed by transformation $\hat{T}_{1\to2}$

Figure 7.5. Net effect of two transformations of a coordinate systems.

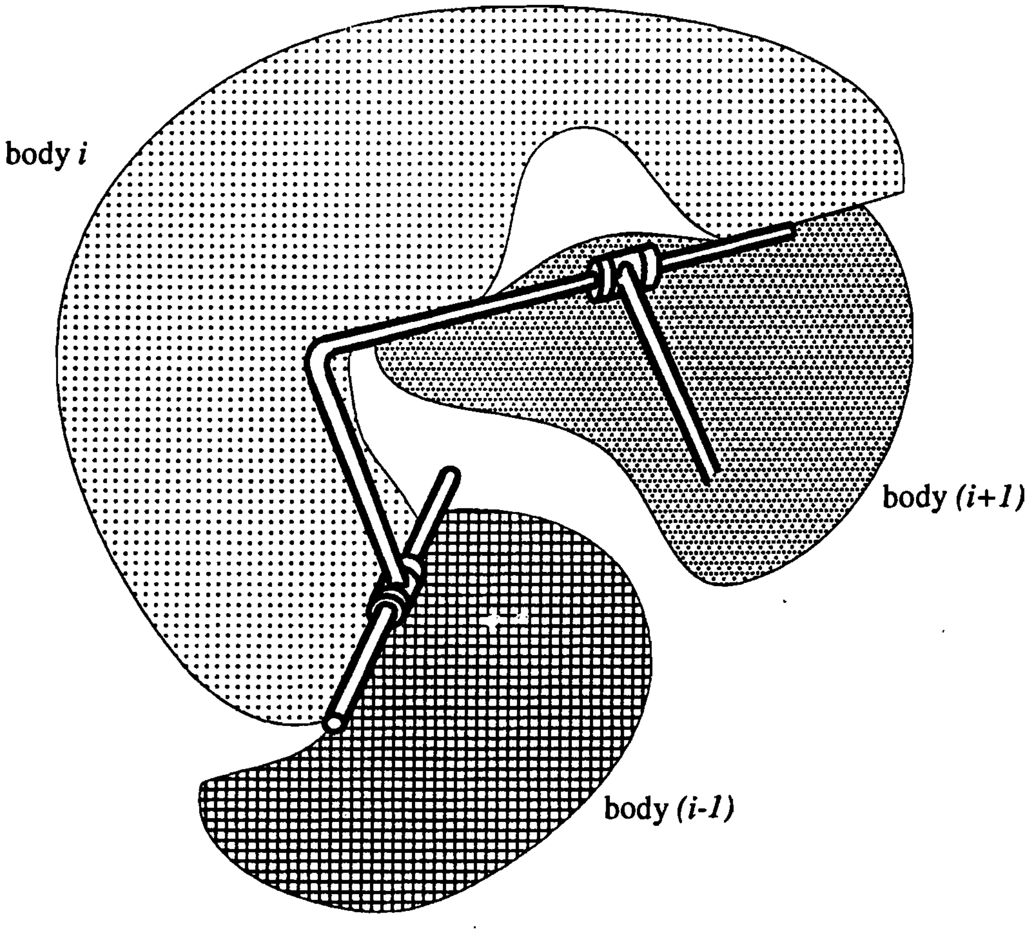

Figure 7.6. The two-bar representation of a rigid body.

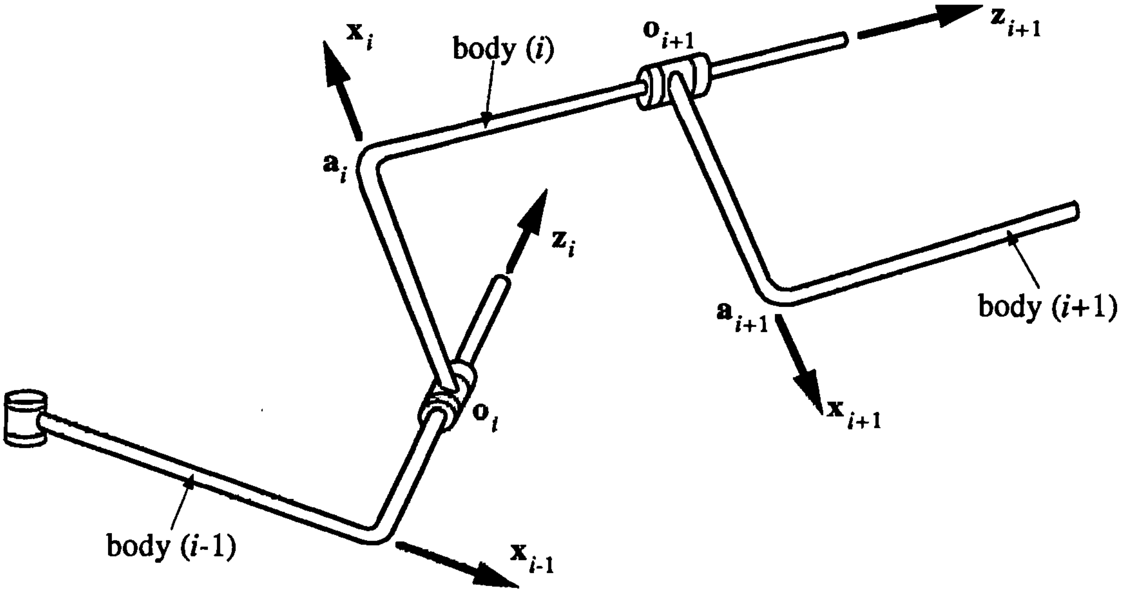

Figure 7.7. Part of a chain of rigid bodies.

The lines and points defined on the chain of bodies can then be used to define a reference frame $[O_i]$ on body i. The origin of $[O_i]$ is at $\mathbf{o}_i$, the z-axis is defined by $\mathbf{z}_i$, and the x-axis by $\mathbf{x}_i$. The y-axis is defined to form a right-handed set. This way of describing a mechanism is closely allied to the Denavit-Hartenburg convention (Hartenburg & Denavit, 1964, page 348), with some minor changes to numbering.

It is now possible to find the dual quaternion which represents the change in coordinate systems from one body to the next, that is the transformation from $[O_i]$ to $[O_{i+1}]$ (i.e. the rigid body transformation which would move a body originally coincident with $[O_i]$ to coincide with $[O_{i+1}]$). This can in turn be simplified by defining an intermediate coordinate system $[A_i]$. $[A_i]$ has its origin at $\mathbf{a}_i$, has an x-axis defined along $\mathbf{x}_i$, but a z-axis defined along $\mathbf{z}_{i+1}$. The transformation from $[O_i]$ to $[A_i]$ is a simple one, and is shown in Figure 7.8. It involves a rotation about $\mathbf{x}_i$ by an angle α_i, and a translation along $\mathbf{x}_i$ by a distance a_i. Thus this motion is a screw along the x-axis. The screw axis is defined by the dual vector $\hat{\mathbf{x}}$, where

$$\hat{\mathbf{x}} = \begin{pmatrix} 1 \\ 0 \\ 0 \end{pmatrix} + \epsilon \begin{pmatrix} 0 \\ 0 \\ 0 \end{pmatrix}$$

and the screw magnitude is given by the dual angle $\hat{\alpha}_i$

$$\hat{\alpha}_i = \alpha_i + \epsilon a_i$$

Note that the dual vector $\hat{\mathbf{x}}$ is defined in the coordinate system $[O_i]$, and so its real part is simply along the x-axis, and its dual part is zero as the axis passes through the origin of coordinates, see equation 7.14.

The screw can be represented by a dual quaternion $\hat{\mathcal{X}}(\hat{\alpha}_i)$, where

$$\hat{\mathcal{X}}(\hat{\alpha}_i) = [\![\cos\frac{\hat{\alpha}_i}{2}, \hat{\mathbf{x}}\sin\frac{\hat{\alpha}_i}{2}]\!] \tag{7.21}$$

which is equivalent to

$$\hat{\mathcal{X}}(\hat{\alpha}_i) = \cos\frac{\hat{\alpha}_i}{2} + \sin\frac{\hat{\alpha}_i}{2}\mathbf{i} + 0\mathbf{j} + 0\mathbf{k}$$

Expanding the dual angle $\hat{\alpha}_i$, this expression can be written as

$$\hat{\mathcal{X}}(\hat{\alpha}_i) = \cos\frac{\alpha_i}{2} + \sin\frac{\alpha_i}{2}\mathbf{i} + \epsilon(-\frac{a_i}{2}\sin\frac{\alpha_i}{2} + \frac{a_i}{2}\cos\frac{\alpha_i}{2}\mathbf{i})$$

The transformation from $[A_i]$ to $[O_{i+1}]$ is also simple, and is shown in Figure 7.9. It involves a rotation about $\mathbf{z}_{i+1}$ by an angle β_i, and a translation along $\mathbf{z}_{i+1}$ by a distance b_i. For this transformation the screw axis is defined by the dual vector $\hat{\mathbf{z}}$, where

$$\hat{\mathbf{z}} = \begin{pmatrix} 0 \\ 0 \\ 1 \end{pmatrix} + \epsilon \begin{pmatrix} 0 \\ 0 \\ 0 \end{pmatrix}$$

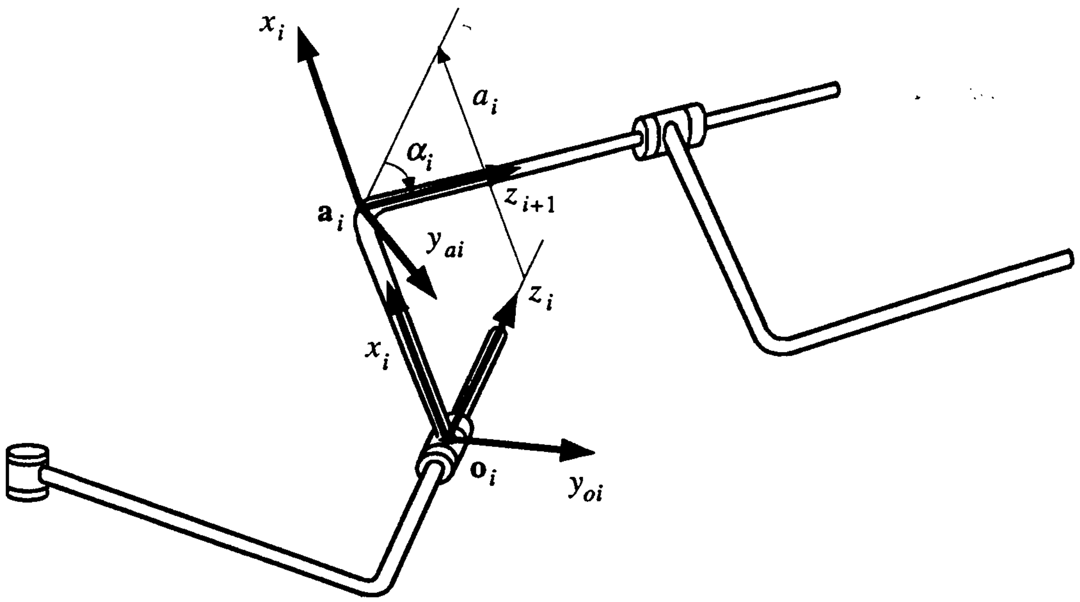

Figure 7.8. The transformation represented by $\hat{\mathcal{X}}(\hat{\alpha}_i)$. y_{oi} and y_{ai} are the y-axes in coordinate systems $[O_i]$ and $[A_i]$ respectively.

and the screw magnitude is given by the dual angle $\hat{\beta}_i$

$$\hat{\beta}_i = \beta_i + \epsilon b_i$$

The screw can be represented by a dual quaternion $\hat{\mathcal{Z}}(\hat{\beta}_i)$, where

$$\hat{\mathcal{Z}}(\hat{\beta}_i) = [\![\cos\frac{\hat{\beta}_i}{2}, \hat{\mathbf{z}}\sin\frac{\hat{\beta}_i}{2}]\!] \tag{7.22}$$

which is equivalent to

$$\hat{\mathcal{Z}}(\hat{\beta}_i) = \cos\frac{\hat{\beta}_i}{2} + 0\mathbf{i} + 0\mathbf{j} + \sin\frac{\hat{\beta}_i}{2}\mathbf{k}$$

Expanding the dual angle $\hat{\beta}_i$, this expression can be written as

$$\hat{\mathcal{Z}}(\hat{\beta}_i) = \cos\frac{\beta_i}{2} + \sin\frac{\beta_i}{2}\mathbf{k} + \epsilon(-\frac{b_i}{2}\sin\frac{\beta_i}{2} + \frac{b_i}{2}\cos\frac{\beta_i}{2}\mathbf{k})$$

Note that the transformation from $[O_i]$ to $[A_i]$ only depends on the geometry of the body, i.e the relative position of the two screw axes, and so α_i and a_i have a fixed value. In contrast, the transformation from $[A_i]$ to $[O_{i+1}]$ depends on the geometry of the body, *and* the orientation of the revolute joint at $[O_{i+1}]$. Thus β_i may vary, while b is fixed. If this were a prismatic joint, b_i could vary while β_i remained fixed, while for a cylindrical joint both b_i and β_i could vary.

Having found $\hat{\mathcal{X}}(\hat{\alpha}_i)$ and $\hat{\mathcal{Z}}(\hat{\beta}_i)$ it is simple to calculate the dual quaternion which represents the transformation from $[O_i]$ to $[O_{i+1}]$, $\hat{\mathcal{T}}_i$, by dual quaternion algebra

$$\hat{\mathcal{T}} = \hat{\mathcal{X}}(\hat{\alpha}_i)\hat{\mathcal{Z}}(\hat{\beta}_i)$$

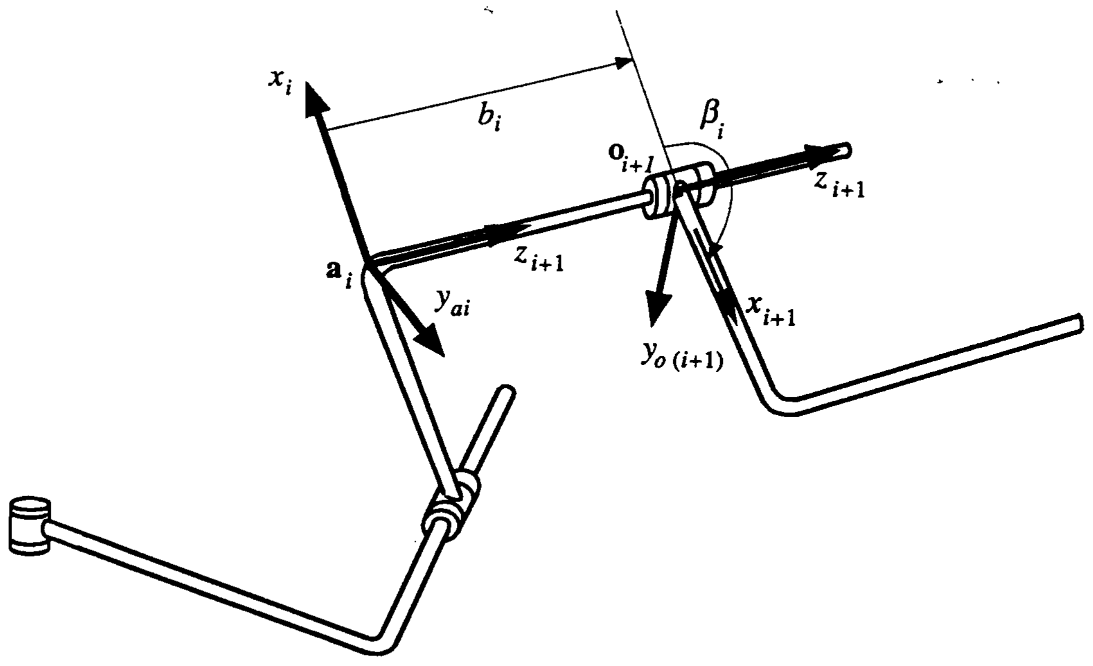

Figure 7.9. The transformation represented by $\hat{\mathcal{Z}}(\hat{\beta}_i)$.

Note the order of multiplication, as explained in Section 7.4.1.

The process described can be repeated to find the dual quaternion which represents the transformation from the base coordinate system to a coordinate system on any body in the chain. This dual quaternion then contains complete information about the orientation of this body, and the position of the origin of coordinates on this body, in the global coordinate system. The first design for a deployable antenna, considered in the next chapter, required only the position vectors of some particular points, and so the next step is to obtain this information from the dual quaternion.

Consider the dual quaternion $\hat{\mathcal{T}}$ which represents the coordinate transformation from the global coordinate system to a coordinate system with its origin at the point of interest in the mechanism. What is required is the position vector $\mathbf{d}_o$, the position that the origin of coordinates has moved to. This is best achieved by splitting $\hat{\mathcal{T}}$ into its real and dual parts

$$\hat{\mathcal{T}} = \mathcal{T} + \epsilon\mathcal{T}^0 \tag{7.23}$$

$\mathcal{T}^0$ represents the displacement part of the transformation, and from equation 7.18 can be written

$$\mathcal{T}^0 = \frac{1}{2}\mathcal{D}\mathcal{T}$$

where

$$\mathcal{D} = [\![0, \mathbf{d}_o]\!]$$

$\mathcal{D}$, and hence $\mathbf{d}$ can be found by post-multiplying equation 7.23 by the inverse quaternion $\mathcal{T}^{-1}$ (see equation 7.10), giving

$$\mathcal{D} = 2\mathcal{T}^0\mathcal{T}^{-1}$$

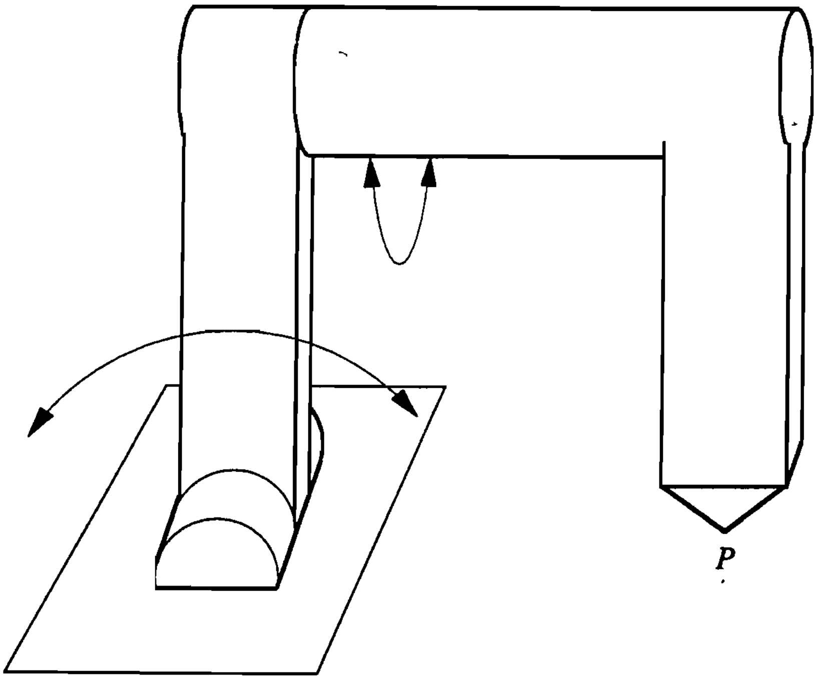

Figure 7.10. A simple robot arm.

and therefore

$$[0, \mathbf{d}_o] = 2T^0T^{-1}$$

The method outlined above gives an explicit method for finding the position vector of any point on a set of rigid bodies connected by revolute hinges for any arbitrary position of those hinges. This method can be implemented algebraically or numerically. However, the algebraic expressions become exceedingly complex for even small chains of bodies. A chain of bodies with only two revolute hinges (the example in the next section) was found to be too complex for sensible hand calculation.

7.6. An Example

An example of the type of open chain mentioned earlier is the simple robot arm shown in Figure 7.10. The arm is a chain of two rigid bodies connected by a revolute hinge and attached by a revolute hinge to a base. The position of the end-effector P is controlled by the position of the two hinges. This mechanism will be analysed using the theory explained earlier to find expressions for the cartesian coordinates of the end-effector for arbitrary positions of the two hinges.

The first step in the analysis is to produce a two-bar model of the structure, as mentioned in Section 7.5. The two-bar model of the robot-arm is shown in Figure 7.11. The figure shows the parameters defining the position of the two hinges, θ_1 and θ_2, which are zero in the position shown. The figure also shows the base coordinate system used in the analysis, and the relative dimensions of the mechanism. Note that kinematically the mechanism in Figure 7.11 is identical to the robot arm shown in Figure 7.10.

The second stage in the analysis is to calculate the dual quaternions required to transform the reference frame from its base position to the end-effector. The

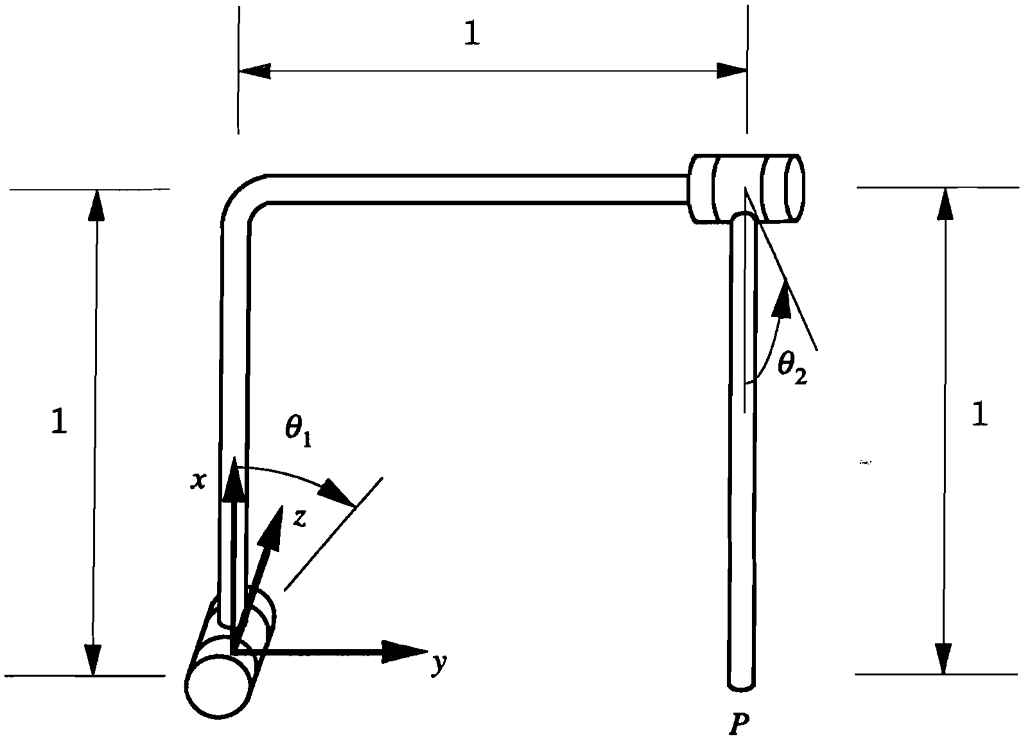

Figure 7.11. The two-bar model of the robot arm.

dual quaternions required are listed; the effect of each dual quaternion on the coordinate system is shown in Figure 7.12 for the case when $\theta_1 = \theta_2 = 0$. Each dual quaternion is given as an $\hat{\mathcal{X}}$- or $\hat{\mathcal{Z}}$- quaternion. The definition of these dual quaternions was given in equations 7.21 and 7.22.

1. $\hat{\mathcal{Z}}_1 = \hat{\mathcal{Z}}(\theta_1 + \epsilon 0)$. The rotation around the first hinge. Rotate the reference frame about the z-axis so that the x-axis lines up with the common normal to the first hinge axis. Note that $\hat{\mathcal{Z}}_1$ varies with θ_1, and that, for $\theta_1 = 0$, no transformation is required.
2. $\hat{\mathcal{X}}_2 = \hat{\mathcal{X}}(-\pi/2 + \epsilon 1)$. Move and rotate the reference frame along and about the x-axis so that the z-axis lines up with the second hinge axis.
3. $\hat{\mathcal{Z}}_3 = \hat{\mathcal{Z}}(\pi + \theta_2 + \epsilon 1)$. The rotation about the second hinge. Move and rotate the reference frame along and about the z-axis so that the x-axis lines up with the normal to the end-effector. Note that $\hat{\mathcal{Z}}_3$ varies with θ_2.
4. $\hat{\mathcal{X}}_4 = \hat{\mathcal{X}}(0 + \epsilon 1)$. Move the reference frame along the x-axis (no need to rotate) to the point P.

The quaternions defined above are then multiplied together, as described in Section 7.4.1, to give a dual quaternion, $\hat{\mathcal{T}}$, which represents the change in coordinates from the origin to point P

$$\hat{\mathcal{T}} = \hat{\mathcal{Z}}_1 \hat{\mathcal{X}}_2 \hat{\mathcal{Z}}_3 \hat{\mathcal{X}}_4$$

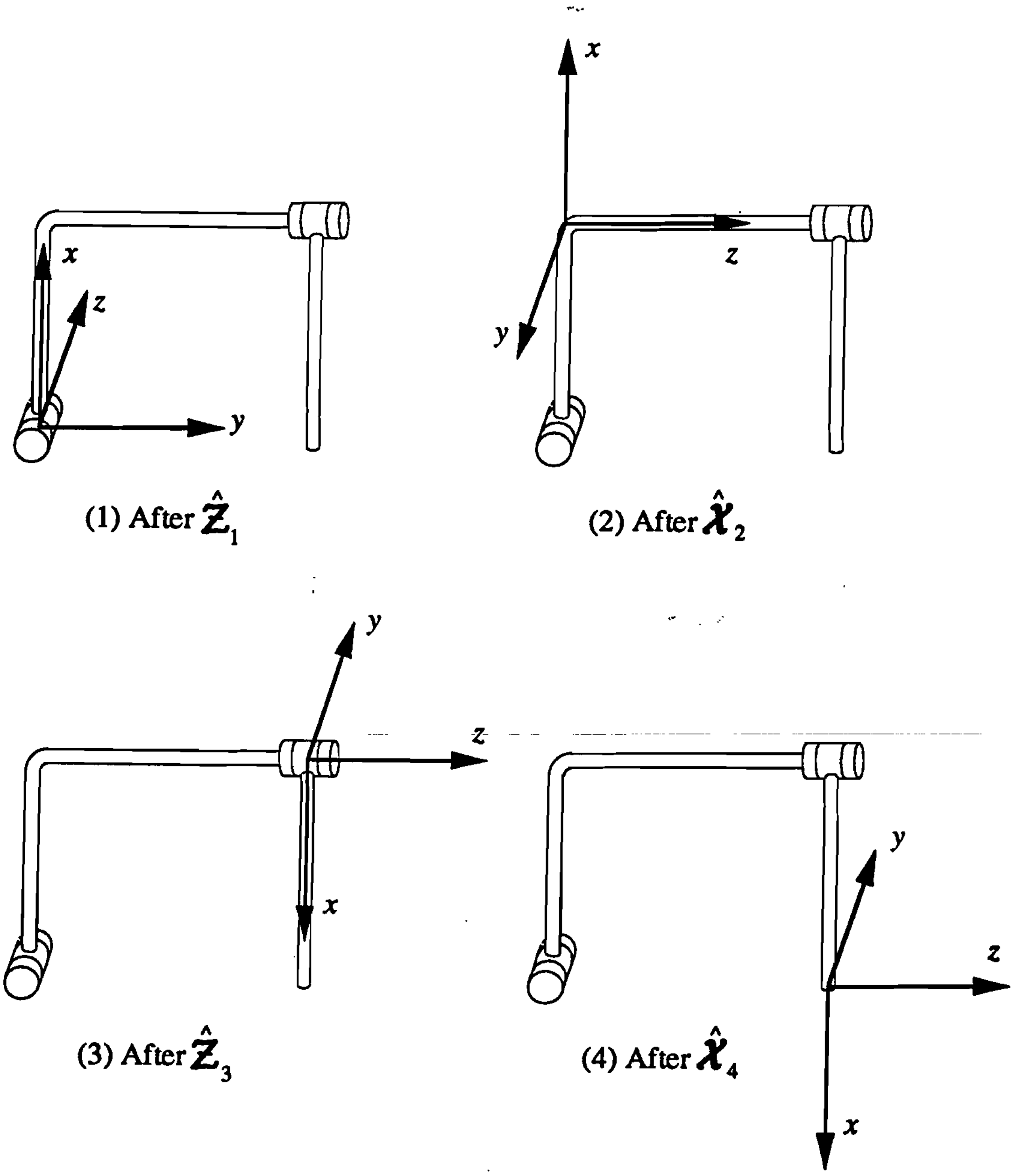

(1) After $\hat{Z}_1$ (2) After $\hat{X}_2$

(3) After $\hat{Z}_3$ (4) After $\hat{X}_4$

Figure 7.12. The moving reference frame on the robot arm.

$\hat{\mathcal{T}}$ can then be written as the sum of its real and dual parts

$$\hat{\mathcal{T}} = \mathcal{T} + \epsilon\mathcal{T}^0$$

where $\mathcal{T}$ and $\mathcal{T}^0$ can be found by applying the rules of dual quaternion algebra to the $\hat{\mathcal{X}}$- and $\hat{\mathcal{Z}}$- quaternions defined above. This gives

$$\begin{aligned}
\mathcal{T} &= \frac{\sqrt{2}}{2}\left(-\cos\frac{\theta_1}{2}\sin\frac{\theta_2}{2} - \sin\frac{\theta_1}{2}\cos\frac{\theta_2}{2}\right) \\
&\quad+\frac{\sqrt{2}}{2}\left(\cos\frac{\theta_1}{2}\sin\frac{\theta_2}{2} - \sin\frac{\theta_1}{2}\cos\frac{\theta_2}{2}\right)\mathbf{i} \\
&\quad+\frac{\sqrt{2}}{2}\left(\cos\frac{\theta_1}{2}\cos\frac{\theta_2}{2} + \sin\frac{\theta_1}{2}\sin\frac{\theta_2}{2}\right)\mathbf{j} \\
&\quad+\frac{\sqrt{2}}{2}\left(\cos\frac{\theta_1}{2}\cos\frac{\theta_2}{2} - \sin\frac{\theta_1}{2}\sin\frac{\theta_2}{2}\right)\mathbf{k}
\end{aligned}$$

$$\begin{aligned}
\mathcal{T}^0 &= \frac{\sqrt{2}}{4}\left(-\cos\frac{\theta_1}{2}\cos\frac{\theta_2}{2} - 2\cos\frac{\theta_1}{2}\sin\frac{\theta_2}{2} + \sin\frac{\theta_1}{2}\sin\frac{\theta_2}{2}\right) \\
&\quad+\frac{\sqrt{2}}{4}\left(\cos\frac{\theta_1}{2}\cos\frac{\theta_2}{2} - 2\cos\frac{\theta_1}{2}\sin\frac{\theta_2}{2} + \sin\frac{\theta_1}{2}\sin\frac{\theta_2}{2}\right)\mathbf{i} \\
&\quad+\frac{\sqrt{2}}{4}\left(-\cos\frac{\theta_1}{2}\sin\frac{\theta_2}{2} + \sin\frac{\theta_1}{2}\cos\frac{\theta_2}{2} - 2\sin\frac{\theta_1}{2}\sin\frac{\theta_2}{2}\right)\mathbf{j} \\
&\quad+\frac{\sqrt{2}}{4}\left(-\cos\frac{\theta_1}{2}\sin\frac{\theta_2}{2} - \sin\frac{\theta_1}{2}\cos\frac{\theta_2}{2} - 2\sin\frac{\theta_1}{2}\sin\frac{\theta_2}{2}\right)\mathbf{k}
\end{aligned}$$

$\mathcal{T}^0$ represents the position of the end-effector, but not in an obvious form. It is possible, however, to express this position as a position vector in the original base coordinates using the method explained in Section 7.5

$$[0, \mathbf{d}_P]] = 2\mathcal{T}^0\mathcal{T}^{-1} \tag{7.24}$$

where $\mathbf{d}_P = (d_{Px}, d_{Py}, d_{Pz})^T$, and d_{Px}, d_{Py}, d_{Pz} are the cartesian coordinates of P. Performing the multiplication in equation 7.24 gives

$$\begin{aligned}
d_{Px} &= -2\cos\frac{\theta_1}{2}\sin\frac{\theta_1}{2} - 4\sin^2\frac{\theta_1}{2}\sin^2\frac{\theta_2}{2} + 2\sin^2\frac{\theta_2}{2} \\
d_{Py} &= 4\cos\frac{\theta_1}{2}\sin\frac{\theta_1}{2}\sin^2\frac{\theta_2}{2} - 2\sin^2\frac{\theta_1}{2} + 1 \\
d_{Pz} &= 2\sin\frac{\theta_2}{2}\cos\frac{\theta_2}{2}
\end{aligned}$$

These expressions can be validated by the trial substitution of simple values of θ_1 and θ_2.

Thus an analytical expression for the position of an end-effector of a simple robot arm has been calculated. However, these expressions are rather complex even for simple systems, and indeed, the expressions given above were calculated using a computer algebraic manipulation program. In the next chapter the same methods are used numerically.

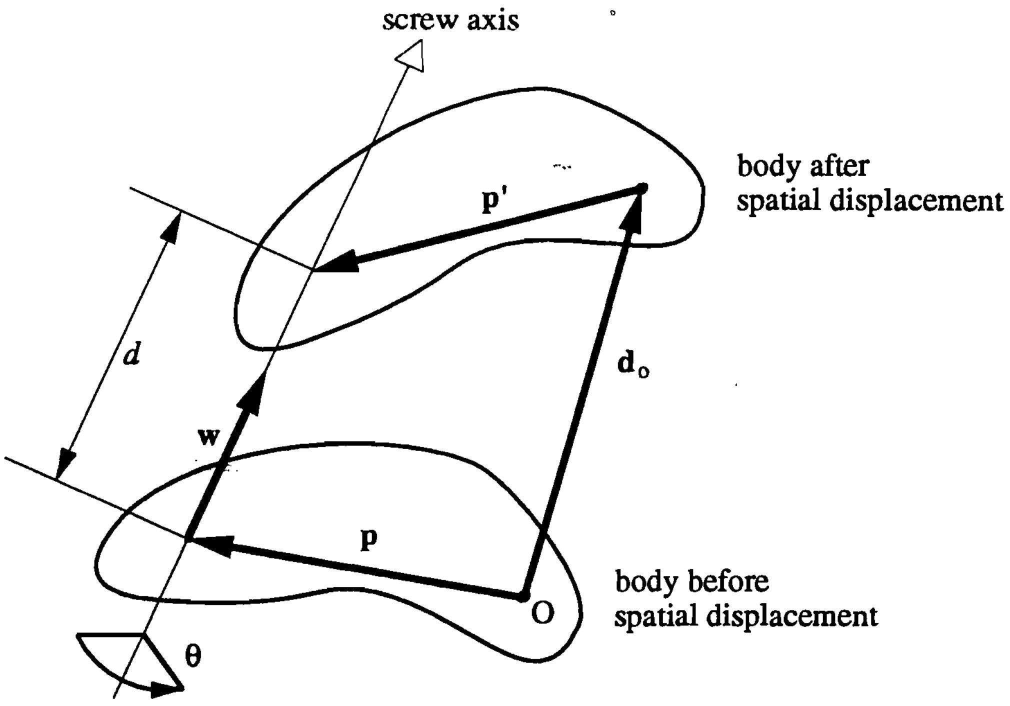

Figure 7.13. The spatial displacement of a body.

7.7. Proof of some Dual Quaternion Properties

This section proves some of the expressions which were given in Section 7.4.

The first property to be shown is that the two alternative ways of defining the dual quaternion representing a spatial deformation, one based on dual vectors and dual angles, equation 7.15, and the other based on defining a real and a dual part of the dual quaternion, equations 7.17 and 7.18, are equivalent.

The proof begins by considering the body shown in Figure 7.13 before and after a spatial displacement. The displacement consists of a screw around the screw axis defined by a point on the axis, $\mathbf{p}$, and a unit direction vector, $\mathbf{w}$ (defining the dual vector $\hat{\mathbf{w}} = \mathbf{w} + \epsilon(\mathbf{p} \times \mathbf{w})$). The body rotates about the axis by an angle θ, and displaces along it by a distance d (defining the dual angle $\hat{\theta} = \theta + \epsilon d$). After the displacement, a vector, attached to the body and originally coincident with $\mathbf{p}$, becomes the vector $\mathbf{p}'$, and the head of the vector moves from $\mathbf{p}$ to $\mathbf{p} + d\mathbf{w}$. The point on the body that was originally coincident with the origin of coordinates has displaced by $\mathbf{d}_o$. This point is coincident with the tail of $\mathbf{p}'$. Therefore

$$\mathbf{d}_o + \mathbf{p}' = \mathbf{p} + d\mathbf{w}$$

$$\mathbf{d}_o = d\mathbf{w} + \mathbf{p} - \mathbf{p}' \tag{7.25}$$

The next step is to consider how an equivalent equation may be written using quaternions. This is based on the idea of using pure quaternions (quaternions with no scalar part) to represent position, and hence fulfil the same job as position vectors. The equivalent pure quaternions to the vectors defined earlier are given by

$$\begin{aligned}\mathcal{D} &= \llbracket 0, \mathbf{d}_o \rrbracket \\ \mathcal{W} &= \llbracket 0, \mathbf{w} \rrbracket \\ \mathcal{P} &= \llbracket 0, \mathbf{p} \rrbracket\end{aligned}$$

Define a quaternion $\mathcal{A}$ which represents a rotation about the screw axis by an angle θ

$$\mathcal{A} = \llbracket \cos\frac{\theta}{2}, \sin\frac{\theta}{2}\mathbf{w} \rrbracket \tag{7.26}$$

It is shown by Altmann (1986, p215) that a pure quaternion, representing position, can be rotated by a unit quaternion using the operation $\mathcal{P}' = \mathcal{A}\mathcal{P}\mathcal{A}^{-1}$, where $\mathcal{P}'$ is the rotated form of $\mathcal{P}$. Equation 7.25 can now be written in its quaternion form

$$\mathcal{D} = d\mathcal{W} + \mathcal{P} - \mathcal{A}\mathcal{P}\mathcal{A}^{-1} \tag{7.27}$$

The proof proceeds by substituting these expressions into equations 7.17 and 7.18, and showing that the resultant form is equivalent to equation 7.15. Substituting 7.27 into equation 7.18

$$\mathcal{A}^0 = \frac{1}{2}\mathcal{D}\mathcal{A}$$

$$\mathcal{A}^0 = \left(\frac{1}{2}\right)(d\mathcal{W} + \mathcal{P} - \mathcal{A}\mathcal{P}\mathcal{A}^{-1})\mathcal{A}$$

A distributive law is valid for quaternions, as they are made up of operators which obey the usual distributive laws, and so

$$\mathcal{A}^0 = \left(\frac{1}{2}\right)(d\mathcal{W}\mathcal{A} + \mathcal{P}\mathcal{A} - \mathcal{A}\mathcal{P})$$

The products can be expanded using the multiplication law for quaternions in equation 7.7, giving

$$\begin{aligned}\mathcal{W}\mathcal{A} &= \llbracket -\sin\left(\frac{\theta}{2}\right), \mathbf{w}\cos\left(\frac{\theta}{2}\right) \rrbracket \\ \mathcal{P}\mathcal{A} &= \llbracket -\mathbf{p}\cdot\mathbf{w}\sin\left(\frac{\theta}{2}\right), \mathbf{p}\cos\left(\frac{\theta}{2}\right) + \mathbf{p}\times\mathbf{w}\sin\left(\frac{\theta}{2}\right) \rrbracket \\ \mathcal{A}\mathcal{P} &= \llbracket -\mathbf{p}\cdot\mathbf{w}\sin\left(\frac{\theta}{2}\right), \mathbf{p}\cos\left(\frac{\theta}{2}\right) - \mathbf{p}\times\mathbf{w}\sin\left(\frac{\theta}{2}\right) \rrbracket\end{aligned}$$

and so

$$\mathcal{A}^0 = \llbracket -\frac{1}{2}d\sin\left(\frac{\theta}{2}\right), \frac{1}{2}d\mathbf{w}\cos\left(\frac{\theta}{2}\right) + \mathbf{p}\times\mathbf{w}\sin\left(\frac{\theta}{2}\right) \rrbracket \tag{7.28}$$

Substituting equations 7.26 and 7.28 into 7.17 gives an expression for the dual quaternion $\hat{\mathcal{A}}$

$$\hat{\mathcal{A}} = \llbracket \cos\left(\frac{\theta}{2}\right) - \epsilon\left(\frac{1}{2}d\sin\left(\frac{\theta}{2}\right)\right), \tag{7.29}$$

$$\mathbf{w}\sin\left(\frac{\theta}{2}\right) + \epsilon\left(\frac{1}{2}d\mathbf{w}\cos\left(\frac{\theta}{2}\right) + \mathbf{p}\times\mathbf{w}\sin\left(\frac{\theta}{2}\right)\right) \rrbracket \tag{7.30}$$

Comparing equations 7.30 and 7.15 shows that equation 7.30 is simply an expanded form of equation 7.15, thereby completing the proof that the two ways of defining a dual quaternion to represent a spatial displacement are equivalent

The next proof shows that, having defined dual quaternions as above, the product of two dual quaternions does indeed describe the net effect of the two spatial displacements that these dual quaternions describe.

Consider two spatial displacements defined by the dual quaternions $\hat{\mathcal{A}}$ and $\hat{\mathcal{B}}$

$$\hat{\mathcal{A}} = \mathcal{A} + \epsilon\mathcal{A}^0$$

$$\hat{\mathcal{B}} = \mathcal{B} + \epsilon\mathcal{B}^0$$

Consider a spatial displacement defined by $\hat{\mathcal{C}}$ which is the result of $\hat{\mathcal{A}}$ followed by $\hat{\mathcal{B}}$

$$\hat{\mathcal{C}} = \mathcal{C} + \epsilon\mathcal{C}^0 \tag{7.31}$$

Assuming equation 7.16 to be true

$$\hat{\mathcal{C}} = \hat{\mathcal{B}}\hat{\mathcal{A}}$$

$$\hat{\mathcal{C}} = (\mathcal{B} + \epsilon\mathcal{B}^0)(\mathcal{A} + \epsilon\mathcal{A}^0)$$

$$\hat{\mathcal{C}} = \mathcal{B}\mathcal{A} + \epsilon(\mathcal{B}^0\mathcal{A} + \mathcal{B}\mathcal{A}^0) \tag{7.32}$$

However, from equation 7.18

$$\mathcal{A}^0 = \frac{1}{2}\mathcal{D}_A\mathcal{A}$$

$$\mathcal{B}^0 = \frac{1}{2}\mathcal{D}_B\mathcal{B}$$

where

$$\mathcal{D}_B = [0, \mathbf{d}_B]$$

$$\mathcal{D}_A = [0, \mathbf{d}_A]$$

and $\mathbf{d}_A$ and $\mathbf{d}_B$ are the displacement vectors of the origin of coordinates for the spatial displacements $\hat{\mathcal{A}}$ and $\hat{\mathcal{B}}$ respectively. Substituting into equation 7.32 gives

$$\hat{\mathcal{C}} = \mathcal{B}\mathcal{A} + \epsilon\frac{1}{2}(\mathcal{D}_B\mathcal{B}\mathcal{A} + \mathcal{B}\mathcal{D}_A\mathcal{A}) \tag{7.33}$$

If this equation can be shown to be true, then the assumption that $\hat{\mathcal{C}} = \hat{\mathcal{B}}\hat{\mathcal{A}}$ will be correct. Comparing equations 7.31 and 7.33, and considering the real and dual parts separately, it can be seen that

$$\mathcal{C} = \mathcal{B}\mathcal{A} \tag{7.34}$$

and

$$\mathcal{C}^0 = \frac{1}{2}(\mathcal{D}_B\mathcal{B}\mathcal{A} + \mathcal{B}\mathcal{D}_A\mathcal{A}) \tag{7.35}$$

Equation 7.34 is obviously true from the definition of the product of quaternions given in Section 7.2. To prove that equation 7.35 is true, however, it is necessary to consider the displacement of the point originally coincident with the

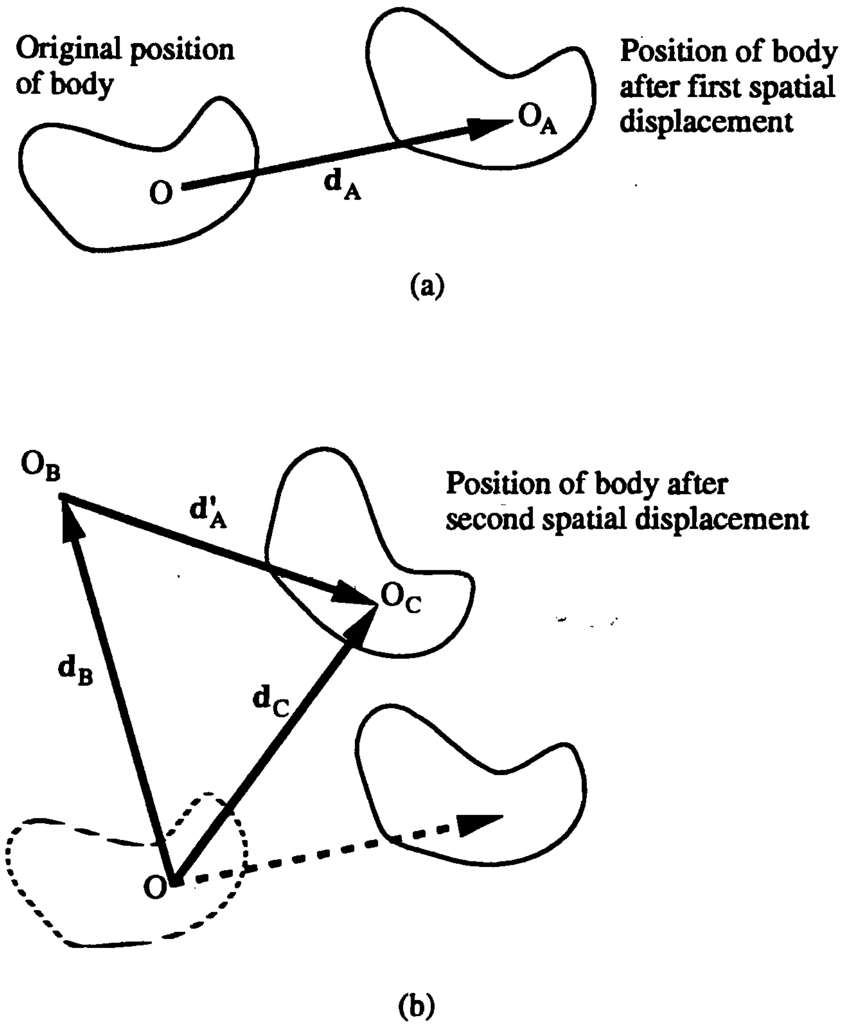

Figure 7.14. The spatial displacement of a body: (a) After $\hat{\mathcal{A}}$. (b) After $\hat{\mathcal{A}}$ followed by $\hat{\mathcal{B}}$.

origin of coordinates after the spatial displacement $\hat{\mathcal{A}}$ followed by the spatial displacement $\hat{\mathcal{B}}$.

Figure 7.14(a) shows the position after the displacement $\hat{\mathcal{A}}$. The point on the body originally coincident with the origin of coordinates O has moved to O_A. O_A is defined in the original coordinate system by the vector $\mathbf{d}_A$.

Figure 7.14(b) shows the position after the displacement $\hat{\mathcal{A}}$ followed by the displacement $\hat{\mathcal{B}}$. The point on the body that was coincident with the origin of coordinates O *after* $\hat{\mathcal{A}}$ but *before* $\hat{\mathcal{B}}$ has moved to O_B. The vector on the body coincident with $\mathbf{d}_A$ has been rotated during the displacement $\hat{\mathcal{B}}$ to become the vector $\mathbf{d}'_A$. The tail of vector $\mathbf{d}'_A$ coincides with O_B as they were coincident before the displacement $\hat{\mathcal{B}}$. The head of vector $\mathbf{d}'_A$ is the point O_C, the point which was coincident with the origin of coordinates before either displacement $\hat{\mathcal{A}}$ or $\hat{\mathcal{B}}$. This point defines the vector $\mathbf{d}_C = \overline{OO_C}$. Therefore

$$\mathbf{d}_C = \mathbf{d}_B + \mathbf{d}'_A$$

Writing this in quaternion form gives

$$\mathcal{D}_C = \mathcal{D}_B + \mathcal{D}'_A$$

$\mathcal{D}'_A$ is $\mathcal{D}_A$ rotated by the unit quaternion $\mathcal{B}$. Using the rule for rotations described earlier

$$\mathcal{D}_C = \mathcal{D}_B + \mathcal{B}\mathcal{D}_A\mathcal{B}^{-1} \tag{7.36}$$

Substituting equations 7.36 and 7.34 into the definition of $\mathcal{C}^0$, equation 7.18

$$\mathcal{C}^0 = \frac{1}{2}\mathcal{D}_C\mathcal{C}$$

gives

$$\mathcal{C}^0 = \frac{1}{2}(\mathcal{D}_B\mathcal{B}\mathcal{A} + \mathcal{B}\mathcal{D}_A\mathcal{A})$$

This is the same formula as equation 7.35. Therefore both equations 7.34 and 7.35 are true, which confirms the original hypothesis that equation 7.16 is true. Thus, when spatial displacements are defined by dual quaternions as described in the previous section, the product of two dual quaternions does indeed describe the net result of the two spatial displacements described by these dual quaternions.

8. DESIGN OF SSDA

This chapter considers the design process followed to reach the final design of Solid Surface Deployable Antenna (SSDA) whose manufacture and test are described in Chapter 9. The aim of the design was to find an effective way of folding a parabolic antenna with a solid surface, while using only simple mechanical connections between the panels.

All of the designs considered took their inspiration from the wrapping fold pattern considered in Part II of this dissertation. Four of the concepts which were considered are described in Section 8.1. One of these was selected, and its kinematic modelling is explained in Section 8.2. The final design process for the selected concept is described in Section 8.3, and the final design in Section 8.4. Finally, some concluding remarks are made in Section 8.5.

8.1. Four Alternative Concepts

A number of different concepts were considered for the SSDA. The four concepts which were developed furthest are described briefly in this section. Each of the concepts went through some of the further development described in Sections 8.2 and 8.3, but the complete design process is only described for the final concept selected.

Each of the concepts considered was developed from the wrapping fold pattern given in Part II. This fold pattern was developed for a flexible membrane, and so needs modification for a set of rigid panels. These modifications were based on the idea of the *mobility* of a mechanism.

A rigid body free in space has six degrees of freedom. Consider n bodies in space. If one body is taken as a reference body, this leaves $6(n-1)$ relative degrees of freedom. Now consider these bodies connected together by g joints: joint i imposes a number of constraints, u_i. For instance, a revolute joint imposes five constraints, and a spherical joint three constraints. The number of relative degrees of freedom between the bodies when the constraints have been imposed is called the relative mobility, M, of the system. Thus

$$M = 6(n-1) - \sum_{i=1}^{g} u_i \tag{8.1}$$

It should be noted that the above formula for mobility is a general formula. It applies when the constraints are independent. Thus there will be instances when a mechanism has a greater mobility than that predicted by equation 8.1. Also, equation 8.1 does not imply that a mechanism with mobility greater than zero can move between all possible configurations; it may be necessary to dismantle and

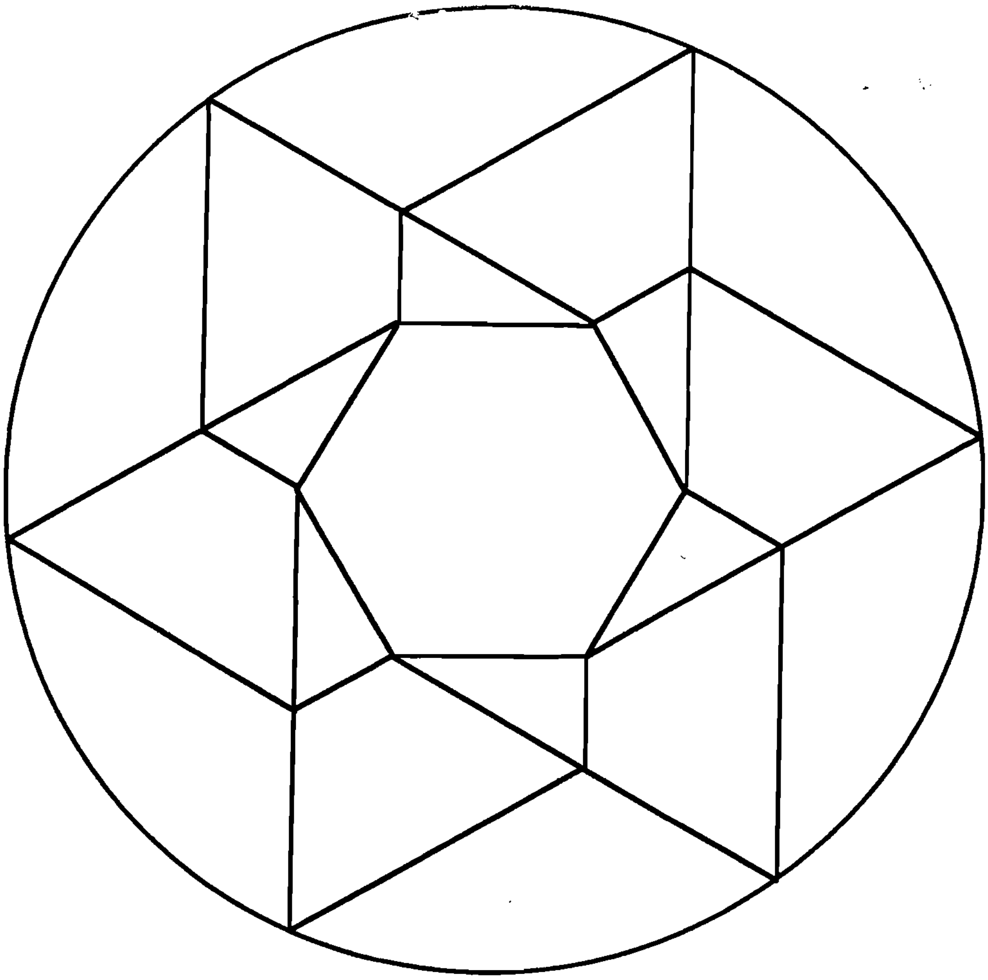

Figure 8.1. The fold pattern developed in Part II.

re-assemble the mechanism to reach some of these configurations. The equation for mobility remains, however, a useful first step in selecting possible designs for the SSDA.

A typical folding pattern developed in Part II is shown in Figure 8.1. This particular pattern has 6 sides, and 2 nodes along each major fold.

The fold pattern splits the surface into a number of panels. Consider each of the 19 panels in Figure 8.1 to be a rigid body, and each of the 30 fold lines to be a revolute joint. Then, the mobility of this system can be calculated as

$$M = (19 - 1) \times 6 - 30 \times 5 = -42$$

Thus, this system is highly overconstrained, and in general will not work as a mechanism. For a general fold pattern having a hub with n sides, and m nodes along each major fold line, the mobility is given by

$$M = n(-4m + 1)$$

Thus the system will be overconstrained for any m and n. This fits in well with the work by Kumar (1993), described in Section 6.3.

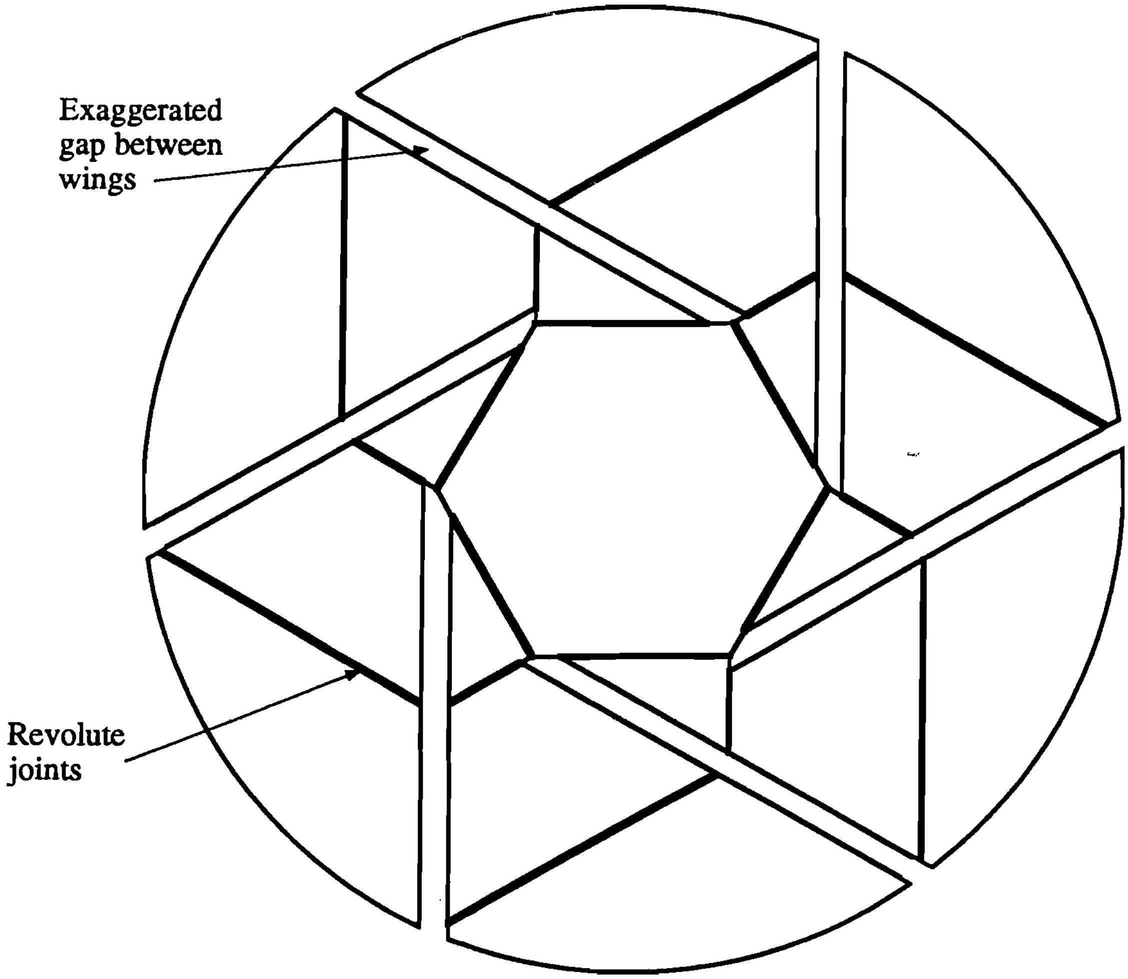

Figure 8.2. The fold pattern split into separate wings.

In order to develop a deployable antenna based on this folding pattern it is necessary to reduce the number of constraints. The simplest way to do this is to cut the pattern along the major fold lines, forming a number of *wings* emanating from the hub, as shown in Figure 8.2. This system now has a mobility of $n(m+1)$. However, for the deployable antenna, the ideal is to have a single way of opening the structure, i.e. $M = 1$. Thus, some constraints now have to be added. One possibility is to connect each wing to the next by a spherical joint. For three panels in each wing, as in Figure 8.2, this gives $M = 0$. If one spherical joint is removed, this gives $M = 3$. This is not the ideal $M = 1$, but could be easily controlled, and so this idea was the first to be considered, leading to Design (a).

8.1.1. Design (a)

Design (a) is shown schematically in Figure 8.3. It was developed initially assuming that each of the panels was thin and flat, with the intention of later extending this to parabolic panels having some thickness.

A simple cardboard model of the thin flat case worked well. Also, this design was analysed using the quaternion theory developed in Chapter 7, and implemented in a similar way to the later description in Section 8.2. The results of a

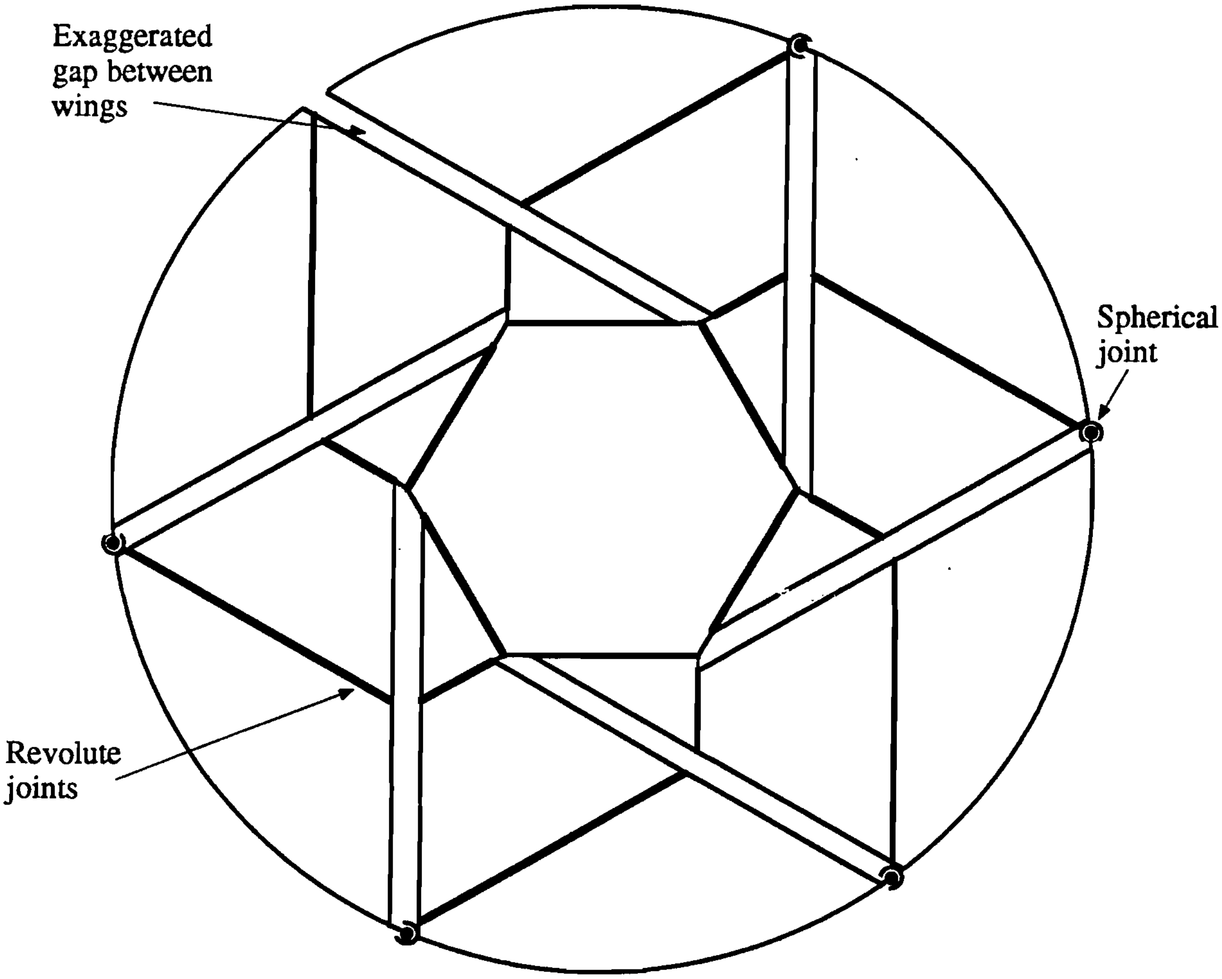

Figure 8.3. Design (a): fully deployed, top view.

simulation are shown in Figure 8.4. As $M = 3$, there is some freedom in the choice of unfolding path, but this simulation follows a particularly simple path. The unfolding is completely strain-free. All possible unfolding paths for Design (a) are similar to the one shown in the simulation results in Figure 8.4. The unfolding starts from the wing whose final panel is not connected by a spherical joint, and proceeds in a wave around the antenna, with the wings unfolding sequentially.

Unfortunately, problems occurred trying to extend these early, successful, results to a parabolic surface. The main problem is the packing of panels in the folded configuration, when these panels are curved. Schematically, the problem is shown in Figure 8.5. The curved panels fold back-to-back, which causes two problems. Not only does it lead to a very poor packing efficiency, but it is also difficult to position the fold lines so the panels can actually fold in this way, because the panels are so far apart. Even if this problem could be overcome, this design could only lead to a structure with a poor packing efficiency, and so Design (a) was taken no further.

The remaining concepts described in this section all have one common feature, which shows a major departure from the wrapping fold pattern: all wings fold in the same direction, in contrast with Design (a), where alternate wings fold up and down. This is to ensure that the curved panels, when folded, can neatly nest inside one another, and give a good packing efficiency.

8.1.2. Design (b)

Design (b) was the first design considered where all of the wings fold in the same direction, and because of this, there are no points on adjacent panels which are coincident before and after folding. Compare this with Design (a) where the points on adjacent wings that are coincident with a spherical joint are obviously coincident before and after folding.

In order to reduce the mobility of the system, *connecting bars* are added between panels at the end of adjacent wings. Design (b) is again based on the arrangement of panels shown in Figure 8.2, i.e. each wing having three panels. Adjacent wings are connected together by a connecting bar which has a revolute joint at one end, and a spherical joint at the other. One possible arrangement for this bar is shown in Figure 8.6.

Consider the mobility of Design (b). For a design based on an n-sided hub, there are $1 + 4n$ bodies (including the connecting bars), $4n$ revolute joints, and n spherical joints. Hence, from equation 8.1

$$M = (1 + 4n - 1) \times 6 - 4n \times 5 - n \times 3 = n$$

Therefore, the design shown in Figure 8.6, where $n = 6$, has a mobility of 6. However this can be easily reduced to a mobility of 1 by a symmetry constraint. If all the wings are forced to unfold concurrently, then this adds five extra constraints to the system, and leaves it with a mobility of 1. These constraints could be added, for instance, by coupling the motion of the revolute joints at the hub. All of designs (b), (c), (d), assume this symmetry constraint, in contrast with the asymmetric folding of Design (a).

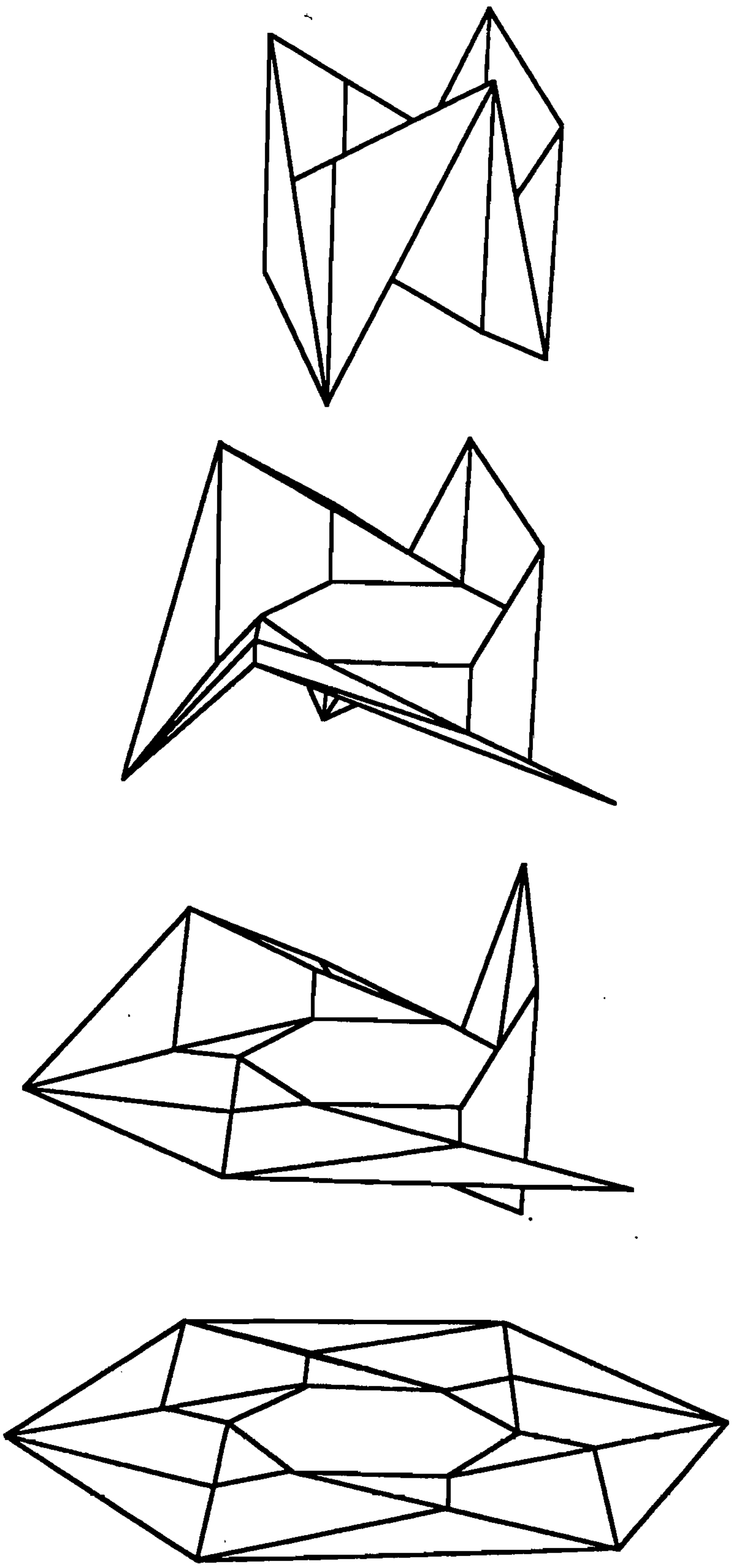

Figure 8.4. Simulated unfolding sequence for Design(a), assuming thin, flat panels.

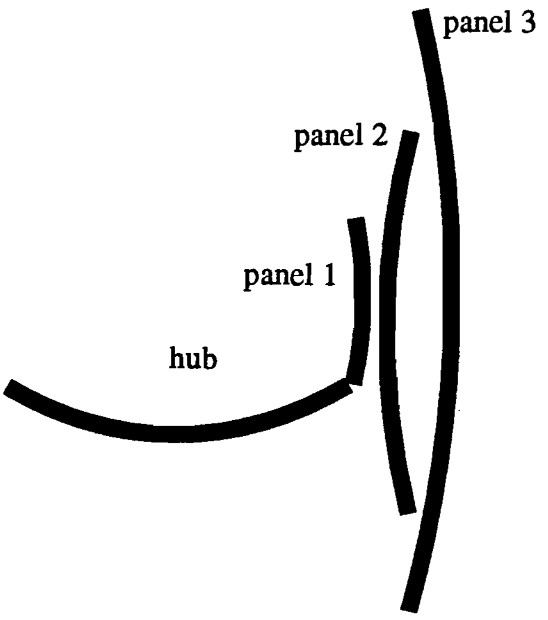

Figure 8.5. Cross-section through a curved surface packaged according to Design (a). Note the panels are folded back-to-back.

Part of the design process is to decide the position of the connecting bar. This is done by ensuring that the system is strain-free both when folded and when deployed. This process is described in detail for the selected design in Section 8.3. Deciding the position of the connecting bar leaves some freedom for both the position and orientation of the revolute hinge at its end. The plan was to choose values for these parameters which allowed strain-free folding. However, a brief investigation of the folding process for some of the various possibilities did not show a strain-free path between the folded and the deployed configurations.

Because of the problems with finding a strain-free path, and more particularly because, even if a solution were found, the antenna would not show a great reduction in diameter during folding, this design was not developed further.

8.1.3. Design (c)

Design (c) is similar to Design (b), but makes use of a connecting bar which has revolute joints at *both* of its ends. Because of the extra constraints that such a connecting bar provides, five panels per wing can be used. This is shown schematically in Figure 8.7. Note that Design (c) again has a mobility, $M = n$ (for an n-sided hub), which is reduced to $M = 1$ by ensuring a symmetrical folding path. Also, note that because five panels per wing are used, this system will potentially show a large reduction in diameter during folding.

Again, one of the steps in the design process is to make sure the system is strain-free both when folded and when deployed, and this again leaves freedom in the positioning of the connecting bar. A brief investigation of the folding process for some of the possible positions of the connecting bar again did not show a

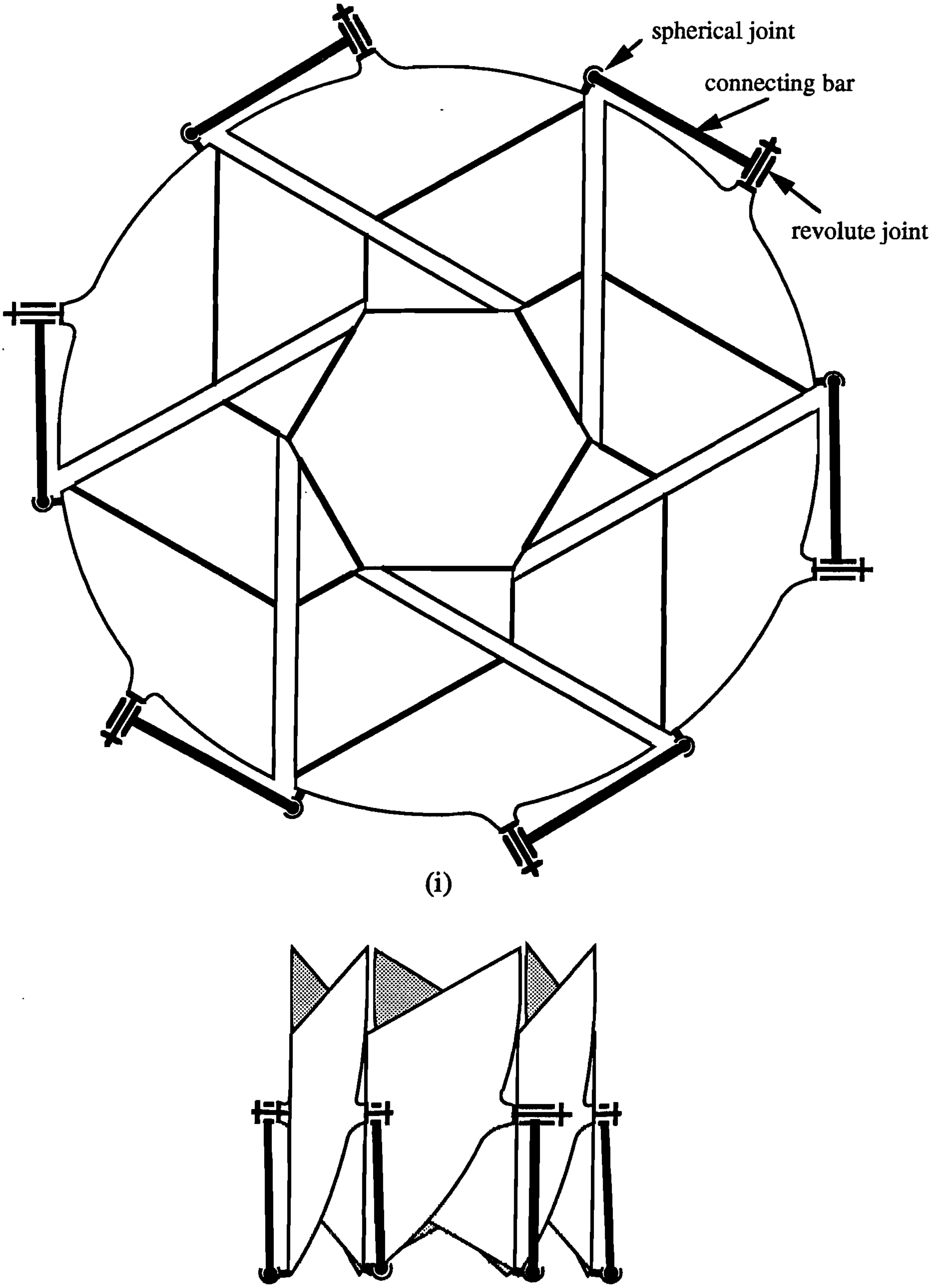

(i)

(ii)

Figure 8.6. Design (b): (i) Fully deployed, top view. (ii) Fully folded, side view.

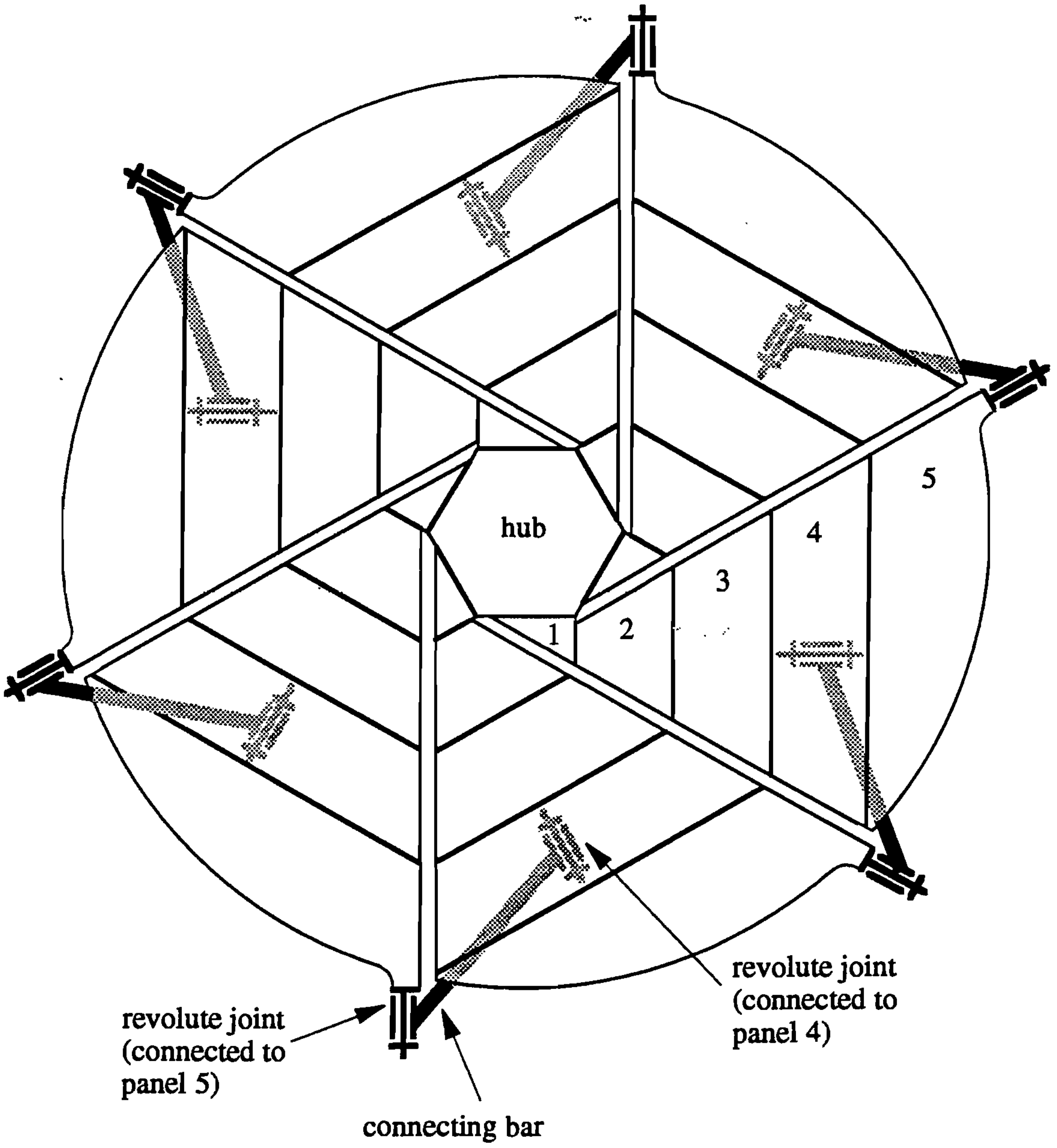

Figure 8.7. Design (c): fully deployed, top view.

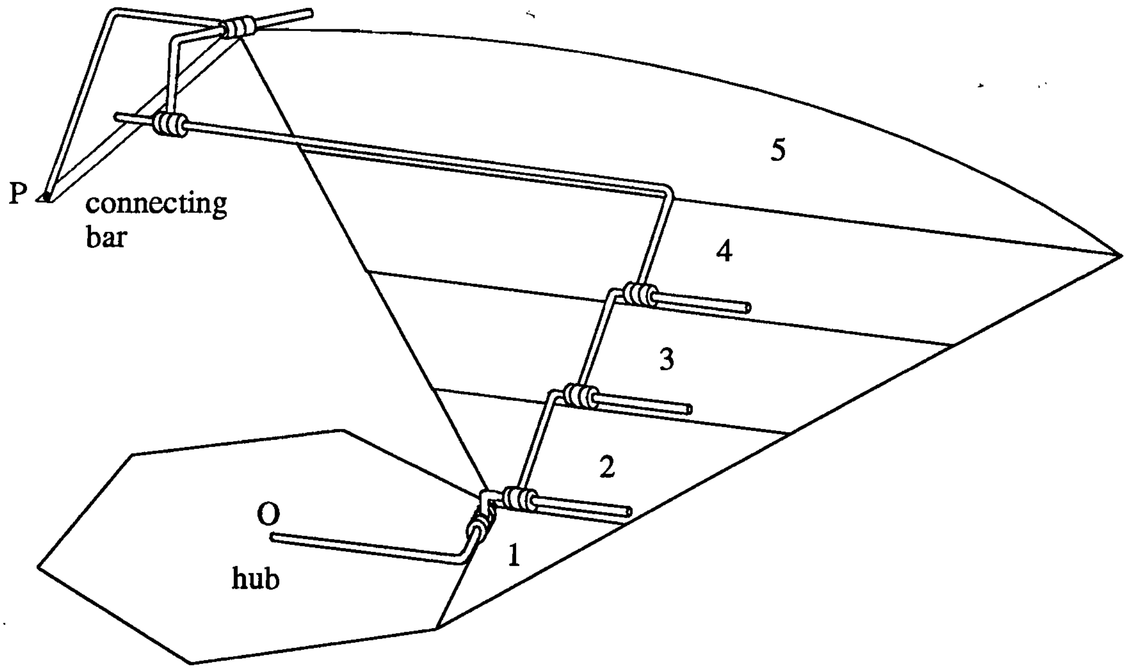

Figure 8.8. Two-bar model of one wing of the SSDA.

strain-free path between the folded and deployed configuration. However, it was found that the strains induced during folding are much smaller than for Design (b). Because of this, and also because of the potentially large packing efficiency, it is this design that is developed further in Sections 8.2 and 8.3.

8.1.4. Design (d)

Design (d), on which very little work was done, was intended as a back-up to Design (c). In Design (d), as in Design (c), the connecting bar has revolute joints at each end, but Design (d) also has an additional revolute joint somewhere along the bar. Because of this, and to keep the mobility during symmetric unfolding equal to one, Design (d) has four panels per wing.

Because Design (d) has an additional hinge in the connecting bar, there is a great deal of freedom during the design process, giving more potential for finding designs which have suitable folding properties. However, the design does not have as good potential packing efficiency as Design (c), and was not developed further.

8.2. Analytical Modelling of Design (c)

The SSDA is modelled using dual quaternions, based on the theory described in Chapter 7. The first step in this analysis is to replace each body in the actual system with its two-bar equivalent. As a symmetric folding mode is being considered, only one wing need be considered. The two-bar model for one wing of a flat version of the chosen design of SSDA is shown in Figure 8.8. It shows an open chain of bodies which connects the origin of coordinates at O to a point on the end of the connecting bar at P.

An important difference between this system and the robot arm modelled as an example in Section 7.6 is that the SSDA consists of kinematically closed loops of rigid bodies. The hinges shown in Figure 8.8 do not have complete freedom of movement. Constraints must be imposed that the revolute joint at the end of the connecting bar (at P) must be connected to the next wing. Because a symmetric folding mode is being considered, the axis of the revolute joint on the next wing is simply the equivalent axis on this wing rotated.

The method used to impose this constraint is best explained by considering how it works if the connection between one wing and the next is by means of a spherical joint (this method was first developed for the analysis of Design (a)). The position of the point at the centre of the spherical joint is calculated in terms of the angles rotated by the hinges connecting the six bodies that make up the wing. The position of the point at the centre of the same spherical joint is also calculated by similarly considering the next wing, but this time the point is located on a panel, rather than at the end of the connecting bar. For a general set of hinge angles, these two positions will be different, and it is possible to measure a distance *d* between them. The hinge angles are varied until this *d* is reduced to zero, when the two wings will be properly connected.

A revolute joint can be similarly modelled, except that it is now necessary to specify a point and a direction on the two halves of the joint. It would be possible to find a measure of the lack of fit between the two halves of the joint, and minimise this. However, computer code had already been written for the connection of a spherical joint. Therefore, a revolute joint is modelled as two spherical joints a fixed distance apart (100 mm in this case), by ensuring that both spherical joints are connected.

For the SSDA the above process was implemented by writing a FORTRAN routine. This routine is passed ~~five~~ six parameters, the hinge angles between every panel on the wing, and also between the final panel and the connecting bar. The routine returns the error in alignment at the revolute joint at the end of the connecting bar, where it is connected to the next wing. The alignment error is quantified as the mean square of the connection errors of the two spherical joints used to model the revolute joint. The error that this routine returns is minimised using the NAG routine `E04JAF` (NAG, 1990).

The SSDA has a mobility of one, and so only one angle on the wing can be specified: the remaining five will be fixed by the above process. For a strain-free motion, the minimum found should be zero. However, if the mechanism is being forced through an impossible configuration, the minimum will be greater than zero.

8.3. Design Process

The previous sections have described how a general design was selected, and how it was modelled analytically. This section describes in more detail how the final detailed design of the SSDA, whose manufacture is described in Chapter 9, was arrived at.

The SSDA model is made from glass-fibre. It was manufactured by being moulded over a parabolic aluminium antenna, which therefore fixed its dimensions. The final SSDA model has a radius of 0.73 m, and its shape is defined by the equation

$$z = 0.405r^2$$

where z is the height above the centre of the antenna, and r is the diameter, both measured in metres. This gives the antenna a focal length/diameter ratio of 0.42. The outer edge of the antenna is 0.22 m above its centre. The antenna is on average 3 mm thick.

An early decision was made to design an SSDA having six wings.

8.3.1. Shape of Panels

The first part of the design process is to consider the shape of the panels which make up the antenna, i.e. how the parabolic surface should be cut up. The panels are initially designed to ensure that the antenna has a compact folded shape, without any consideration of the folding mode or the position of the connecting bar. This initial design, however, is later modified to take account of these factors. A number of design rules are used to determine the shape of the panels.

The first design rule is that the revolute hinge line between adjacent panels should pass through the corners of the panels. If the hinge line passes above any part of the panel, it requires either part of the hinge mechanism to protrude above the surface of the antenna, or a complex hinge design. If the hinge line passes through the panels some distance in from the corners, the parts of the panels that are beyond these points would have to be specially shaped to avoid clashing, which would interfere with the packing arrangement described below.

The second design rule is that all hinges between panels should be vertical in the folded configuration, thus implying that all the hinges on one wing must be parallel. This is a similar consideration to that used in Part II to design the wrapping fold pattern. It would be possible to design an antenna where some or all the hinge lines are not vertical when folded, but it would be difficult to achieve a good folded shape.

Using the second design rule it becomes easy to consider the antenna in the folded configuration. Allowing an equal spacing between panels, the folded configuration is shown schematically in Figure 8.9. (Note that the panels are shown as flat, to simplify the diagram.) From this configuration, the distance between adjacent hinges on one wing, i.e. the width of the panels, is determined. These widths are shown in Figure 8.11. In the final design the radial distance between adjacent hinges in the folded configuration, the parameter u in Figure 8.9, was 3.5 mm. This may seem small, but as the panels are curved, and actually nest inside one another, it is actually fairly conservative. This spacing was modified to allow a gap of 14 mm between the first and second hinge lines, to prevent collisions between panels during unfolding. This spacing was decided in the light of results from the unfolding simulations explained in Section 8.3.3. Also, the spacing was modified to allow a much larger gap of 220 mm between the final hinge line and the edge of the last panel, to leave room for the connecting bar.

Taking these considerations into account, and ensuring that the outside of the antenna coincides with the edge of the last panel, the radius of the hub in the

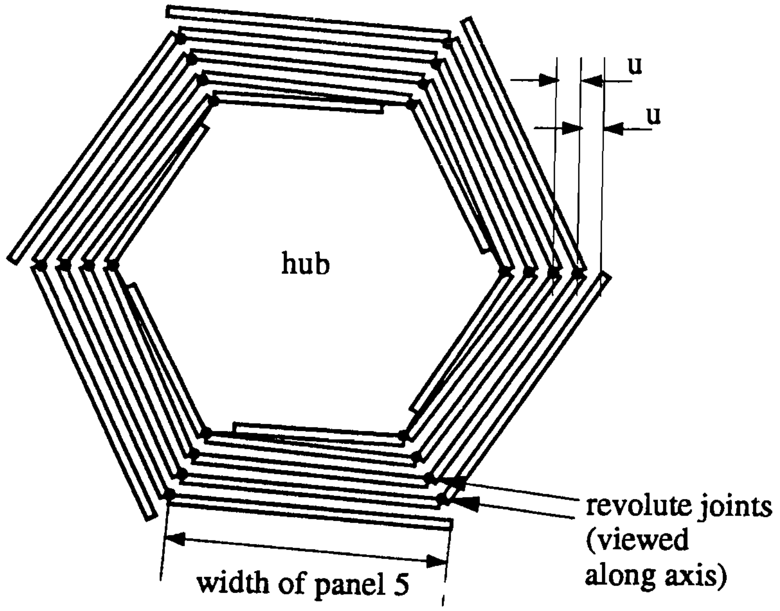

Figure 8.9. Schematic of folded SSDA, top view.

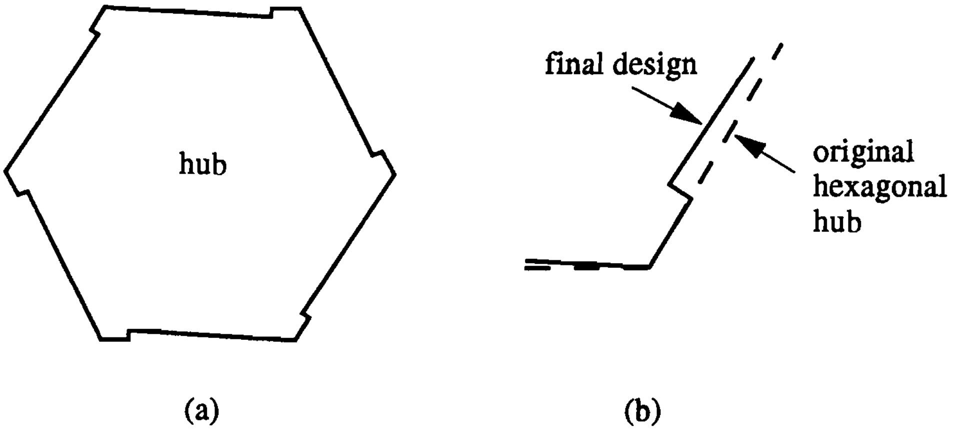

Figure 8.10. (a) Final design of hub. (b) Detail around a corner

final design was 0.143 m, and the panels have widths of 0.143 m, 0.149 m, 0.158 m, 0.162 m, and 0.201 m.

The hub has to be carefully designed to avoid problems at its vertices. If the hub was simply a hexagon, the thickness of the antenna would cause a clash between the first panel on one wing, and the second panel on the next in the folded configuration. This is avoided by re-designing the hub to allow space for the thickness of the first panel, as shown in Figure 8.10.

The next step in the design process is to decide, having fixed the hub design and the widths of the panels, the exact position of the panels on the antenna. This is done by numbering the ends of the hinge lines, as shown in Figure 8.11. The numbering scheme seems strange, but allows for the definition of the connecting bar in Section 8.3.2. These numbered points are then consecutively fixed in position as follows. Note that all of these points must lie on the parabolic antenna surface.

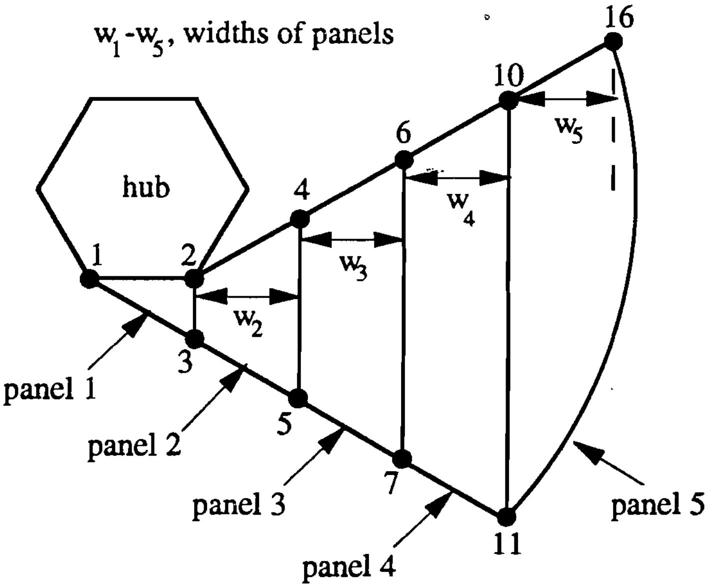

Figure 8.11. Numbering scheme for the points defining panels.

1. Points 1 and 2 are already fixed. Point 3 must lie on a line that passes through the vertical when rotated about 1–2, i.e. line 2–3 must be perpendicular to line 1–2. The distance of point 3 along this line is a variable
2. Point 4 is fixed on a line which is both parallel to 2–3, and at a distance w_2 away from it. w_2 is the width of panel 2. The position of point 4 along this line is a variable
3. Point 5 is now completely fixed as it must lie at the point of intersection between a line parallel to 2–3 and passing through point 4, and the surface of the paraboloid.
4. Points 6 and 7, and 10 and 11, and point 16, are fixed in the same way as points 4 and 5.

It may appear that there is a great deal of freedom in the SSDA design, as the position of a number of points can be varied. However, it must be remembered that this is one of six identical wings, which together must cover the antenna surface. Therefore the variable parameters must be optimised to give a design where adjacent wings come close to matching. The whole process was encoded as a MATLAB (MathWorks, 1992) routine, where these parameters could be varied, and a plot of the panel design produced. This was run a number of times to achieve a good match between adjacent panels. The final design is shown in Figure 8.12. This shows that, where gaps between adjacent wings would have occurred, material has been added to one or other of the wings. This gives panels with more than four sides, but does not affect the folding in any way. The position of the points is given later in Table 8.1, which also gives the position of the connecting bar.

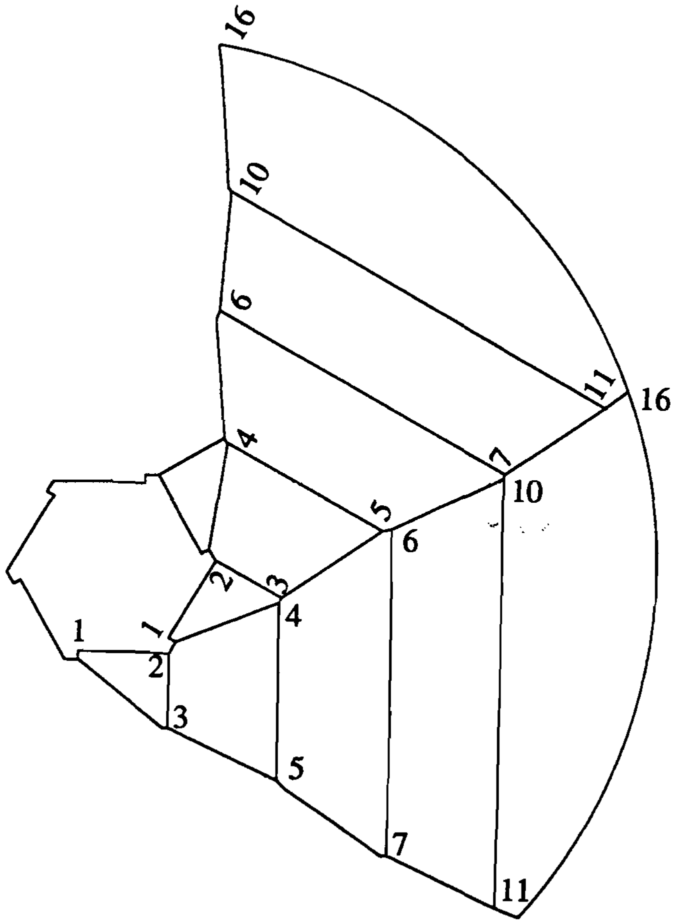

Figure 8.12. Final panel design.

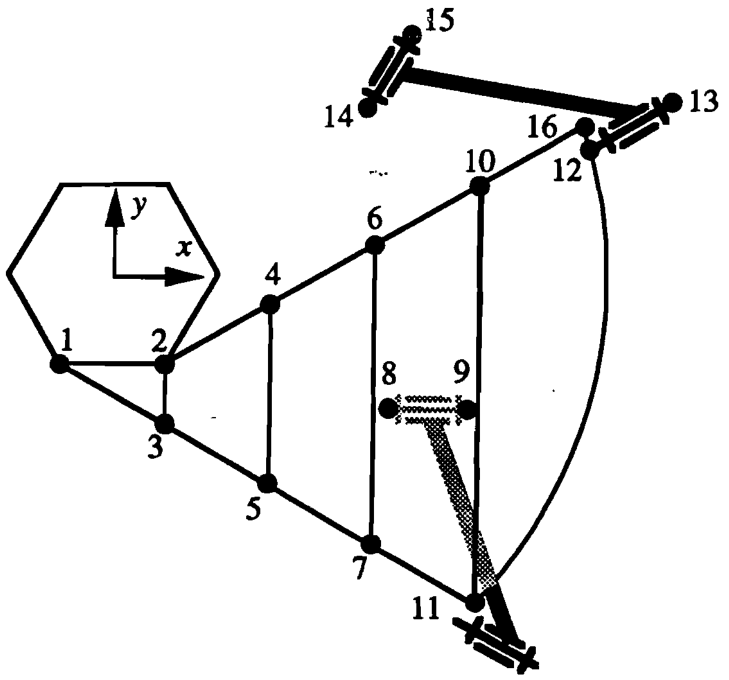

Figure 8.13. Joint numbering for connecting bar.

8.3.2. Positioning of the Connecting Bar

Having configured the panels of the SSDA, the next step is to fit the connecting bar. One end of the connecting bar is fixed, by a revolute joint, to panel 5 on one wing. The other end of the bar is connected, by a revolute joint, to panel 4 on the next wing. While it is feasible to connect the other end of the bar to panels 3 or 5 on the next wing, difficulties occurred with both of these choices. A schematic diagram of the numbering scheme used to define the position of the connecting bar is shown in Figure 8.13. The coordinate system used for the analysis is also shown in the figure. The position of points 1–7, 10, 11 and 16 have already been defined in the previous section. Points 12 and 13 define the revolute joint connecting panel 5 to the connecting bar. Points 14 and 15 define the revolute joint at the other end of the connecting bar. Points 8 and 9 define the revolute joint where the connecting bar from the previous wing is attached. As a symmetric mechanism is being considered, points 14 and 15 are simply points 8 and 9 rotated about the centre of the hub by $\pi/3$ radians.

Points 8 and 9, and 12 and 13, cannot be placed with complete freedom. A number of conditions must be fulfilled. Firstly, it is essential that the connecting bar should fit the antenna, both when open and when folded. Secondly, it is desirable that the points do not lie far from the antenna surface, so that the connecting bar should not hinder the efficient packaging of the panels. To fulfil this, both points 8 and 12 were defined to coincide with the antenna surface. Thirdly, point 12 must be placed so that the connecting bar can rotate from its open to its closed configuration without interfering with panel 5. This can be done by ensuring that point 12 is on the outer edge of the antenna.

The positioning of the connecting bar was analysed by means of a FORTRAN routine, `design.f`. The routine is passed information about the antenna surface and 15 parameters which can be varied. It returns 15 parameters which are measures of constraint violation; the 15 constraints are derived from the conditions the antenna has to fulfil. When all of these output parameters return zero, an acceptable design has been calculated.

`design.f` can be 'solved' by the NAG routine `C05NJF` (NAG, 1990). `C05NJF` is designed to simultaneously solve a number of non-linear equations. `C05NJF` varies the 15 inputs to `design.f` until the 15 conditions return zero.

The 15 variable parameters passed to `design.f` are:

1–5 The rotation of the 5 hinges between panels, from the open to the folded configuration.

6 The rotation of the hinge between panel 5 and the connecting bar, from the open to the folded configuration.

7–9 The cartesian coordinates of point 8 in the open configuration.

10–12 The cartesian coordinates of point 9 in the open configuration.

13–15 The cartesian coordinates of point 13 in the open configuration.

A number of constants are also passed to `design.f`. They include the coordinates of points 1–7, 10, 11, and 16, which are already known, and a number of design parameters. The design parameters are the coordinates of point 12, the angle at which hinge 12-13 lies from the x-y plane, ϕ, and the x-coordinate of point 8, $8x$. Different values of these parameters produce different designs of antenna.

The routine `design.f` calculates the position of all points after folding, and returns 15 values, such that when these 15 values are zero, the 15 parameters which have been passed specify a satisfactory design. This is an antenna that not only fits together when folded, in the way shown in Figure 8.9, but also satisfies the design parameters (e.g. the x-coordinate of point 8).

The 15 values which `design.f` returns are given below.

1 Distance from point 3, when folded, to a radial plane through the vertex of the hub. This distance is zero if the folded shape is as shown in Figure 8.9.

2 Distance from point 4, when folded, to a radial plane through the vertex of the hub, see (1).

3 Distance from point 6, when folded, to a radial plane through the vertex of the hub, see (1).

4 Distance from point 10, when folded, to a radial plane through the vertex of the hub, see (1).

5 Distance from point 16, when folded, to a radial plane through the vertex of the hub, see (1).

6 Difference between the x-coordinate of point 8, and that specified by the design parameter.

7 Distance from point 8 to the antenna surface, which should be zero

8 Distance from point 9 to point 8 minus 100 mm. This difference should be zero, because the distance between the two spherical joints defining a revolute joint is defined to be 100 mm. This condition also includes a penalty formulation to ensure that $9x > 8x$ else there would be two possible positions for point 9.

9 Distance from point 13 to point 12 minus 100 mm, see (8). This condition also includes a penalty formulation to ensure that $13x > 12x$.

10 Difference between the angle of line 12-13 and the x-y plane when the antenna is open, and that specified by the design parameter, ϕ. This difference should be zero.

11–13 Differences in the cartesian coordinates of point 8 when folded, and rotated about the hub by $\pi/3$ radians, and the cartesian coordinates of point 14 when folded. This difference should be zero, as the points should coincide.

14–15 Differences in the coordinates of point 9 when folded, and rotated about the hub by $\pi/3$ radians, and the coordinates of point 15 when folded. Only two conditions need be fulfilled for this, as points 8 and 9, and points 14 and 15, must be the same distance apart.

Thus the routine `design.f` and the NAG routine `C05NJF` calculate a design for the antenna which fits together both when open, and when folded. It is possible to vary the design using three design parameters. These are, in the open configuration:

1. How far round the circumference of the antenna point 12 is placed, which can be defined by its y-coordinate, $12y$.
2. The x-coordinate of point 8, $8x$.
3. The angle of the hinge-line 12-13 from the x-y plane, ϕ.

For any sensible choice of these three parameters, a design can be produced. However, the design is guaranteed to fit together only when open and when folded. It is necessary to simulate the folding process to consider what happens between these two extremes.

8.3.3. Unfolding Simulation

The SSDA has a mobility of one. Therefore, performing a simulation of the folding process requires that, at each stage, the angle of one revolute joint is fixed. It should then be possible to calculate the other five angles to ensure that the mechanism still fits together. For all the simulations described here, the angle fixed is the angle between panel 5 and the connecting bar. This is for two reasons. The first is that this choice produced successful results for the simulation. The second reason is that, in the manufactured antenna described in Chapter 9, it is this hinge that is motorised.

The simulations were performed using a FORTRAN routine, `unfold.f`. This routine is passed six parameters, θ_1–θ_6, which are respectively the 5 angles between panels, and the angle between panel 5 and the connecting bar . `unfold.f` returns a single value which is the sum of the squares of the errors at the two spherical joints used to simulate the revolute joint at the end of the connecting bar (as described in Section 8.2). This value takes into account both positional and angular errors.

At each step during the simulation, the value of θ_6 is fixed, and the other values θ_1–θ_5 are found. This is done by the NAG routine **E04JAF**, a minimisation routine. It varies the angles θ_1–θ_5 to find a minimum in the error returned by `unfold.f`. If the antenna fits together at all stages, and thus remains a mechanism, this minimum will be zero.

Unfortunately, none of the designs tried remained a mechanism during the folding process. This destroys many of the assumptions used to set up the simulations. The antenna is required to deform during folding, and correctly modelling this would be much more complex. Despite this, the method is still useful, and was used to design the prototype antenna described in Chapter 9. However, the emphasis on what is being done now changes. It is no longer a correct simulation of the kinematics of deployment. It is now an attempt to prove that a path exists between the folded and deployed configuration which does not require large deformations. The system is effectively being modelled as rigid, apart from the hinge between the connecting bar, and panel 4 on the next wing, where an error is allowed, as explained above. This error is minimised at each stage of the folding process. Thus, during folding, a plot of error is produced. The various design parameters mentioned in the previous section can be varied to produce new plots. The next section explains how these parameters were varied to produce an optimum design.

Each simulation in fact models the antenna unfolding. Each of the angles, θ_1–θ_6, starts at their folded values (found from `design.f`). θ_6 is reduced to zero in steps, and at each stage the best set of angles θ_1–θ_5 is calculated. None of the angles are allowed to become less than zero, as this is not allowed on the manufactured antenna. Also, a ratchet mechanism is simulated so that each angle can only go towards zero, to aid convergence. This may not occur in practice, but the aim is to show the existence of a low-deformation path between the folded and deployed configurations. If necessary a practical antenna could be guided towards such a path by spring-loaded joints.

8.3.4. Optimisation

From the sections above, it is possible to design a number of SSDAs by varying the position of the correcting bar. However, none of the designs investigated fit the ideal of a strain-free folding. Given this, the best approach is to design an SSDA which undergoes the smallest possible deformation during folding.

What is required is an optimisation process. Three parameters can be varied: $12y$, the y-coordinate of point 12; 8x, the x-coordinate of point 8; ϕ, the angle hinge 12–13 makes with the x-y plane (ϕ is positive above the plane). The 3 parameters are defined in the configuration when the antenna is deployed.

Specifying the parameters $12y$, $8x$, and ϕ fixes the design of the antenna.

By varying $8x$, $12y$, and ϕ, an antenna must be designed which undergoes the minimum deformation during folding. Deformation is measured in the sense of the previous section, i.e. as if it were all concentrated at one joint. Although this is obviously unrealistic to obtain the exact folding process, an antenna showing small deformations by this measure will only have to undergo small, distributed deformations in practice. This approach is validated by the antenna manufactured in Chapter 9.

The optimisation technique was was fairly crude. A grid of the variables $12y$ and $8x$ was generated. At each point on this grid, the value of ϕ was varied to find the value which gave the smallest deformation during unfolding. The deformation was measured by the simulation process described in the previous section, with θ_6 being reduced to zero in 20 steps. This resulted in a grid of values of maximum deformation during unfolding, for varying coordinates $8x$ and $12y$. From this grid the lowest value of deformation was chosen.

Figures 8.14–8.19 show typical values obtained during the optimisation process. Figure 8.14 shows the deformation, and Figure 8.15 the folding angles, during the unfolding simulation when $8x = 0.500\,\mathrm{m}$, $12y = 0.000\,\mathrm{m}$, and $\phi = 0.02\,\mathrm{rad}$. This is not the optimum value for $8x$ and $12y$, but is the optimum ϕ for this particular value of $8x$ and $12y$. The deformation plot consists of two peaks. The end of the first peak corresponds to a jump in the value of some of the hinge angles, particularly θ_1. This peak appears to correspond to the mechanism being forced through an impossible position. The second peak occurs when a number of the hinges have been reduced to their minimum value of zero, and hence have reduced the mobility of the mechanism.

Figure 8.16 shows the deformation, and Figure 8.17 the folding angles, during the unfolding simulation when $8x = 0.382\,\mathrm{m}$, $12y = 0.251\,\mathrm{m}$, and $\phi = 0.10\,\mathrm{rad}$. This is the optimum value found for $8x$ and $12y$, but not for ϕ. Note that this design has point 8 on the edge of panel 4, and point 12 corresponding with point 16. The deformation plot again consists of two peaks. Now, however, the first peak has almost disappeared.

Figure 8.18 shows the deformation, and Figure 8.19 the folding angles, during the unfolding simulation when $8x = 0.382\,\mathrm{m}$, $12y = 0.251\,\mathrm{m}$, and $\phi = 0.34\,\mathrm{rad}$. This is the optimum value found for all parameters. The deformation plot again consists of two peaks. These peaks are now, however, very much reduced. The maximum value of deformation of $0.0005\,\mathrm{m}^2$ corresponds to an error at the connecting bar hinge of 22 mm, compared with the overall diameter of the antenna of 1.46 m. This amount of deformation should easily be accommodated within the panels, and it was on this design that the final SSDA design was based, as described in the next section.

8.4. Final Design

This section describes the final design of SSDA, the manufacture of which is described in Chapter 9. Table 8.1 gives the position of all of the design points, shown in Figure 8.13, for this design. The design was arrived at by using the design process described in Section 8.3.

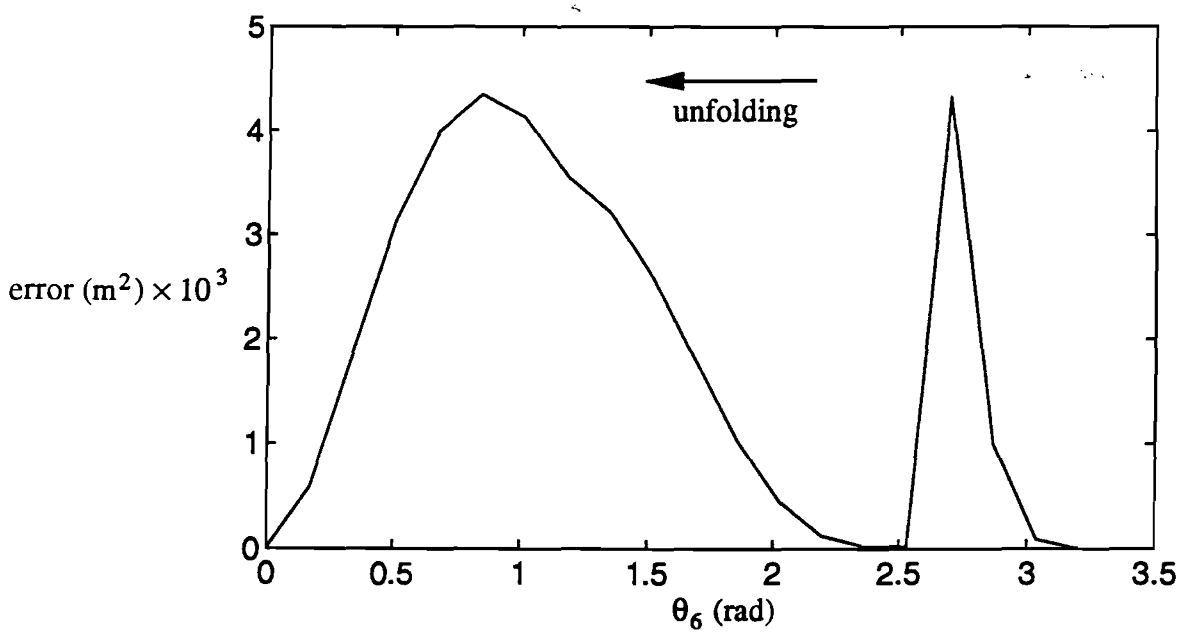

Figure 8.14. Deformation of SSDA where $8x = 0.500\,\mathrm{m}$, $12y = 0.000\,\mathrm{m}$, $\phi = 0.02\,\mathrm{rad}$, during unfolding.

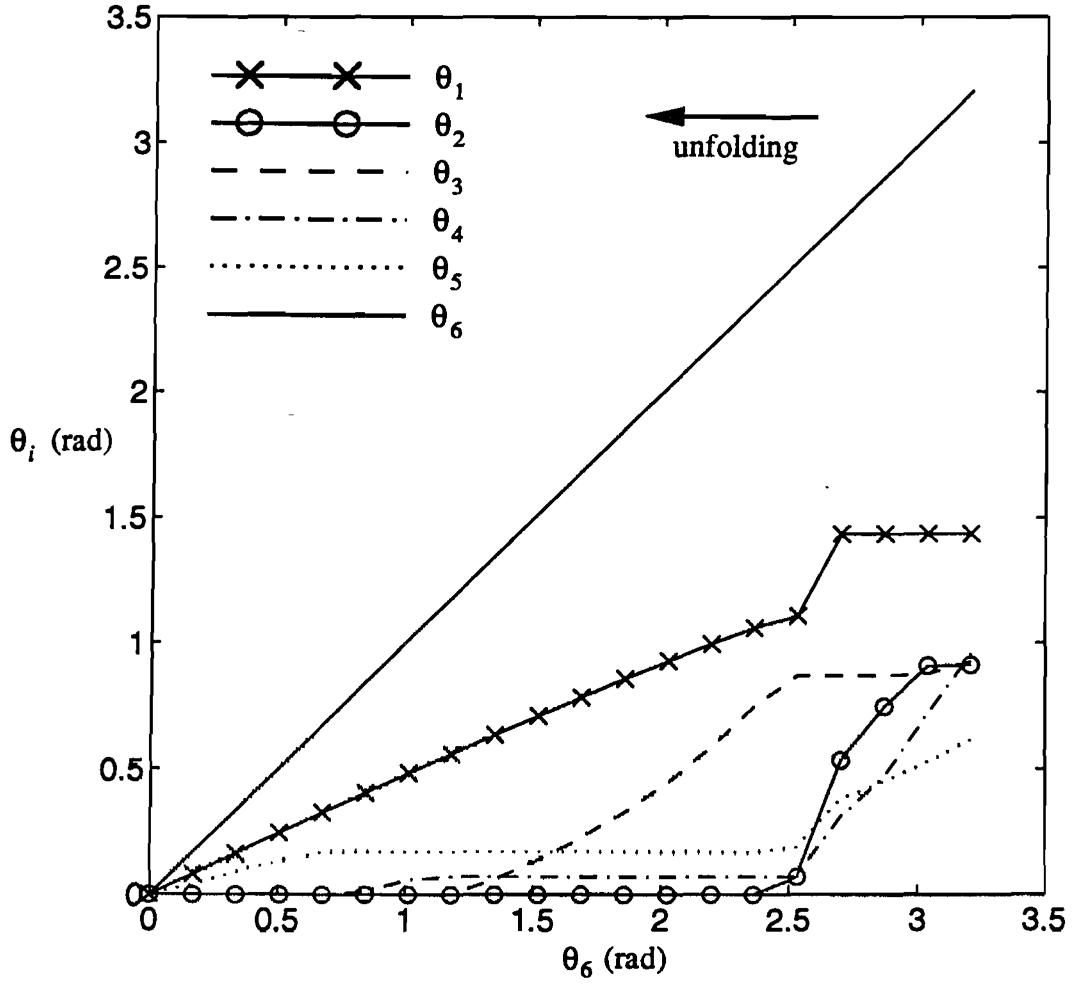

Figure 8.15. Hinge angles of SSDA where $8x = 0.500\,\mathrm{m}$, $12y = 0.000\,\mathrm{m}$, $\phi = 0.02\,\mathrm{rad}$, during unfolding.

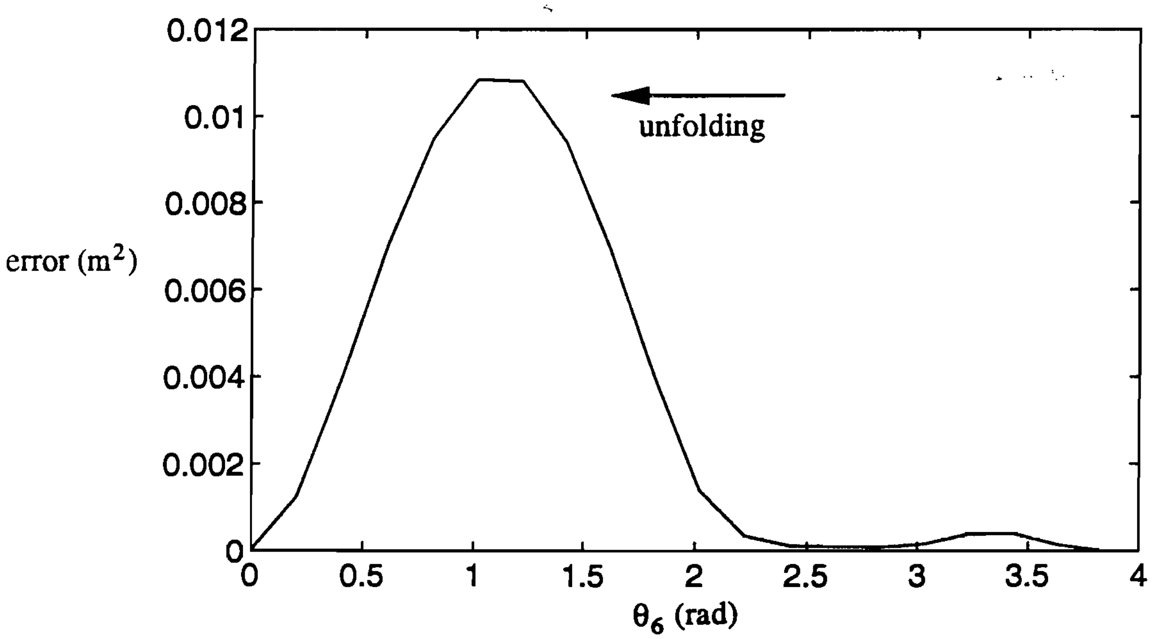

Figure 8.16. Deformation of SSDA where $8x = 0.382\,\mathrm{m}$, $12y = 0.251\,\mathrm{m}$, $\phi = 0.10\,\mathrm{rad}$, during unfolding.

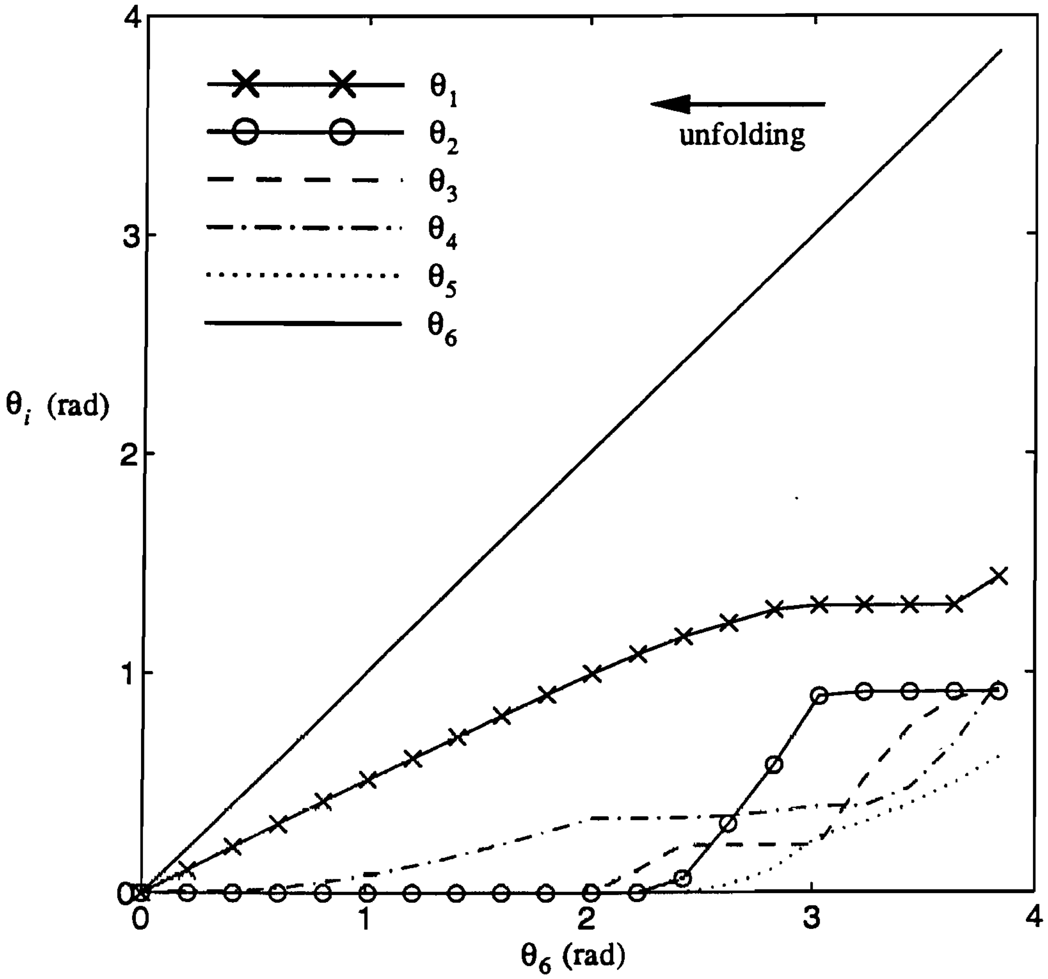

Figure 8.17. Hinge angles of SSDA where $8x = 0.382\,\mathrm{m}$, $12y = 0.251\,\mathrm{m}$, $\phi = 0.10\,\mathrm{rad}$, during unfolding.

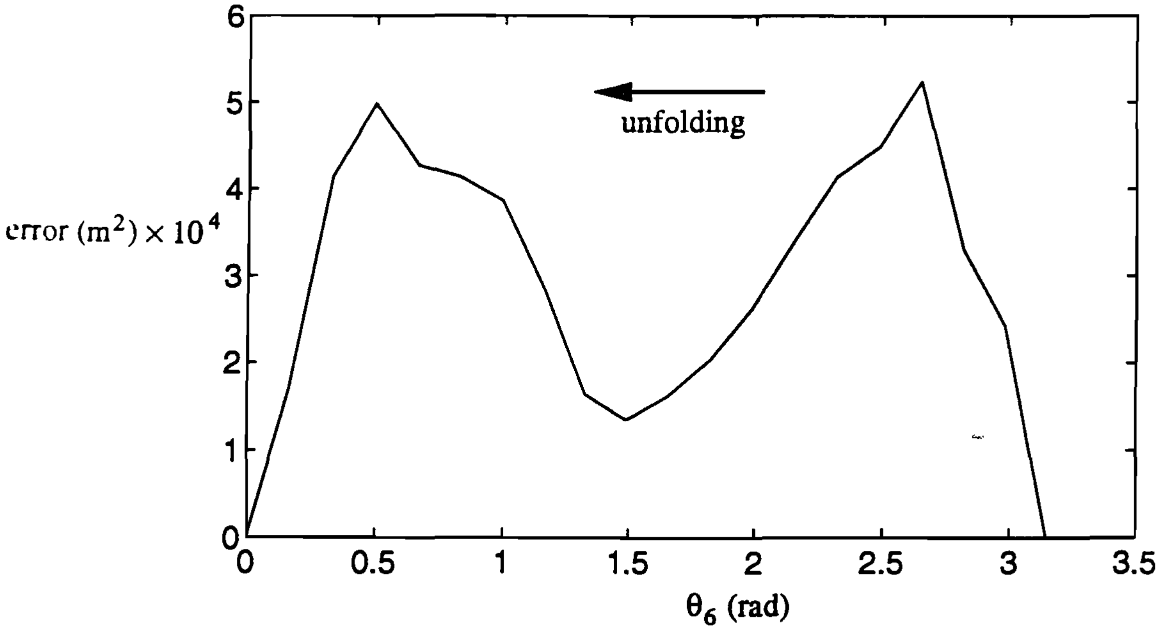

Figure 8.18. Deformation of SSDA where $8x = 0.382\,\text{m}$, $12y = 0.251\,\text{m}$, $\phi = 0.34\,\text{rad}$, during unfolding.

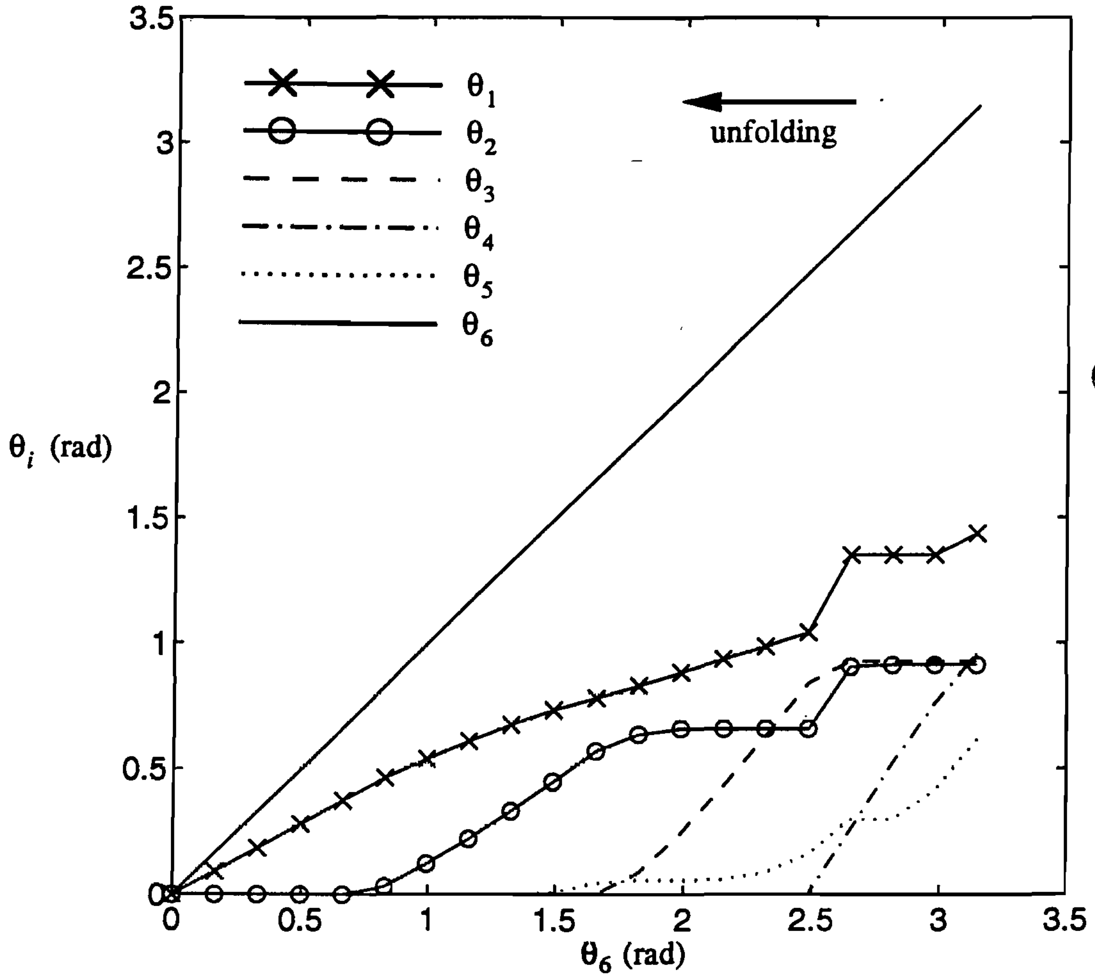

Figure 8.19. Hinge angles of SSDA where $8x = 0.382\,\text{m}$, $12y = 0.251\,\text{m}$, $\phi = 0.34\,\text{rad}$, during unfolding.

Table 8.1. Position of all points (all dimensions in m)

Point no.	x-coordinate	y-coordinate	z-coordinate
1	-0.042	-0.117	0.006
2	0.081	-0.117	0.008
3	0.083	-0.219	0.022
4	0.228	-0.044	0.022
5	0.231	-0.287	0.055
6	0.376	0.059	0.059
7	0.382	-0.386	0.120
8	0.426	-0.132	0.073
9	0.526	-0.134	0.069
10	0.522	0.131	0.117
11	0.530	-0.455	0.198
12	0.686	0.251	0.216
13	0.767	0.304	0.241
14	0.327	0.303	0.073
15	0.379	0.388	0.069
16	0.686	0.251	0.216

The design described here is slightly different from the optimum described in Section 8.3.4. This is because, in order to prevent the connecting bar from colliding with panels during folding, it is necessary for the hinge axis to be some distance below the the antenna surface. Therefore, the hinge was initially placed further along the *same* hinge axis, which placed it on the other side of the panel (next to panel 5), 40 mm below the antenna surface. The design was finally changed slightly from this to allow a little extra space, and the hinge is in fact 50 mm below the antenna surface.

A more detailed simulation was performed to check for collisions between panels, and between panels and the connecting bar. Obviously, this simulation is subject to the errors inherent in a model where the deformation is concentrated in one place. However, as the deformation in the chosen design is small, this should make little difference. This is verified by comparing the final simulation results with the actual deployment, as shown in the next chapter.

The position of a large number of points on the antenna, both on the front and the back face, were calculated as the antenna unfolded. The antenna was then displayed using a MATLAB routine, and by looking at the antenna from various positions in space, collisions between panels were checked for. The design followed an iterative process. Larger gaps between the folded panels were introduced, as mentioned in Section 8.3.1, to avoid collisions. Also, a non-straight connecting bar was introduced, also to avoid collisions.

Four views from the simulation of the final design of the SSDA unfolding are shown in Figures 8.20–8.23.

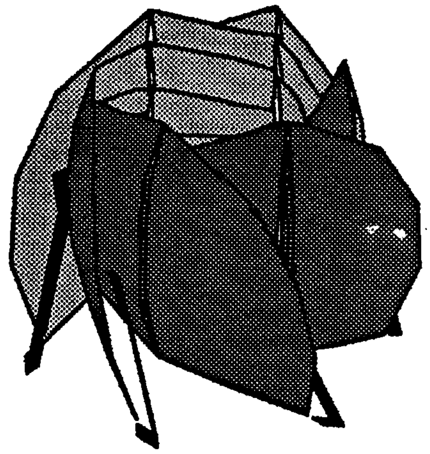

Figure 8.20. Simulation of the deployment of the SSDA: fully folded.

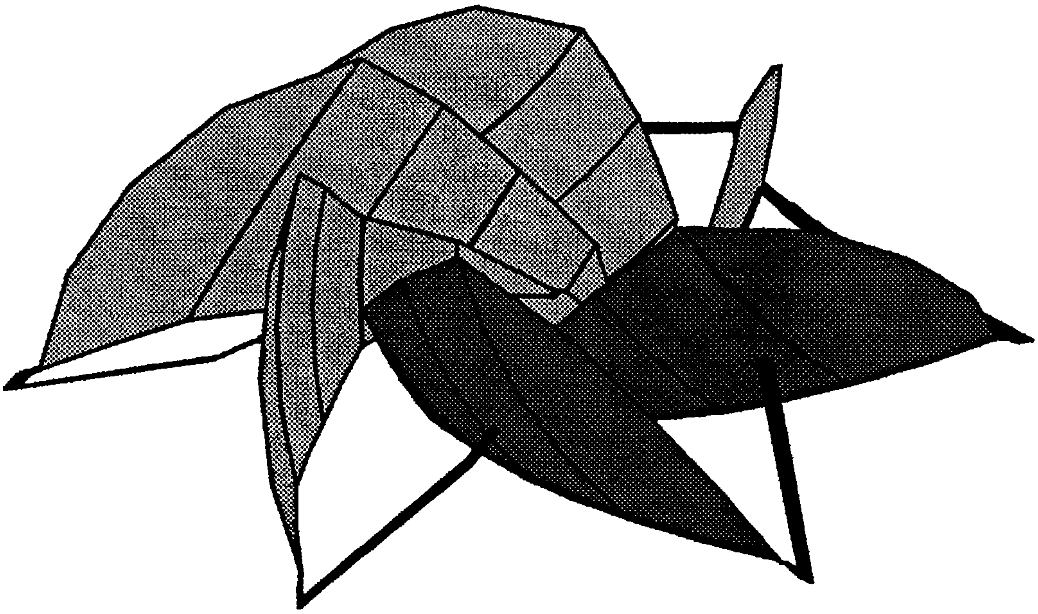

Figure 8.21. Simulation of the deployment of the SSDA: one-third deployed.

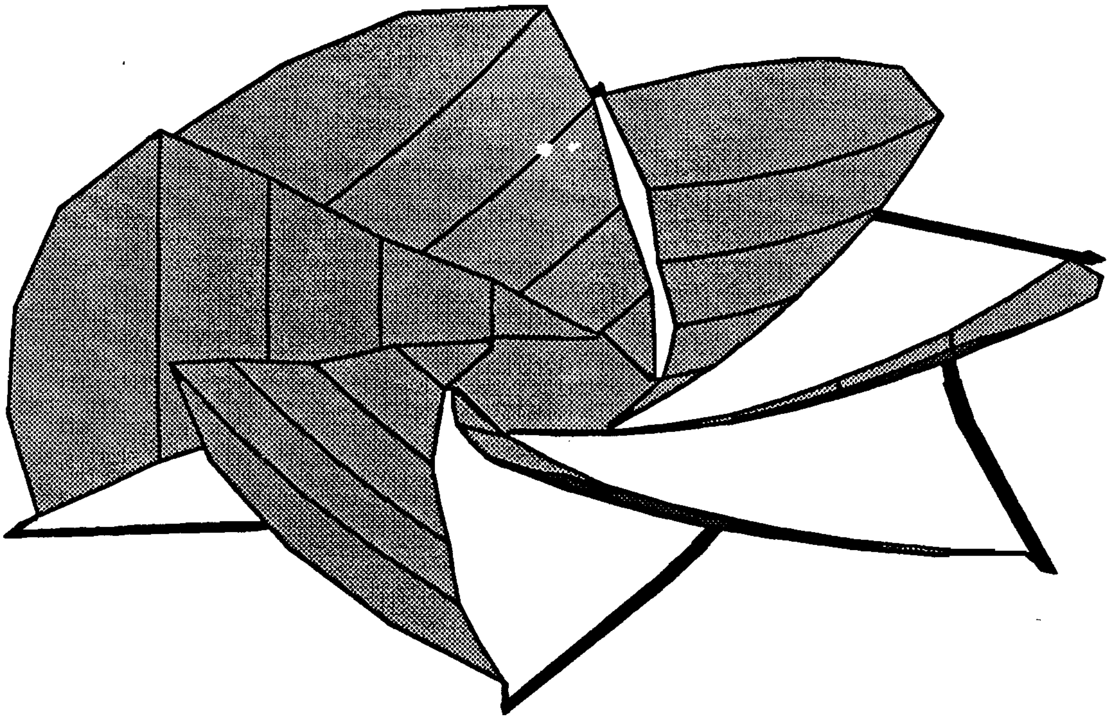

Figure 8.22. Simulation of the deployment of the SSDA: two-thirds deployed.

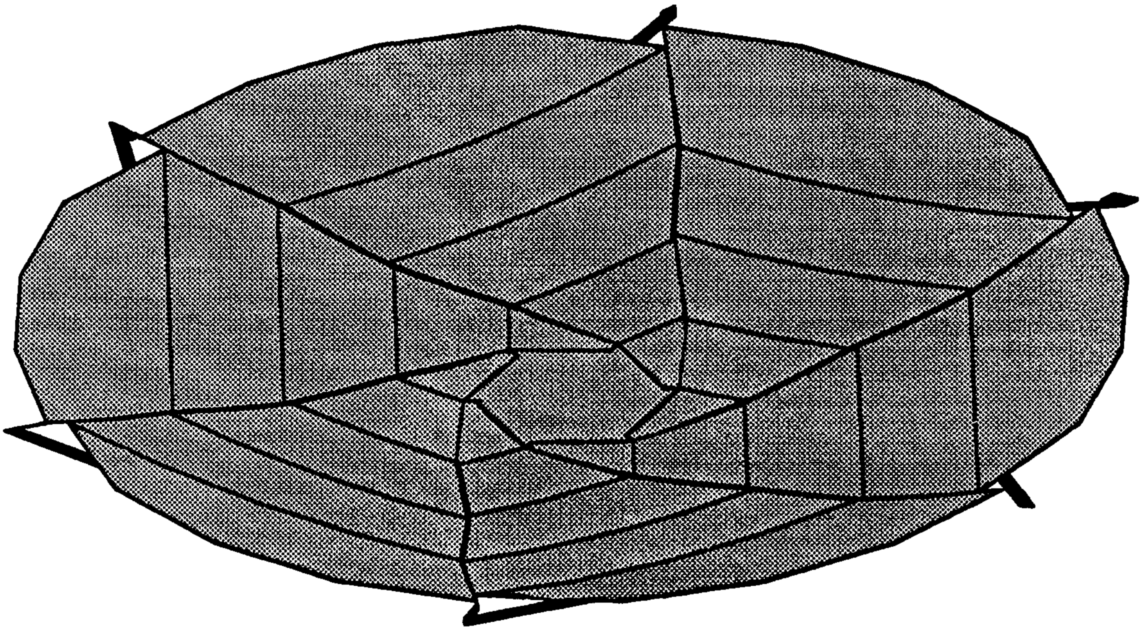

Figure 8.23. Simulation of the deployment of the SSDA: fully deployed.

8.5. Concluding Remarks

This chapter has explained how the SSDA, whose manufacture is described in the next chapter, was designed. The design process relies heavily on the tools based on dual quaternions described in Chapter 7.

Dual quaternions were used in the design process in two ways. Firstly, they were used to design the position of the connecting bar, and to determine how the antenna fitted together when folded. For this they were entirely successful. It was necessary to have a method where the position of the parts of the system could be calculated, for an arbitrary position of the hinges of the system.

The second use of dual quaternions was to simulate the folding process, and here the method is less suitable. For a purely kinematic simulation there is no problem with the method, although the solution process for a closed chain could be considerably improved. The method is much less suitable for simulations where the system does not remain a strain-free mechanism, but requires deformation of panels. The method was not designed for this purpose. However, although the method of simulating the folding process was greatly simplified, this has the advantage of reaching a solution quickly, which is particularly important in an optimisation setting.

A more realistic simulation would require additions to the theory outlined in the previous chapter. Dual quaternions could be included in the simulation to describe the deformation of the panels, which could lead to a more realistic simulation. An alternative solution would be to use commercially available software for the simulation, such as MECANO (Geradin *et al.*, 1989). An improved simulation could then be used to give a much better measure of the deformation of the antenna, e.g. the maximum strain energy during the unfolding, and this could form the basis of an optimisation, but the computational cost is likely to be prohibitive.

9. MANUFACTURE AND TESTING OF SSDA

A model was made of the SSDA whose final design is described in Section 8.4. A photograph of the final model is shown in Figure 9.1. This model is meant to prove the viability of the concept discussed, and not to be a development prototype for space hardware. There are a number of features which would not be acceptable for a real antenna; these areas would of course be changed in a better prototype.

Sections 9.1–9.4 describe different aspects of the model, and also mention how each aspect may be changed on actual flight hardware. Section 9.5 briefly describes the simple testing that has taken place, and Section 9.6 concludes the work on the SSDA.

9.1. Antenna Surface

The antenna surface is made of 3 mm thick glass-fibre. It was made by moulding the glass fibre over an existing aluminium antenna. A base was added, in the form of an aluminium annulus, to what would eventually become the hub. It was fastened to the centre of the rear of the antenna using an epoxy, Araldite.

A large number of points were marked onto the glass-fibre surface. These points not only included the corners of each of the panels, the coordinates of which are given in Table 8.1. They also included the positions where other hardware was bolted to the surface, e.g. hinges and hinge stops (see Section 9.2). The points were marked on the surface using a pen fitted to an arm on a Kearns Horizontal Boring Machine in the Cambridge University Engineering Department workshops. This machine could accurately position the pen in space, and so mark the correct coordinates.

The hinges which connect the panels together (described in more detail in Section 9.2) were accurately bolted to the uncut surface. The surface was then cut into panels using a woodworking jigsaw. The cuts between panels were not made accurately, as they are neither important to the kinematics of deployment, nor to the way the antenna fits together when folded. These properties depend on the positions of the hinges.

In practice, of course, the antenna surface would not be made from glass-fibre. It would probably be made using a honeycomb material of e.g. aluminium or Kevlar, with the front face metallised to form a reflective surface. This would give a much lighter structure for a given required stiffness.

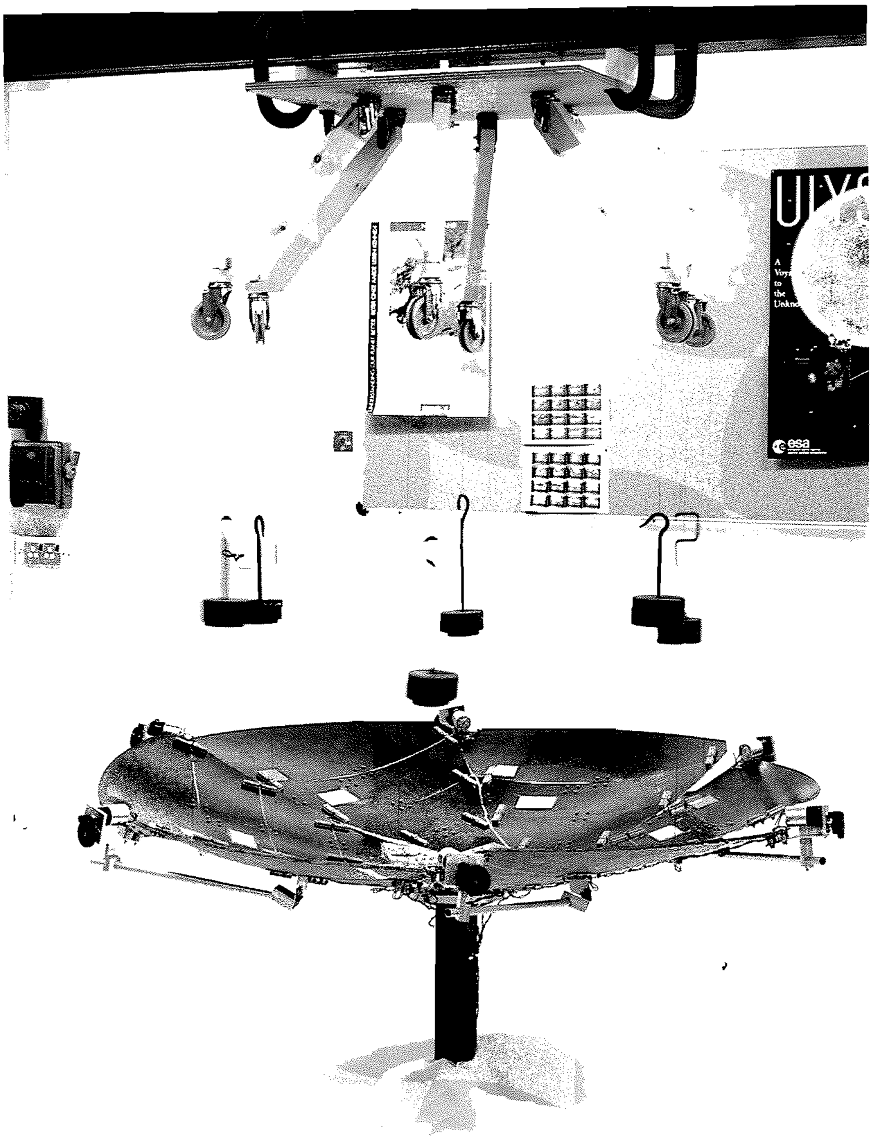

Figure 9.1. Model of SSDA, showing anti-gravity system.

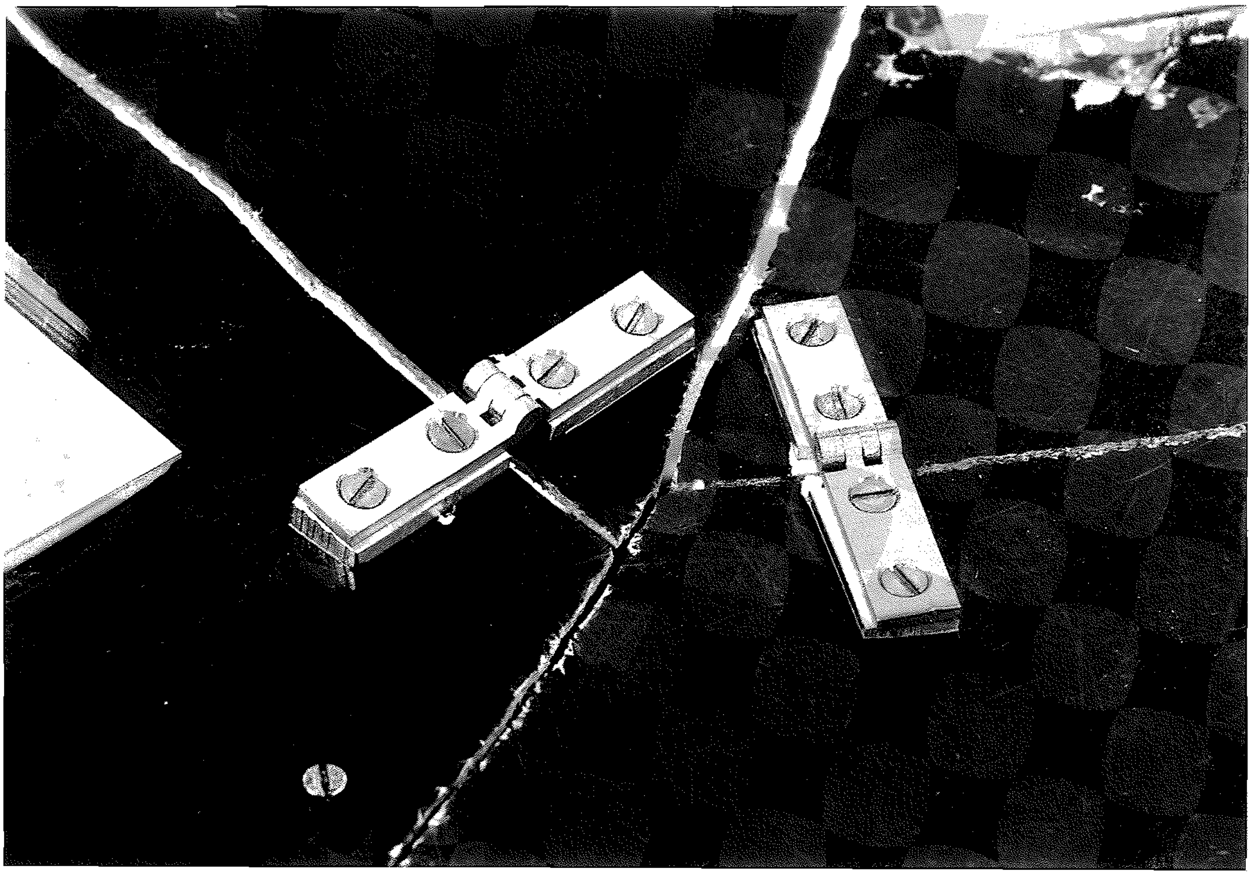

Figure 9.2. Typical hinges between panels.

9.2. Hinges Between Panels

The hinges between panels are simple brass hinges which were bought in a local hardware shop. These hinges are bolted on to the front of the antenna. Typical hinges on the antenna surface are shown in Figure 9.2.

The hinges could not simply be bolted directly to the antenna surface. All connections between panels, except between the first and second panel, were made using two revolute hinges. The axes of these hinges must coincide with the assumed hinge axis, which passes through the corners of the panels. This is shown schematically in Figure 9.3. In order for this to be achieved, appropriately sized wedges of Al-alloy were manufactured to fit beneath the hinges.

The hinges were positioned on the antenna surface by accurately marking the positions where the bolts holding the hinge to the surface pass through the surface. This was done as mentioned in the previous section. These holes were drilled, and the hinges positioned, before the antenna was cut into individual panels.

It was found that for the hinges near the hub it was not possible for the hinge axis of the brass hinges to lie on a hinge line passing through the corners of the hub. This was because the offset of the axis of the brass hinges was too great for it to be hidden by the curvature, as it is in Figure 9.3. To avoid this problem, all hinge axes on the surface were raised by 3 mm. This avoids any change in

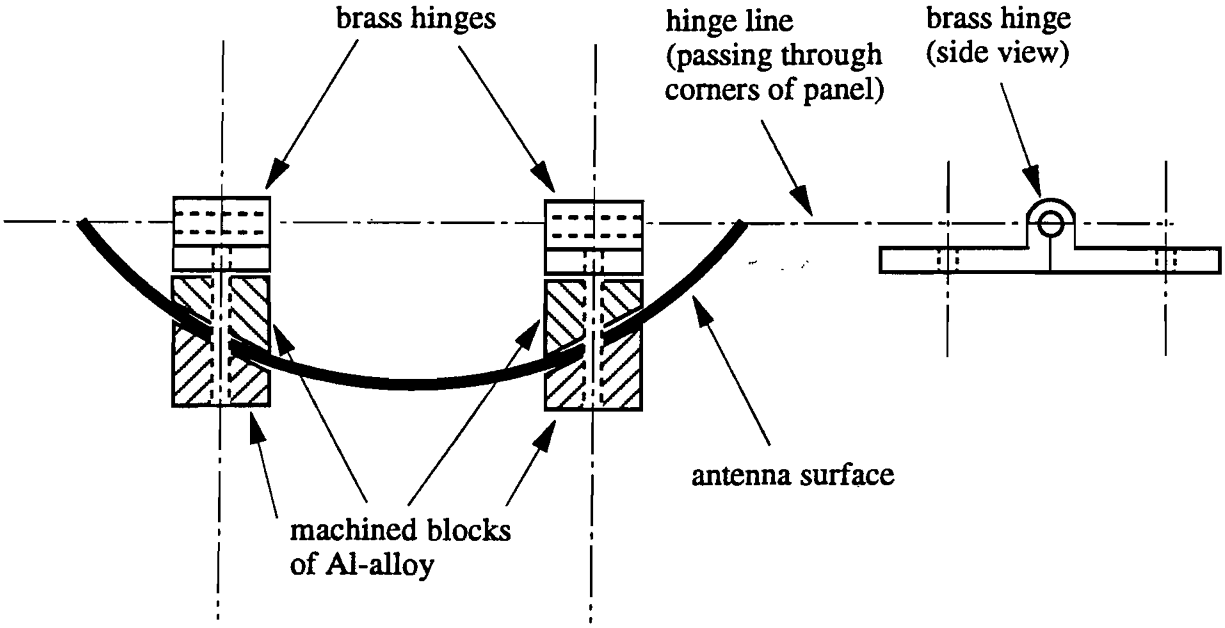

Figure 9.3. Hinges lying on the hinge line.

the kinematics or the folded shape of the structure, and is equivalent to having a surface 3 mm thicker. The change was accounted for in the simulations by making the antenna 3 mm thicker, so the back face of the computer model and the back face of the practical model coincide.

Hinge stops were also added to the model. These are small lengths of aluminium angle which are bolted to the rear of the panels at hinge lines. They were added to the surface before it was cut into panels, and they prevent the hinge from rotating past its deployed configuration.

In practice it would be necessary for the hinge mechanism not to interrupt the antenna surface. A simple way of achieving this would be for the hinges to consist of two spherical joints, one at each end of the hinge line. This would require minimal protrusion onto the antenna surface, and would eliminate any potential problem in aligning two revolute hinges.

9.3. Connecting Bar

The connecting bar connects panel 5 on one wing to panel 4 on the next. It is connected via a motorised revolute joint to panel 5, and a passive revolute joint to panel 4. The connecting bar is made of aluminium tube with an outside diameter of 16mm, and a wall thickness of 0.5mm. It can be seen in both the photograph of the passive joint in Figure 9.4, and of the motorised joint in Figure 9.5.

The passive revolute joint connecting the bar to panel 4 is again a simple brass hinge. The hinge is connected to panel 4 by an aluminium bracket. This bracket was carefully manufactured to ensure that the axis of the hinge is where it was designed to be. The bracket is connected to the panel by carefully positioned holes on the surface, which were marked as described earlier. The hinge is connected to the connecting bar through a rectangular aluminium block, in which a hole had been drilled to correctly orient the connecting bar. A photograph of the complete passive hinge mechanism is shown in Figure 9.4.

The connecting bar is attached to panel 5 by a motorised hinge. The connecting bar is initially connected through a carefully oriented hole in a rectangular aluminium block. This block can be rotated about the hinge axis by a heavily geared-down electrical motor. The whole active hinge assembly is attached to the panel by carefully positioned holes in the surface, which were marked as described earlier. A photograph of the complete active hinge mechanism is shown in Figure 9.5.

On a practical antenna, the connecting bar could be a very similar system, although more carefully engineered. A more carefully designed connecting bar could allow for a tighter packaging of the antenna when folded. The method of driving the mechanism, having distributed motors around the circumference of the antenna, is very similar to that utilised on the Hoop-Column Antenna (Campbell *et al.*, 1988). If required, the motorised hinges could easily be replaced by some other driving mechanism, e.g. a spring-damper system, or a hinge driven by memory-metal alloy. There is potential for considerable redundancy in this method of driving the antenna. If a symmetric mechanism was ensured passively, e.g. by synchronising all of the revolute joints connected to the hub (this is done

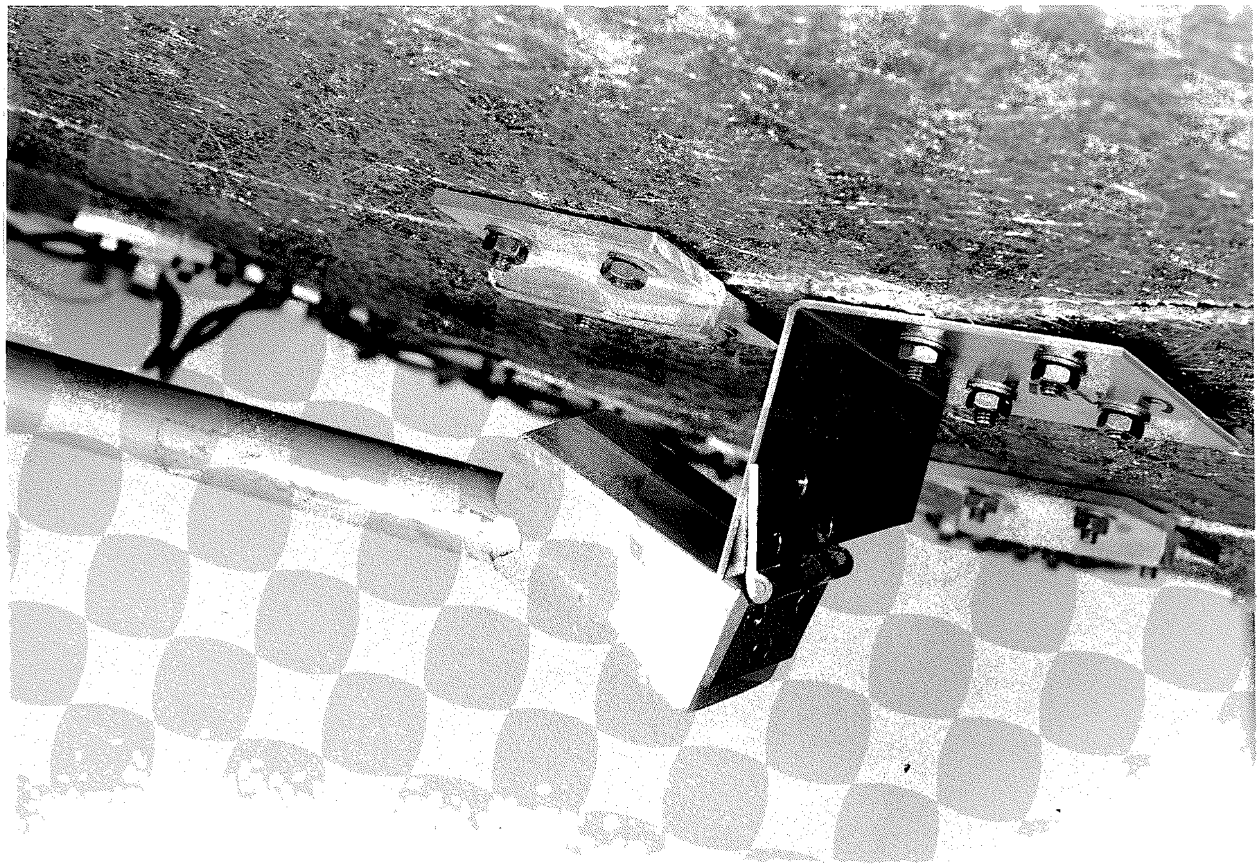

Figure 9.4. The connecting bar passive hinge mechanism.

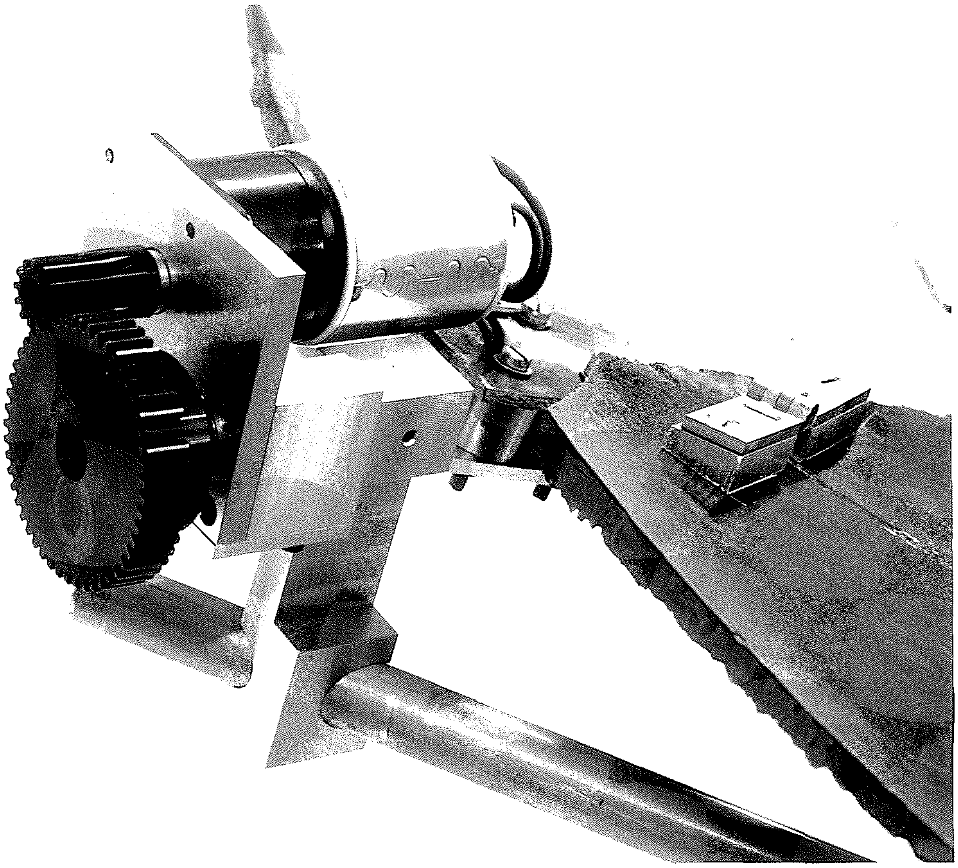

Figure 9.5. The connecting bar active hinge mechanism.

on the TRW Sunflower), then it may not be necessary for all the connecting bars to be driven by motors.

9.4. Anti-Gravity System

The model antenna surface is too flexible to retain a good parabolic shape when cut into panels. In order to test the antenna, an anti-gravity system is required.

In order to correctly simulate zero-gravity, every body should be supported at its centre of gravity. However, this would be too complex for this early model. Instead, each wing has its own anti-gravity system. A wire is attached to the surface, and runs over a pulley to an appropriate weight. The pulley itself is on a rotating bar, to allow it to remain approximately above the point on the surface where the wire is attached during deployment. The wire is attached to the surface on panel 5, close to the motorised hinge assembly. This is because this assembly represents a significant part of the weight each wing has to carry. The anti-gravity system can be seen above the antenna in figure 9.1.

9.5. Testing

The only testing that has been performed on the model has been to show that it can deploy and fold. The model is deployed and folded by simultaneously turning all the motors connected to all six wings. This ensures a symmetric folding/unfolding path. The model has been deployed and folded a number of times without problems.

A single deployment can take as little as 30 s. Four views from a deployment are shown in Figures 9.6–9.9. These views are very similar to the ones produced by the simulation of the final design, shown in Figures 8.20–8.23. This validates the simplified modelling approach for this antenna.

During the deployment, there is some evidence of both the peaks in deformation predicted by the simulation, and shown in figure 8.18. During deployment, when the antenna reaches the first peak, where the simulation predicts a jump in the angle of the hinges connected to the hub, these hinges do in practice quickly start to open. Also, where the simulation predicts a second peak in deformation, the antenna shows a small snap-through to the final, deployed, configuration.

The model SSDA deploys entirely successfully, with no manual intervention required. However, the antenna does not fold so well. During folding, when the antenna reaches the last peak in deformation predicted by the simulation (i.e. the first reached during deployment), the antenna starts to follow an incorrect path, and manual intervention is required for it to fold correctly. No studies were done on the retraction of the antenna. If an antenna was required which could both deploy and retract, then some design changes would have to be made to ensure that the correct path was followed during folding.

The final model antenna is 1.48 m in diameter (slightly larger than assumed in the design). When folded, it fits into a cylindrical envelope, 0.55 m in diameter, and 0.80 m long. Defining the initial antenna diameter as D, and the final package dimensions as diameter d and length l, this gives a d/D ratio of 0.37, and an l/D

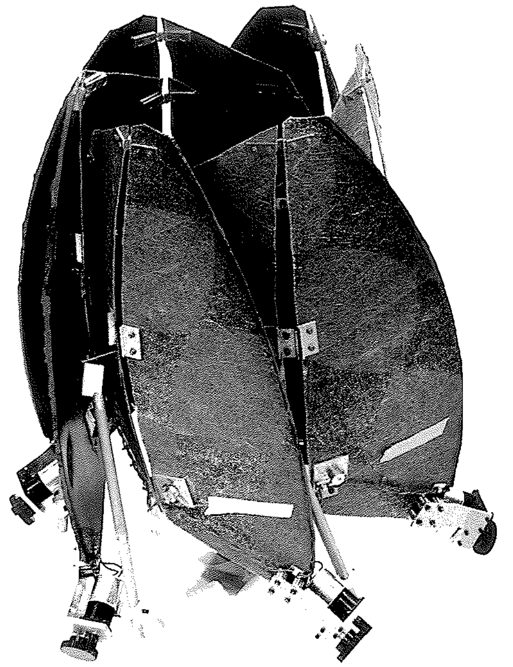

Figure 9.6. Deployment of SSDA: fully folded.

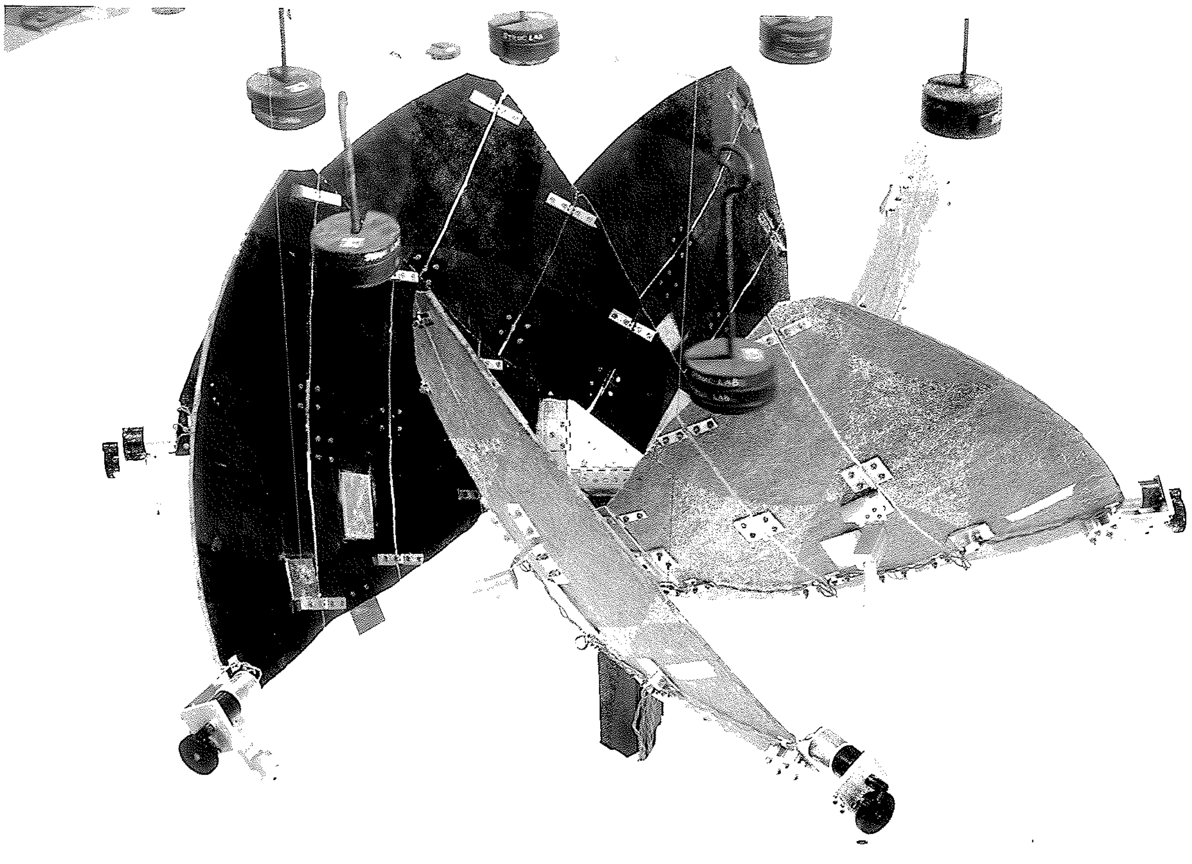

Figure 9.7. Deployment of SSDA: one-third deployed.

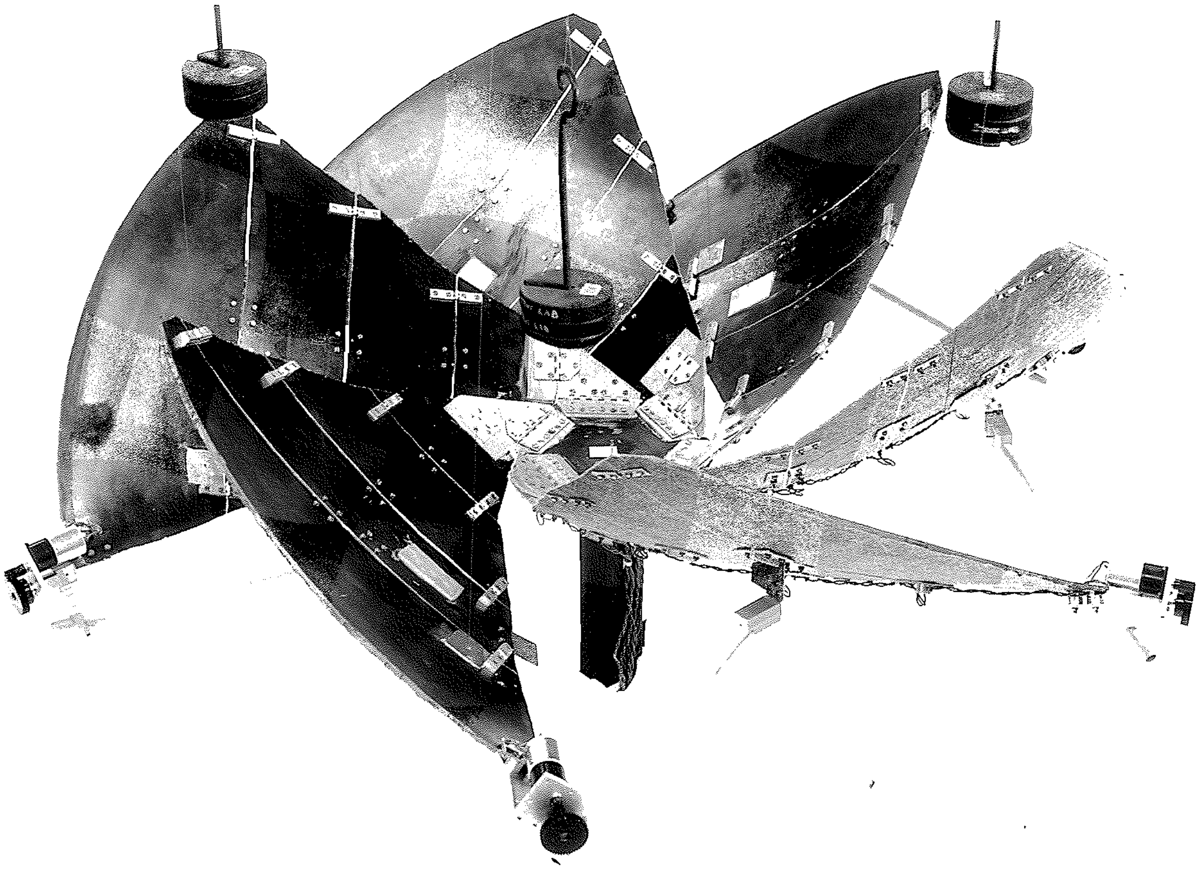

Figure 9.8. Deployment of SSDA: two-thirds deployed.

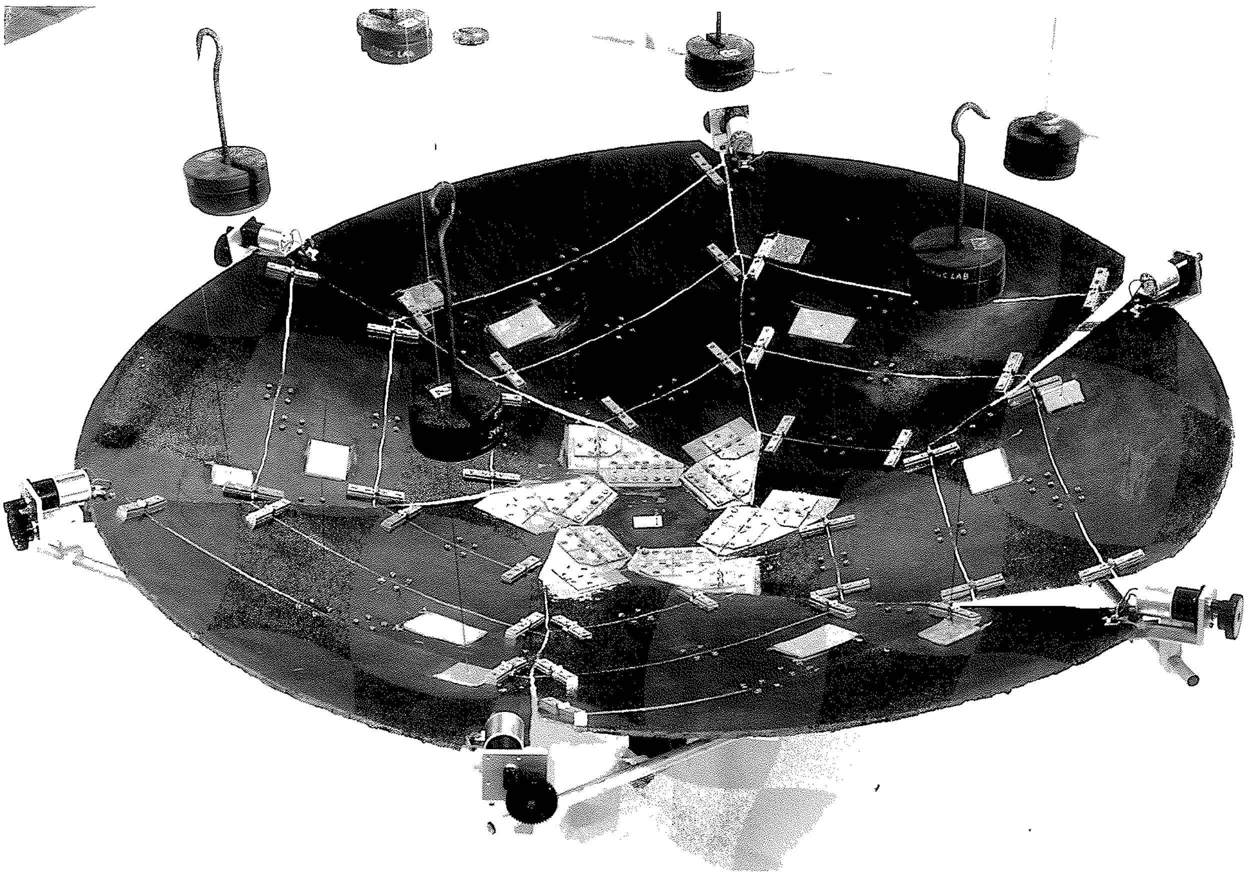

Figure 9.9. Deployment of SSDA: Fully deployed.

Table 9.1. Comparison of packaging for various deployable antennae.

Concept	d/D	l/D
SSDA (current model)	0.37	0.54
SSDA (with simple improvements)	0.29	0.50
TRW Sunflower	0.44	0.37
TRW Extended Sunflower	0.29	0.43
ESA/Dornier DAISY/MEA	0.36	0.51

ratio of 0.54. With more careful design of the connecting bar, and less conservative gaps between panels, a very similar antenna could fit into a cylindrical envelope 0.43 m in diameter, and 0.74 m long. This then reduces the packaging ratios to $d/D = 0.29$, and $l/D = 0.50$.

9.6. Conclusions

This chapter has shown a successful demonstration of the concept of the SSDA. Table 9.1 compares the SSDA with other published concepts of deployable antennae based on solid panels. Also included are figures for an improved SSDA, which could now easily be manufactured with the experience of the making the original model, by using less conservative design. The other concepts used for comparison are the TRW Sunflower concept (Archer & Palmer, 1984), and the ESA/Dornier DAISY/MEA concept (Specht, 1990). Also included are figures taken from a drawing in Hedgepeth (1989) of the TRW Extended Sunflower. It is difficult to make comparisons with this concept, as it is not clear how it works. It does, however, rely on 55 panels, considerably more than any other concept.

The most critical dimension of a payload is generally its diameter, and hence the parameter d/D is the most important packaging ratio. By this measure, the SSDA, even in its present primitive form, packs as well as the DAISY/MEA concept, and considerably better than the TRW Sunflower. With some simple improvements, the SSDA would show a much better packing ratio than the DAISY/MEA, and be equal with the Extended Sunflower. Note, however, that the DAISY/MEA concept has a much more complex deployment mechanism, while the Extended Sunflower relies on a very large number of panels, and an unknown deployment mechanism.

In terms of packaged length, the SSDA is similar to the DAISY/MEA, and worse than both TRW Sunflowers. However, the SSDA has one important advantage, because it allows for more usable space for other equipment when folded. The other concepts fold entirely in front of the mechanism hub, and so all of the space within their packaged envelopes cannot be used for other purposes. With the SSDA, half of the antenna folds by wrapping around empty space at the rear of the hub. This space could then be used for other equipment, e.g. the antenna pointing mechanism, or other parts of the satellite.

10. CONCLUSION OF DISSERTATION

This dissertation has developed a number of new concepts for use as deployable structures. Each concept has undergone some preliminary development and analysis to prove its viability. A common conceptual approach has been followed for much of the dissertation. For the design of the SSDA, and for both the geometric and computational modelling of foldable cylinders, no attempt was made to develop a model which exactly reproduced the real behaviour of the system. The approach was to find an appropriate simplified model which reproduced the important aspects of the system.

Each concept has been developed as generally as possible, mostly without reference to any specific end uses. The following three sections considers how each of the concepts developed in this dissertation may be used, and how practical issues relating to their use may be resolved. It is hoped that the lists of potential applications are not complete. The concepts have been developed in a non-specific way in the hope that this may inspire new applications.

10.1. Foldable Cylinders

Foldable cylinders are the most abstract of the new ideas developed in this dissertation. There are a number of potential application for foldable cylinders, and Chapter 5 took some steps in considering the practical issues relating to two of them.

The first, and most obvious, application of foldable cylinders is as a protective sheath around deployable booms. Such sheaths are necessary to protect thin walled booms from the effects of thermal shock. For this, the concept has two advantages over other systems. Firstly, a foldable cylinder is a developable surface. This means that it can be made from an extruded tube which is folded in the correct places. This eliminates one of the problems with a bellows type structure, where a large number of joins have to be made by e.g. ultrasonic welding, in a difficult and costly manufacturing process.

The second advantage of foldable cylinders is that they unfold, in an entirely predictable way, into a structure with stiffness and strength. It is always an advantage in deployable structures design to be able to predict what will happen during deployment, to prevent potential problems of fouling during deployment or retraction.

Another potential application of foldable cylinders is as a collapsible fuel tank. The fuel tank collapses as fuel is used, so that the fuel within the tank is always in a known place. This is an advantage for e.g. the attitude control of spacecraft. The concept is particularly apt for hydrazine, a highly corrosive rocket fuel which reacts with rubber seals. It may also be possible, by varying cylinder parameters, for the fuel tank to pressurise the fuel. This is discussed below.

A possible use of foldable cylinders further in the future is as deployable volumes. These have a number of potential uses, such as living habitats for space flight, or as space hangars (Cox & Nelson, 1982).

A number of further applications for foldable cylinders may be opened up by some adjustment of the parameters defining the cylinders, so that they are no longer strain-free both in the open and closed configurations. This alteration was suggested by the geometry plots of Chapter 3. It may give the potential for cylinders which release strain energy to open automatically, and thus become deployable booms. These booms would have the potential to carry sensitive services, such as gas pipes or data cables, within them, in a protected environment. It may also be possible to have cylinders which automatically fold, and could be used to pressurise fuel in a collapsible fuel tank, thereby eliminating the need for pumps. If these cylinders folded by forming a transition zone, the pressure supplied to the fuel would remain constant during collapse.

Another possible area of work is the application of the geometrical methods developed in Chapter 3 to other systems, specifically coilable masts. The design of coilable masts appears not to be well understood, and this method may give some valuable insights into how coilable masts work, and how they may be designed.

10.2. Wrapping Fold Pattern

The obvious application of the wrapping fold pattern is as a solar sail. This is how the present interest in this concept began. Many of the practical issues of using the pattern as a solar sail have been considered by Cambridge Consultants Ltd. (1989). The concept could also be used in other applications where a large area in space is required, such as to provide solar power.

The work on the fold pattern itself is not complete. No consideration has been given to the degenerate case mentioned in Section 6.2.2. This could lead to fold patterns where the membrane is folded into a conical shape, which may be useful to fit inside the nose cone of a launch vehicle. Another area that is worth investigating is the use of the extra fold lines called minor folds by Scheel (1974), and shown in Figure 2.3. These limit the packaged height of the membrane, and thus may be useful in packaging a membrane within a certain fixed shape.

10.3. Solid Surface Deployable Antenna

This dissertation has developed a new type of deployable reflector, the SSDA. The design philosophy behind this antenna is to keep the detailed mechanical design as simple as possible. Thus, although the geometry and the overall design process is complex, the final antenna relies only on simple revolute joints. To develop the SSDA into a flight-ready mechanical design would not require new technology; the level of technology would certainly be simpler than that required by, e.g., the MEA reflector.

The SSDA described in Chapter 9 is simply a proof of concept of the idea. A number of elements could be changed, while still utilising the same basic design. A more advanced optimisation may improve the positioning of the connecting bar, and the packing could be improved with less conservative design. The actuators, which would not have to be motors, could be placed elsewhere in the system. A coupling of the joints at the hub would lead to a system with considerable redundancy. The choice of six wings was completely arbitrary, and another number may be found to be optimum.

Major changes could also be made to the SSDA. Examples include applying the same concept to an offset parabola. There are no fundamental problems with this, but the design process would become more complex due to the lack of symmetry. Also the concept could be extended to larger reflectors by having more than five panels and more than one connecting bar per wing. There is no fundamental limit to how far this may be taken, theoretically allowing any packing efficiency to be achieved. This contrasts with other, existing concepts.

REFERENCES

Altmann, S.L. 1986. *Rotations, Quaternions and Double Groups.* Clarendon Press.

Altmann, S.L. 1989. Hamilton, Rodrigues, and the Quaternion Scandal. *Mathematics Magazine*, **62**(5).

Archer, J.S., & Palmer, W.B. 1984. Antenna Technology for QUASAT Application, ~~Large Satellite Antennas and Space Technology~~. In: *Large Satellite Antennas and Space Technology.* NASA CR-2368 part 1.

Bernasconi, M.C. 1984. Development of a 2.8m Offset Antenna Using Inflatable Space Rigidised Structure Technology. In: *Proceedings, 2nd ESA Workshop on 'Mechanical Technology for Antennas'.* ESA SP-261.

Bush, H. G., Herstrom, C. L., Heard Jr., W. L., Collins, T. J., Fichter, W. B., Wallson, R. E., & Phelps, J. E. 1991. Design and Fabrication of an Erectable Truss for Precision Segmented Reflector Application. *Journal of Spacecraft and Rockets*, **28**(2).

Calladine, C.R. 1978. Buckminster Fuller's Tensegrity structures and Clerk Maxwell's rules for the construction of stiff frames. *International Journal of Solids and Structures*, **14**, 161 - 172.

Calladine, C.R. 1983. *Theory of Shell Structures.* Cambridge University Press.

Cambridge Consultants Ltd. 1989. *Design Study for a Mars Sailcraft.* Technical Report. Cambridge Consultant Ltd.

Campbell, G., Bailey, M.C., & Belvin, W.K. 1988. The Development of the 15-meter Hoop Column Deployable Antenna System with Final Structural and Electromagnetic Results. *Acta Astronautica*, **17**(1), 69 - 77.

Cawsey, T.R. 1982. A Deployment Mechanism for the Double Roll-Out Flexible Solar Array on the Space Telescope. In: *Proceedings of the 16th Aerospace Mechanisms Symposium.* NASA CP-2221.

Cox, R.L., & Nelson, R.A. 1982 (October). *Development of Deployable Structures for Large Space Platform Systems, part 1 interim report.* NASA CR-170690.

Coxeter, H.S.M. 1980. *Introduction to Geometry.* second edn. John Wiley & Sons.

de Kam, J. 1984. Eureca Application of the RARA Solar Array. In: *Proceedings, 5th European Symposium: 'Photovoltaic Generators in Space'.* ESA SP-607.

Dent, R.N. 1980. *Principles of Pneumatic Architecture.* London: The Architectural Press.

Duffy, J. 1980. *Analysis of Mechanisms and Robot Manipulators.* Edward Arnold Ltd.

Duncan, J.P., & Duncan, J.L. 1982. Folded Developables. *Proceedings of the Royal Society of London Series A*, **383**, 191 - 205.

Eiden, M., Brunner, O., & Stavrinidis, C. 1984. Deployment Analysis of the Olympus Astromast and Comparison with Test Measurements. In: *Proceedings, 4th Europ. Symp., 'Photovoltaic Generators in Space'.*

Euler, L. 1775. Formulae Generales Pro Translatione Quaeunque Corporum Rigidorum. *Novii Comentarii AcademiæScientiarum Petropolitanæ*, **20**, 189–207. *cited by* Altmann (1986).

Geradin, M., Cardona, A., & Granville, D. 1989. *Numerical Simulation in the Deployment of Space Structures.* LTAS report. University de Liège.

Gibson, L.J., & Ashby, M.F. 1986. *Cellular Solids: Structure & Properties.* Oxford: Pergamon Press.

Goldstein, H. 1980. *Classical Mechanics.* second edn. Addison-Wesley.

Hartenburg, R.S., & Denavit, J. 1964. *Kinematic Synthesis of Linkages.* McGraw-Hill.

Hedgepeth, J. M. 1989. *Structures for Remotely Deployable Precision Antennas.* NASA CR-182065.

Hunt, K.H. 1978. *Kinematic Geometry of Mechanisms.* Oxford University Press.

Huso, M.A. 1960. *Sheet reel.* U.S. Patent no. 2942794.

Johnson, W., & Yu, T.X. 1980. The Angle of Fold and the Plastic Work Done in the Folding of Developable Flat Sheets of Metal. *Journal of Mechanical Engineering Science*, **22**, 233–241.

Jordan, J.F., Freeland, R.E., Levy, G.S., & Potts, D.L. 1984. QUASAT — An Orbiting Very Long Baseline Interferometer Program Using Large Space Antenna Systems. In: *Large Satellite Antennas and Space Technology.* NASA CR-2368 part 1.

Knouse, G., & Weber, W. 1984. NASA Mobile Satellite Program. In: *Large Satellite Antennas and Space Technology.* NASA CR-2368 part 1.

Kumar, P. 1993. *Motion of Foldable Structures Through Kinematic Bifurcations.* First Year PhD Report, Cambridge University Engineering Department.

Kwan, A.S.K. 1991. *A Pantographic Deployable Mast.* Ph.D. Dissertation, Cambridge University.

Kwan, A.S.K., You, Z., & Pellegrino, S. 1993. Active and Passive Cable Elements in Deployable/Retractable Masts. *International Journal of Solids and Structures*, **8**(1/2), 29–40.

Lanford, W.E. 1961. *Folding Apparatus.* U.S. Patent no. 3010372.

Lanford, W.E. 1963. *Reflector Space Satellites.* U.S. Patent no. 3115630.

Livesley, K.R. 1975. *Matrix Methods of Structural Analysis.* second edn. Pergamon Press.

MathWorks. 1992. *Matlab Reference Guide.* The MathWorks, Inc.

McCarthy, J.M. 1990. *An Introduction to Theoretical Kinematics.* The MIT Press.

Miura, K. 1980. Method of Packaging and Deployment of Large Membranes in Space. In: *Proceedings of the 31st IAF Congress.* Paper no. IAF-80-A31.

Miura, K. 1989. *A Note on Intrinsic Geometry of Origami.* International Meeting on Origami Science and Technology, Ferrara, Italy.

Miura, K., & Miyazak, Y. 1989. Concept of the Tension Truss Antenna. *American Institute of Aeronautics and Astronautics Journal*, **28**(6).

Miura, K., Sakamaki, M., & Suzuki, K. 1980. *A Novel Design of Folded Map.* Congress of the International Cartographical Association, Tokyo.

NAG. 1990. *The Nag Fortran Library Manual, Mark 14.* The Numerical Algorithms Group Ltd.

NASA. 1984. *Large Satellite Antennas and Space Technology.* NASA CR-2368.

O'Conner, L. 1992. Toronto Skydome, The House That Engineers Built. *Mechanical Engineering*, **114**(10), 54–57.

Okazaki, K., Sato, S., Obata, A., Natori, M, & Miura, K. 1986. Design Consideration of Mechanical and Deployment Properties of a Coilable Lattice Mast. In: *Proceedings, 15th International Symposium on Space Technology and Science, Tokyo.*

Pellegrino, S. 1993. Structural computations with the Singular Value Decomposition of the equilibrium matrix. *International Journal of Solids and Structures*, **30**(21), 3025–3035.

Pellegrino, S. 1994. Large Retractable Appendages in Space. To appear in *Journal of Spacecraft and Rockets.*

Rimrott, F.P.J. 1967. STEM Self-Extension Velocities. *Canadian Aeronautics and Space Journal*, **13**(1).

Rodrigues, O. 1840. Des Lois Géométriques qui Régissent les Déplacements d'un Système Solide dans l'espace, et de la Variation des Coordonnées Provenant de ses Déplacements Considérés Indépendamment des Causes qui Peuvent les Produire. *Journal de Mathématiques Pures et Appliquées*, **5**, 380–440. *cited by* Altmann (1986).

Roederer, A. G., & Rahmat-Samii, Y. 1989. Unfurlable Satellite Antennas: A Review. *Annales des Télécommunications*, **44**, 475–488.

Rusch, W.V.T. 1992. The Current State of the Reflector Art—Entering the 1990's. *Proceedings of the IEEE*, **80**(1), 113–126.

Scheel, H.W. 1974. *Space-Saving Storage of Flexible Sheets.* U.S. Patent no. 3848821.

Specht, P. 1990 (January). *Dynamics of Large Reflectors: DAISY/MEA Reflector—Description.* Technical Report 2100—2. Dornier GmbH.

Timoshenko, S.P., & Gere, J.M. 1980. *Theory of Elasic Stability.* second edn. McGraw-Hill Book Company, Inc.

Wade, W.D., & McKean, V.C. 1981. The Technology Development Methodology for a Class of Large Diameter Space Borne Deployable Antennas. In: *Proceedings of the 15th Aerospace Mechanisms Symposium.*

Wittenburg, J. 1977. *Dynamics of Systems of Rigid Bodies.* Stuttgart: B. G. Teubner.

Wright, J.L. 1991. *Space Sailing.* Gordon and Breach Science Publishers.

Yoshimura, Y. 1955. *On the Mechanism of Buckling of a Circular Cylindrical Shell Under Axial Compression.* NACA TM-1390.

You, Z., & Pellegrino, S. 1994. Deployable Mesh Reflector. In: *Proceedings, IASS-ASCE International Symposium 1994, Spatial Lattice and Tension Structures.*